Ductile Interfaces in Stretchable Electronics

Multi-Scale Mechanics and Inverse Methods

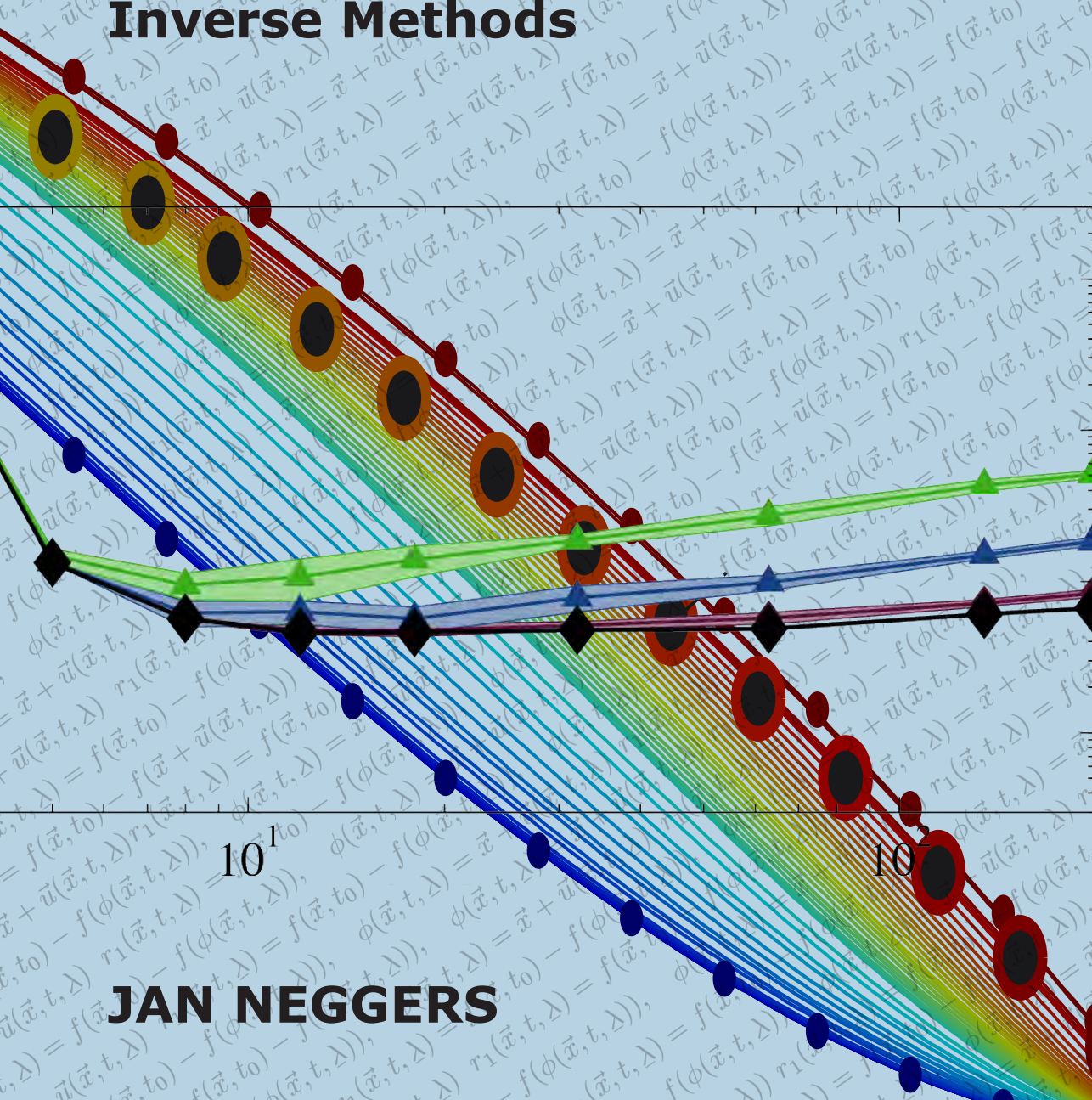

JAN NEGGERS

Ductile interfaces in stretchable electronics

Multi-scale mechanics and inverse methods

Ductile interfaces in stretchable electronics: Multi-scale mechanics and inverse methods
by Jan Neggers
Technische Universiteit Eindhoven, 2013

A catalogue record is available from the Eindhoven University of Technology Library
ISBN: 978-90-386-3511-8

Reproduction: Uitgeverij BOXPress
Cover design: J.G.P. Neggers

This research was supported by the Dutch Technology Foundation STW and the Dutch Organization for Scientific Research NWO, under grant number 08097

Ductile interfaces in stretchable electronics

Multi-scale mechanics and inverse methods

PROEFSCRIFT

ter verkrijging van de graad van doctor aan de
Technische Universiteit Eindhoven, op gezag van de
rector magnificus, prof.dr.ir. C.J. van Duijn, voor
een commissie aangewezen door het College van
Promoties in het openbaar te verdedigen op
woensdag 18 december 2013 om 14.00 uur

door

Jan Neggers

geboren te Eindhoven

Dit proefschrift is goedgekeurd door de promotoren en de samenstelling van de promotiecommissie is als volgt:

voorzitter:	prof.dr. L.P.H. de Goey
promotor:	prof.dr.ir. M.G.D. Geers
copromotor:	dr.ir. J.P.M. Hoefnagels
leden:	prof.dr. G. de With
	prof.dr. F. Hild (ENS Cachan)
	prof.dr.ir. J. Vanfleteren (Universiteit Gent)
	prof.dr. F. Pierron (University of Southampton)
	prof.dr. G.C.A.M. Janssen (TUD)

Contents

Summary

Stretchable electronics is a new field of research which focuses on integrating electronics closer to the human body. Examples of stretchable electronics are sensitive prosthetic skin, foldable displays, neuron- or retina-interfaces, skin-wearable body-monitoring applications and many more. Typical stretchable electronic products are made of electronic components and wiring, embedded in rubber films. This creates a stretchability conflict between the highly elastic rubber and the stiff components especially with the metal wiring. It has been shown that, an important factor in the failure behavior is the metal-rubber interface. A strong interface allows the load to be distributed, consequently, loss of interface integrity is quickly followed by device failure. Understanding the interface mechanics is important of improving future stretchable electronic devices. Moreover, identifying interface properties is an essential step towards modeling and predicting interface failure.

The first part of the dissertation discusses the interface delamination micromechanics by analyzing peel test experiments at three defining length scales. High magnification visualization revealed up to 30 µm long fibrils that initiate, elongate and fail at at the peel-front. The fibrillation mechanism is initiated by the high roughness of the metal surface. It is suggested that, the elastically stored energy stored in the fibrils and the nearby rubber material is lost upon fibril failure, leading to remarkably high interface toughness. This mechanism can possibly be exploited to improve the interface integrity of similar ductile interfaces.

The second part discusses a new experimental technique, focused on microscale testing of structured samples. Testing at the micro-scale is notoriously challenging, especially the handling and mounting of the small and delicate samples. The discussed method applies a pressure to deform a thin film membrane to a complex bulged shape. In order to capture the sample mechanics, the deformed sample is measured with 3D surface profilometry. The proposed method confronts the unknown material model directly with the full-field data to find the unknown material parameters, while providing robustness and noise suppression to the experimental data. The resulting framework is highly versatile, opening the experimental world by promoting the application and analysis of complex experiments, benefiting from their complexity, for instance as required to analyze stretchable electronic interfaces.

Chapter 1
Introduction

1.1 Motivation

The possible treatments available to improve the mechanical behavior of a pure material are limited, however, researchers discovered already ages ago that the way to improve the properties of a material is to mix it with other materials, for example as in 17^{th} century cold worked swords [102]. Historically, mixing of materials has mostly been concentrated on the molecular level, for instance, by mixing carbon with iron to create steel [25]. These improved materials tend to have improved properties independent of their orientation. However, the materials found in nature are typically highly directional, as for instance; bone, wood, or nacre (abalone shell) [93], but also spider silk [30].

Natural composites achieve their remarkable properties by combining tough (but soft) materials with strong (but brittle) materials in a complex hierarchical structure. For years engineers have been inspired by these materials, which resulted in a wealth of new structural materials. For instance, composite laminates [26, 41, 71], protective coatings [17, 99, 100], microelectronics [120, 145] and flexible and stretchable electronics [67, 107, 113, 137] (see figure 1.1). In all mentioned examples, stiff yet brittle materials are mixed with soft yet tough materials, however, these new structural materials excel because of the particular way the components are structured with respect to each other.

It is the synergy between the materials which is important; they need to be able to communicate and assist their partner materials. Mechanical communication occurs through load transfer, which requires sufficiently strong interfaces. Therefore, a loss of interface integrity often compromised the mechanical communication, which promotes localization, quickly followed by failure. For instance, the loss of adhesion of the protective polymer coating of a steel coke can, leading to accelerated corrosion shortening the shelf life of the product [12]. In micro-electronics applications it is hypothesized that interface failure due to thermomechanical loading accounts for over 65% of the reliability issues [120, 146].

The mentioned examples share the feature that the applied materials are particularly dissimilar in elastic moduli. At the extreme end of elastic mismatch are stretchable electronic devices, where highly stretchable elastomers (rubbers) are used to enrich the device with overall stretchability by embedding metal interconnects and rigid microelectronic components embedded in elastomer materials [5, 22, 58, 83, 84].

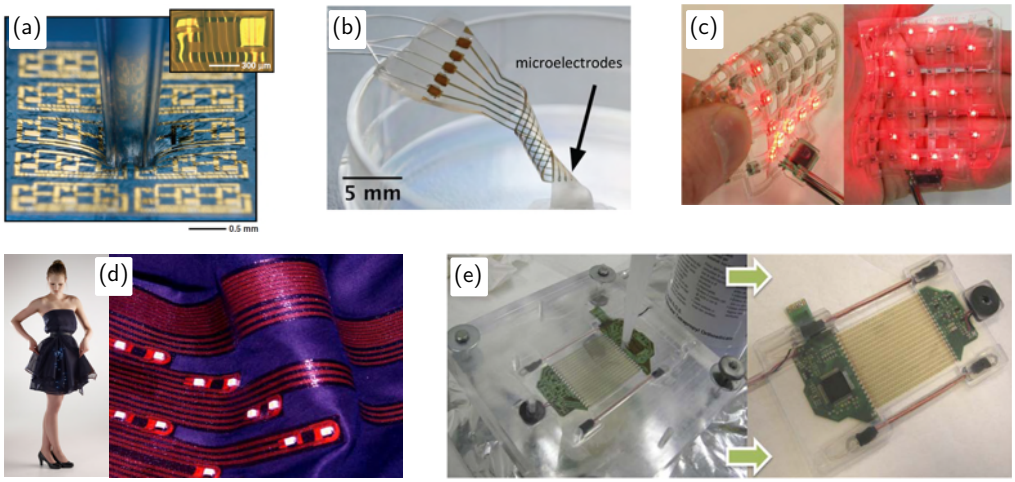

Figure 1.1: Stretchable electronics examples. (a) A stretchable silicon circuit [107]. (b) A stretchable microelectrode array, applied to neural sensing [34] (c) Stretchable LED array for wearable applications [132], (d) The Klite, light emitting haute couture [130]. (e) Stretchable Mould Interconnect (SMI) technology example [130].

Typically, the reliability of these products is improved by optimizing the geometry of the stiff components, e.g. the metal interconnect lines [18, 60]. Design optimization is more efficient in a numerical setting, where simulations provide means to analyze the performance before manufacturing expensive prototypes. Since interface delamination is often a precursor to device failure [58, 79, 80], it is important to include the interface response in the simulations. Currently, the interface mechanics of these large elastic mismatch interfaces is poorly understood [23, 82]. Consequently, the available interface modeling tools have limited predictive capabilities [116].

The interface fracture toughness is best defined as the amount of energy that is dissipated during the fracture process. The energy of adhesion between two materials depends on their particular bond type, which for these interfaces is typically a Van der Waals bond. However, for large elastic mismatch interfaces, the energy of adhesion is often not the dominant contribution to the fracture toughness [23, 31, 33]. It is the energy dissipated in the area surrounding the crack tip, i.e. the fracture process zone, or cohesive zone, which is typically responsible for the considerable fracture toughness observed for these interface types. The size of the fracture process zone depends on the properties of the bulk materials, and the properties of the interface. Consequently, the investigation of the fracture toughness of large mismatch interfaces is a multi-scale problem: (*i*) the interface is loaded at the macroscale, i.e. the length scale defined by the geometry of the device; (*ii*) the fracture process zone lives at the intermediate scale, the mesoscale, where the dominant contribution to the macroscopic fracture toughness is generated; and (*iii*) the response of the fracture process zone is driven by the underlying micromechanics and micro topology.

1.2 Goal

The goal is therefore to investigate these large elastic mismatch interfaces, and unravel the micromechanics which are responsible for the macroscale interface fracture toughness, with a focus on the elastomer-metal interface as found in stretchable electronics. Therefore, multi-scale analyses of delamination experiments is performed, and a microscale experimental method is developed to perform identification of structured functional interfaces.

1.3 Strategy

1.3.1 Part A: Multi-scale delamination analyses

In the first part of the thesis, the interface mechanics is investigated by means of peel testing. In this method the interface between an elastomer and a copper foil is peeled apart at a constant rate. The steady state nature of the experiment allows for real-time microscopic visualization, giving experimental access to all three length scales.

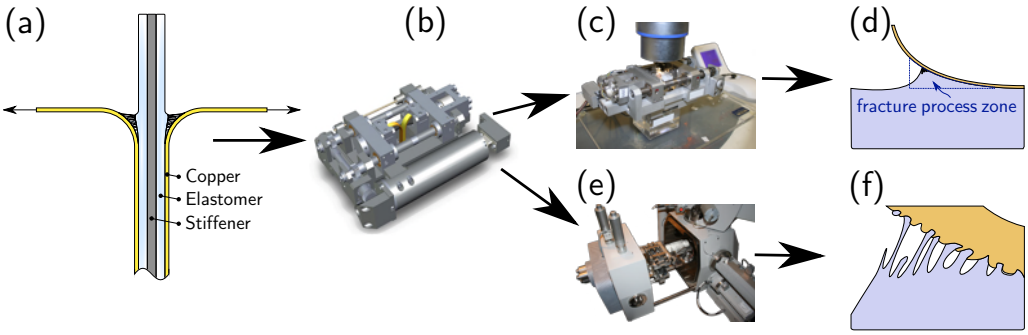

Figure 1.2: peel testing through the scales. The peel test sample (a) is mounted in a micro tensile stage (b), and is placed underneath the objective of an optical microscope (c), to analyze the fracture process zone (d). Additionally, the tensile stage is fitted in the vacuum chamber of a Environmental Scanning Electron Microscope (e), to analyze the mechanisms at the microscale (f).

It will be shown that, the multi-scale interface analyses reveals that the fracture process of these large elastic mismatch materials is a multi-scale phenomenon. The micrometer sized interface roughness initiated a fibrillation process which caused a fracture process zone of the order of millimeters (figure 1.2). This type of copper foil is common in large area stretchable electronic products. However, for small scale applications, these rough surfaces do not seem suitable as they are competing with the design length scales. To develop small scale stretchable electronic products, there is a need to analyze these interfaces at that small scale.

1.3.2 Part B: Micro-scale identification method development

One difficulty with small scale testing is mounting the samples in the test setup [95]. Therefore, the bulge test method is chosen as a starting platform to build the experimental method on, as it greatly simplifies this problem [135]. This part of the thesis will discuss a method to extend the bulge test to structured inhomogeneous membranes. First, the current application limits are investigated. Second, a custom Digital Image Correlation (DIC) method is developed based on the Global DIC method discussed by [50, 51], which is applied to the 3D surface topology imaging technique which is applied to the bulge test method. Finally, it will be shown that enhancing the bulge test with DIC did not create the required freedom to measure complex structured sample. Consequently, a fully integrated DIC method will be discussed, where the Finite Element Method is applied for increased geometrical freedom, while improving the robustness of the method by limiting the DIC degrees of freedom to the bare minimum, i.e. the unknown interface parameters (figure 1.3.2).

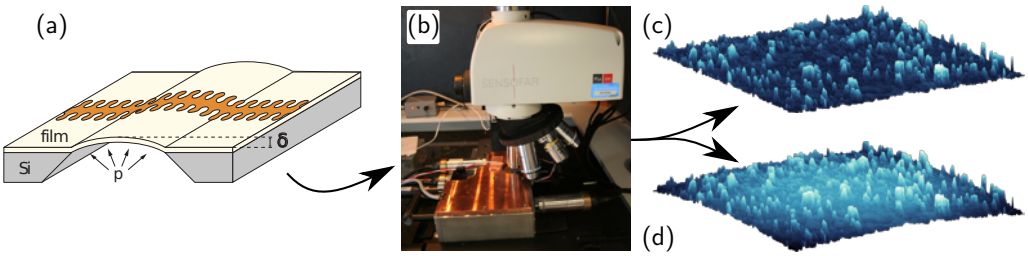

Figure 1.3: The microscale identification method; a stretchable sample with microscale structures which under pressure deflects to a bulged deformation topography (a), which is measured with a surface profilometer (b) in the reference state (c) and the deformed state (d). The displacement fields of the imaged topographies is then matched to simulated displacement fields to identify the unknown material parameters.

1.4 Scope of the thesis

In Part A, the multi-scale analyses of interface delamination experiments will be discussed in the chapters 2, 3, and 4. In Part B, the development of the microscale identification method will be discussed in the chapters 5, 6, 7, 8. The thesis ends with a reflection to the general conclusions, recommendations, and further challenges in chapter 9. It should be noted that all chapters are written with journal paper formatting in mind, such that they are individually readable. Some of the chapters have already been submitted or accepted as peer reviewed journal papers.

Part A

Multi-scale delamination analyses

Chapter 2
Copper-rubber interface delamination in stretchable electronics

Reproduced from; J.P.M. Hoefnagels, J. Neggers, P.H.M. Timmermans, O. van der Sluis and M.G.D. Geers, *Copper-rubber interface delamination in stretchable electronics*, Scripta Materialia, 63 (2010) 875–878

Abstract

Interface delamination in metal-rubber type stretchable electronic systems leads to early failure. Metal-rubber interfaces are investigated through in-situ SEM imaging of the progressing delamination front of 90° peel tests of rubber on copper samples. Results show that the energy dissipated in the forming, elongation and rupture of ~ 50 µm long fibrils constitutes the major part of the work of separation. The experiments are characterized and modeled using a cohesive zone enriched finite element model.

2.1 Introduction

To open up a realm of new electronic devices with applications close to or inside the human body, flexibility and even stretchability of the device is required. Examples of such devices are smart clothing, sensitive skin for robots or prostheses, biomedical parameter monitoring, neural activity monitoring, and intra ocular retinal prostheses [70, 85]. These devices will most likely consist of rigid functional components connected with a stretchable interconnect system [70, 85, 113, 137].

Some research groups have proposed a stretchable interconnect system by using metal (e.g. copper) interconnects embedded in a rubber matrix material [22, 74, 96]. This invokes an apparent stretchability conflict between the highly stretchable rubber (∼100%) and the metal which has a typical elastic stretchability of $< 1\%$. This conflict is typically addressed by mechanistic patterns which reduce the local stretch of the metal [22, 68, 69, 74, 96, 119]. Nevertheless, some fundamental problems remain, including low maximum stretchability and limitations to miniaturization. A key denominator in these problems is the interfacial integrity, as an initiator towards failure [78]. Debonding of the interface leads to localization of stress inside the metal interconnect, which accelerates necking and ultimately leads to failure.

A better understanding of these metal rubber interfaces may improve the interface integrity and thereby improve the stretchability. In this paper, the microscopic delamination mechanics of these interfaces are analyzed in detail through *in-situ* Environmental Scanning Electron Microscope (ESEM) imaging of the progressing delamination front in a 90° peel test. Additionally, the metal-rubber interface is characterized and simulated using a cohesive zone model, of which the traction-separation law parameters are confirmed using the experimentally obtained peel front deformation geometry.

2.2 Experimental methodology

Peel test experiments are carried out because it is an established method for measuring interface delamination properties such as the Work of Separation (WOS) [72]. A peel test experiment consists of separating the two layers of an interface at a specific angle while measuring the peel force and displacement. In this research, two bi-layer samples are glued back-to-back and both bi-layer interfaces are delaminated simultaneously using a T-type peel test, resulting in two stationary 90° peel fronts.

A micro tensile stage[1] is used, which fits in the vacuum chamber of an Environmental SEM[2] and under an optical microscope, to perform the peel tests, thereby, allowing *in-situ* imaging of the progressing delamination front. The setup is also placed inside a box, with controlled temperature and humidity, to asses the influence of environmental parameters.

All samples consist of two layers, one copper and one rubber. Two types of Cu surface roughnesses are investigated using printed circuit board grade Cu foil, 35 µm thick, which is delivered with one side roughened, exhibiting a $3-5$ µm deep fractal surface (Fig. 2.2a). Subsequently, the roughened side is covered by molding a $\sim$1 mm thick layer of PDMS[3]. The second Cu surface roughness type is processed by roughening the same Cu foil further with an electroplating technique, thereby yielding a significantly increased surface roughness with $5-10$ µm sized protrusions (Fig. 2.2b). This surface is then also covered with a $\sim$1 mm thick layer of PDMS. The as-received Cu rough surface is further on called "rough" and the electroplated extra rough surface is further on called "extra rough".

Additionally, two more types of rubber are investigated. To this end, the "extra rough" copper is laminated with a 50 µm thick layer of TPU[4]. The TPU layer is laminated at two different process temperatures, namely 180 °C and 200 °C, which will be referred to as interfaces TPU180 and TPU200. The uniaxial elongation response of the pre-laminated, TPU, PDMS, and copper is shown in Fig. 2.1a.

Typical force-displacement curves from a peel test consist of an initiation regime, followed by a steady state peeling regime where the delamination velocity equals the clamp displacement velocity (Fig. 2.1b). From this steady-state force plateau, the peel energy

[1] Kamrath & Weiss GmbH
[2] FEI XL30 ESEM-FEG
[3] PDMS: Polydimethylsiloxane, Sylgard 186 by Dow Corning
[4] TPU: Thermo plastic polyurethane, Walopur by Epurex

G can be determined as $G = F/b$, where F is the peel force and b the width of the peel front[40].

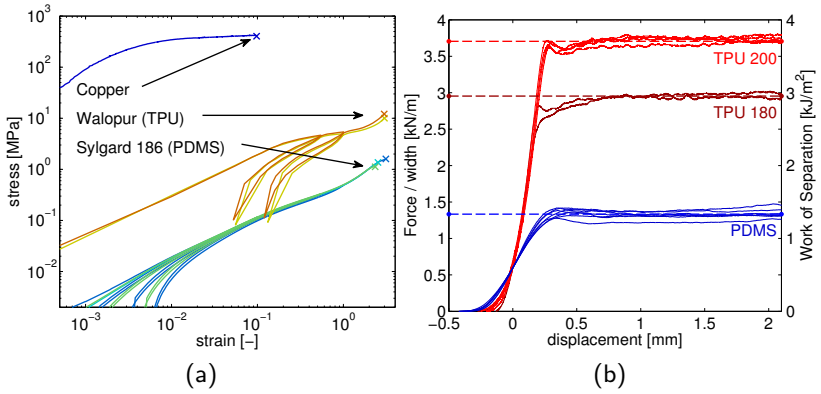

Figure 2.1: (a) Uniaxial stress-strain curves obtained from bulk samples of the as-received copper sheets and pre-laminated rubber sheets. (b) Work of separation versus clamp displacement for the three different rubber types deposited on the "extra rough" copper.

2.3 Results, analysis and discussion

As a first step, the influence of Process Temperature, Relative Humidity (RH), Temperature (T), and, Velocity (v), on the delamination behavior is investigated by comparing the WOS to that of a reference peel test ("extra rough" copper with TPU180, $RH = 25\%$, $T = 295$ K and $v = 5$ mm/s). For each parameter, the influence on the WOS to the specific parameter was determined: The relative humidity and velocity showed a negligible effect on the WOS, i.e. $< 2\%$ over the tested ranges of $0 \leq RH \leq 75$ % and $5 \leq v \leq 20$ mm/s, whereas the temperature showed a small influence of $\sim$4 % within the tested range of $295 \leq T \leq 318$ K. The TPU process temperature showed a significant influence of $\sim$23 % between the two tested processing temperatures of 453 K and 473 K. The influence of the process temperature is therefore investigated further. First, the influence of the copper roughness is addressed.

In figure 2.2, SEM images of the two types of copper roughness are shown for uncovered (pre-laminated) copper and copper after delamination of PDMS. Of the two types of copper roughness the "extra rough" copper was found to have a 40% higher WOS. More remarkably, figures 2.2c and 2.2d show that the rubber fractures during delamination leaving rubber on the copper surface after delamination, which is confirmed by energy dispersive X-ray spectroscopy. Both surfaces were laminated/molded with the same rubber (PDMS), therefore no difference in the chemical bonding characteristics are expected. Yet, figure 2.2d shows that much more rubber remains on the "extra rough" copper then on the "rough" copper (Fig. 2.2c).

Analyzing a cross-section of the "extra rough" copper samples (Fig. 2.2e) provides interesting details on this point. Even though macroscopically the interface is loaded under 90°, locally, only part of the interface at the bottom of the roughness "valleys" is loaded in mode I, whereas the part of the interface at the side walls of the "valleys" are loaded close to mode II. In addition, the irregular surface morphology increases the surface area, effectively increasing the interface strength. Finally, figure 2.2e shows that the "extra rough" copper surface contains some "valleys" that geometrically enclose the rubber, thereby mechanically locking it inside. This shows that rubber fracture is influenced by the fine scale geometrical details of the bonded interface, resulting in a larger rubber fraction left behind on the copper surface after delamination. The fact that the WOS is also 40% higher shows that a significant amount of energy is dissipated in fracturing the rubber (not in the interface debonding).

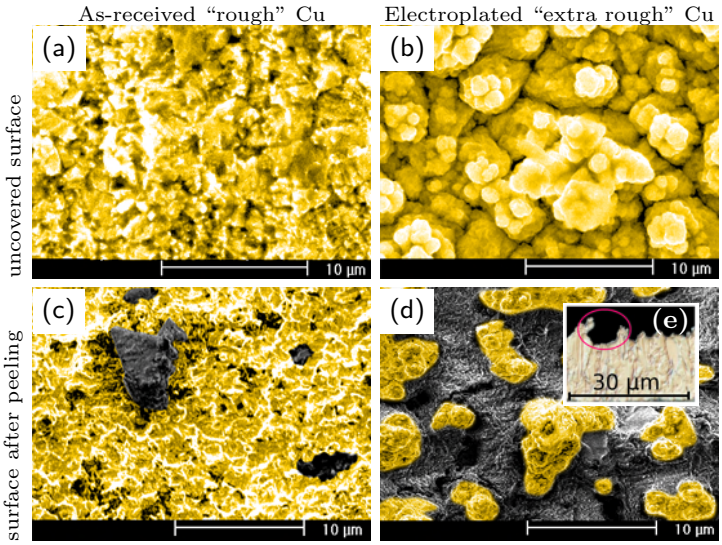

Figure 2.2: SEM images of the copper surface for two samples with different surface roughness. The bottom two images are made after delamination, showing PDMS (black) which fractured and remained on the copper (yellow) surface. Inset figure (e) shows a cross-section of a "extra rough" copper sample with rubber interlocked in the roughness valleys.

To investigate the influence of the rubber type on the delamination, the three above-mentioned rubber types were delaminated from the copper surface. The amount of rubber remaining on the surface after delamination, A_r, was determined by segmenting SEM images of the delaminated surface (top images of Fig. 2.3). Surprisingly, the results showed an inverse relation between the WOS and A_r, with the TPU200 samples having the highest WOS but lowest rubber area fraction A_r, whereas, the PDMS samples combine the lowest WOS with the highest remaining rubber area fraction.

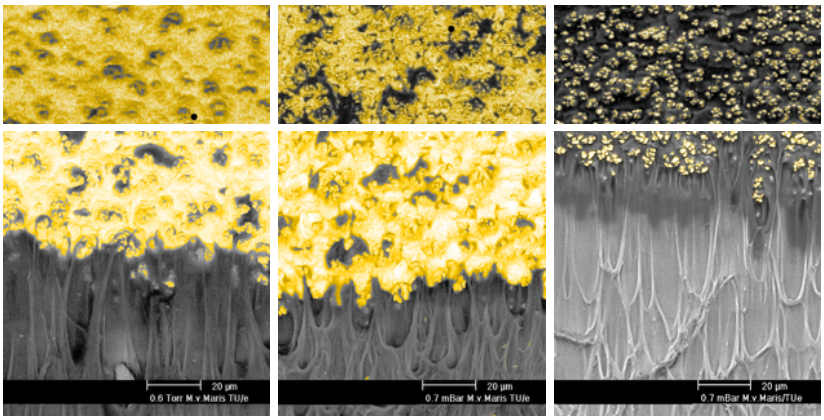

(a) TPU200
$A_r = 6\% \pm 2.5\%$
$G_c = 3.7$ kJ/m^2

(b) TPU180
$A_r = 12\% \pm 1\%$
$G_c = 2.9$ kJ/m^2

(c) PDMS
$A_r = 87\% \pm 3\%$
$G_c = 1.3$ kJ/m^2

Figure 2.3: Real-time ESEM images of the progressing delamination front (bottom) and resulting delaminated copper surface (top images). Copper and rubber appear yellow and black respectively. A_r is the rubber area fraction and G_c is the Work of Separation.

At first glare, one expects that A_r increases with increasing WOS, because a stronger interfacial bonding will keep more rubber on the surface. However, this reasoning neglects the influence of the rubber strength because a stronger rubber material will fracture less easily thereby leaving less rubber on the surface. It thus becomes clear that the rubber strength is in competition with the interface adhesion. In particular, the high A_r for the PDMS sample shows that the interface adhesion was strong enough to fracture the PDMS, whereas the low A_r for the TPU samples shows that the interface adhesion was not strong enough to fracture the TPU. This is in agreement with Fig. 2.1a, which shows that TPU is much stronger than PDMS, while it also dissipates more energy in fracturing than PDMS, on the macroscopic scale.

Hypothetically, if the interface adhesion of the TPU200 samples would be high enough to result in a rubber area fraction equal to that of PDMS (i.e. $A_r = 87\%$), then the corresponding Work of Separation of the TPU sample would be (much) higher than the current $G_c = 3.7$ kJ/m^2. Recognizing that for rubber area fractions close to 100% the work to separate the interface almost entirely consists of energy dissipated in the rubber material, it can be concluded that the fracture process of TPU during delamination dissipates at least three times more energy than that of PDMS. This shows that the dissipation in the rubber is an important factor to consider in the delamination process. Therefore, the energy dissipation mechanisms in the rubber during delamination are next investigated in more detail.

To investigate the real time fracture behavior of the progressing delamination front, the tensile stage is placed inside the vacuum chamber of the Environmental SEM. Typical images resulting from the *in-situ* 90° peel tests show that during delamination fibrils form, elongate and rupture both for PDMS and TPU (Fig. 2.3).

The fibrils which are formed are typically between 20 µm and 60 µm long with no significant differences in geometry for the three rubber types. During the formation of these fibrils, energy is dissipated while simultaneously the interface bonds are loaded. If the copper-rubber interface is strong enough, the fibril will rupture, which results in fractured rubber on the surface after peeling. However, if the fibril is strongest, then interface debonding will occur first, resulting in a (locally) clean copper surface.

The fact that, for all PDMS and TPU samples, the delaminated Cu surface was never found to be 100% clean or 100% covered with rubber illustrates the dynamic interplay between interfacial debonding on the one hand and fibril formation, stretching and rupture on the other. This delicate interplay was confirmed from the fact that SEM observations with an intentionally large electron flux and high beam voltage show early rubber fracture due to excess heating of the fibrils by the electron beam, which makes the fibrils more compliant. Because the formation, elongation and rupture of fibrils controls the delamination process, it is investigated if this behavior can be captured and quantified using a fibril oriented simulation model.

To substantiate the role of fibrilation, a fibril dominated interface model is evaluated next. The delamination of PDMS on "extra rough" copper is chosen to be modeled, since the delamination process of this interface system consists predominantly of rubber fracture instead of interface debonding (Fig. 2.3c). The interface delamination is modeled with a FEM model of a thin film of copper on a rubber substrate with equal sample dimensions as used in the experiment and with cohesive zone elements at the interface. The cohesive zones are implemented using the Smith-Ferrante traction separation law (Fig. 2.4b), which is well suited to describe fibrilation without taking surface morphology into account [47]:

$$\tau = \tau_{\max} \frac{\lambda}{\lambda_c} \exp\left(1 - \frac{\lambda}{\lambda_c}\right), \tag{2.1}$$

where $\tau = \sqrt{t_n^2 + \beta^{-2} t_s^2}$ is the equivalent traction and $\lambda = \sqrt{\delta_n^2 + \beta^2 \delta_s^2}$ the effective separation, with $t_n, t_s, \delta_n, \delta_s$ the traction and separation in normal and tangential direction respectively. The β parameter is the ratio between maximum shear and normal traction, which is set to 1, since fibrils connecting two separating surfaces are only expected to transmit tractions along their fibril axis [16].

The work of separation G_c is the area underneath the traction separation law. This formulation has three parameters G_c, $\tau_{\max}$, and λ_c, of which only two need to be identified due to their coupling: $G_c = \tau_{\max} \lambda_c \exp(1)$. G_c can be directly obtained from the level of the force plateau of the steady-state part of the peel test experiment, i.e. $G_c = 1.3\ \mathrm{kJ/m^2}$, while the value of $\tau_{\max} \approx 1.5$ MPa is found through fitting the simulated initiation regime of the force-displacement curve on the experimental data.

From the in-situ experiments (Fig. 2.3) it was observed that the rubber is severely lifted from the bulk layer at the peel front. Simulations for various values of $\tau_{\max}$ showed that this lift-off geometry is clearly influenced by $\tau_{\max}$ (Fig. 2.4c). Therefore, the shape of this lift-off geometry can be used to validate the obtained value of $\tau_{\max}$. For the values of $G_c = 1.3\ \mathrm{kJ/m^2}$ and $\tau_{\max} = 1.5$ MPa, the model is in quite good agreement with both the experimental force-displacement data (Fig. 2.4a) and the lift-off geometry (Fig. 2.4c).

This confirms that copper-rubber interface delamination, which is here dominated by rubber fracture, can be described well with a fibril-based cohesive zone model.

Despite the satisfactory agreement, it should be realized that a cohesive zone model spatially homogenizes all effects that occur at the interface, which demands for caution when comparing the cohesive zone parameters with experiments. For example, the fibril length observed in Fig. 2.3 is approximately ~ 50 µm, while the combination of $G_c = 1.3$ kJ/m^2 and $\tau_{\max} = 1.5$ MPa corresponds to a much larger critical separation of $\lambda_c = 330$ µm. One explanation for this is that the fibril microstructure is very different than the spatially homogenized cohesive zone elements, i.e. the cohesive zone overestimates the load carrying area with a factor of 10 to 100 and therefore underestimates the tractions with the same factor thereby overestimating λ_c with a factor 10 to 100 (for constant G_c). Besides the geometrical aspects in the homogenization of the interface, the model also assumes a hyper-elastic bulk material. As a result, all ignored energy dissipation taking place near the interface (in the bulk) is also lumped into the cohesive zone dissipation. Therefore, it is concluded that this type of cohesive zone modeling is obviously useful when elucidating the delamination mechanisms, but care must be taken when using the obtained parameters to simulate the same interface under different loading conditions or substrate thicknesses.

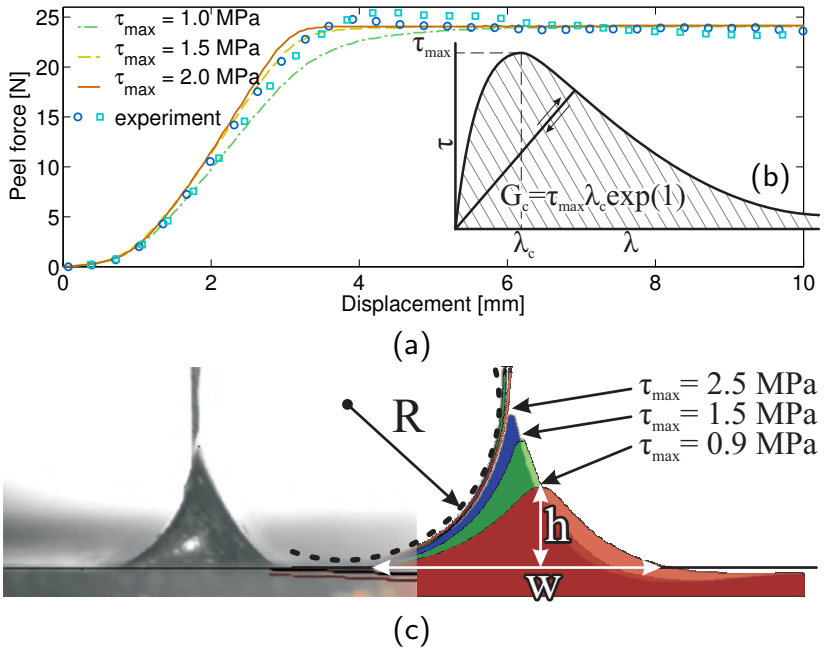

Figure 2.4: (a) Cohesive model simulations compared with experimental data. (b) Smith-Ferrante traction separation law as described by equation 2.1. (c) Three snapshots from simulations (right) for three different values of $\tau_{\max}$, showing the dependency of the lift-off geometry on $\tau_{\max}$, compared with the experimentally obtained lift geometry (left).

2.4 Conclusions

During the delamination of the investigated copper-rubber interfaces fibrilation is observed, where the dominant energy dissipation mechanism is the forming, elongation and rupture of ∼50 µm long rubber fibrils. The interaction between the rupture of the fibrils and debonding of the interface governs the final overall delamination response. The degree to which the delaminated Cu surface is still covered with rubber decreases with increasing rubber strength and/or decreasing interface adhesion. The predictive results obtained from the cohesive zone model supports the conclusion that fibrilation is indeed a dominant factor in the delamination mechanics of the investigated types of copper rubber interfaces.

The separation energy increases with increasing copper roughness with deep "valleys". Mechanical interlocking in the roughness "valleys", local surface enlargement and complex mixed-mode loading of the interface were identified as the underlying physical mechanisms that enhance the interface integrity.

The cohesive zone model neglects the microscopic surface morphology, yet provides an adequate agreement with the peel force-displacement curves and the rubber-lift geometry. Even though the peel test experiment is an adequate tool for characterizing the macroscopic interface characteristics (in particular if complemented by *in-situ* ESEM imaging during a real-time progressing delamination front) it remains debatable whether or not this test is suited for testing interface structures scaled at realistic stretchable electronics interconnect systems. For instance, will fibrilation still occur under pure mode II loading, typical for stretchable electronics operating conditions, or for interconnect dimension(s) (much) smaller than the ∼50 µm long fibrils observed here? Therefore, in future work, the delamination mechanisms of interface structures with microscopic dimensions will studied under real-time *in-situ* full-field microscopic observation.

Acknowledgments

J. Vanfleteren of IMEC Ghent and T. Löher of the University of Berlin are thankfully acknowledged for their support and input in this research, and for generously providing the sample material. P. Timmermans and O. van der Sluis thank the European Commission for partial funding of this work under project Stella (IST-028026)

Chapter 3
Multi-scale experimental analysis of rate dependent metal-elastomer interface mechanics

Reproduced from; J. Neggers, J.P.M. Hoefnagels, O. van der Sluis, O. Sedaghat and M.G.D. Geers, *Multi-scale experimental analysis of rate dependent metal-elastomer interface mechanics*, *submitted*

Abstract

A remarkable high fracture toughness is sometimes observed for interfaces between materials with a large elastic mismatch. To unravel the micromechanical origin of this high toughness, a multi-scale experimental analysis is presented. Two urethane-copper interfaces are considered with distinctly different copper surface roughness. T-peel delamination tests at a wide range of peel rates are conducted under *in-situ* optical and environmental scanning electron microscopic observation to unravel the characteristic features of the mesoscopic and microscopic peel front. For both interfaces, a fibrillation mechanism was observed, in which micron-sized TPU fibrils initiate and stretch to a huge extent, followed by either fibril rupture or surface debonding. From a detailed analysis at the microscale, it is argued that this fibrillation process is the origin of the observed high fracture toughness. The assumed mechanism is the dynamic release of the elastically stored energy upon fibril rupture.

The fibril shape, distribution, and location are shown to be related to the copper topography, clarifying the cause of fibril nucleation through a combination of (a) mechanical interlocking of the fibril base in the copper roughness 'valleys' and (b) cavitation due to large negative hydrostatic stresses at the roughness peaks. In other words, an inhomogeneous microscale interface load, triggers the initiation of the fibrillation process, which causes the macroscopic fracture behavior to be tougher. These results suggest that a fracture toughness enhancement must be feasible by engineering particular surface topographies.

3.1 Introduction

Interfaces between materials with a large elastic mismatch are of increasing scientific and industrial interest, as they are more frequently used in advanced engineering materials and devices, including, e.g., composites [71], coatings [17], microelectronics [118, 145], and flexible [131, 144] and stretchable electronics [59, 83]. The main benefit of the synergy between these materials lies in combining the high stiffness of one material with the high toughness and compliance of the other, usually soft material. Major improvements in material properties can be achieved if the interfaces are strong enough to transfer the applied loads and deformations. Consequently, interface failure often is a precursor to device failure [58, 79, 120]. Improving the interface properties thereby generally improves the robustness of multi-layered devices.

In chapter 2 a two elastomer-metal interface system is discussed with a large elastic mismatch and a large interface roughness, for which a remarkably high macroscopic fracture toughness was observed ($G_c > 2$ kJ/m^2). The coarse scale toughness largely exceeds the adhesion energy of metal-rubber valence bonds, reported to be in the range of $0.1 < \Gamma_{ad} < 10$ J/m^2 [31–33]. *In-situ* observation of the delaminating peel front of these interfaces reveal the formation of microscopic fibrils. However, the exact micromechanical origin of the enhanced fracture toughness is so far not fully understood. To enable the engineering of interfaces with enhanced fracture toughness, it is important to understand the underlying mechanics that amplifies the fracture toughness of these interface systems.

Therefore, the goal of this paper is to unravel the delamination micromechanics which are responsible for dissipating the large quantities of energy in such ductile interfaces. To this end, the 'ThermoPlastic Urethane (TPU)'-copper interface system will serve as a model system for this investigation. The strategy departs from *in-situ* high-magnification visualization of the delaminating TPU-copper peel front for different copper roughnesses. The interface micromechanics is next evaluated at a large range of peel rates to investigate delamination rate sensitivity and activate the mechanisms to different extents without altering the interfaces.

3.2 Experimental methodology

The samples are created from commercially available laminated bi-layer TPU-copper foils (TPU: 50 µm Walopur, Epurex; copper: 37 µm TW-YE, ArcelorMittal), similar to what is used in stretchable electronic applications [54, 83]. The TW-YE is a circuit grade, rolled copper foil with one relatively smooth untreated side ($R_a \approx 0.5$ µm) and one rough side, which received an extra electroplating step ($R_a \approx 1.9$ µm). Four-layer specimens are made by laminating two as-received TPU-copper bi-layer foils, enabling peel tests to be performed by clamping and pulling on a copper foil at each specimen arm, effectively creating a T-peel test. Such a T-peel test is chosen because of its optical accessibility and the stationary location of the peel front which is beneficial for imaging at high magnifications.

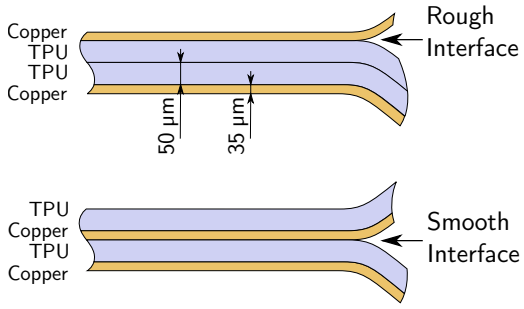

Figure 3.1: Two sample configurations, where the rough interface type is created by laminating to TPU-copper sheets TPU side to TPU side and the smooth interface type is created by laminating two sheets TPU side to copper side, effectively creating four layer samples.

Sample type 'rough' is created by laminating TPU to TPU at 180 °C, with one part of the foil not laminated to form a pre-crack (figure 3.1, top figure). Sample type 'smooth' is created by laminating TPU to the smooth copper side (figure 3.1, bottom figure), using the same lamination procedure to induce as little variation with the rough sample type as possible. Figure 3.2a shows a cross-section image taken with an optical microscope (Zeiss Discovery V20), which shows that the layer thicknesses are close to the specified thickness. Additionally, a cross-section of the copper was prepared by polishing a specimen which was embedded in epoxy, for optimal image quality. This cross-section is then imaged in a scanning electron microscope to show the complex roughness topology (figure 3.2b). The roughness topology of the electroplated copper side is additionally visualized by carefully embedding the copper foil in epoxy and polishing a cross-section, afterwards

The topography of the smooth and rough side of TW-YE copper foil are measured directly using Confocal Optical Profilometry (Sensofar Plµ2300), see figure 3.3, clearly showing the contrast in roughness between the two surfaces. Nicely shown is the cauliflower-type topography of the rough surface, which is typical for electroplated metal.

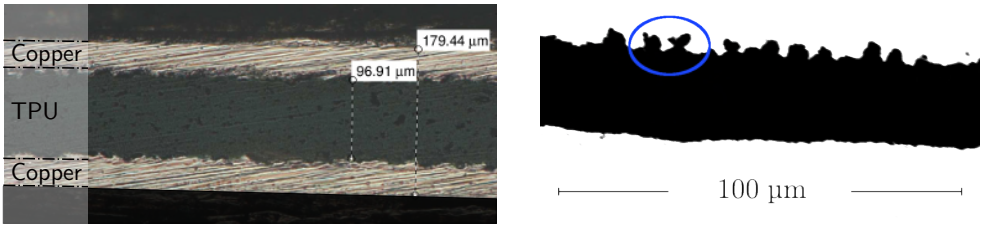

Figure 3.2: (a) Optical microscope image of the cross-section of the rough interfaces, showing the sample layer thicknesses. (b) An SEM image of copper foil (black) embedded in epoxy (white) to carefully create a polished cross-section, showing the interlocking structures of the rough interface.

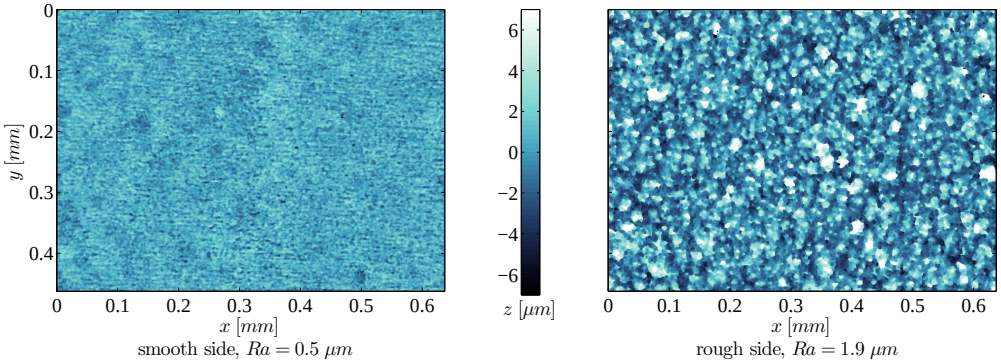

Figure 3.3: Surface topographies of the two sides of the TW-YE circuit grade rolled copper foil, as measured with confocal profilometry.

The samples are delaminated in a T-peel test or 180° peel test configuration (figure 3.4a) using the micro-tensile stage (Kammrath & Weiss GmbH) shown in figure 3.4b. In such a configuration, the two arms of the pre-crack are clamped, while the laminated part of the sample is supported in a low-friction guide to enforce a perpendicular angle with respect to the loading direction, without significantly dissipating energy.

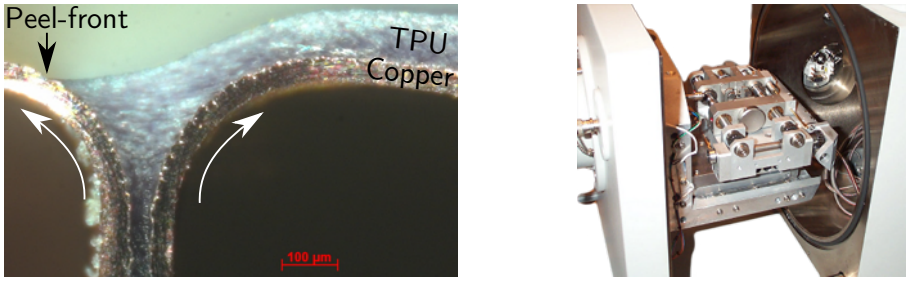

Figure 3.4: (a) *In-situ* optical microscopy side-view of a T-peel test, showing the large deformations in the TPU near the peel front. (b) The micro-tensile stage mounted in the vacuum chamber of an ESEM.

The tensile stage is small enough to fit underneath the objective of the optical microscope, or inside the vacuum chamber of an environmental scanning electron microscope (ESEM). By using the environmental mode of the ESEM, it is possible to prevent 'charging' effects, enabling high resolution imaging of the TPU. The tensile setup is such that the peel front propagates stationary allowing *in-situ* high magnification ESEM imaging of the progressing delamination front, see e.g. figure 3.5. This image shows the complex micromechanics at the peel front, which is the focus of investigation in this paper. Note, that the electron beam irradiation might easily alter the fibrillation process. This becomes clear by temporarily exposing the progressing delamination front with a typically-used

electron beam intensity, indicated by the rectangles in figure 3.5. Obviously, influence of the imaging technique on the delamination micromechanics is undesirable. Therefore, a preliminary study was carried out by careful comparison of exposed and unexposed adjacent surfaces, yielding optimized ESEM electron beam settings that stay away from influencing the fibrillation process. As the specific electron beam settings depend on the peel rate, the scanning dwell-time, and the magnification, the imaging settings have separately been optimized for each experiment.

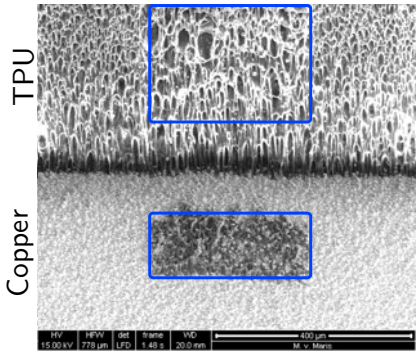

Figure 3.5: *In-situ* ESEM visualization of the delaminating peel front. In this example the possible influence of the beam on the delamination process is visualized by temporarily exposing the progressing peel front to a higher intensity (blue boxes). For all other ESEM images, the e-beam intensity is optimized to prevent this effect.

3.3 Results and discussion

3.3.1 Roughness-induced fibrillation

First, the bulk material behavior of the employed copper foil and TPU sheet are measured, see figure 3.6, which will serve as a reference for the microscopic analysis. As expected, a large elastic mismatch is visible from the large difference in modulus and fracture strain (copper Young's modulus: $E \approx 86$ GPa, TPU Neo-Hookean modulus: $C_{10} \approx 4$ MPa). Moreover, by comparing the stress-strain data at different strain rates, it becomes clear that the TPU is not a typical hyper-elastic rubber. The material shows an increase in stress level of $\sim$8% for a two times larger strain rate. Additionally the materials shows load-unload hysteresis and permanent deformation after unloading to zero stress. The constant slope between the initial loading and the initial unloading points is usually observed in glassy polymers, indicating that the TPU polymer chain segments show some stress induced mobility, at least at room temperature.

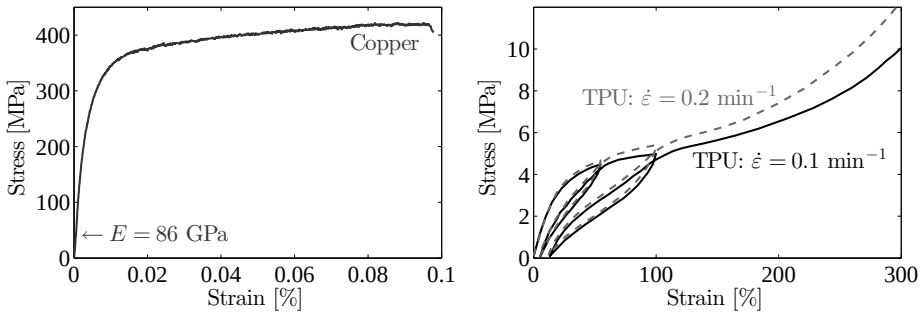

Figure 3.6: Engineering stress-strain curves, measured from macroscopic uniaxial tensile tests of TW-YE circuit grade rolled copper foil and Walopur TPU sheet (at two strain rates).

Typical force-displacement curves of peel tests of smooth and rough TPU-copper samples are shown in figure 3.7. The force-displacement curves show the expected trend; a gradual increase of the force during the crack initiation phase, followed by a constant force plateau during the stable crack growth regime. The fracture toughness is characterized by the so-called 'work of separation', WOS, which is defined as the work required to progress the peel front dU, per unit of advanced crack area, dA. Similar to what is commonly done, the WOS is calculated by dividing the applied clamp force F by the specimen width b [66, 72],

$$WOS = \frac{1}{b}\frac{dU}{da} = \frac{F}{b}, \tag{3.1}$$

where da is the increase in crack length, which in this case is assumed to be equal to the clamp displacement du, which is reasonable considering that the low peel force does not significantly strain the TPU-copper arms, by which the interface is loaded. The WOS is the macroscopic fracture toughness G_c, and includes many dissipative mechanisms for the meso and micro scales. It is exactly the purpose of this paper to investigate the lower scales and identify these various contributions.

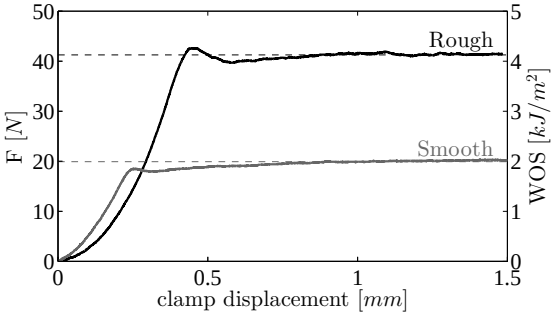

Figure 3.7: Work of separation (WOS) versus opening displacement for peel tests of the smooth and rough TPU-copper interface samples.

Macroscopically, two main observation can be made: (*i*) the fracture toughness is high, well above 1 kJ/m^2; (*ii*) a significantly larger fracture toughness is found for the rough interface. The latter was expected, as it is well-known from engineered examples that roughness influences the fracture toughness. For instance, the TW-YE copper foil is often used in large-area stretchable electronic products [57, 83, 137] due to its improved adhesion properties. The amount of fracture toughness for the smooth interface was already outstanding, and the increase in fracture toughness caused by the increase in copper surface roughness is even more remarkable.

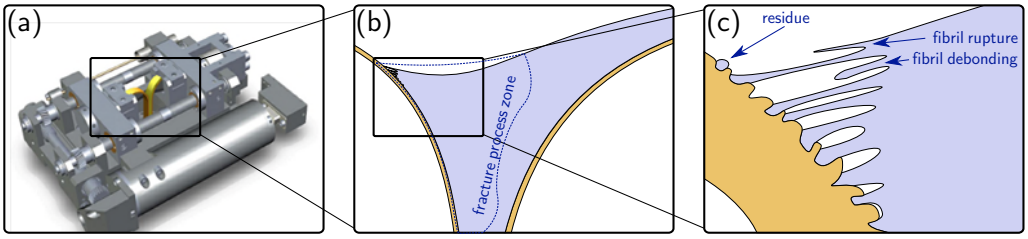

Figure 3.8: The three length scales at which the delamination process is analyzed, (a) macroscale, (b) mesoscale, (c) microscale.

At the mesoscale, defined here as the scale where typically FEM interface elements are applied, it is reasonable to decompose the WOS into the contribution of the fracture process zone Γ_{fpz} and the remaining part of the sample, i.e. the structural part of the sample Γ_{str}. The structural part contains contributions from the bulk (figure 3.8), for instance, the plastically dissipated energy due to the bending of the copper films. In a FEM model this would be the response of the bulk elements. The decomposition is akin to what is already discussed by Hutchinson and Suo [61]

$$\text{WOS} = \Gamma_{\text{fpz}} + \Gamma_{\text{str}}. \tag{3.2}$$

The effect of the structural dissipation on the WOS has been discussed before, for instance by Tvergaard and Hutchinson [129] and Wei and Hutchinson [140]. However, models based on the WOS tend to be dependent on the geometry and loading conditions of the sample. Instead, in this paper the attention is focused on the relation between the delamination micromechanics and the energy dissipated at the mesoscale (i.e. in the fracture process zone).

For the discussed T-peel test, the only significant structural dissipation component comes from the bending of the 37 µm thick copper films. The maximum strain, and thereby also the amount of plastic flow, is directly related to the bending radius of the copper. This radius was measured from images like the one showed in figure 3.4a. It was observed that the bending radius of the copper was approximately 300 µm, and did not significantly change between experiments. By performing simulations with cohesive zone interface elements with a traction opening relation, as described by van den Bosch et al. [17] and Hoefnagels et al. [54], it was observed that the structural dissipation was approximately 30% of the WOS for the rough interface. Since the copper film thickness and the peel test geometry remain constant throughout the paper, observed changes in WOS are

attributed to changes in the fracture process zone, as was also argued by Kim and Sham [71].

The fracture process zone dissipation is subdivided into several components,

$$\Gamma_{\mathrm{fpz}} = \Gamma_{\mathrm{ad}} + \Gamma_{\mathrm{ecz}} + \Gamma_{\mathrm{icz}}, \tag{3.3}$$

with Γ_{ad} is the interface adhesion energy required to brake the bonds between the materials, Γ_{ecz} is non-recoverable elastic energy in the cohesive zone, and Γ_{icz} is energy dissipated by irreversible deformation in the cohesive zone. The adhesion energy is reported to be in the range of $0.1 < \Gamma_{\mathrm{ad}} < 10$ J/m^2 [31–33], and is therefore assumed negligible considering the WOS > 2 kJ/m^2. The other two terms will be investigated further.

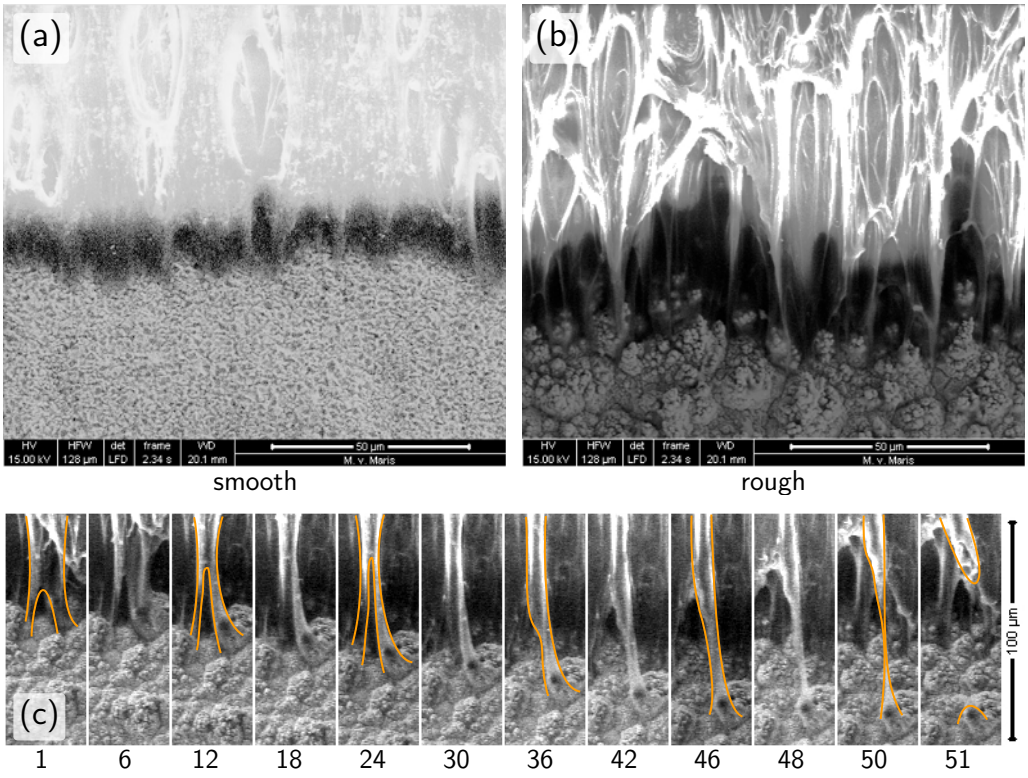

Figure 3.9: *In-situ* ESEM visualization of a delaminating peel front, showing a distinct difference in micromechanisms of both interface roughnesses. The lower image strip shows the evolution of a fibril up to failure from the rough copper. The numbers denote the image frame numbers, recorded at 1 frame per second. Guidelines have been added to mark the outline of the fibril.

Typical examples of *in-situ* ESEM images of the smooth and rough peel front, recorded during steady-state crack growth, are shown in figure 3.9ab. Both the smooth and rough interface exhibit a fibrillation process, i.e. TPU fibrils are formed. However, pronounced

differences are observed. For the rough interface, the fibrils are slender with a large fibril failure length of $L_f \approx 30$ µm, whereas the smooth interface reveals shorter and wider fibrils. The location of the fibrils on the smooth interface does not show a direct relation to the copper topography. Conversely, the rough interface fibrils are connected at the bases of the roughness peaks, implying that their distribution and geometry is initiated by the copper topography. This difference in fibril micromechanics may be related to the fact that only the rough copper surface has sufficiently large and rough protrusions to mechanically interlock the TPU material in the valleys between the protrusions, as can be seen in the detailed view of the cross-section of the rough interface shown in figure 3.2b.

The evolution of a single fibril ~~up~~ failure is shown in the lower series of images in figure 3.9. Frame 1 is the first frame where the fibril geometry can be identified. The fibril is attached at a roughness valley and elongates with increasing time. The fibril partially fails in frame 36, after which it continues to be stretched until it finally ruptures leaving TPU residue on the copper surface. From the evolution of this fibril and other studied fibrils some observations are made. First, extreme elongation of the TPU fibrils occurs, especially for the rough interface. Careful assessment of the evolution of single fibrils shows that the fibrils, after prior significant stretching to become visible at the peel front, typically exhibit a subsequent stretch ratio up to 5 before failure sets in. This corresponds to a TPU fracture strain well beyond the macroscopic TPU strain shown in figure 3.6b. It is hypothesized that, the rough copper surface creates locally strong interface spots due to mechanical interlocking, as was also observed in chapter 2, and causes large deformations in the soft TPU. Due to the geometry of the roughness, locations with large negative hydrostatic pressure are created at the peaks of the roughness, enhanced by the near incompressibility of the TPU. These hydrostatic stresses are known to initiate voids through cavitation [31, 33] which would thus first occur at the roughness peaks. Subsequently, the fibrils are elongated up to approximately 30 µm until they either rupture or debond from the copper surface.

The macroscopic peel tests show an increased fracture toughness for the rough sample type, and this extra fracture toughness must be related to the fibrillation process. Since the TPU is not fully hyperelastic, and has shown energy dissipation at the macroscale (figure 3.6), a part of the energy will be dissipated viscously during the elongation of the fibrils. Nevertheless, it is unlikely that this is the major dissipative mechanism, since the same relation between roughness and fracture toughness is observed for PDMS (Polydimethyl Siloxane) which is hyperelastic [54, 116]. Besides irreversible energy, a large portion of elastically stored energy is present in the fracture process zone, Γ_{ecz}. When the fibril fails, the elastically stored energy in the fibril, and in the adjoining TPU material is released. It is hypothesized that the majority of this energy does not contribute the to fracture process but is dynamically lost. In the image strip shown in figure 3.9, it can be seen that the moment the fibril fails, the distance to the next (younger) fibril is too far to efficiently transfer tractions. Additionally, the complex roughness geometry forces the crack to run along the side of the roughness protrusions, i.e. parallel to the opening direction, which causes crack arrest, or crack branching into the tougher TPU material. Both processes increase the macroscopic fracture toughness.

3.3.2 Rate dependent peel testing

The rate-dependent response of the TPU at macroscale (figure 3.6b) triggered an investigation to how this translates to the microscale. To this end, the rough interface is peeled in the T-peel test at various peel rates while measuring the macroscopic fracture toughness and performing *in-situ* analyses of the micromechanisms. The following microscale analyses will consist of a quantification of the fibrillation geometry as a function of peel rate, complemented with a detailed analyses of the post-delamination surfaces.

Peel rate results

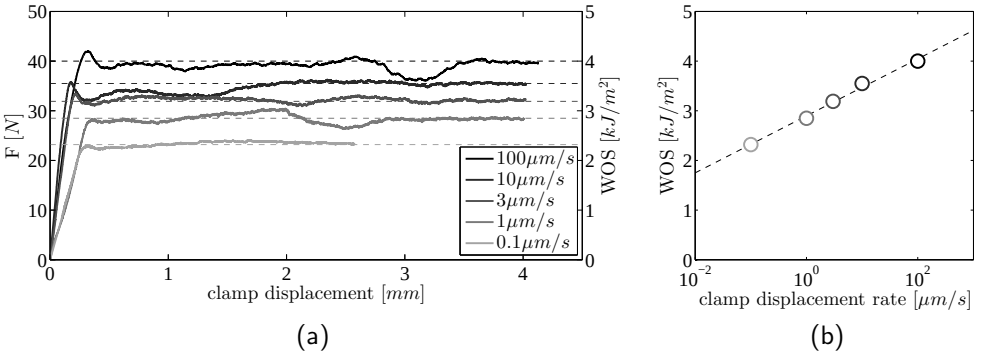

Figure 3.10: (a) the work of separation (WOS) versus opening displacement for five peel tests, performed at different peel rate, $\dot{u}$, covering three orders of magnitude and (b) the WOS-level at the steady state crack propagation plateau plotted as a function of the logarithm of the peel rate. The logarithmic fit shows a high correlation confidence with a R^2 value of 0.992.

Figure 3.10 shows the macroscopic experimental data for five typical peel test experiments with peel rates ranging from $\dot{u} = 0.1$ µm/s to $\dot{u} = 100$ µm/s. Interestingly, the measured WOS shows a linear trend with the logarithm of the peel rate,

$$\mathrm{WOS}(\dot{u}) = a \ln \dot{u} + b \tag{3.4}$$

where $a \approx 0.6$ and $b \approx 2.9$ are fitted with linear regression ($R^2 = 0.992$).

The mesoscale lift-off geometry is evaluated by imaging the peel test *in-situ* from the side, using optical microscopy. Figure 3.11 shows three of the analyzed images, illustrating that the deformed geometry is remarkably constant. For instance the radii of the copper foils have been measured by image processing of 20 images per peel rate, and was found to be 300 ± 20 µm, for each peel rate. A constant copper bending radius translates to a constant contribution of the copper plasticity to the WOS. Therefore, changes in measured WOS must be caused by the mechanisms within the fracture process zone.

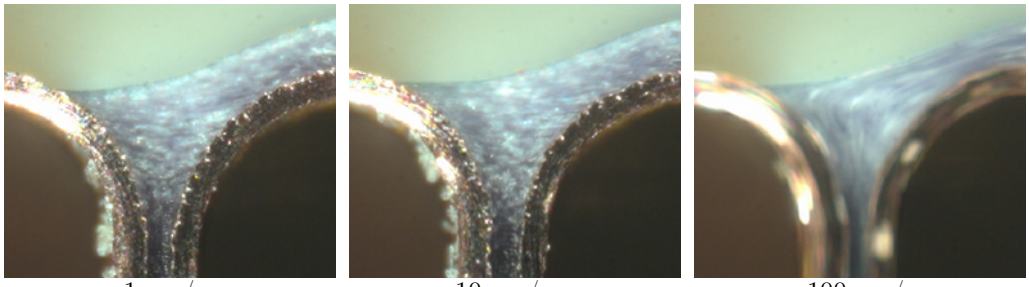

1 µm/s 10 µm/s 100 µm/s

Figure 3.11: Side-view optical microscopy images of mesoscopic peel front at various peel rates. Note that, although the work of separation in each test is significantly different, the deformed peel test geometry seems independent of the peel rate.

Similarly to the roughness microscale experiments, the progressing peel front is imaged in the ESEM, now for various peel rates. Due to frame-rate limitations of the ESEM, the faster peel rates are not analyzed. Figure 3.12, shows a typical ESEM image for each peel rate. Analogous to the mesoscale, the fibrillation process shows no significant influence by the peel rate. This is understandable from the proposed hypothesis, that the fibrillation process is initiated by the interlocking and cavitation mechanisms, which are both determined by the geometry of the copper roughness. Figure 3.13, shows the measured lengths of the fibrils, just before failure. A linear fit through the measured lengths highlights the independence of the fibril failure length on the peel rate.

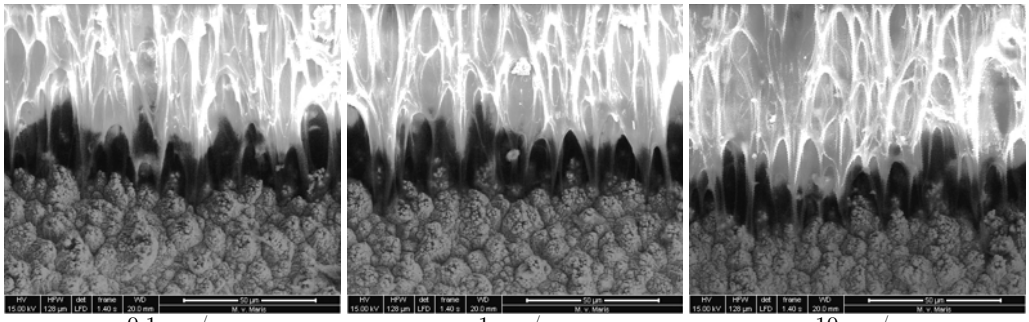

0.1 µm/s 1 µm/s 10 µm/s

Figure 3.12: *In-situ* ESEM visualization of the delaminating peel front, showing the fibrillation mechanisms at different peel rates. Interestingly, the fibril geometry appears independent of the peel rate

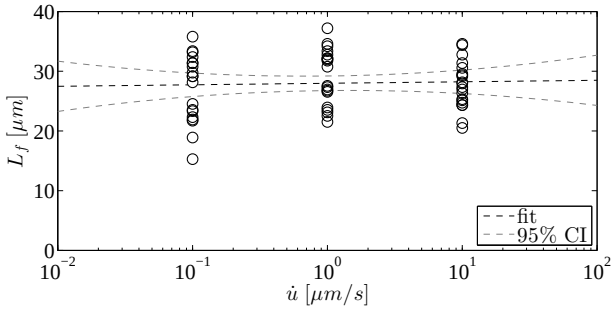

Figure 3.13: Fibril length measured from *in-situ* microscopic movies of peel tests at various peel rates. The fibril length is measured in the frame before it fractures. Note that the measured lengths are similar for all peel rates.

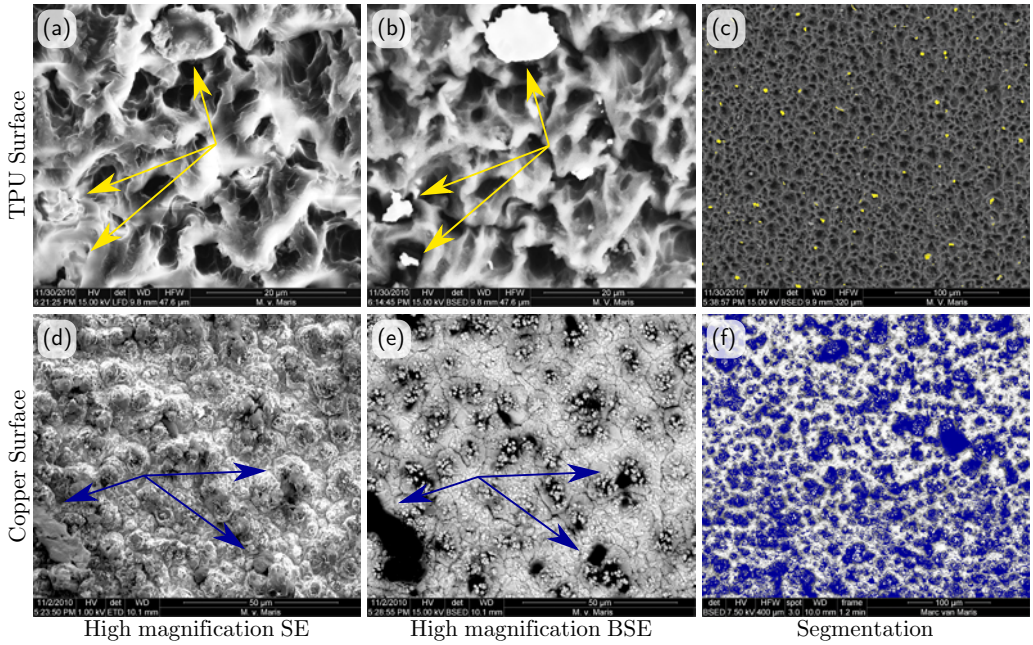

Figure 3.14: ESEM images of the post delamination TPU surface (a,b,c) and copper surface (d,e,f). On the left the topography of the surface is shown using the secondary electron (SE) detector. The center images is taken at the same location using the back scatter electron (BSE) detector in "z-contrast" mode creating maximum contrast between the copper (bright) and TPU (dark). The right images are typical examples of large-area threshold images, used to segment the image to compute the relative area of residue each surface.

During the detailed fibril evolution investigations it was noticed that some fibrils debond from the interface while others rupture, leaving residue on the copper surface, see figure 3.8c. Occasionally, a copper roughness peak is pulled of the copper surface, leaving

copper residue on the TPU surface. With the z-contrast mode of the back scatter electron detector images are created of both surfaces with high contrast between the heavy atomic mass copper (bright) and the light TPU (dark). A thresholding technique is used to compute the relative area of residue on each surface as a function of the peel rate (figure 3.14).

The relative area of residue is measured on a number of high definition images (4096×3536 px^2) of a large field of view (345×400 µm^2) for statistical reasons. The measured relative area of copper on the TPU surface A_c for each image is shown in figure 3.15a, and the relative area of rubber on the copper surface A_r of each image is shown in figure 3.15b. From these figures a few details are observed: (*i*) The amount of copper residue on the TPU surface is small for all peel rates implying that the copper fracture process does not significantly contribute to the fracture toughness; (*ii*) The amount of copper fracture increases with peel rate. Assuming a normal distribution among the copper peaks, then more fracture of roughness peaks suggests that, on average, the surface experienced higher loads indicating that the tractions in the fibrils increase for increasing peel rates; (*iii*) The significant amount of TPU residue on the copper surface indicates that fibril fracture is an important mechanism, suggesting that regularly, the crack front deviates into the fibril instead of following the interface; (*iv*) The amount of TPU residue increases for increasing peel rates, demonstrating that more fibrils fracture when the interface is loaded faster.

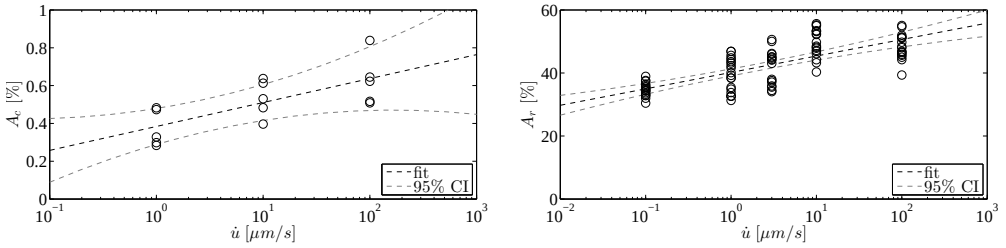

(a) A_c (b) A_r

Figure 3.15: (a) The relative area of copper on the TPU surface, A_c, as a result of the delamination as a function of the peel rate. (b) The relative area of TPU on the copper surface, A_r, as a result of the delamination as a function of the peel rate. Note that both show an increasing trend for increasing peel rates.

Peel rate discussion

Interpretation of the peel rate dependent results starts with the observed increase in fibril traction (i.e. observation (*ii*) above). The TPU showed a viscoelastic response macroscopically (3.6), from which the higher tractions observed at the micro scale can be explained. Higher tractions in the fibrils may result in the observed higher energy dissipation, either through increased irreversible deformation in the fibrils, or through increased dynamically lost elastic energy. Just the higher traction alone can explain the higher energy dissipation, even if the observed fibril geometry (microscale) and fracture process ~~are~~ zone geometry (mesoscale) are constant.

Higher tractions in the fibrils imply higher tractions at the copper-fibril interface, from which more fibril debonding would be expected. Interestingly, the TPU residue measurement shows the opposite, i.e. more fibril fracture and less fibril debonding occurs for higher peel rates. This suggests that the adhesion of the fibrils to the copper increases with the peel rate, i.e. the interlocking mechanism is more effective at higher peel rates, which would lead to improved adhesion and therefore more fibril fracture. Delaminating an interlocked area requires that the TPU flows out of the copper geometry. Because the flow stress is naturally rate dependent, this theory is consistent with the observed behavior.

Finally, the fibril fracture length was measured to be independent of the peel rate within measurement uncertainty, suggesting that the fibril fracture strain is also rate independent. Additionally, the mesoscale deformed geometry was also measured to be rate independent within measurement uncertainty (figure 3.11), suggesting that the fracture process zone does not change with peel rate. This leads to the assumption that the shape of the traction profile along the fracture process zone is a rate-independent function $f_\tau(\vec{x})$ of the position, and only the traction amplitude $c(\dot{u})$ scales with the peel rate,

$$\tau(\vec{x}, \dot{u}) = c(\dot{u}) f_\tau(\vec{x}), \tag{3.5}$$

For the T-peel test, the WOS is computed from the measured force, which is balanced by the traction profile of the fracture process zone,

$$\mathrm{WOS}(\dot{u})b = F(\dot{u}) = \int \tau(\vec{x}, \dot{u})\,\mathrm{d}\vec{x} = c(\dot{u}) \int f_\tau(\vec{x})\,\mathrm{d}\vec{x}. \tag{3.6}$$

This would suggest that the logarithmic relation between the WOS and the peel rate, shown in figure 3.10b, transfers to the fracture process zone as a logarithmic relation between the flow stress and the strain rate, as also discussed by e.g. Liechti and Wu [81] and Geiß-ler and Kaliske [39]. Such single relaxation time behavior reminds of Eyring flow typically observed in glassy polymers, possibly indicating that stress induced polymer chain mobility is contributing to the rate-dependent fracture toughness observed at the macro scale [36].

3.4 Conclusions

Interfaces between materials with a large elastic mismatch, which are of increasing interest for advanced engineering materials and applications, may exhibit an exceptionally high fracture toughness. To unravel the micromechanical origin underlying this high toughness, a detailed characterization was conducted on two elastomer-metal (TPU-copper) interfaces, which only differ in the copper surface roughness. To this end, T-peel tests were performed under *in-situ* optical and environmental scanning electron microscopic observation. This enabled a multi-scale experimental analysis that included the macroscopic work of separation, real-time observations of the mesoscopic and microscopic peel front with its underlying micromechanisms, and postmortem microscopic analyses of the delaminated surfaces. Moreover, the rate-dependency of this TPU-copper was

investigated by comparing the experimental results for peel tests delaminated over three rate decades.

It was found that the interface roughness triggers a fibrillation mechanism at the delamination front, in which micron-sized TPU fibrils are formed with a distribution and geometry that is governed by the copper topography. Specifically for the rough interface, fibrils were clearly shown to be connected at the 'valleys' of the roughness protrusions, and individual fibrils were observed to continue to deform after the peel front passed, thereby exhibiting a huge elongation, until fibril fracture or interface debonding set in. The origin of this fibrillation process, as well as the large difference in fibrillation micromechanics between the smooth and rough interface, was attributed to an inhomogeneous interface load, caused by locally interlocking areas in the valleys of the roughness and cavitation at the peaks of the roughness. Arguably, this fibrillation process spreads out the energy dissipation over a larger (process) zone by forcing the interface crack to arrest and even kink or branch away from the interface and into the bulk materials.

Peel tests at a wide range of peel rates provided new insight in the delamination micromechanisms, such as the extent of crack branching into the TPU fibrils. From a detailed microscale analysis, it was suggested that the macroscopically observed increase of the work of separation (WOS) with increasing peel rate is due to an increase in flow stress of the TPU material within the process zone, probably accompanied by more effective mechanical interlocking at high peel rates. Finally, it was found that the major contribution of the work of separation is the consequence of the fibrillation process, i.e. the formation, stretching, and rupture of the fibrils, where part of the energy is dissipated viscously, and by dynamically dissipating the elastically stored energy in the fibrils, or in the near-fibril bulk material, released upon fibril rupture.

In the fibrillation mechanism, a delicate balance exists between the fibril debonding at the interface and fibril rupture. If the (microscale) fibril-copper adhesion is insufficient, the fibrils will debond before building up strain energy and reaching their full dissipative capacity. Therefore, the key to optimize the fracture toughness is to maximize the allowable tractions of the fibrils, for which a strongly interlocking structure is required at the base of the fibrils. One way to achieve this, is by employing similar high roughness interfaces as the ones investigated here. This is indeed being applied in large-area stretchable electronics (demonstrators), because these applications allow for relatively large interconnect sizes. It is interesting to see if an artificial roughness, designed to initiate cavitation and interlocking, can initiation fibrillation and provide similar enhancements in fracture toughness.

Acknowledgment

T. Löher of the University of Berlin is gratefully acknowledged for his support and input in this research, and for providing sample materials. Additionally, the following students are acknowledged for their contributions; O. Sedaghat, A.P. Ruybalid, K. Hu, T. v. Lochem, U. Hoeberichts, and J.L.T.P. Basten. Finally, M.P.F.H.L. van Maris is acknowledged for his general technical support on the experiments.

Chapter 4
Characterization and analyses of metal-elastomer interface fibrillation

Reproduced from; J. Neggers, J.P.M. Hoefnagels, O. van der Sluis, and M.G.D. Geers, *Characterization and analyses of metal-elastomer interface fibrillation*, *submitted*

Abstract

Interfaces between materials of with large a elastic mismatch are commonly found in stretchable electronic applications, where metal interconnect wires are adhered to stretchable elastomer substrates. High fracture toughness values are observed for these interfaces. This research investigates the multi-scale experimental mechanics linking the macroscopic fracture toughness to the microscopic delamination mechanisms.

Two interface types are tested, which differ in surface roughness, by means of a T-peel test and a shear-peel test. The interfaces are characterized on the macro-meso scale by matching the experiments with FEM simulations where the interface is modeled with cohesive zone interface elements. This reveals an improved fracture toughness with increasing roughness. Additionally, both roughness types showed a low (macroscopic) mode angle dependency.

To analyze the physical origin of this interfacial response, the delamination experiments are visualized at high magnification in a scanning electron microscope. A fibrillation mechanism was observed at the peel front, where 30 µm long fibrils are formed by a combination of interlocking in the roughness valleys and cavitation at the roughness peaks. A significant portion of the fibrils rupture, instead of debonding at the copper surface, suggesting that the complex roughness geometry causes the crack to deflect into the PDMS material instead of may propagating along the interface.

4.1 Introduction

The field of stretchable electronics is increasing in research momentum due to the envisioned impact this technology can make in our every day life [70, 107, 113, 137]. In stretchable electronics, metals are typically applied as the conductor in a stretchable matrix, for which elastomers or rubbers are a common choice [57, 84]. This creates a

stretchability conflict between the highly stretchable elastomers and the stiff metal conductors. It has been shown that metal-elastomer interface delamination often occurs, which leads to accelerated fatigue in the delaminated metal interconnects [58, 80, 142]. Typically, the interconnect designs are optimized for shape to postpone failure as much as possible, which is a process that relies on the predictive capabilities of Finite Element Method (FEM) simulations [42, 59, 96]. Therefore, these simulations have to include interface failure, which is usually implemented through zero thickness Cohesive Zone (CZ) interface elements, described by a Traction Separation Law (TSL) [15, 17, 81, 116].

In chapter 2, two stretchable electronics interfaces are discussed, which showed an exceptional fracture toughness $G_c > 2$ kJ/m^2, especially when compared to the pure physical adhesion energy, which is reported to be in the order of $\Gamma_{\text{ad}} \approx 1$ J/m^2 [31, 32]. This remarkable fracture toughness was attributed to a fibrillation mechanism in the process zone, where micron size elastomer fibrils are initiated, stretched and elongated until they either rupture or debond from the interface. Chapter 2 also compared the fibrillation mechanism quantitatively with the macroscopically characterized TSL parameters, where a large mismatch was found between the critical cohesive zone opening parameter and the observed fibril length. It was concluded that in the CZ method all dissipative mechanisms occurring near the interface are effectively lumped into the CZ element. This homogenization effect is a consequence of characterizing and applying the CZ method at the macroscale. Consequently, the predictive capabilities of the characterized interface model are limited to applications where the interface is loaded in conditions resembling the characterization experiment. Moreover, in chapter 2 the "rubber lift-off" geometry was used to characterize the additional TSL parameters (critical opening, maximum traction). This "lift-off" geometry is formed by the interface tractions on the stretchable elastomer, pulling part of the material out of the bulk at the scale of the process zone. This mesoscale phenomenon introduces a rotation of the effective opening angle with respect to the macroscopically applied opening angle. Consequently, the quantification of the load angle is ambiguous. For a large elastic mismatch, the angle at which is the load is applied is usually different than the load angle in the fracture process zone, which typically is not constant through the fracture process zone [61]. Moreover, at the microscale, the surface roughness and fibrillation change the mode angle again.

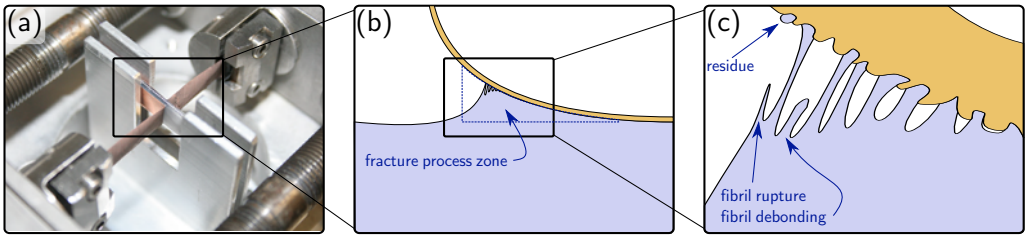

Figure 4.1: The three length scales which analyzed in this chapter, visualized for a T-peel test, (a) macroscale, the scale at which the load is applied, (b) mesoscale, defined by the fracture process zone, (c) microscale, the scale where the dissipative mechanisms are active.

The understanding of these large elastic mismatch interfaces will need to be improved in

order to obtain models with enhanced predictive capabilities, required for device design and optimization. Moreover, through a better understanding, opportunities may arise to enhance the fracture toughness to exploit novel insights to smaller length scales needed for future microelectronic applications. Clearly, the fracture mechanics of these interfaces is a multi-scale problem. Typically three scales can be identified, (*i*) the macroscale, defined by the sample dimensions and the locations where the load is applied, (*ii*) the mesoscale, defined by the fracture process zone, (*iii*) the microscale, defined by the delamination micromechanics, e.g. the fibrillation process and the interface roughness, see figure 4.1.

The goal of this chapter is to unravel the micromechanisms responsible for the enhanced fracture toughness and their relation to the mode angle sensitivity in these ductile interfaces. The adopted strategy is to analyze the mode dependent response of PDMS-copper interfaces with two macroscopically distinct opening angles (0° and 90°), varying the interface roughness to analyze the effect of microstructure. The macro-meso mechanics are first studied by applying a mode-dependent interface model that is identified from experiments, taking the mesoscopic deformations at the process zone into account. Second, *in-situ* high magnification Environmental Scanning Electron Microscopy (ESEM) is applied to reveal the micromechanics and unravel their contribution to the macroscopically observed mode dependency.

4.2 Macro-mesoscale investigation

Before analyzing the delamination mechanisms at the microscale, a typical interface analysis is performed. For these ductile interfaces, the critical interface opening is an important parameter. Measured force-displacement data of a delamination experiment is not enough to characterize all the constitutive parameters of an interface model. Consequently, the mesoscale is also considered in the interface characterization process.

4.2.1 Peel testing

The samples (50×7 mm^2) are cut with a ultra thin razor blade from (100×100 mm^2) bilayer sheets of PDMS (polydimethylsiloxane, Sylgard 186, Dow Corning) with a thickness of 0.75 mm, adjoined to commercially available circuit grade 17 µm thick copper foil (TW-YE, ArcelorMittal). This interface system is common in large area stretchable electronics [58], due to its exceptional fracture toughness (see chapter 2). The TW-YE foil is a rolled copper foil with one untreated side, with a roughness of $R_a \approx 0.5$ µm while the other side is treated with an electroplating step to increase the roughness to $R_a \approx 1.9$ µm. This roughened side is typically applied in large area stretchable electronic applications [42, 84], because of its enhanced adhesion properties. The PDMS is molded (in liquid state) to the untreated side of the copper foil to create a "smooth" interface type, and molded to the electroplated side of the copper foil to create a "rough" interface type, after which the PDMS is fully cured.

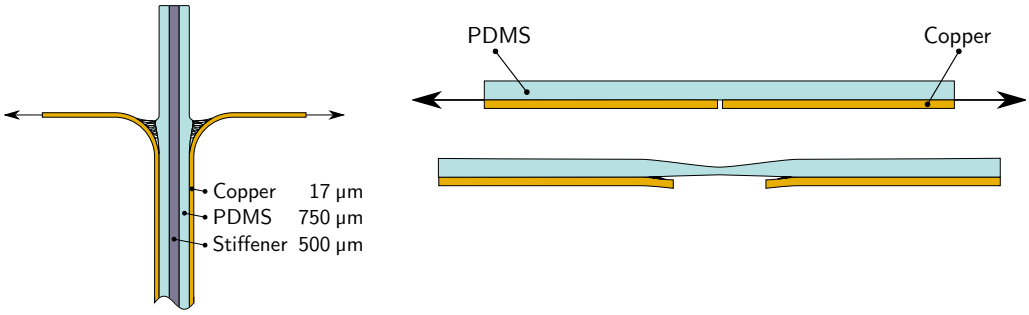

(a) 90° (b) 0°

Figure 4.2: (a) the 90° peel test configuration, where two bi-layer samples are glued to an Al stiffener such that the peel front remains stationary which simplifies imaging. (b) the 0° sample configuration, where the copper foil is damaged such that it will fracture first allowing the PDMS layer to stretch and load the interface in shear.

To investigate interface mode-dependency, two delamination experiments are applied with distinct macroscopic opening angles. To test the interface in mode I (i.e. opening) a 90° peel test is applied (figure 4.2a). For this experiment, two bi-layer samples are glued (Loctite 406 glue with 770 primer) to a 0.5 mm thick Aluminum stiffener, which creates a peel front that is stationary, facilitating imaging. The glued Al-PDMS interface is strong enough in order not to delaminate and add an additional source of dissipation. To test the interface in mode II (i.e. shear), a 0° peel test is applied (figure 4.2b). These experiments require a precrack in the foil, created by damaging the copper with a knife edge along a line perpendicular to the loading direction. The damaged copper will fracture upon loading, thereby transferring the load to the PDMS. Consequently, due to the large elastic mismatch, the interface is loaded in shear.

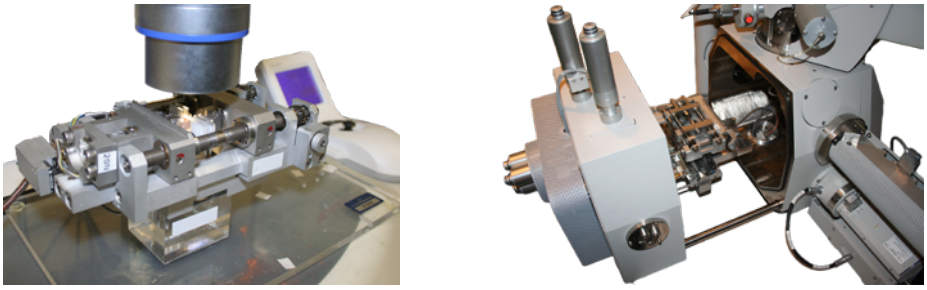

(a) (b)

Figure 4.3: (a) The micro tensile stage placed underneath the objective of an optical microscope. (b) The tensile stage placed on the positioning stage of the Environmental Scanning Electron Microscope for high magnification *in-situ* imaging of the peel front.

The peel tests are performed with a micro tensile stage (Kammrath & Weiss GmbH) equipped with a 20 N loadcell (figure 4.3). The small size of the tensile stage allows op-

eration underneath the objective of an optical microscope, or inside the vacuum chamber of an Environmental Scanning Electron Microscope (ESEM), see figure 4.3. For the 90° peel test, a low friction guide is placed to enforce a 90° angle with respect to the loading direction, shown in figure 4.1a. The guide is required to ensure symmetric loading of the sample.

During a peel test, the force and clamp displacement are measured. Typically the force-displacement curve exhibits an initiation regime, loading the interface until a steady crack propagation regime is reached. If the sample structure, which transfers the load, does not strain significantly, then the clamp displacement is directly linked to the increase in crack length. As shown by Kendall [66], Kim and Aravas [72] for the 90° peel test, the work of separation (WOS) is directly related to the observed force plateau,

$$\mathrm{WOS} = \frac{1}{b}\frac{dU}{da} = \frac{F}{b}. \tag{4.1}$$

The cohesive zone elements for which the traction separation law is characterized represent only the dissipative mechanisms in the fracture process zone Γ_{fpz}, therefore, the WOS is decomposed in a contribution of the fracture process zone Γ_{fpz} and the structural dissipation in the bulk of the sample Γ_{str}, similarly as done by Hutchinson and Suo [61]

$$\mathrm{WOS} = \Gamma_{\mathrm{fpz}} + \Gamma_{\mathrm{str}}. \tag{4.2}$$

The structural part contains dissipated energy in the sample, for instance plasticity due to the bending (and straightening) of the copper foil, but also stored elastic energy in the bulk of the sample, like for instance the increase in strain energy in the loaded copper foil per unit of extra crack length. Due to the limited copper thickness (17 µm) the bending strains are small, and occur in a small volume of material. Consequently, for the 90° experiment, the structural contribution to the WOS can be assumed neglected.

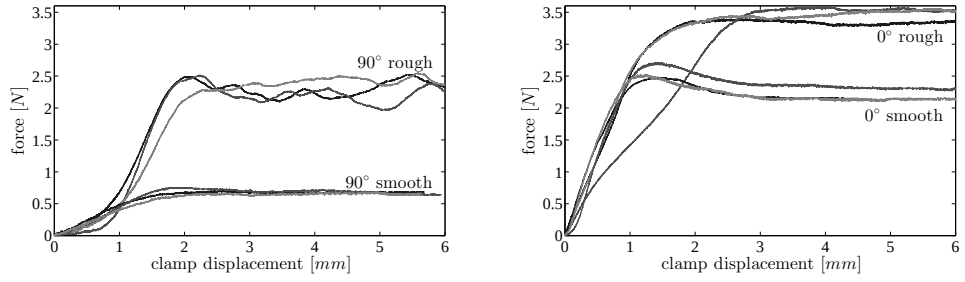

(a) 90° (b) 0°

Figure 4.4: Experimental force-displacement data for the four peel test experiment types, i.e. two interface roughness types peeled at two macroscopic angles.

In contrast, for the 0° peel test, the force is applied through the soft PDMS, which stores a significant portion of energy per unit of crack length. Therefore, the 0° WOS is obtained by matching a Finite Element Method (FEM) simulation with the experimental results. Besides the WOS, additional interface parameters are required to characterize the

interface, therefore this inverse method is applied to both experiments. As a consequence, the structural term in the WOS is correctly separated from the contribution of the fracture process zone for both experiment types.

To detail the dissipative sources in the fracture process zone further, the following decomposition is proposed,

$$\Gamma_{\mathrm{fpz}} = \Gamma_{\mathrm{ad}} + \Gamma_{\mathrm{ecz}} + \Gamma_{\mathrm{icz}}, \tag{4.3}$$

where Γ_{ad} is the physical adhesion energy, i.e. the bond energy, Γ_{ecz} is the elastic non-recoverable (trapped) energy in the cohesive zone, and Γ_{icz} is energy dissipated by irreversible processes in the fracture process zone. The cohesive energy terms will be the subject of microscale analyses, while the energy of adhesion is assumed to be neglibible ($\Gamma_{\mathrm{ad}} \approx 1$ J/m^2 [31–33]) compared to the observed WOS > 150 J/m^2.

4.2.2 Mesoscale characterization

For the FEM model, the bulk material properties of the copper and PDMS are determined separately. For both materials, dog bone shaped samples are cut from identical foils as used in the peel samples, which are loaded in uniaxial tension. From the elastic part of the copper stress-strain curve, a Young's modulus of 85 GPa and a yield stress of 300 MPa is measured. The copper was modeled with an isotropic elasto-plastic model, where the hardening response was implemented as a table. For the PDMS, a Neo-Hookean model with $C_{10} = 0.165$ MPa is identified from the uniaxial data (figure 4.5).

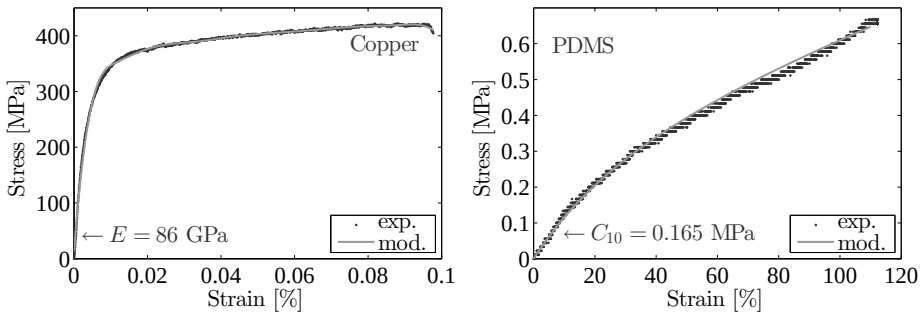

Figure 4.5: Experimental uniaxial response of the Copper and PDMS bulk materials, along with the response of the corresponding identified models.

In chapter 2, a fibrillation mechanism was observed at the peel front. Therefore, the fibril mechanics based mixed-mode interface model of van den Bosch et al. [17] with a large displacement formulation, is applied to model the PDMS-copper interface (figure 4.6). In this model, the relation between the traction T and the opening Δ (traction-separation law, TSL) is formulated as,

$$T = \frac{\phi}{\delta}\left(\frac{\Delta}{\delta}\right)\exp\left(-\frac{\Delta}{\delta}\right)\exp\left(\alpha\frac{d}{2}\right) \tag{4.4}$$

where ϕ is the fracture toughness, δ the critical interface opening, α the ratio of the fracture toughness for mode II relative Mode I. The opening mode is described by d, which ranges from $d = 0$ for pure Mode I to $d = 2$ for pure Mode II. The interface strength is reached at the peak of the Traction-Separation-Law (TSL), giving,

$$T_{\max} = \frac{\phi}{\exp(1)\delta}. \tag{4.5}$$

The interface model is implemented as a zero thickness user element, (figure 4.6a).

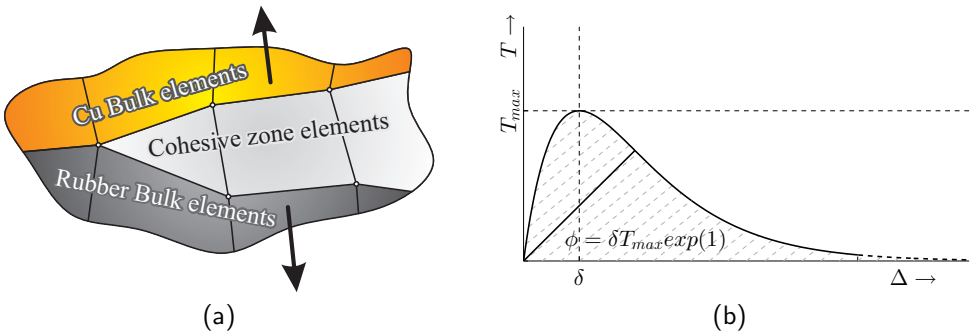

(a) (b)

Figure 4.6: The cohesive zone interface elements with initial zero thickness (a) and the adopted exponential traction separation law [17](b).

The 0° and 90° experiments are simulated with the same specimen dimensions as described above. Both 2D plane-strain and 3D simulations (figure 4.7) are performed for both peel test types. For the 90° peel test, negligible differences were observed between the 2D and 3D results, however for the 0° peel test the rubber contraction has a significant impact on the shape of the peel front. Consequently, the 90° simulations are 2D only, while the 0° simulations are performed in 3D. The simulations are stopped at the point where a steady state force level is reached, at which point the simulated response is compared to the experimental results

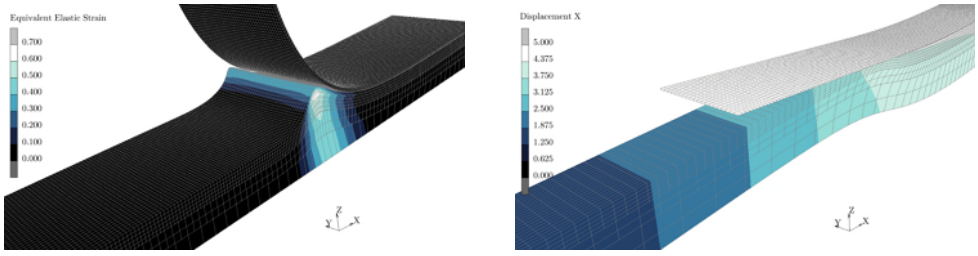

(a) 90° (b) 0°

Figure 4.7: The 3D deformed geometries for the simulations of the 90° and 0° experiments, the CZ elements are excluded from visualization to better show the PDMS deformed geometry.

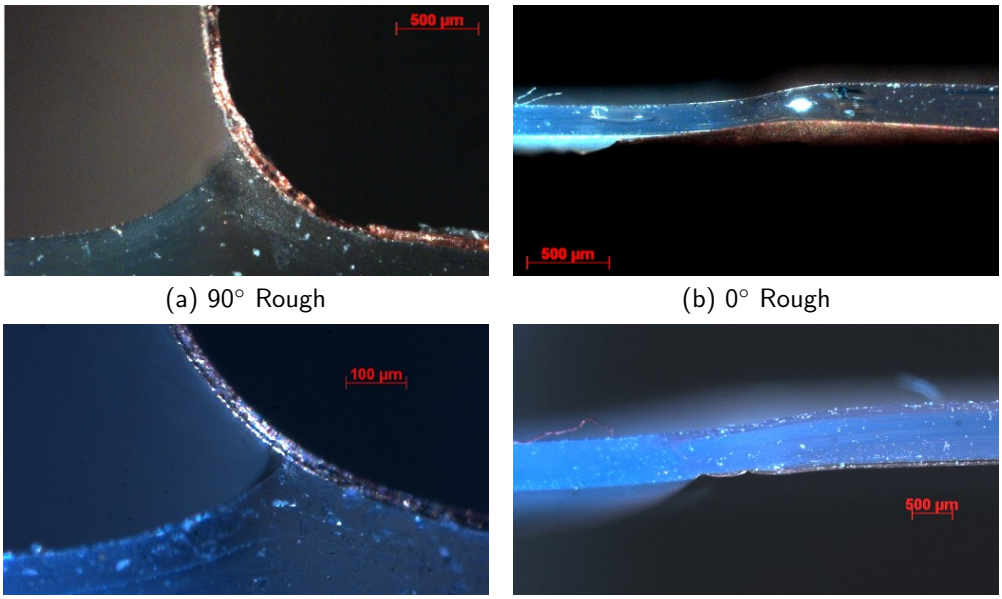

(a) 90° Rough (b) 0° Rough

(c) 90° Smooth (d) 0° Smooth

Figure 4.8: The PDMS deformed geometry (i.e. "Lift-off geometry") shown by side-view optical microscope images for both interface roughness types and both macroscopic load angles.

The interface constitutive behavior is described by $T_{\max}$, ϕ, δ, and α (equation 4.4). The first three parameters are coupled (equation 4.5), reducing the problem to three degrees of freedom. It is expected that the peel force of two peel test experiments (90° and 0°) is sensitive to ϕ and α, but not to $T_{\max}$ or δ [116]. Therefore, to identify $T_{\max}$ or δ uniquely, the simulated PDMS deformation profile is matched with the measured deformation profile (figure 4.8).

The TSL parameters of one roughness type should be the same for the 0° and 90° experiment. Therefore, the experimental results of both experiment types are compared to the numerical response in a single identification step for each roughness type. The sensitivity of the deformation profile to $T_{\max}$ (and indirectly δ) is shown in figure 4.9. The adopted minimization scheme identifies the TSL parameters, with respect to the measured lift-off geometry and peel force.

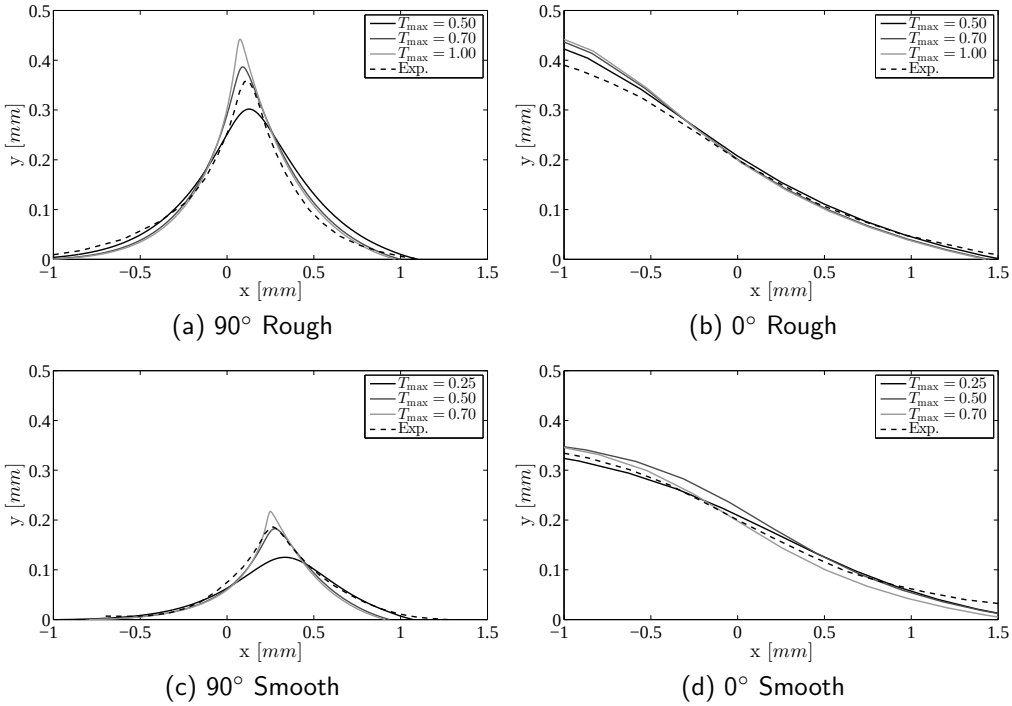

Figure 4.9: The extracted experimental PDMS deformed geometry compared with simulated geometries at various $T_{\max}$. This difference between the experimental and simulated geometries is minimized for each interface roughness type.

The result of the identification procedure is presented in table 4.10. As expected, a higher fracture toughness is obtained for the rough interface compared to the smooth interface. The increase in fracture toughness is caused by both an increase in interface strength $T_{\max}$ and interface ductility δ, as shown graphically in figure 4.10. Both interface types show a low mode angle dependency α. Only the smooth interface shows a 10% increase in fracture toughness for shear loading, relative to mode-I opening (at the macroscopic level).

CZ property		smooth	rough
ϕ	[J/m^2]	100	300
$T_{\mathbf{max}}$	[MPa]	0.5	0.75
δ	[µm]	75	150
α	[-]	0.1	0.0

(a)

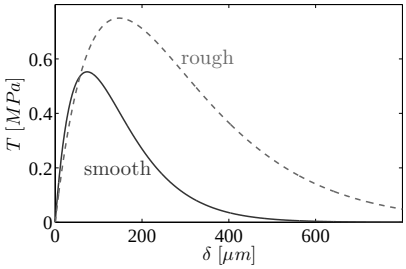

(b)

Figure 4.10: (a) Characterized CZ properties for the rough and smooth samples (b) The corresponding traction-opening curves. The rough interface is tougher, stronger and more ductile.

4.2.3 Mesoscale mode-angle

After identifying the cohesive zone parameters, the interface opening angle can be evaluated at the mesoscale. Macroscopically, the sample is loaded in pure mode I (90°) or pure mode II (0°), but due to the large elastic mismatch, these opening angles are not transferred to the mesoscale, which is consistent with the work of Gross and Seelig [45]. Figure 4.11 shows the computed opening parameter d, at steady-state, along the process zone. For the 0° experiment, the mesoscale opening parameter is close to pure shear loading ($d = 2$) throughout the entire process-zone. For the 90° experiment however, the mesoscale opening angle is only in mode I at the peel front and rotates towards mode II ahead of the crack tip. To quantify the effective mode angle, the opening parameter is averaged over the process zone $\bar{d}$, using the normalized traction $T/T_{\max}$ as a weight function, yielding $\bar{d} \approx 2$ for the 0° experiment, and $\bar{d} \approx 1$ for the 90° experiment. This indicates that the macroscopically observed peel force for the 90° experiment, is actually transferred through the mesoscale with a load angle of 45°.

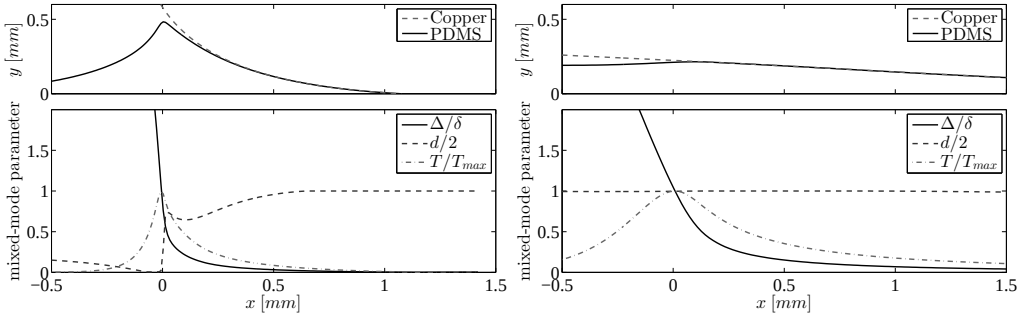

(a) 90° Rough (b) 0° Rough

Figure 4.11: The cohesive zone profile and mixed-mode parameter evaluated along the process zone. (a) For the 90° peel test the mode angle drastically changes from normal opening at the peel front to shear opening further ahead of the crack. (b) The mode angle parameter d remains close to pure shear over the entire process zone for the 0° peel test.

The tendency to rotate the mode angle towards the mesoscale interface follows from geometrical considerations. The copper film is very thin, resulting in a low bending stiffness. Consequently, the film is curved away from the crack tip, since there are no opening tractions far ahead of the crack tip. On the PDMS side, the material drawn into the lift-off geometry necessitates large deformations in the the surrounding material. Particularly the inward deformation of PDMS from the area ahead of the crack tip will create a shear load on the interface (figure 4.12). These combined effects tend to reorient the load towards shear at the mesoscale, which is consistent with Hutchinson and Suo [61].

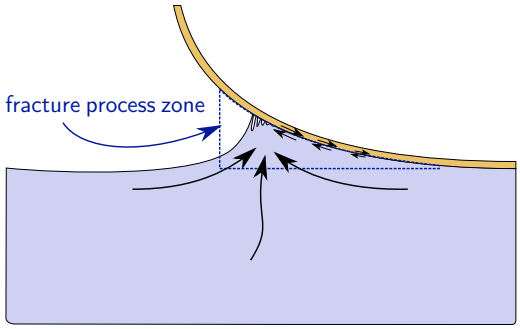

Figure 4.12: The lift-off geometry deforms in surrounding material, triggering a rotation in the fracture process zone ahead of the crack tip.

4.2.4 Model validation

The interface identification method is based on a comparison of the lift-off geometry (i.e. the side view) between the experiment and simulation. To test the quality of the model, additional 0° experiments are performed on samples, with a Digital Image Correlation (DIC) speckle pattern, which are observed from the top with a telecentric camera of the DIC system (Aramis, GOM). The DIC system extracts the displacement fields from the digital images, from which the strain fields are computed and superposed on the experimental images (figure 4.13). These strain fields are quantitatively compared with the simulated strain fields. The maximum relative difference in strain is found to be less than 10%. This confirms that the characterized model adequately describes the experiment on the macro- and mesoscale.

The cohesive zone model is applied on the mesoscale, and thus naturally homogenizes all the phenomena occurring at lower scales. Figure 4.14 reveals the mismatch between scales, whereby the cohesive zone elements still carry a significant traction in an area where there is no material. It is already discussed in chapter 2 that, by applying such a mesoscale approach, all dissipative mechanisms near the interface are lumped in the cohesive zone element. Consequently, the identified interface properties are not pure interface properties, since they are significantly influenced by the nearby material. This limits the predictive capabilities of these models, since they do not incorporate the detailed micromechanics.

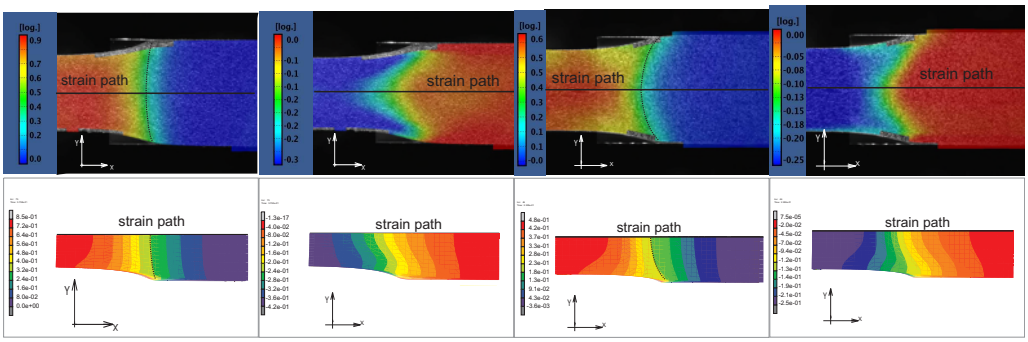

(a) ε_{xx} Rough (b) ε_{yy} Rough (c) ε_{xx} Smooth (d) ε_{yy} Smooth

Figure 4.13: (Top) Digital image correlation strain fields for the rough and smooth interface roughness types obtained from the PDMS side of the sample of a 0° peel test. (Bottom) FEM simulated strain fields obtained from the same surface, notice the quantitative agreement for the strains and geometry of the peel front.

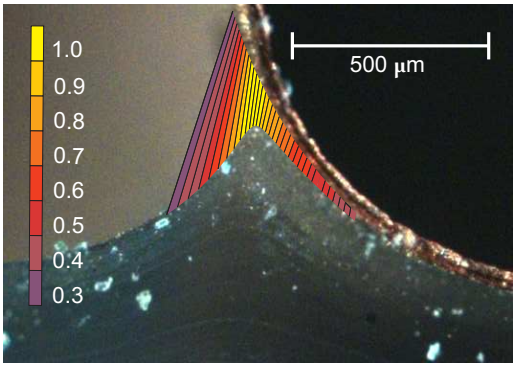

Figure 4.14: Experimental-numerical mismatch: the traction carried by the cohesive zone elements are non-zero in an area where physically no material is present.

4.3 Micromechanical analysis

The macro-meso analyses showed that the interface toughness is significant for both interfaces, whereby the rough interface is three times tougher. Additionally, both interfaces showed a low sensitivity to the mesoscopically observed interface opening angle (table 4.10). To analyze the mechanisms underpinning this response, the delamination experiments are next *in-situ* analyzed at high magnification with an ESEM.

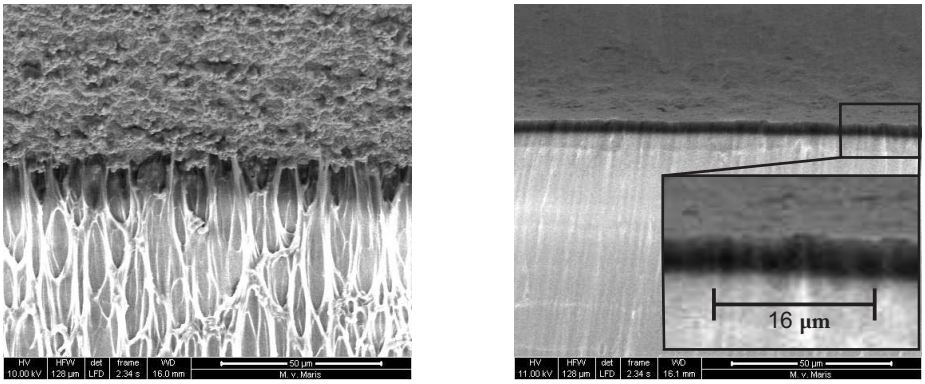

(a) Rough (b) Smooth

Figure 4.15: *In-situ* ESEM image of the progressing peel front for both interface roughnesses, peeled at a 90° macroscopic load angle. Although materials and processing are identical, the delamination micro-mechanics are distinct. Note that both images are taken at the same magnification (except the inset).

The peel front of the 0° test is not accessible by the electron beam, due to the shape of the sample, therefore, only the 90° experiments are *in-situ* visualized with an ESEM (FEI, Quanta 600). Figure 4.15 shows high magnification images of the delaminating peel fronts for each interface roughness. The images show a distinct difference in the delamination microstructure between the two roughness types. The high roughness interface produces approximately 30 µm long fibrils, whereas the fibrillation process is not visible. However, the fibrils might be too small to be detected by the ESEM. The limited ESEM resolution follows from the high frame rate requirements, associated with *in-situ* imaging. Moreover, a minimal electron beam intensity is applied to prevent disturbance of the fibrillation process by the imaging technique, see chapter 3.

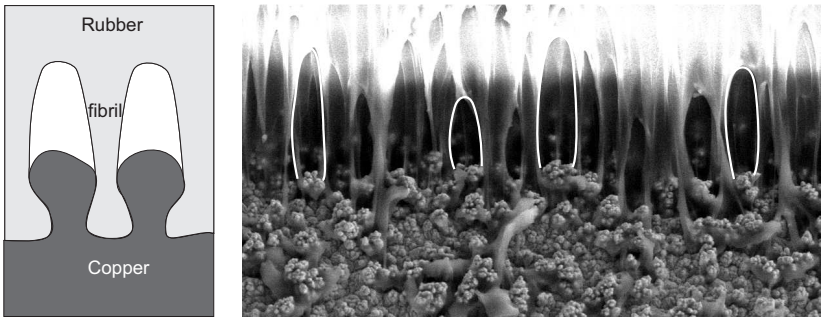

Figure 4.16: The interface roughness causes PDMS interlocking in the valleys of the roughness profile and cavitation at the peaks of the roughness profile. This initiates the fibrillation mechanism, where approximately 30 µm fibrils are formed which either rupture or debond at the interface.

Figure 4.16 shows that the high interface roughness creates locations of enhanced adhesion, due to the complex interlocking shape of the copper protrusions. This interlocking mechanism combined with the large elastic mismatch, creates areas of large negative hydrostatic pressure at the roughness peaks. These two effects trigger the initiation of the fibrils, which are then elongated until they rupture or debond from the interface. Note that, this mechanism is remarkably similar to what is observed for the "Thermoplastic urethane"-copper interface discussed in chapter 3, where a copper foil is applied with the same electroplated roughness. This correspondence is remarkable, since PDMS is known to be nearly hyper-elastic and is unlikely to dissipate energy during deformation.

4.3.1 Crack surface matching

The hyper-elastic properties of PDMS suggests that no energy is dissipated in the fracture process zone during deformation, which implies that the dominant energy dissipation mechanism is the release of elastically stored energy upon fibril failure, which is also discussed in chapter 3. However, large stretch ratios are observed in the fibrils (i.e. $\lambda > 3$), and the response of PDMS at these values may deviate from a purely elastic response. To analyze the occurrence of any significant irreversible deformations, the two separated fracture surfaces are geometrically confronted.

The two surfaces are first measured with an optical profilometer (Sensofar Plμ2300), which measures the surface topology in 3D (figure 4.17ab). Next, the original location of the PDMS surface with respect to the copper surface is recovered by applying a customized Digital Image Correlation (DIC) routine detailed in appendix A. This DIC routine assumes that the PDMS surface is simply inverted with respect to the copper surface, as shown in figure 4.17c. All subfigures shown in figure 4.17 are translated by the DIC routine such that corresponding features are shown in the same location in the field of view, e.g. the large "camel-shaped" feature marked with an ellipse, which is at the same coordinate in all four figures. Due to the common coordinate system it is next possible to compare the surface profiles quantitatively, e.g. by determining the residual difference between the PDMS and copper surface (figure 4.17d), or by reconstructing cross-sections (figure 4.17ef). The residual image is a measure for the mismatch of the two surfaces, and is used to assess the presence of irreversible deformations.

Due to the molding manufacturing process of the samples, it is fair to assume that the copper topology is initially fully covered by PDMS. The obtained residual image (figure 4.17d) therefore serves as a measure for the mismatch between the two topologies after delamination. Possible contributions to this mismatch are: irreversible deformation, algorithmic matching errors, contamination which occurred after delamination, mismatch which was present before delamination, measurement inaccuracies. Additionally, this method is insensitive to a homogeneous irreversible opening, because the thickness of the materials is not measured. However, such a global permanent deformation is unlikely without any observable effects on the local geometry (figure 4.17ef). Whereas it is not possible to identify each separate contribution to the residual image, it can be stated that, the irreversible crack opening cannot exceed the measured residual. Consequently, the mean residual amplitude $\delta_i \approx 1$ µm implies that the average irreversible crack opening

is smaller than 1 µm. The resulting amount of dissipated energy is seems therefore insignificant compared with the mesoscopic critical interface opening (e.g. $\delta \approx 150$ µm, see table 4.10). This confirms the hypothesis that the amount of energy dissipated during the deformation of the fibrils and the nearby PDMS material remains negligible.

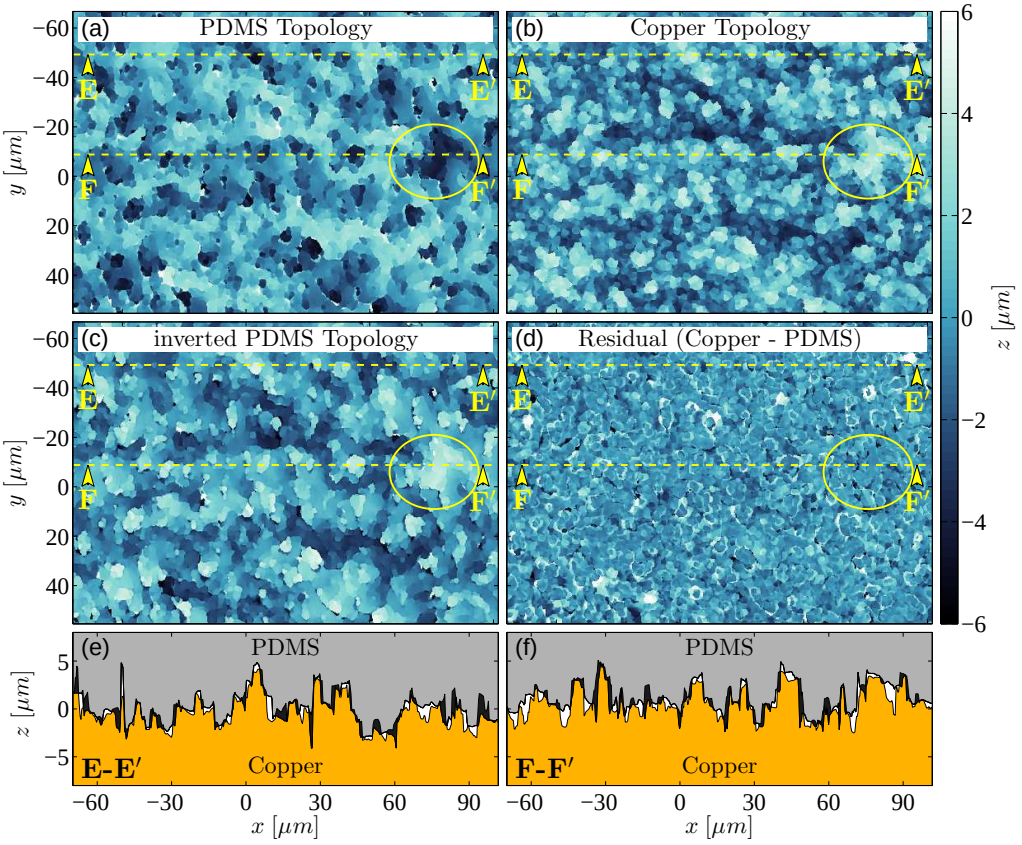

Figure 4.17: (a,b) Optical surface profilometer topologies of the PDMS and copper delamination surfaces. (c) The inverted image of the PDMS topology. (d) The residual topology, i.e. the difference between the copper and PDMS topologies (e,f) Reconstructed Cross-sections, of which the locations are indicated with dashed lines in the other subfigures.

4.3.2 Peel surface analyses

Similarly as discussed in chapter 3, the delaminated copper surfaces are analyzed for the presence of PDMS residue. Figure 4.18a shows the complex topology of the surface roughness by using the Secondary Electron detector of the ESEM. To measure the relative area of the copper surface covered with PDMS residue, the Back Scatter Electron (BSE) composition contrast technique is used, which yields a high contrast between the

large atomic mass copper (bright) and the low atomic mass PDMS (dark), as shown in figure 4.18b. Ten images with a 213×184 µm^2 field of view are segmented to measure fraction of the area covered with PDMS residue, denoted by A_r.

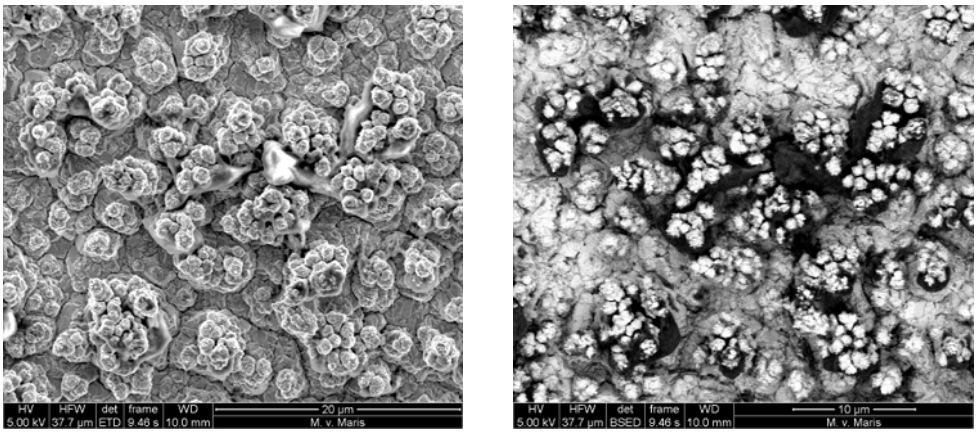

(a) SE (b) BSE

Figure 4.18: High magnification ESEM images of the delaminated copper surface. (a) Secondary Electron (SE) composition contrast image showing the copper topology. (b) Back Scatter Electron (BSE) image, showing high contrast between the copper (bright) and the PDMS (dark).

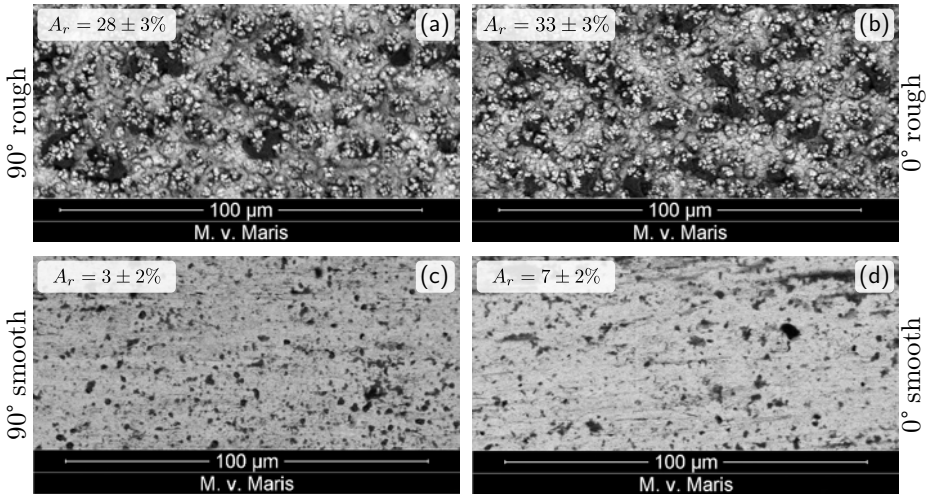

Figure 4.19: Post delamination BSE images of the copper surfaces of both interface roughnesses and both peel tests. The copper area covered with PDMS residue A_r averaged over 10 images is indicated in the corner of each subfigure.

Figure 4.19 shows typical BSE detector images for each interface roughness type for the 0° and 90° peel test, with the average PDMS covered area in the corner. Comparing

the results between the rough and smooth interfaces (figure 4.19ab vs. cd), it is obvious that more PDMS residue appears on the rough copper surface, which implies that the interface did not fail, but instead the crack progressed through the PDMS by rupturing the fibrils. Consequently, an increase in A_r suggests an increase in the amount of energy dissipated during delamination. Clearly, this dissipation is not just interface debonding at the microscale, but it does contribute to the fracture toughness at the mesoscale.

Comparing the measured PDMS area fractions between the 0° and 90° peel test, shows that the 0° experiments trigger more PDMS fracture (i.e. less interface debonding). For the rough interface type the relative difference in A_r is small. The comparable amount of PDMS fibril fracture events for the two load types, is consistent with the low mode angle dependency obtained by interface characterization. However, for the smooth interface type, a considerable increase in A_r is measured for the 0° experiment (compared to the 90° experiment). This increase in the amount of PDMS fracture compared to interface debonding is qualitatively in line with the identified mode dependence parameter $\alpha = 0.1$.

4.3.3 Discussion

The fibrillation micromechanism in PDMS is remarkably similar to the fibrillation observed in the TPU-copper interface, as discussed in chapter 3. Between the two interface systems, the copper roughness is the common factor, indicating that the fibrillation process is initiated and controlled by the copper roughness. The high roughness mechanically interlocks the PDMS creating areas of enhanced bonding. This allows for significant loading of the interface, causing cavitation which initiates the fibrillation process. The drawing of the fibrils does not significantly contribute ~~the~~ the fracture toughness, due to the hyperelastic behavior of the PDMS, which is confirmed by the negligible irreversible crack opening displacement. However, a significant amount of fibril fracture is observed, leaving PDMS residue on the copper surface. This means that the fracture front deflected into the PDMS material instead of progressing along the interface. This suggests that large stress concentrations occurred during delamination, most likely caused by the complex copper geometry, similar to what is numerically observed by Litteken and Dauskardt [82], van der Sluis et al. [117, 118]. This process of crack arrest, and crack kinking or crack branching effectively affects a larger material volume to the fracture process, improving the macroscale fracture toughness.

The mesoscale characterization revealed only a small mode dependence for the smooth interface, and no significant mode dependence for the rough interface. This is consistent with the occurrence of PDMS fibril fracture. Fibrils can almost freely rotate aligning the fibril axis to the traction direction. Moreover, at the scale of the roughness, the process of crack arrest and crack branching will most likely occur independently of the mesoscopic mode angle, because the complexity of the roughness pattern ~~does not~~ change ~~significantly~~ if the interface is loaded at an angle. The minor mode dependency observed for the ~~smooth interface is therefore most likely due the friction between the PDMS and the copper.~~

4.4 Conclusions

Metal-elastomer interfaces typically exhibit large deformations in the elastomer during interface crack propagation. As a result, additional dissipative mechanisms, besides the adhesive interface separation, contribute to the macroscopic fracture toughness. This work addressed the roughness-induced elastomer fibrillation resulting in a significant process zone. To analyze the relevant mechanisms, three length scales were discussed in this paper: (*i*) the macroscale, the scale on which the load is applied, (*ii*) the mesoscale, defined by the size of the fracture process zone, which is typically the finest scale included in FEM simulations, (*iii*) the microscale, at which the delamination micromechanisms and the interface roughness influence the fracture process.

The observed fibrillation mechanism is remarkably similar to the mechanism observed for TPU-copper discussed in chapter 3. In both systems, the fibrillation is initiated by mechanical interlocking in the copper roughness valleys, accompanied with cavitation at the roughness peaks as a consequence of large negative hydrostatic stresses. However, the TPU system behaves visco-elastically, while PDMS is essentially hyperelastic. Yet, both systems dissipate a significant amount of energy, which yields a macroscopically enhanced fracture toughness. Since the PDMS is not expected to dissipate energy during deformation, it is hypothesized that a large part of the fracture toughness originates from the sudden loss of elastically stored energy in the fracture process zone. The large process zones created by the high elastic mismatch stores a considerable amount of elastic energy in the fibrils and the material attached to the fibrils. This energy is released upon fibril failure and almost completely dissipated dynamically.

Analyses of the amount of PDMS residue on the copper surface after delamination revealed that a significant part of the surface (up to 30%) was covered by PDMS residue. The crack regularly deviated into the PDMS bulk instead of progressing along the interface. The PDMS toughness is known to be much higher than the interface adhesion energy. Therefore, in order for the crack to branch into the PDMS, large stress concentrations must have been present, caused by the complex geometry of the copper roughness.

It is shown that the macroscopically applied peel angle does not replicate itself at the mesoscale, where the mode angle typically rotates towards shear interface loading. Moreover, both tested interface roughness types reflect a low to negligible mode sensitivity in the mesoscale characterized parameters. This is due to the fibrillation process (where the fibrils tend to align with the traction direction) and to the complex roughness geometry (the complexity of which does not change for different loading perspectives).

Acknowledgment

J. Vanfleteren of IMEC Ghent is gratefully acknowledged for his support and input in this research, and for generously providing the sample material.

Part B

Micro-scale identification method development

Chapter 5
On the validity regime of the bulge equations

Reproduced from; J. Neggers, J.P.M. Hoefnagels and M.G.D. Geers, *On the Validity Regime of the Bulge Equations*, Journal of Materials Research, 27-9 (2012) 1245–1250

Abstract

The plane strain bulge test technique is a powerful and acknowledged technique for characterizing the mechanical behavior of thin films. In a bulge test analysis the stress and strain are derived from the measured quantities using analytical approximations of the deformed geometry (bulge equations). To improve the bulge test, the systematic error introduced by these approximations is evaluated and quantified by scrutinizing the method on a finite element model of the bulge test, used as an idealized experiment.

5.1 Introduction

Thin films are used in many modern high-tech systems [63, 95, 101]. In these systems distinct materials with specific differentiating properties are often mixed. Therefore, profound understanding of the mechanical behavior of these thin films is required to predict failure due to thermo-mechanical loading [95]. Many materials behave differently than their bulk counterparts when one or more dimensions are in the range of an intrinsic length scale [44, 46, 125, 133], which is often the case for thin films. The mechanical behavior can also depend on the adjacent (adhered) films [3], the film microstructure and the fabrication process [38]. Therefore, experimental methods that can measure the mechanical performance of thin films in an accurate manner are of great value. The bulge test is such a valuable technique, acknowledged as one of the easier techniques to measure full (isothermal) stress-strain curves of freestanding thin films [64, 135, 142], even partly into the compression regime [143].

In the bulge test, a membrane is deflected using a pressurized medium while the deflection is measured (Fig. 5.1a). Typically, the stress and strain are calculated from the pressure P and out-of-plane deflection at the membrane apex δ by means of an analytical description of the membrane deformation, called the bulge equations [6, 128].

These bulge equations are sensitive to the membrane geometry which has been a source of inaccuracy for bulge test measurements in the past. However, with the currently available Si micro-machining sample production techniques, these problems are largely overcome [135]. Nevertheless, when material parameters obtained from bulge tests are compared with parameters obtained with other small scale testing methods, such as nano-indentation, substrate warpage or micro-beam bending, some discrepancies emerge [87, 121].

Bulge test experiments can be classified with respect to the shape of the tested membrane (circular, rectangular, etc.). The plane strain bulge test, which uses a rectangular membrane with aspect ratio larger than 4 [133], is currently the most widely used bulge test for thin film testing, due to its favorable combination of micro-fabrication routes, its well-defined strain state (at least far away from the membrane boundaries), and its straightforward pressure versus deflection relation [133, 142]

$$P = 2\frac{Eh}{a^2}\delta\epsilon_0 + \frac{4}{3}\frac{Eh}{(1-\nu)a^4}\delta^3, \tag{5.1}$$

where P is the pressure, a is the width of the membrane, ν the Poisson's ratio, ϵ_0 is the initial residual (elastic) strain in the membrane, h the thickness of the film, δ the maximum deflection and E Young's modulus. Under the assumption that the membrane hinges freely at the boundaries (due to local plasticity and negligible bending stiffness of the thin film), the membrane profile is assumed to take the shape of the section of a cylinder. The stress σ and strain ε are then homogeneous through the major part of the membrane, and are given by

$$\sigma_{\mathrm{be}} = \frac{P}{h\bar{\kappa}}, \tag{5.2}$$

$$\varepsilon_{\mathrm{be}} = \frac{1}{a\bar{\kappa}}\arcsin(a\bar{\kappa}) - 1, \tag{5.3}$$

$$\bar{\kappa} = \frac{2\delta}{a^2+\delta^2}, \tag{5.4}$$

where $\bar{\kappa}$ is the curvature of the (assumed) cylindrical shape of the loaded membrane. Note that any initially present strain (pre-strain) in the membrane should be added to the bulge strain, i.e. $\varepsilon = \varepsilon_{\mathrm{be}} + \varepsilon_0$.

Figure 5.1 shows the results of a virtual bulge experiment, explained below, in which stress-strain curves obtained by applying the bulge equations (Eq. 5.2-5.4) to bulge profiles are compared to the reference (input) stress-strain behavior of the virtual experiment. Figure 5.1b confirms that the bulge equations adequately predict the stress and strain from the pressure and deflection for thin films of, e.g., 0.5 µm thickness, as reported in [143], although a small (systematic) error can be noticed. Figure 5.1c shows, however, that this systematic error is significantly amplified when the bulge equations are applied on thicker films, e.g., of 5 µm thickness, which are for instance used in MEMS applications [8]. Note also that the systematic error increases when the membrane has some residual strain before starting the bulge test experiment. Residual strains are common in bulge membranes, and are usually caused by the (large) thermal stresses during

processing. Therefore, pre-strains are often as high as 90% of the yield strain [143]. This triggers two important concerns: (*i*) it is unclear how the magnitude of these systematic errors depend on the membrane thickness and (*ii*) the error concentrates around the elastic regime, which is important for finding the elastic material parameters including the elastic limit and for which the larger measurement noise in bulge experiments can obscure such systematical errors.

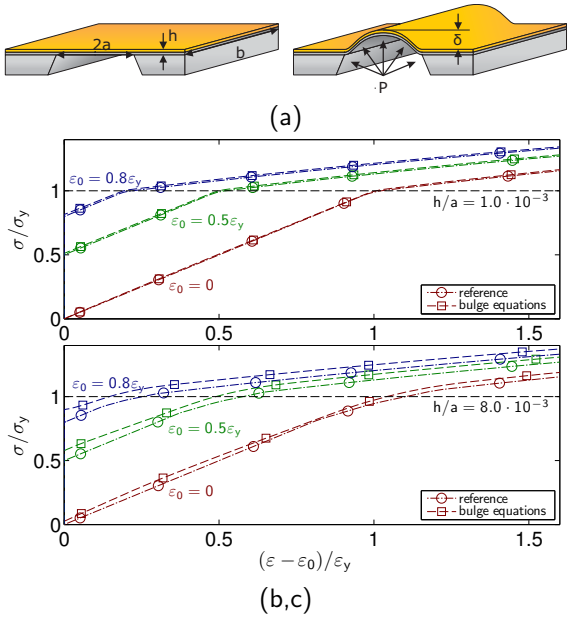

Figure 5.1: (a) Schematic of a plane strain bulge test experiment. A slender rectangular membrane with width $2a$ and thickness h is deflected δ out-of-plane by a pressure P. (b,c) Stress-strain curves obtained by application of the bulge equations to a simulated virtual experiment (explained in the text), compared with the reference (input) stress and strain data, for a membrane thicknesses of 500 nm (b) and 5 µm (c).

The goal of this research is to identify and quantify these systematic errors in order to support the proper use and exploitation of the bulge test technique. At the same time, the regime where the (cylindrical) bulge equations are valid is identified.

Finite Element Method (FEM) simulations are used to define a virtual experiment, allowing a comparison of the stress and strain taken directly from the simulation with the stress and strain calculated by the bulge equations (using the pressure-deflection data from the same simulation). This provides a direct comparison, eliminating all experimental uncertainties, enabling a detailed investigation of the systematic uncertainties in the bulge equations. Additionally, not only the deflection but also the shape of the profile of the loaded bulge membrane can be analyzed. The analysis will focus on the ("miniature") plane strain bulge test, because it is becoming increasingly more popular, yet the resulting conclusions apply to the bulge test in general. The "miniature" plane

strain bulge test is described in [142], where the use of lithographic "micro-machining" techniques allows for the fabrication of samples with very high dimensional accuracy, thereby greatly improving the accuracy of the method.

5.2 Virtual experiments

Due to symmetry, only half of the geometry of the miniature plane strain bulge test is modeled with 8-node quadratic quadrilateral elements. The symmetry edge is only confined in the x direction, whereas the other "clamped" edge is confined in the x and z directions while allowing contraction (Fig. 5.2a). The validity of this "fully rigid" boundary condition was verified by performing 2D simulations including the Si substrate. When the boundary is more compliant, the point of rotation (hinge) is moved further outward, creating a larger effective membrane width, $a_{\text{eff.}}$, which effects σ_{be} and ε_{be} through $\bar{\kappa}$ (Eqs. 5.2-5.4). However, the calculated effective bulge membrane width for simulations with the substrate was only 0.1% larger than for simulations with the fully rigid boundary conditions over the entire simulated h/a range, which shows that the fully rigid boundary conditions are an adequate approximation. The dimensions of the modeled bulge membrane are taken equal to 6 mm by 1 mm. However, the membrane thickness to width ratio h/a is varied to assess its effect on the validity regime of the bulge equations. The model was optimized for mesh convergence, resulting in a mesh of 600 by 2 elements in the x and z directions respectively. Additional 3D simulations were performed, including the Si substrate, which showed that the ratio between the principal strains in the center was $\varepsilon_y/\varepsilon_x \approx 4 \cdot 10^{-3}$ for all ratios h/a investigated in this work. Therefore, it is assumed that 2D plane strain simulations (Fig. 5.2a) are representative for the mechanical state at the center of these membranes.

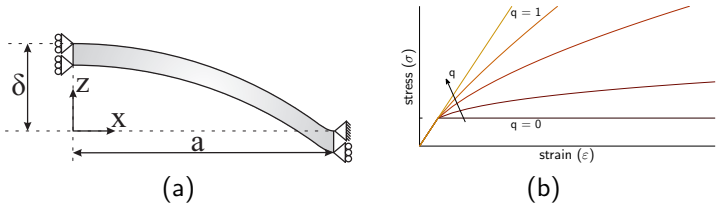

Figure 5.2: (a) The simulated 2D model of half of the membrane, indicating the boundary conditions. (b) Stress-strain curves of the elasto-plastic material model, illustrating the effect of the hardening parameter q.

Since the bulge test is often used to measure the elasto-plastic response of thin films the

following typical elasto-plastic material model was used [143]

$$\sigma = E\varepsilon, \qquad \sigma \leq \sigma_{\mathrm{y}} \tag{5.5}$$

$$\sigma = K\varepsilon^{q}, \qquad \sigma > \sigma_{\mathrm{y}} \tag{5.6}$$

$$K = \sigma_{\mathrm{y}} \left(\frac{E}{\sigma_{\mathrm{y}}} \right)^{q}, \qquad (0 \leq q \leq 1) \tag{5.7}$$

where σ_y is the yield stress, E the Young's modulus, and q a hardening exponent defining the hardening rate. Note that $K = E$ for $q = 1$, resulting in a purely elastic model and $K = \sigma_y$ for $q = 0$, resulting in an ideal plastic model (Fig. 5.2b). The base material parameters are chosen to simulate the material behavior of copper $E = 120$ GPa, $\sigma_y = 300$ MPa, $q = 0.36$ and a Poisson's ratio $\nu = 0.36$ [143], although the influence of material parameters will be evaluated later over a wide range.

5.3 Bulge test analysis

In Figure 5.3a, the bulge profiles for one specific thickness to width ratio h/a are plotted normalized with their maximum deflection δ. This figure shows the evaluation of the bulge profile shape for an increasing pressure P. It is obvious that not all profiles exhibit the cylindrical shape assumed by the bulge equations. Still, all profiles are bounded by a lower and upper limit case. Initially, at low pressures, there is no plasticity in the film, i.e. its deformation remains fully elastic, revealing the Double Clamped Plate (DCP) solution [49] as the lower limit case. At a higher pressure, plasticity sets in at the clamped edge, initiating a plastic hinge, at which stage the profile shape starts to deviate from the DCP profile. Increasing the pressure further allows the plastic hinges to form completely, at which stage the profile deflects cylindrically, above that pressure the assumptions in the bulge equations are valid. The two limit profiles, the DCP profile, and the cylindrical shape of the bulge equations, can be expressed as [49]

$$z_{\mathrm{dcp}} = \frac{P}{2Mh^3} \left(a^2 - x^2 \right)^2, \tag{5.8}$$

$$z_{\mathrm{c}} = 2\bar{\kappa}^{-1} - \delta - \frac{1}{2}\bar{\kappa}x^2 - \frac{1}{8}\bar{\kappa}^3 x^4 - \ldots, \tag{5.9}$$

where M is the plane strain modulus, i.e. $M = E/(1 - \nu^2)$.

To quantify the transition from the DCP profile to the cylindrical profile a cylindricity factor is introduced

$$\text{Cylindricity} = \frac{\chi_c}{a}, \qquad 0 \leq \frac{\chi_c}{a} \leq 1 \tag{5.10}$$

where χ_c is the smallest x-coordinate where the local curvature, $\kappa(x)$, deviates more that 0.1% from the curvature in the center, $\kappa_0(x = 0)$.

The cylindricity can be interpreted as the relative part (around the bulge center) of the bulge profile that is cylindrical. Figure 5.3b shows the evolution of the cylindricity as a

function of the (normalized) strain, for membranes with various thickness to width ratios h/a. All profiles start on the left side of the figure, where the cylindricity is close to zero. At a given strain the cylindricity increases, which happens sooner for the thinner films, and a regime is entered where neither the DCP nor the bulge equations are accurate. Finally, when the global strain in the material is high enough all membrane thicknesses reach the point where the cylindricity condition is fulfilled (i.e. $\chi_c/a \approx 1$).

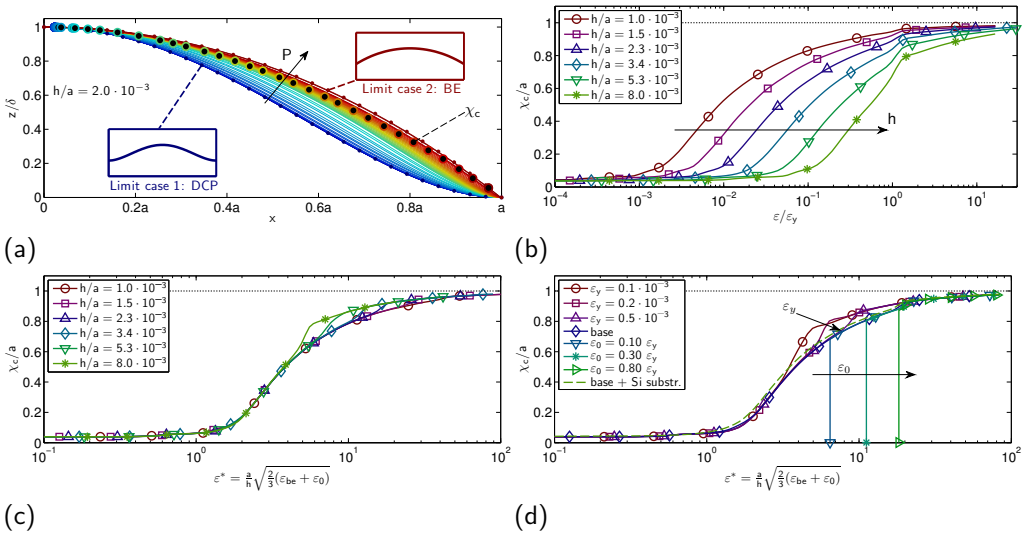

Figure 5.3: (a) Evolution of the bulge profiles, for increasing pressure P, normalized with their deflection δ. The inset figures show the two limiting cases; (i) the Double Clamped Plate (DCP), and (ii) the cylindrical shape of the Bulge Equations. The (color-coded) dots marked χ_c are the limit positions, for which the curvature κ at the left side of the marker deviates less then 0.1% from the curvature in the center. (b) The "cylindricity" (i.e. the relative circular part) of each bulge profile as a function of the dimensionless strain $\varepsilon/\varepsilon_y$ for films with various thickness to width ratios h/a. (c) The cylindricity χ_c/a of each bulge profile shifted to one mastercurve by plotting the curves of subfigure b as a function of the scaled strain. (d) The same mastercurve now for various material properties, where "base" refers to the reference copper material properties, "base + Si Substr." refers to a simulation where the rigid boundary is replaced with the micro-machined Si substrate. The variation of ε_y is achieved by both varying the Young's modulus and the yield stress.

Looking at the limit cases in more detail, the observation can be made that the DCP solution neglects the effect of membrane stress σ_m and only considers the effect of bending stresses σ_b, whereas the bulge equations do the opposite, neglecting σ_b and only considering σ_m. This argumentation suggests that the ratio of σ_m/σ_b could be a good candidate for the scaling of the cylindricity curves in Figure 5.3b. A scaling parameter

can be extracted by analyzing the corresponding expressions of the (local) stresses

$$\sigma_m = \frac{1}{6} M a^2 \kappa^2, \tag{5.11}$$

$$\sigma_b = \frac{1}{2} M h \kappa, \tag{5.12}$$

where σ_b is the bending stress at the (top) surface of the membrane under pure bending and $\bar{\kappa}$ is the measured membrane curvature. Equation 5.11 results from the Bulge Equations 5.2 and 5.3 under the assumption $a \gg \kappa$. The scaling ratio can then be expressed as

$$\frac{\sigma_m}{\sigma_b} = \frac{1}{3} \frac{a^2}{h} \kappa. \tag{5.13}$$

To allow experimentalists to calculate this ratio using their already available data, the above equation is written in terms of the strain that is obtained by the bulge equations. Therefore, an approximation of equation 3, i.e. $\kappa \approx \sqrt{6\varepsilon_{\mathrm{be}}/a^2}$, is used to write:

$$\varepsilon^* = \frac{a}{h} \sqrt{\frac{2}{3} \varepsilon_{\mathrm{be}}}. \tag{5.14}$$

Figure 5.3c shows the same cylindricity curves as in Figure 5.3b, now plotted against the scaled strain ε^* as defined in equation 5.14. It is seen that all profiles for different h/a ratio fall on top of a scaled master curve. This is interesting, as equation 5.14 suggests that the scaling is nearly independent of the material parameters. To verify this, the elasto-plastic material parameters are varied over a wide range. For all compared combinations of σ_y, M, and q the scaled master-plot is nearly identical (Fig. 5.3d). For low ε_y, i.e. low σ_y and/or high M, plastic deformation initiates everywhere in the membrane before the plastic hinges at the boundaries are fully formed, resulting in a slight deviation from the mastercurve in the transition regime. Additionally, the figure shows the effect of pre-strain ($\varepsilon_0 > 0$) in the membrane, which causes the membrane to deform elastically until a threshold strain is reached, at which point the membrane profile "jumps" to the pre-strain free profile, after which it follows the mastercurve again.

The scaled strain shifts all cylindricity curves to one master curve (Figure 5.3c and 5.3d), which directly shows the validity regime of the bulge equations. In other words, the master curve allows the experimentalist to assess whether the assumptions in the bulge equations are valid for each bulge data point, measured at a certain strain, with a certain membrane geometry, and for certain material properties. Additionally, the errors as a result of using the bulge equations outside of this regime are quantified and plotted in Figure 5.4. This logically shows that for small strains the DCP solution is more accurate than the bulge equations, which start with a relative error in the strain of $> 9\%$. Nevertheless, the error in the stress σ_{be} obtained with the bulge equations is relatively low from the start but increases around the curvature range where the bulge equations become valid. This error in the stress is slightly more pronounced if the pre-strain in the membrane is larger. Exploiting the data beyond its validity regime yields an error, which is largest for the plane strain modulus, the initial membrane stress and the

yield strain. This is because, even for relatively unfavorable ratios of h/a, at some point in the bulge test experiment the plastic hinges start to form and with their evolution the corresponding error made by the bulge equations decreases. The result is that the systematic error is most severe in the low strain regime, where the modulus is usually fitted and which is used to backward extrapolate towards the unknown zero stress state and the yield strain [143].

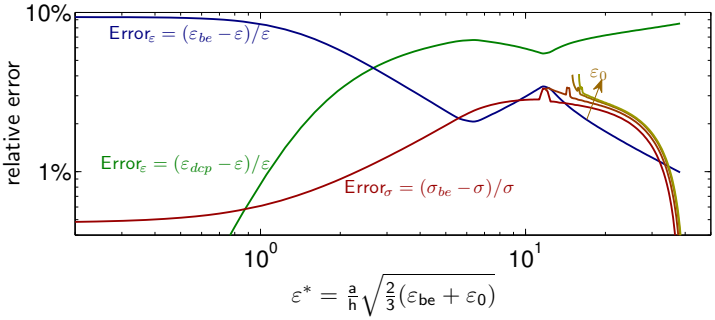

Figure 5.4: The relative systematic error in the stress σ_{be} and strain $\varepsilon_{\mathrm{be}}$ obtained with the bulge equations and in the strain $\varepsilon_{\mathrm{dcp}}$ obtained with the DCP solution as a function of the scaled strain ε^* (compared with the reference stress and strain from the simulation). Additionally, the relative systematic error in the stress from the bulge equations is shown for various levels of pre-strain (i.e. $\varepsilon_0 = [0, 0.5, 0.8, 0.9]\varepsilon_y$). Logically, for small strains, the DCP solution is more accurate in the strain than the bulge equations.

The relative systematic errors in strain and stress resulting from the bulge equations may not be acceptable. Since the systematic error under discussion in the article originates from the boundary conditions, a solution would be to measure the curvature and calculate the stress directly from the curvature. To measure the strain in that same area of the membrane a direct method like Digital Image Correlation can be used. This combination has been successfully applied on axisymmetrically inflated bio-membranes at large strains [55] and on micro-machined SiN rectangular bulge membranes at small strains [94].

5.4 Conclusions

Plane strain bulge test experiments are a valuable and acknowledged tool for measuring thin film properties. Yet, some quantitative mismatches exist in literature when comparing the results of the bulge tests with other small scale tests, see e.g. [87, 121]. One of the reasons for this is that the membrane deformation may be more complex than assumed, especially near the boundaries.

It was found that all bulge experiments start in a regime where the bulge equations are not valid, i.e. the Double Clamped Plated regime. When enough stress is applied to the system, plastic hinges start to form at the clamped edges initiating a transition regime. At some point, the plastic hinges have fully formed and the membrane profile deforms to

a cylindrical profile, from which point onward the cylindricity assumption in the bulge equations is (sufficiently) valid.

A scaled strain is proposed that can be calculated from the measured deflection and the membrane thickness to width ratio. With this scaled strain, a master plot has been constructed that can be used to make a reliable assessment of the bulge test to identify the region where the data can be trusted. Finally, a solution is proposed to improve the accuracy of the bulge test method, especially for thicker films.

Chapter 6
A consistent solution scheme for digital image correlation

Reproduced from; J. Neggers, B. Blaysat, J.P.M. Hoefnagels and M.G.D. Geers, *A consistent solution scheme for digital image correlation*, Experimental Mechanics, *review in progress*

Abstract

In digital image correlation (DIC), the unknown displacement field is typically found by minimizing the linearized form of the brightness conservation equation, while the minimization scheme also involves a linearization, yielding a two-step linearization with possibly hidden assumptions. This article reveals these assumptions by minimizing the non-linear brightness conservation equation in a consistent mathematical setting yielding a one-step linearization. Four silent assumptions are uncovered and their impact discussed according to an academic example.

6.1 Introduction

In DIC, a visible surface pattern is imaged with a camera during sample deformation. The "reference" image f, is compared with a "deformed" image g. Assuming that the observed brightness of one material point is not affected by the deformation, and relatively low acquisition noise, the brightness conservation is formulated as is common in DIC literature [1, 4, 24, 27, 28, 37, 51, 77, 105, 114, 122, 138, 139]:

$$f(\underline{x}) \approx g(\underline{\Phi}(\underline{x})) = g \circ \underline{\Phi}(\underline{x}), \tag{6.1}$$

$$\underline{\Phi}(\underline{x}) = \underline{x} + \underline{U}(\underline{x}), \tag{6.2}$$

where f and g are scalar fields of the imaged light intensity recorded by the camera sensor, $\underline{U}$ is the displacement vector field of the material points from f to g, and $\underline{\Phi}$ is a vector function which maps the reference coordinate $\underline{x}$ to the deformed coordinate.

To solve for the unknown displacement field, the typical approach is to (i) linearize the brightness conservation equation to the deformed coordinate, (ii) iteratively solving the problem, usually using a Gauss-Newton (or Levenberg-Marquardt) algorithm [10, 50, 52, 104]. Resulting in a two-step linearization, since the iterative algorithm also requires

Table 6.1: Nomenclature

$f(\underline{x})$: reference image	$g(\underline{x})$: current image
$\underline{U}(\underline{x})$: true displacement field	$\underline{u}(\underline{x},\underline{\lambda})$: approximated displacement field
$\underline{\Phi}(\underline{x})$: true mapping	$\underline{\phi}(\underline{x},\underline{\lambda})$: approximated mapping
$\tilde{g} = g \circ \underline{\phi}$: back-deformed image	$r(\underline{x},\underline{\lambda}) = f(\underline{x}) - \tilde{g}(\underline{x},\underline{\lambda})$: residual map
Ω : region of interest	$\underline{\underline{F}} = \underline{\mathrm{grad}}(\underline{\phi})$: deformation gradient tensor
$\underline{\lambda}$: column of degrees of freedom	$\Psi(\underline{\lambda})$: $\mathcal{L}_2(\Omega)$ norm of the residual

a linearization of the cost function with respect to the degrees of freedom (*dof*). The assumptions silently included in this approach have not been discussed before.

The goal of this article is to reveal and evaluate these silent assumptions. To achieve this, the linearized system of equations is derived departing from the original non-linear brightness conservation (Eq. 6.1), by directly linearizing with respect to the *dof*, resulting in a consistent Gauss-Newton DIC minimization scheme. The obtained general system of equations will be reduced thereafter, to recover the form commonly found in DIC literature, thereby unraveling the underlying assumptions.

6.2 Two step linearization

Before deriving the consistent system of equations, first the current two step linearization is revisited in order to carefully detail the steps involved to allow a detailed comparison to the later derived consistent system of equations. First Eq. 6.1 is written in a linearized form [4, 10, 37, 50–52, 77, 104, 105, 114],

$$f(\underline{x}) \approx g(\underline{x}) + \underline{\mathrm{grad}}(g)(\underline{x}) \cdot \underline{U}(\underline{x}). \tag{6.3}$$

Throughout this paper, coordinate space $\underline{x}$ is local to the camera frame, and thus fixed in space and time. The introduced gradient function is defined as the gradient towards the local coordinate $\underline{x}$, i.e. $\underline{\mathrm{grad}}(\cdot) = (\partial \cdot / \partial x_i)\underline{e}_i$.

Identifying the displacement field that will satisfy the above equation is an *ill-posed* problem, which deteriorates through the always present additional noise field. Therefore, DIC methods approximate the true displacement field with a field represented by a finite number of unknowns,

$$\underline{U}(\underline{x}) \approx \underline{u}(\underline{x},\underline{\lambda}), \tag{6.4}$$

$$\text{and} \quad \underline{\Phi}(\underline{x}) \approx \underline{\phi}(\underline{x},\underline{\lambda}), \tag{6.5}$$

where $\underline{\lambda}$ is a list of *dof*, i.e. $\underline{\lambda} = [\lambda_1, \lambda_2, \ldots, \lambda_n]$. Applying more pixels per *dof* allows for attenuation of acquisition noise (e.g. [51]), provided that the discretized displacement field can adequately describe the true displacement field.

Moreover, due to the high non-linearity of the pattern, linearization Eq. 6.3 is only valid for a limited range. This problem is commonly managed by iteratively updating the

deformed image, bringing it closer to the reference image. The updated back-deformed image is then defined as,

$$\tilde{g}(\underline{x}) = g \circ \underline{\phi}(\underline{x}, \underline{\lambda}), \tag{6.6}$$

which is the image g interpolated at the estimated deformed coordinates $\underline{\phi}$. Consequently, the linearized brightness conservation is written as,

$$f(\underline{x}) \approx \tilde{g}(\underline{x}) + \underline{\text{grad}}(\tilde{g})(\underline{x}) \cdot \underline{u}(\underline{x}, \underline{\lambda}), \tag{6.7}$$

$$\approx \tilde{g}(\underline{x}) + \underline{\text{grad}}(f)(\underline{x}) \cdot \underline{u}(\underline{x}, \underline{\lambda}), \tag{6.8}$$

where the displacement field $\underline{u}$ now is an incremental displacement, consistent with the iterative approach. When close to the solution, $\underline{\text{grad}}(\tilde{g})$ resembles $\underline{\text{grad}}(f)$ which is usually preferred due to its cheaper computational cost [10, 50].

Early DIC implementations used the cross-correlation product to determine the rigid body translations of small Zones Of Interest (ZOI) [28, 122, 138, 139]. These implementations are rather cost effectively solved in the frequency domain, but require that the pixels in the ZOIs move as one. To accommodate non-constant deformation fields (i.e. strain) within a ZOI [1, 24, 27] or even within the entire Region Of Interest (ROI, denoted Ω) [10, 50, 52, 104], it has become common practice to solve for $\underline{\lambda}$ by minimizing a cost function iteratively. The benefit is that displacement field discretization can be chosen tailored to the kinematics of the experiment, at the cost that the satisfaction of Eq. 6.8 now is a coupled problem.

To find the optimal approximate solution of Eq. 6.8 $\underline{u}^{\text{opt}}$ a minimization problem is formulated,

$$\underline{u}^{\text{opt}}(\underline{x}) = \underline{u}(\underline{x}, \underline{\lambda}^{\text{opt}}) \text{ with } \underline{\lambda}^{\text{opt}} = \underset{\underline{\lambda}}{\text{Argmin}} \left\{ \Psi(\underline{\lambda}) \right\}, \tag{6.9}$$

where the cost function Ψ is defined as the $\mathcal{L}_2(\Omega)$ norm of the residual of the linearized brightness conservation (Eq. 6.8),

$$\Psi(\underline{\lambda}) = \frac{1}{2} \int_{\Omega} \left[f - \tilde{g} - \underline{\text{grad}}(f) \cdot \underline{u} \right]^2 \mathrm{d}\underline{x}. \tag{6.10}$$

Minimization of Ψ implies;

$$\underline{\Gamma}(\underline{\lambda}^{\text{opt}}) = \frac{\partial \Psi}{\partial \underline{\lambda}} \left(\underline{\lambda}^{\text{opt}} \right) = \underline{0}. \tag{6.11}$$

The resulting non-linear system is linearized, and solved using a Gauss-Newton algorithm. At each iterative step, the *dof* $\underline{\lambda}^{k+1}$ are decomposed in an initial guess $\underline{\lambda}^{k}$ and an iterative update $\underline{\delta\lambda}$,

$$\underline{\lambda}^{k+1} = \underline{\lambda}^{k} + \underline{\delta\lambda}, \tag{6.12}$$

$$\underline{\Gamma}(\underline{\lambda}^{k+1}) = \underline{0} \Rightarrow \underline{\Gamma}(\underline{\lambda}^{k}) + \frac{\partial \underline{\Gamma}}{\partial \underline{\lambda}} \left(\underline{\lambda}^{k} \right) \underline{\delta\lambda} = \underline{0}. \tag{6.13}$$

Eq. 6.13 is written in matrix form as,

$$\underline{\underline{M}} \cdot \delta\underline{\lambda} = \underline{b} \qquad \text{with} \begin{cases} M_{ij} = \frac{\partial \Gamma_i}{\partial \lambda_j}(\underline{\lambda}^k), \\ b_i = \Gamma_i(\underline{\lambda}^k), \end{cases} \tag{6.14}$$

thereby arriving at conventional two-step linearized system of equations:

$$M_{ij} = -\int_\Omega \underline{\varphi}_i \cdot \underline{\mathrm{grad}}(f)\, \underline{\mathrm{grad}}(f) \cdot \underline{\varphi}_i \, \mathrm{d}\underline{x}, \tag{6.15}$$

$$b_i = -\int_\Omega \underline{\varphi}_i \cdot \underline{\mathrm{grad}}(f)\, \left[f - \tilde{g}\right] \mathrm{d}\underline{x}, \tag{6.16}$$

where $\underline{\varphi}_i$ is the linearization of $\underline{\phi}$, i.e.

$$\forall i \in [1,n],\ \underline{\varphi}_i = \frac{\partial \underline{u}}{\partial \lambda_i^k} = \frac{\partial \underline{\phi}}{\partial \lambda_i^k}. \tag{6.17}$$

The fields $\underline{\varphi}_i$ are usually referred to as the basis functions. The basis functions are not required to be linearly independent, but if chosen as such, then the approximated displacement field can be written in the familiar form found in literature, e.g. [10, 50–52, 104],

$$\underline{u}(\underline{x}, \underline{\lambda}^k) = \sum_{i=1}^{n} \lambda_i^k \underline{\varphi}_i(\underline{x}). \tag{6.18}$$

6.3 One step linearization

The next section discusses the derivation of a similar system of equations, however, now starting from the non-linear form of the brightness conservation equation (Eq. 6.1). The finally obtained result will be compared to the system of equations defined above (Eq. 6.15 and 6.16). Obtaining the solution of the non-linearized brightness conservation starts with formulating a consistent cost function:

$$\Psi(\underline{\lambda}) = \frac{1}{2} \int_\Omega \left[f(\underline{x}) - g \circ \underline{\phi}(\underline{x}, \underline{\lambda}) \right]^2 \mathrm{d}\underline{x}. \tag{6.19}$$

Analogous to the two-step linearization, the iterative Gauss-Newton algorithm is applied (Eq. 6.11 to 6.14). Reusing the definition of $\underline{\Gamma}$ (Eq. 6.11), $\underline{b}$ becomes, $\forall i \in [1,n]$,

$$b_i = -\int_\Omega \frac{\partial}{\partial \lambda_i} \left[g \circ \underline{\phi}\right](\underline{x}, \underline{\lambda}^k) \Big[\underbrace{f(\underline{x}) - g \circ \underline{\phi}(\underline{x}, \underline{\lambda}^k)}_{r(\underline{x}, \underline{\lambda}^k)} \Big] \mathrm{d}\underline{x}, \tag{6.20}$$

where, from now on, $\underline{\lambda}^k$ is simplified as $\underline{\lambda}$. Applying the chain rule on the first term in the integral yields,

$$\forall i \in [1,n],\ \frac{\partial}{\partial \lambda_i} \left[g \circ \underline{\phi}\right] = \frac{\partial \underline{\phi}}{\partial \lambda_i} \cdot \underbrace{\underline{\mathrm{grad}}(g) \circ \underline{\phi}}_{=\underline{G}}. \tag{6.21}$$

Note that this is the true definition of the image gradient $\underline{G}$, which can be approximated in various ways (see the legend of Fig. 6.1). Finally, $\underline{b}$ is expressed as,

$$\forall i \in [1,n],\ b_i = -\int_\Omega \underline{\varphi}_i(\underline{x},\underline{\lambda}) \cdot \underline{G}(\underline{x},\underline{\lambda})\, r(\underline{x},\underline{\lambda}) \mathrm{d}\underline{x}. \tag{6.22}$$

The corresponding tangent operator $\underline{\underline{M}}$ consists of three terms,

$$\underline{\underline{M}} = \underline{\underline{M}}^a + \underline{\underline{M}}^b + \underline{\underline{M}}^c, \tag{6.23}$$

with, $\forall (i,j) \in [1,n]^2$

$$M^a_{ij} = -\int_\Omega \underline{\varphi}_i(\underline{x},\underline{\lambda}) \cdot \underline{G}(\underline{x},\underline{\lambda}) \frac{\partial r}{\partial \lambda_j}(\underline{x},\underline{\lambda})\, \mathrm{d}\underline{x}, \tag{6.24}$$

$$M^b_{ij} = -\int_\Omega \underline{\varphi}_i(\underline{x},\underline{\lambda}) \cdot \frac{\partial \underline{G}}{\partial \lambda_j}(\underline{x},\underline{\lambda}) r(\underline{x},\underline{\lambda})\, \mathrm{d}\underline{x}, \tag{6.25}$$

$$M^c_{ij} = -\int_\Omega \frac{\partial \underline{\varphi}_i}{\partial \lambda_j}(\underline{x},\underline{\lambda}) \cdot \underline{G}(\underline{x},\underline{\lambda})\, r(\underline{x},\underline{\lambda})\, \mathrm{d}\underline{x}. \tag{6.26}$$

Expanding $\underline{\underline{M}}^a$ in a manner similar to b_i, one can write, $\forall (i,j) \in [1,n]^2$

$$M^a_{ij} = \int_\Omega \underline{\varphi}_i(\underline{x},\underline{\lambda}) \cdot \underline{G}(\underline{x},\underline{\lambda})\, \underline{G}(\underline{x},\underline{\lambda}) \cdot \underline{\varphi}_j(\underline{x},\underline{\lambda})\, \mathrm{d}\underline{x}. \tag{6.27}$$

The second term, $\underline{\underline{M}}^b$, involves the derivative of $\underline{G}$ towards the *dof*. Applying the chain rule on (Eq. 6.21) yields, $\forall j \in [1,n]$

$$\frac{\partial \underline{G}}{\partial \lambda_j} = \frac{\partial \underline{\phi}}{\partial \lambda_j} \cdot \underline{\mathrm{grad}}(\underline{\mathrm{grad}}(g)) \circ \underline{\phi} = \underline{\varphi}_j \cdot \underline{\underline{\mathcal{G}}}, \tag{6.28}$$

where $\underline{\underline{\mathcal{G}}}(\underline{x},\underline{\lambda})$ is the second gradient of image g, evaluated at $\underline{\phi}$. Subsequently, M^b_{ij} becomes,

$$M^b_{ij} = -\int_\Omega \underline{\varphi}_i(\underline{x},\underline{\lambda}) \cdot \underline{\underline{\mathcal{G}}}(\underline{x},\underline{\lambda}) \cdot \underline{\varphi}_j(\underline{x},\underline{\lambda}) r(\underline{x},\underline{\lambda})\, \mathrm{d}\underline{x}. \tag{6.29}$$

Eqs. 6.22, 6.26, 6.27, and 6.29 constitute the consistent solution for the iterative Gauss-Newton minimization of the (non-linear) brightness conservation. Using this formulation provides the expected fast convergence behavior attributed to Gauss-Newton methods, if close to the solution (e.g. the dashed line in Fig. 6.1). For a more detailed derivation of the DIC system of equations, including expansion to topology (height) correlation please see appendix B.

6.4 Discussion

Let us now focus on the assumptions that need to be made to recover the formulations used in DIC literature. Starting with the terms $\underline{\underline{M}}^b$ and $\underline{\underline{M}}^c$, both terms involve the image

residual r, which tends to be large at the beginning of the iterative process, possibly driving the minimization into a local minimum. Moreover, $\underline{\underline{M}}^b$ also contains the second gradient of the image, making it highly sensitive to noise. Finally, the adopted basis is often linearly independent, reducing $\underline{\underline{M}}^c$ to zero. Therefore, to improve robustness, omitting both terms seems an intelligent choice, yielding a relaxed tangent operator, i.e.

$$\underline{\underline{M}} \equiv \underline{\underline{M}}^a. \tag{6.30}$$

$\underline{\underline{M}}^a$ contains the true image gradient $\underline{G}$, which relates to the gradient of the commonly reported back-deformed image $\underline{\mathrm{grad}}(\tilde{g})$ through,

$$\underline{\mathrm{grad}}(\tilde{g}) = \underline{\mathrm{grad}}\left[g \circ \underline{\phi}\right], \tag{6.31}$$

$$= \underline{\mathrm{grad}}(\underline{\phi}) \cdot \underline{\mathrm{grad}}(g) \circ \underline{\phi}, \tag{6.32}$$

thus,

$$\underline{G} = \underline{\mathrm{grad}}(g) \circ \underline{\phi} = \underline{\mathrm{grad}}(\tilde{g}) \cdot \underline{\underline{F}}^{-T}, \tag{6.33}$$

where $\underline{\underline{F}}$ is the deformation gradient tensor. To simplify this form to the one regularly found in literature, first, small deformations need to be assumed, i.e. $\underline{\underline{F}}^T \equiv \underline{\underline{I}}$. Second, $\underline{\mathrm{grad}}(\tilde{g})$ is replaced with $\underline{\mathrm{grad}}(f)$, which has been justified in the literature because $\tilde{g}$ is updated at each iteration and converges towards f [10, 105],

$$\underline{G} \approx \underline{\mathrm{grad}}(f). \tag{6.34}$$

By substituting the above in equations 6.22 and 6.27 the commonly used DIC formulation is retrieved (Eq. 6.15 and 6.16). A total of four silent assumptions are uncovered:

$$\begin{aligned} &\underline{\underline{M}}^b \equiv \underline{\underline{0}}, \qquad \underline{\underline{F}}^T \equiv \underline{\underline{I}}, \\ &\underline{\underline{M}}^c \equiv \underline{\underline{0}}, \quad \underline{\mathrm{grad}}(\tilde{g}) \equiv \underline{\mathrm{grad}}(f). \end{aligned} \tag{6.35}$$

Depending on the DIC case at hand, each assumption is defensible or even intelligent, yielding a tangent operator which is independent of the *dof*, and thus can be computed once for all iterations.

The above discussions have led to six possible tangent operators, each with different levels of approximation. Moreover, mixed gradients have been proposed in literature, e.g. [10],

$$\underline{G} \approx \frac{1}{2}\left(\underline{\mathrm{grad}}(\tilde{g}) + \underline{\mathrm{grad}}(f)\right), \tag{6.36}$$

which, due to anti-symmetry in the *dof* estimates that are obtained by $\underline{\mathrm{grad}}(\tilde{g})$ or $\underline{\mathrm{grad}}(f)$, leads to a lower truncation error of the linearization of the pattern, and in the case of acquisition noise allows for additional noise attenuation by the averaging of both image gradients. The same mixing of gradients is also possible for the proposed large deformation image gradients, e.g.

$$\underline{G} \approx \frac{1}{2}\left(\underline{\mathrm{grad}}(\tilde{g}) + \underline{\mathrm{grad}}(f)\right) \cdot \underline{\underline{F}}^{-T}, \tag{6.37}$$

resulting in a total of eight tangent operators.

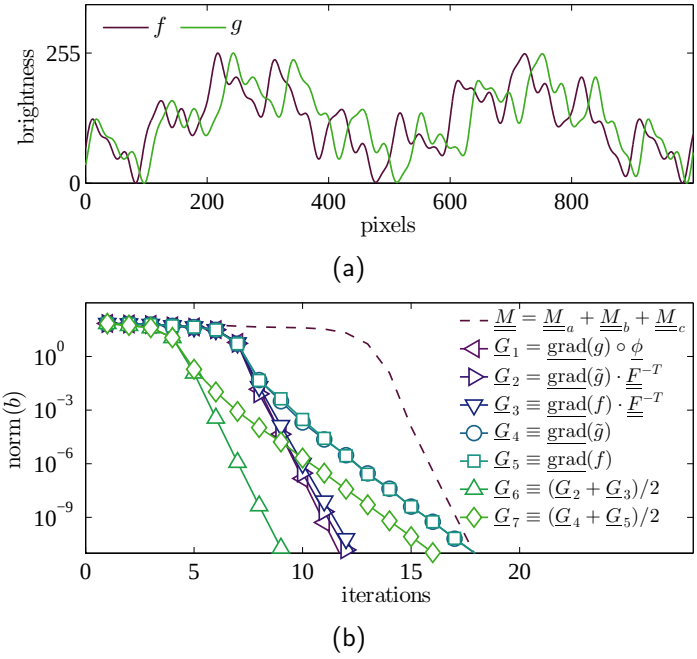

Figure 6.1: (a) A 1D example, where a non-linear (quadratic) displacement field is applied to the pattern f to generate g. (b) The convergence-rate is shown for the eight tangent operators discussed in this article. For each curve a rapid converging regime follows a slow regime, the main differences are in the onset of the rapid regime and the convergence-rate in the rapid regime.

To illustrate the effect of each tangent operator, the iterative results for a simple characteristic example are discussed here. For this example, a 1D pattern is generated and artificially deformed with a quadratic displacement field to obtain images f and g (Fig. 6.1a). A cubic polynomial basis is chosen, such that the basis can capture the exact solution of the applied displacement field. Fig. 6.1b shows the convergence-rate for the eight tangent operators, for each curve two regimes can be identified, an initial regime far from the solution where convergence is slow, followed by a regime with rapid conversion close to the solution. Considering the second (rapid) regime, clearly two convergence-rates can be identified. The fully consistent operator ($\underline{\underline{M}} = \underline{\underline{M}}^a + \underline{\underline{M}}^b + \underline{\underline{M}}^c$), and all other formulations using the large deformation formulation ($\underline{G}_1, \underline{G}_2, \underline{G}_3, \underline{G}_6$) show an improved convergence-rate with respect to the small deformation formulations (i.e. G_4, G_5, G_7). Considering the initial (slow) regime, the formulations appear in three groups, transitioning from slow to rapid convergence at iteration 12, 7 and 4 respectively. In agreement with the above discussion, the fully consistent operator converges poorly when far from the solution, even for the relatively smooth pattern applied in this example case. The single image gradient formulations (i.e. G_1 to G_5) form the center group, transitioning at the 7^{th} iteration. The third group are the mixed gradients (i.e. G_6, G_7) which con-

verge fastest in the slowly converging regime. Of course, these results are specific for this test-case. Although the general trend, that mixed gradients converge faster in the slow regime and large deformation formulations converge faster in the rapidly converging regime, is expected for typical DIC cases.

6.5 Conclusions

To conclude, the discussed consistent "one-step" derivation of the Gauss-Newton scheme, directly from the non-linear brightness conservation, yielded a minimization scheme with improved convergence-rate close to the solution. The proposed minimization scheme can be reduced to the one typically discussed in DIC literature if four assumptions are made; (i) a small residual ($\underline{\underline{M}}^b \equiv \underline{\underline{0}}$), (ii) linearly independent basis functions ($\underline{\underline{M}}^c \equiv \underline{\underline{0}}$), (iii) small strains ($\underline{\underline{F}} \equiv \underline{\underline{I}}$) and (iv) a good initial guess ($\underline{\mathrm{grad}}(\tilde{g}) \equiv \underline{\mathrm{grad}}(f)$). Since most current DIC applications consider small deformations, these assumptions are typically valid, leading to the conclusion that the common DIC formulation is appropriate for most cases, as confirmed by many authors who have investigated the accuracy of the method. Nonetheless, by clearly identifying the limits it is now possible to assess when they will be violated.

Acknowledgements

The authors acknowledge professors F. Hild and S. Roux for the fruitful discussions regarding this topic and DIC in general.

Chapter 7
Direct stress-strain measurements from bulged membranes using topography image correlation

Reproduced from; J. Neggers, J.P.M. Hoefnagels, F. Hild, S.G. Roux and M.G.D. Geers, *Direct stress-strain measurements from bulged membranes using topography image correlation* Experimental Mechanics, *review in progress*

Abstract

This paper discusses an experimental method to characterize thin films as they are encountered in micro-electronic devices. The method enables the measurement of the stress and strain of pressure deflected bulged membranes without using a priori defined bulge equations. An enrichment to the Global Digital Image Correlation method is detailed to capture the membrane strain and curvature while robustly dealing with acquisition noise. The accuracy of the method is analyzed and compared to the standard bulge test method. The method is applied to a proof of principle experiment to investigate its applicability and accuracy. Additionally, it is shown for two experimental cases that the method provides accurate results, although the bulge equations do not hold.

7.1 Introduction

Thin films are key in miniaturizing components in consumer electronic devices. It is known that the properties of most thin films are size dependent, since their intrinsic microstructural length scale is of comparable size to the design length scale [95, 133]. Moreover, the processing techniques, and the adjacent materials, also influence the mechanical response [3, 46]. It is therefore important to perform an *in-situ* characterization of these films, i.e. with the selected manufacturing processes as used in the device.

The bulge-test is a well known technique for testing thin film properties, especially at small scales [95]. In a bulge-test, a membrane of specific shape (rectangular, circular) is deflected under pressure. The deflection and pressure can be converted into stress and strain using shape specific equations. Generally, bulge equations are derived using energy minimization methods [6, 123, 126] resorting to approximate membrane displacement

fields. In these derivations several assumptions are used to make the system solvable. Although these assumptions may be clearly specified, they are often only approximately fulfilled and hence the resulting error/uncertainty on the estimates of the mechanical properties of these films is difficult to evaluate.

For micro-electronic systems the miniaturized rectangular bulge equations developed by Vlassak et al. [135, 141] are popular. The reason is that, for these systems, it is possible to manufacture the rectangular membranes with high precision by back etching a Si wafer using KOH (potassium hydroxide), thereby improving the accuracy significantly. Vlassak et al. have shown that for rectangular membranes (width $2a$ along the x direction, length $2b$ along the y axis, and thickness t), with sufficiently large width-to-length aspect ratio $b/a > 6$, the center part of the membrane closely approximates a plane-strain state and deflects cylindrically. The bulge equations then obtained to compute the stress and strain from the pressure and deflection are,

$$\kappa_{xx} = \frac{2\delta}{a^2 + \delta^2}, \tag{7.1}$$

$$\sigma_{xx} = \frac{P}{t\kappa_{xx}}, \tag{7.2}$$

$$\varepsilon_{xx} = \frac{1}{a\kappa_{xx}} \sin^{-1}(a\kappa_{xx}) - 1, \tag{7.3}$$

where, P is the pressure and δ the deflection at the center (or apex) of the membrane and κ_{xx} its curvature along direction x. Equation (7.2) is also known as the hoop stress equation, and is derived from static equilibrium assuming negligible flexural moment. Equation (7.3) is purely geometrical and based on the assumption that the membrane deflects to a circular profile. It has been shown that this method is accurate for films with large width-to-thickness ratios $a/t > 1000$ (depending on the level of strain) because these thin films approximate a free rotating hinge at the boundary [94]. Thicker films conform poorly to the circular deflection profile that connects the two edges. In particular close to their edge, flexural moments are the largest and hence the evaluation of the curvature from Equation (7.1) may lead to significant errors. Alternatively, as long as the film edges are removed from the analysis, the hoop stress equation, Equation (7.2) may still be valid.

More importantly, all bulge equation methods are limited to homogeneous, unstructured membranes, with specific shapes. Nonetheless, in current microelectronic applications more complex thin film shapes are often found [86, 107], even with multiple layered and structured heterogeneous thickness materials. Since a bulge-equation based method can only provide a global (or averaged) material response, it would not apply to such thin films.

In this paper, a new method is proposed for measuring thin films that are loaded with a pressure medium similar to the bulge test method. In this new method, full-field Optical Confocal Profilometry is combined with dedicated Global Digital Image Correlation (GDIC). The proposed method enables the full-field strain and curvature fields to be measured for any type of deformed sample measured with a profilometric full-field technique.

Using the fact that the pressure is uniform under the sample, the full-field membrane stresses are derived from the pressure and curvature if the bending stresses are negligible and the local stress state (e.g., plane-strain, biaxial loading) is known (Section 7.2.3). The proposed method utilizes the wealth of full-field data that allows for noise attenuation, resulting in improved accuracy in cases where the bulge equations apply, as discussed in Section 7.3. Moreover, the proposed method is direct, i.e. measuring the local stress and strain without assuming any global deformed shape. The method is therefore more widely applicable in terms of e.g. membrane thickness, membrane shapes, and structured membranes, as demonstrated in Section 7.4.

7.2 Methods

The proposed method has been developed for thin films as they are used in micro-electronics applications. For these films, the small strain regime is usually the most relevant for service conditions. This regime also implies small curvatures, which puts high demands on the used experimental technique. Therefore, a microscopic surface profilometry technique (such as confocal profilometry or phase shift interferometry) is chosen as a measurement method. This type of system measures the "surface profile" of the sample, which is the height of the sample at every pixel location. The resulting data are images (i.e. 2D matrices), where the pixel information is not a gray value but height. As a result, in this study, GDIC is applied to identify the 3D displacement vector field, from (2D) height-images, and therefore called *Quasi-3D*. Such a Quasi-3D GDIC method has been used before on Atomic Force Microscopy data [48]. Additionally, the proposed method aims to capture the curvature field, which is the second derivative of the position field. It is well known that noise has a detrimental effect on derivatives. It is therefore imperative to deal with the acquisition noise robustly, for which particular choices are made in the GDIC procedure.

7.2.1 Global digital image correlation

Digital Image Correlation (DIC) in general consists of measuring the displacement field between two images obtained from two increments of loading in an experiment [24, 28, 50]. The first image is usually a picture of the reference configuration f, and the second image a picture of the deformed configuration g. If the pictures capture a (speckle) pattern, which is deformed with the underlying sample, then the gray level conservation for a pixel at location $\vec{x}$ reads

$$\eta(\vec{x}) = f(\vec{x}) - g(\vec{x} + u(\vec{x})\vec{e}_x + v(\vec{x})\vec{e}_y), \tag{7.4}$$

where u and v are the in-plane components of the displacement respectively in x and y direction, and η is the acquisition noise. In the case of profilometric data, the pixel values contain height information, which may evolve between two measurement increments. Thus the gray level conservation is rewritten as "topography" conservation,

$$\eta(\vec{x}) = f(\vec{x}) - \Big(g(\vec{x} + u(\vec{x})\vec{e}_x + v(\vec{x})\vec{e}_y) - w(\vec{x})\Big), \tag{7.5}$$

where w denotes the out-of-plane displacement, and η now represents noise, but also height distortions not captured in w. Note that the topography is in data structure similar to a 2D image, thus the position vector remains 2D,

$$\vec{x} = x\vec{e}_x + y\vec{e}_y, \tag{7.6}$$

in contrast with the 3D displacement vector,

$$\vec{u}(\vec{x}) = u(\vec{x})\vec{e}_x + v(\vec{x})\vec{e}_y + w(\vec{x})\vec{e}_z. \tag{7.7}$$

To write the problem in terms of a limited number of unknowns, the displacement field is obtained through the minimization of a functional over of subspace of functions $\vec{\varphi}$,

$$\vec{u}(\vec{x}) \approx \vec{u}^*(\vec{x}, \underline{\lambda}) = \sum_{i=1}^{3n} \lambda_i \vec{\varphi}_i(\vec{x}), \tag{7.8}$$

where $\underline{\lambda}$ is a column vector with the degrees of freedom for a chosen set of basis functions $\vec{\varphi}$, detailed later on. The displacement field $\vec{u}^*$ is then obtained by minimizing the squared residual with respect to $\underline{\lambda}$,

$$\underline{\lambda} = \underset{\underline{\lambda}}{\text{Argmin}}(\Phi) = \underset{\underline{\lambda}}{\text{Argmin}} \int_\Omega \left(\eta(\vec{x}, \vec{\lambda})\right)^2 \, \mathrm{d}\vec{x}, \tag{7.9}$$

where η is now dependent on the degrees of freedom through the substitution of Equation (7.8) into Equation (7.5).

For this purpose, an iterative procedure is performed, where $\underline{\lambda}$ consists of a current value $\underline{\lambda}^k$, and an unknown iterative update $\underline{\delta\lambda}$

$$\underline{\lambda}^{k+1} = \underline{\lambda}^k + \underline{\delta\lambda}. \tag{7.10}$$

where k denotes the current iteration. The update is found by solving the linearized form of Equation 7.9,

$$\forall_j \quad \sum_{i=1}^{3n} \int_\Omega (\vec{\varphi}_j \cdot \vec{G})(\vec{G} \cdot \vec{\varphi}_i) \, \mathrm{d}\vec{x} \, \delta\lambda_i = \int_\Omega \vec{\varphi}_j \cdot \vec{G} \, (f - \tilde{g}) \, \mathrm{d}\vec{x}, \tag{7.11}$$

where $\vec{G}$ is the image gradient, defined below, and,

$$\tilde{g} = g(\vec{x} + u^*(\vec{x}, \underline{\lambda}^k)\vec{e}_x + v^*(\vec{x}, \underline{\lambda}^k)\vec{e}_y) - w^*(\vec{x}, \underline{\lambda}^k),$$

is the corrected version of $g(\vec{x})$ using the current estimate of the displacement field. Equation 7.11 is usually written in matrix form,

$$\underline{\underline{M}} \, \underline{\delta\lambda} = \underline{b}, \tag{7.12}$$

where the tangent matrix $\underline{\underline{M}}$ and the right-hand member $\underline{b}$ are conceptually similar to established GDIC [50, 51]. The main difference is the vector $\vec{G}$, which is the image gradient enriched with an out-of-plane component

$$\vec{G} = \frac{\partial f}{\partial x}\vec{e}_x + \frac{\partial f}{\partial y}\vec{e}_y - \vec{e}_z, \tag{7.13}$$

and the three-dimensional nature of the basis functions

$$\vec{\varphi} = \varphi_x \vec{e}_x + \varphi_y \vec{e}_y + \varphi_z \vec{e}_z. \tag{7.14}$$

To build $\tilde{g}(\vec{x})$, the image $g(\vec{x})$ needs to be estimated at locations $\vec{x} + \vec{u}_2(\vec{x})$, for which a cubic spline interpolation scheme is used, where $\vec{u}_2$ denotes the in-plane displacement field. This interpolation is not exact, and is a source of error [111, 112]. Interestingly, the out-of-plane component does not enter the interpolation scheme, and does not suffer from interpolation errors in a direct way.

The iterative system is solved until convergence is reached. The chosen criterion is such that the norm of the degree of freedom increments, $\underline{\delta\lambda}$, becomes sufficiently small, i.e. $\|\underline{\delta\lambda}\| < 10^{-6}$.

The implementation used in this paper is considered a "global" DIC method because the system is minimized globally, instead of minimizing each zone of interest independently. However, the out-of-plane enrichment can also be applied to "local" DIC methods by following exactly the same procedure.

7.2.2 Basis functions

In a general DIC problem, a displacement vector is to be determined for each pixel in an image. This makes the problem ill-posed, even when not considering image noise. The solution is to reduce the number of unknowns to less than the number of pixels, for instance as was done in Equation 7.8. If there is uncorrelated (i.e. white) noise, then using more pixels per unknown will further reduce the noise sensitivity, thereby improving the accuracy. However, using too few unknowns restricts the kinematics of the solution, which decreases the accuracy. For that reason, it is important to use a basis that adequately captures the full kinematics of clamped bending membranes, inside the Region Of Interest (ROI), with a minimum number of degrees of freedom. Inspired by continuum solutions for loaded plates, a 2D polynomial basis is used. The C^∞ continuity property of polynomials makes these functions well suited for calculating curvature fields, noted that polynomials of at least second order are required to be sensitive to curvature.

The basis functions are vector functions where one component of the field is expressed as the product of two terms of a polynomial series,

$$\varphi_x = \varphi_y = \varphi_z = \chi^a \zeta^b, \tag{7.15}$$

where χ and ζ are normalized coordinates for x and y such that $-1 \leq \chi, \zeta \leq 1$. The complete basis is formed by using all combinations of a and b up to a certain order p, see Figure 7.1 for some examples. Each basis function is used three times, each with its own degree-of-freedom (for each component of the displacement vector). For example for

$p = 2$,

$$
\begin{aligned}
u^* &= \lambda_1\chi^0\zeta^0 + \lambda_2\chi^0\zeta^1 + \lambda_3\chi^1\zeta^0 \\
&\quad + \lambda_4\chi^0\zeta^2 + \lambda_5\chi^1\zeta^1 + \lambda_6\chi^2\zeta^0, \\
v^* &= \lambda_7\chi^0\zeta^0 + \lambda_8\chi^0\zeta^1 + \lambda_9\chi^1\zeta^0 \\
&\quad + \lambda_{10}\chi^0\zeta^2 + \lambda_{11}\chi^1\zeta^1 + \lambda_{12}\chi^2\zeta^0, \\
w^* &= \lambda_{13}\chi^0\zeta^0 + \lambda_{14}\chi^0\zeta^1 + \lambda_{15}\chi^1\zeta^0 \\
&\quad + \lambda_{16}\chi^0\zeta^2 + \lambda_{17}\chi^1\zeta^1 + \lambda_{18}\chi^2\zeta^0.
\end{aligned}
$$

This particular decomposition into separate degrees of freedom for each component of the displacement vector is one of the possible ways to define the basis functions. In particular, this will give 3 basis functions for $p = 0$, 9 basis functions for $p = 1$, 18 basis functions for $p = 2$, 30 basis functions for $p = 3$, etc.

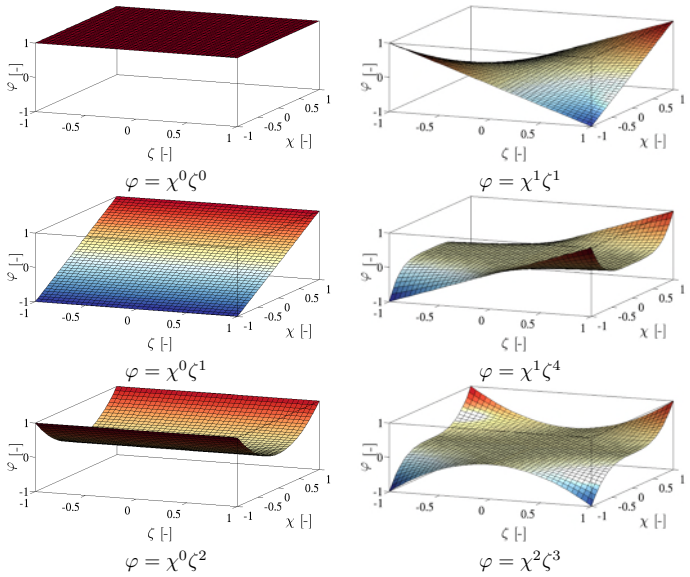

Figure 7.1: Example 2D basis-functions φ.

Because of the fact that the matrix elements M_{ij} involve the scalar product of pairs of functions with a "weight" that is the tensor $G \otimes G$, there is no gain in choosing an orthogonal polynomial basis. The same space of function will be generated by the above polynomials and say Legendre polynomials of the same order. Hence the resulting displacement, and convergence rate is independent of the particular choice provided the generated space is the same.

7.2.3 Curvature, stress and strain

Let us revisit the assumptions in the bulge equations discussed in the introduction. Equation (7.1) is a purely geometrical formulation to obtain the curvature from the deflection, assuming the membrane deflects according to a circular profile. For thin membranes and deflections larger than the membrane thickness this assumption holds, attributing to the established accuracy of the bulge test method. However, with the GDIC method discussed in this paper the curvature tensor $\boldsymbol{\kappa}(\vec{x})$ at each pixel location can be computed without resorting to the circularity assumption (see also [94]), by first defining

$$\boldsymbol{\kappa}(\vec{x}) = \vec{\nabla}\vec{n}(\vec{x}), \tag{7.16}$$

which in turn is the gradient of the position field $z(\vec{x})$ (corrected for rotations)

$$\vec{n}(\vec{x}) = \frac{\vec{\nabla}z(\vec{x})}{||\vec{\nabla}z(\vec{x})||}. \tag{7.17}$$

The position field is measured as the topography $g(\vec{x})$, however, it also includes the additional pattern. The membrane topography (i.e. the required position field) is more accurately obtained by by applying the measured displacement field to the initial (flat) membrane position. Because the displacement fields are forced to be smooth, by the polynomial basis, noise in the curvature is here controlled by the basis order, as will be shown further down.

Equation (7.3) is a similar geometrical formulation as Equation (7.1), which expresses the strain as function of the curvature assuming a circular deflection profile. For thicker or inhomogeneous membranes the circular deflection profile assumptions is violated, especially at the membrane boundary and heterogeneous points. However, the GDIC method recovers the displacement field, from which the strain field is easily obtained without assumptions, by e.g. computing the Green-Lagrange strain tensor $\boldsymbol{E}$ in the membrane plane.

Equation (7.2) is a simple balance equation evaluated without recourse to the small displacement hypothesis. It is valid as long as the bending moment can be neglected, but the actual size of the membrane does not come into play. Its validity depends on the flexural moment within the region over which the curvature is evaluated. However, the flexural moment is proportional to the change in curvature, which is measured and thus can be assessed.

At the apex of bulged square membranes, the pressure is balanced with membrane stresses in two directions. If the curvatures in both directions are equal then the principal stresses are also equal if the material is isotropic,

$$\sigma_{xx} = \sigma_{yy} = \frac{P}{2t\,\kappa}. \tag{7.18}$$

If a part of the membrane deforms axisymmetrically, the principal stresses of that mem-

brane part are related to the meridional and circumferential curvatures [53, 56],

$$\sigma_m = \frac{P}{2t\,\kappa_c}, \tag{7.19}$$

$$\sigma_m = \frac{P}{t\,\kappa_c}\left(1 - \frac{\kappa_m}{2\kappa_c}\right). \tag{7.20}$$

where c and m denote the meridional and circumferential directions respectively. For kinematically more complex cases, closed-form expressions cannot be obtained, and numerical schemes are required, such as Finite Element Method Updating [4].

To conclude, the assumption of neglecting flexural stiffness remains in the proposed methodology, yet only for relating stress to curvature. The assumption is appropriate if a restrained region is analyzed, such that the change in curvature is insignificant over the analyzed region.

7.2.4 Experimental procedure

Two types of samples are used in the present paper, a square (1×1 mm^2) membrane and a rectangular (1×6 mm^2) membrane (Figure 7.2). Both samples are manufactured by deposition a 100 nm thick Si_3N_4 layer on a monocrystalline 200 µm thick Si wafer. A freestanding membrane is created by back KOH etching the wafer up to the Si_3N_4 layer. The membrane dimensions are chosen such that the bulge equations are known to perform well [135], enabling a comparison with the GDIC method presented in this paper.

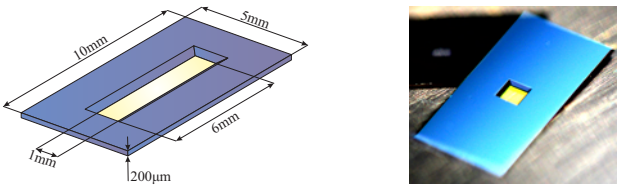

Figure 7.2: The two sample types used in the experiments, the Si_3N_4 membrane is 100 nm thick in both types, (a) a drawing of a rectangular membrane (1×6 mm^2), (b) a photograph of a square membrane (1×1 mm^2).

These samples are processed with high precision micro-manufacturing techniques, resulting in a surface roughness that is smaller than measurable with the used optical profilometer. Since a height correlation is to be performed on these samples, a height pattern is required. This pattern is created by coating the membrane surface with a colloidal suspension of Ag particles (80-500 nm diameter) dispersed in ethanol. After evaporation of the suspending fluid, the deposited particles (or rather clusters of particles as they tend to aggregate) showed enough physical adhesion to withstand the bulge test without detaching from nor moving on the surface. Note that the basis functions in

the GDIC method have support over the entire ROI, allowing the GDIC method to work efficiently with relatively sparse patterns. The sparse pattern allowed the evaluation of the unloaded freestanding film with and without the pattern. Application of the pattern did not cause a measurable deformation, confirming the insignificant influence on the mechanics.

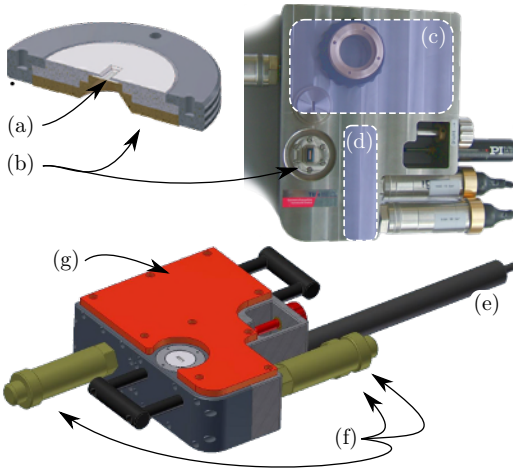

Figure 7.3: The bulge test apparatus with, (a) the sample, (b) the sample holder, (c) the 270 ml chamber, (d) the 30 ml chamber, (e) the linear actuator connected to the piston, (f) the three pressure sensors, (g) the heating stage.

To test the membranes a custom made low profile bulge test apparatus is specifically designed to allow for optical access to the sample surface (Figure 7.3). The apparatus consists of two ethanol filled stainless steel chambers of 270 ml and 30 ml respectively (Figure 7.3cd), which are connected with a valve. The sample is mounted on the smaller chamber with an interchangeable sample holder (Figure 7.3b). Additionally, the apparatus is equipped with three pressure sensors with respective pressure ranges [0–5], [0–15], [0–50] bar (Figure 7.3f). The pressure sensors are high performance millivolt output transducers from GE Sensing, with an accuracy of 0.04% of their rated maximum. The two large range sensors are mounted on the smaller chamber while the most sensitive sensor is mounted on the larger chamber. The pressure difference is applied with a piston radius of 1.6 mm, connected to the smallest chamber, driven by a linear actuator with a closed-loop DC motor (Figure 7.3e). The actuator steps in 50 nm increments with a total stroke of 25 mm, and a maximum applied force of 70 N. The two chamber design allows experiments in two pressure ranges, i.e. by closing the valve to the second chamber the most sensitive pressure sensor is naturally protected from overloading, while at the same time, the effect of the piston motion on the pressure is amplified. Finally, a heating stage (Figure 7.3g) serves to keep the entire system at a constant temperature, slightly above the room temperature ($\sim$28°C), to eliminate pressure changes due to thermal expansion.

The bulge test apparatus fits under the Sensofar Optical Profilometer, which is used to measure the surface roughness of each pressure increment. The experimental procedure

is controlled via custom NI LabVIEW code that follows a user-defined pressure loading curve in a closed loop, with intermittent pressure hold periods for the profile measurements. The height profile is captured by a Sensofar Plμ2300 Optical Confocal Microscope using a CCD camera (definition: 557×557 pixels) with a Nikon EPI 50x objective lens, resulting in a square field of view of 184×184 μm^2. The objective lens has a numerical aperture of 0.80, which together with the monochromatic blue light ($\lambda = 470$ nm) results in an in-plane resolution of 358 nm (i.e. slightly larger than the resolution of one pixel of the CCD sensor (332 nm)). For the patterned membranes discussed in this paper, the out-of-plane resolution has been measured to be ∼20 nm from the RMS of the difference between two height profiles of the same area on the sample. The difference between in-plane and out-of-plane resolution will also be apparent in the accuracy analysis of Section 7.3.

7.2.5 Virtual experiment

In this paper, proof of principle experiments on square and rectangular membranes are performed. To make a thorough evaluation of the accuracy of the method, virtual experiments are used. A virtual experiment is a synthetic procedure that produces similar data as expected from the real experiment, yet, with the additional knowledge of the reference.

To create realistic virtual height profiles, the virtual experimental procedure consists of deforming a real experimental height profile f (Figure 7.4b) with an FE displacement field (Figure 7.4c) to obtain a virtual deformed height profile g (Figure 7.4d). Different increments in the FE simulation are used to obtain the incremental pressure height profiles similar to a real experiment.

Two different FE geometries are used, corresponding to the rectangular (Figure 7.2a) and to the square (Figure 7.2b) membrane. In the FE simulations, a dense mesh is chosen to match the pixel discretization level of the height images. This results in a mesh of approximately 50,000 3D 4-node bilinear Mindlin shell elements, which is densest at the field of view (FOV) and opens towards the boundaries. Note that, for illustrative reasons, the grid shown in (Figure 7.4c) is not the actual used mesh, which would be too dense to show any meaningful detail.

At this stage it is possible to determine the order of the basis functions required to accurately capture the kinematics in the virtual experiment. Figure 7.5 shows the mean absolute displacement error between the FE displacement field $\vec{u}_{\text{fem}}$ and displacement fields approximated with increasing polynomial order $\vec{u}^*$. An error measure is introduced as the average of the lengths of all difference vectors between the FE displacement field and the approximated displacement fields, evaluated over all pixels k,

$$\mathcal{E}_u = \frac{1}{n} \sum_{k=1}^{n} \left(\| \vec{u}_{\text{fem}}(\vec{x}_k) - \vec{u}^*(\vec{x}_k) \| \right). \tag{7.21}$$

where the norm is defined as the Euclidean norm of, in this case, the difference vector. As expected, the mean absolute error decays for increasing order, and reaches an error

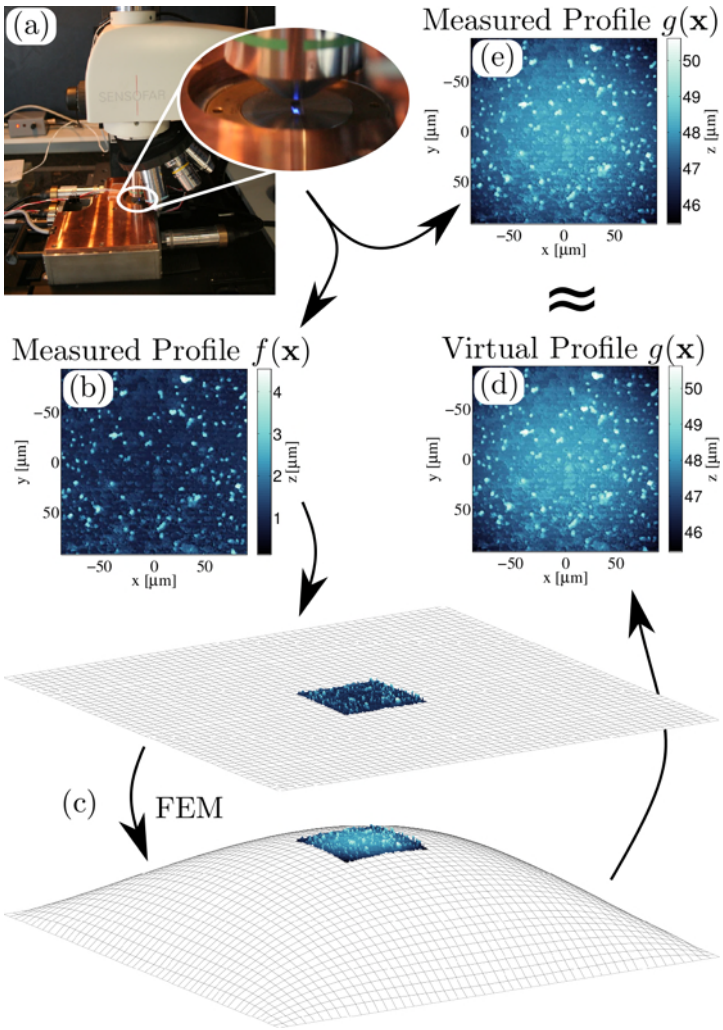

Figure 7.4: The reference profile $f(\vec{x})$ and the deformed profile $g(\vec{x})$ are measured with the experimental setup (a,b,e). Additionally, the reference profile is virtually deformed with an FE displacement field (c) to obtain a virtually deformed profile (d), which approximates the real experiment.

level of less than one nanometer for sets of basis functions with $p \geq 4$. Since this error is smaller than the resolution of the measurement system, it is chosen to truncate the series of basis functions at $p = 4$.

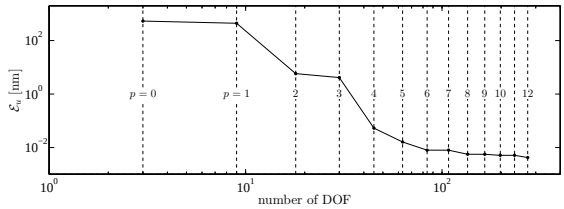

Figure 7.5: The mean absolute error as a function of polynomial order obtained by comparing the FE displacement field with approximated displacement fields with increasing polynomial order.

7.3 Accuracy analysis

7.3.1 Error fields

The use of the virtual experiment allows for direct comparisons between the results obtained with the proposed GDIC method and the FE reference solution. Similarly to Equation 7.21, a pixel-wise displacement error is computed as the vector difference between reference and the displacements estimated by GDIC. The different components and magnitude of the displacement error fields are shown in Figure 7.6 for the correlated ROI. More importantly, Figure 7.6a shows that the maximum error in displacement is approximately 10 nm while the average absolute error is much smaller. Even though there is no noise present in this virtual experiment, the result is based on a real experimental image f with the same pixel discretization and pattern as the real experiment. Note the difference in the in-plane accuracy versus the out-of-plane accuracy (Figure 7.6b-d). The error in w is approximately 20 times smaller than in u and v. This coincides with the observed accuracy of the confocal microscopy set-up itself.

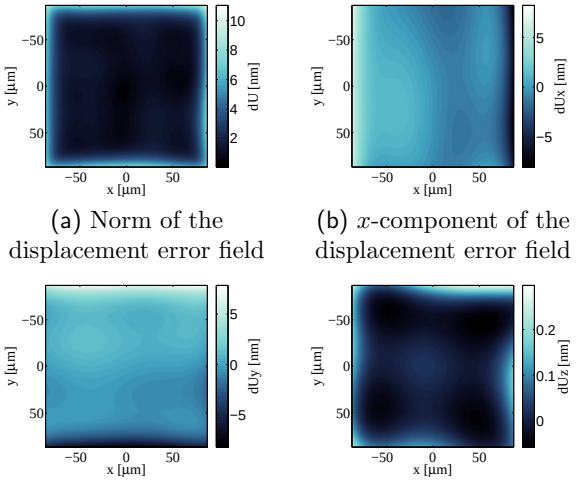

(a) Norm of the displacement error field

(b) x-component of the displacement error field

(c) y-component of the displacement error field

(d) z-component of the displacement error field

Figure 7.6: Error in the estimated displacement fields for the ROI for a full 4^{th} order set of shape functions without additional noise. The Euclidean norm is used as the vector norm shown in subfigure (a). Note that the accuracy of the out-of-plane displacement is approximately 20 times better than the accuracy of the in-plane displacement, which coincides with the observed accuracy of the confocal microscopy set-up.

7.3.2 Error vs. number of DOFs

The error sources in DIC are in general threefold:

1. acquisition noise or pattern changes;
2. subpixel interpolation;
3. displacement approximation.

To minimize the impact of the second error sources, a local cubic spline subpixel interpolation method is used. More interestingly, the first and third error source are dependent on the chosen basis. Using too few (or incorrect) basis functions will introduce systematic errors because the kinematics of the experiment cannot be captured. Conversely, giving the system more freedom, allows the solution to be sensitive to noise, resulting in statistical errors.

In Figures 7.7ab, image correlations are performed on virtual experiments for an increasing number of degrees of freedom, for various levels of (white) noise added to the deformed profile g. The virtual experiment method allows the application of artificial acquisition noise by adding generated noise fields to the images. The various noise levels are quantified as the standard deviation of the white noise, relative to the image gray level dynamics. It is clearly shown that for the noise-free situation, increasing the number of degrees of freedom only improves the result, while when noise is included, an opti-

mum accuracy is found using a conservative number of degrees of freedom (i.e. 10 to 20 DOFs). These results demonstrate that choosing the right kinematic basis for the GDIC procedure enhances the accuracy. The preferred basis is the one that captures the full kinematics with the minimum number of degrees of freedom. The applicability of a narrow basis, which is ideal in terms of accuracy and robustness, is limited to experiments within the range of this narrow basis. In contrast, the polynomial basis, discussed in this paper, is applicable to many types of experiments, provided they have slowly varying displacement fields, making the proposed method relatively general.

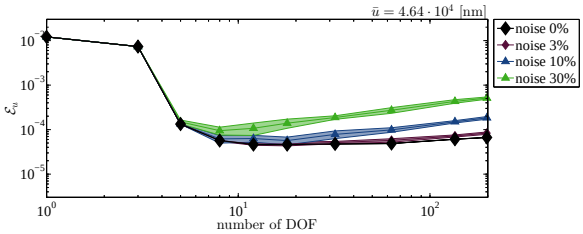

(a) Displacement error, normalized with the mean displacement $\bar{u}$

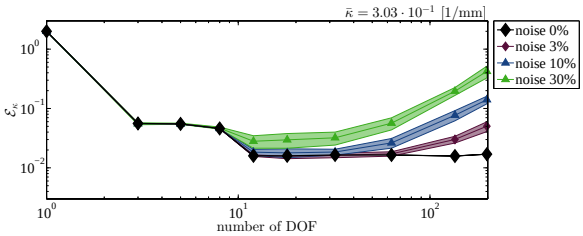

(b) Curvature error, normalized with the mean curvature $\bar{\kappa}$

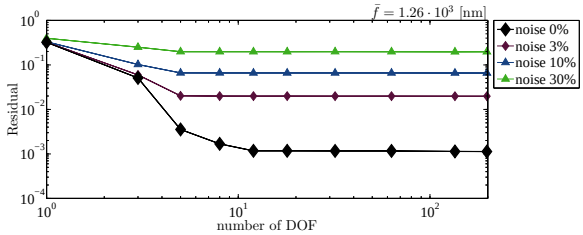

(c) Residual, normalized with the pattern RMS $\bar{f}$

Figure 7.7: Effect of increasing the number of degrees of freedom on (a) the residual, (b) the error in displacement, (c) the error in curvature.

In a real experiment, no reference case exists. Therefore, the recommended procedure to select a proper set of basis functions, is to perform the correlation for increasingly rich sets of basis functions. The residual (Figure 7.7c) will decrease for richer bases (if converged), yet the decrease will flatten at some level of richness. At this point, adding more degrees of freedom to the system tends to make the correlation less accurate due to noise sensitivity. Another method for evaluating the chosen basis, is by examining the

residual field. A correlation with too few basis functions will result in a residual field exhibiting long wavelength modulations, while the residual field for an appropriate basis will only contain the acquisition noise, and thus will resemble white noise.

7.4 Demonstration experiments

7.4.1 Proof of principle experiments

To investigate the accuracy of the method on real cases, four experiments are performed: two experiments deal with rectangular membranes, and two with square ones. The samples are chosen for allowing optimal accuracy when using the bulge equations, to make a fair comparison with the discussed GDIC method, see Section 7.2.4.

The membranes are pressurized with the bulge test apparatus to a pressure of 1 bar in 100 increments (above atmosphere), and then unloaded to 0 bar in 20 increments. One increment takes approximately 90 seconds including the pressure change, and scanning of the confocal microscope. On each of the recorded images the polynomial GDIC procedure is performed with all basis functions up to $p = 2$ for the square membranes (i.e. 18 DOFs). For the rectangular membrane the DOFs that operate in y-direction are removed leaving 15 DOFs.

Figure 7.8 shows the stress and strain results after processing the topographies with both the GDIC method and the bulge equations. The square membrane response is more stiff, which is expected since it is in a more confined biaxial strain state when compared to the plane strain state at which the rectangular membrane is deformed. Consequently, the obtained moduli are the plane strain modulus and the biaxial modulus that are directly related to the Young's modulus ($E \approx 234$ GPa) and the Poisson's ratio, ($\nu \approx 0.16$) and are as expected for these thin Si_3N_4 films. For the square membranes the stress-strain curves in both x and y-directions are shown, using κ_{xx} and κ_{yy} respectively. The curves overlap showing that the membranes are not anisotropic, at least not within the membrane plane. More importantly, the figure shows that both the bulge equations and the GDIC method give the same results, confirming the validity of the method.

7.4.2 Beyond the bulge equations

The previous results show that the method is comparable to the accuracy obtained by using the bulge equations. However, the goal of this method is to go beyond the validity regime of the bulge equations. Therefore, the GDIC method is applied to data of thicker membranes which are created by the virtual experiment framework.

A number of virtual experiments are performed (see Section 7.2.5). All virtual experiments use the same linear elastic material properties with Young's modulus of 235 GPa. Figure 7.9 shows the stress strain response taken from the center of membranes for all virtual experiments. As expected the bulge equations start deviating from the correct response for thicknesses above 2 µm, for this 1 mm wide membrane. In contrast, applying

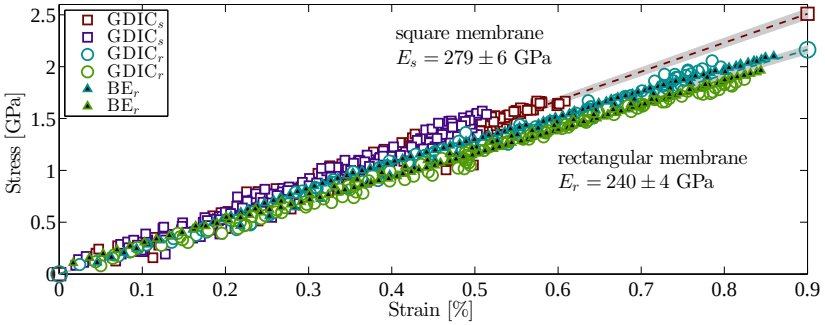

Figure 7.8: Measured stress strain response for two square and two rectangular 100 nm thick membranes. The GDIC method and the bulge equations perform equally well for such thin membranes.

the GDIC method to the same data shows correct stress strain response up to thicknesses of 20 µm. The GDIC method considers only the membrane inside the ROI, and thus is much less restricted by the flexural stiffness assumption.

For even thicker membranes the stress across the thickness is far from uniform, and no longer satisfies the assumptions made in Equation 7.2. It may be possible to obtain a corrected stress from the curvature for thicker membranes, but this requires a modification that is outside the scope of this paper.

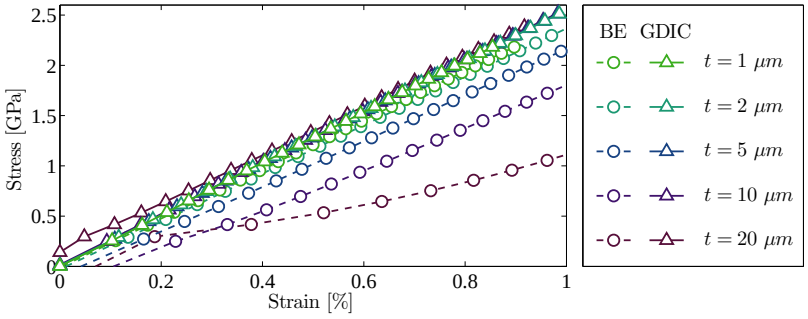

Figure 7.9: GDIC method and the bulge equations applied to virtual experimental data with the same material properties, but with various membrane thicknesses. The GDIC results do not deviate from the reference elastic response up to a thickness of 20 µm.

7.4.3 Inhomogeneous films

The previous results use only the stress and strain at the center of the membrane, but the GDIC method gives full-field stress strain results. To show that the GDIC method captures features in the membranes, the virtual experiment framework is again applied to generate experimental data. In this case a 24 µm wide strip along the y-axis is modeled

using a Young's modulus of $E_{\text{str.}} = 235$ GPa, while the remaining membrane material is modeled three times with different moduli, i.e. $E_{\text{mem.}} = [130, 170, 235]$ GPa.

The generated topography images are processed with the GDIC method twice, once masking the structure, and once masking everything but the structure. For all three virtual experiments the stress-strain curves are collected in one point on the structure and in two points on the membrane (See Figure 7.10). This shows that it is possible to obtain the correct stress strain results for two different materials from a single full-field measurement.

With the proposed method it is always possible to obtain curvature fields and strain fields. However, obtaining the stress fields relies on applying either Equation 7.2, 7.18, or 7.19, which are only valid for particular cases (e.g. plane-strain, biaxial, or axisymmetric states).

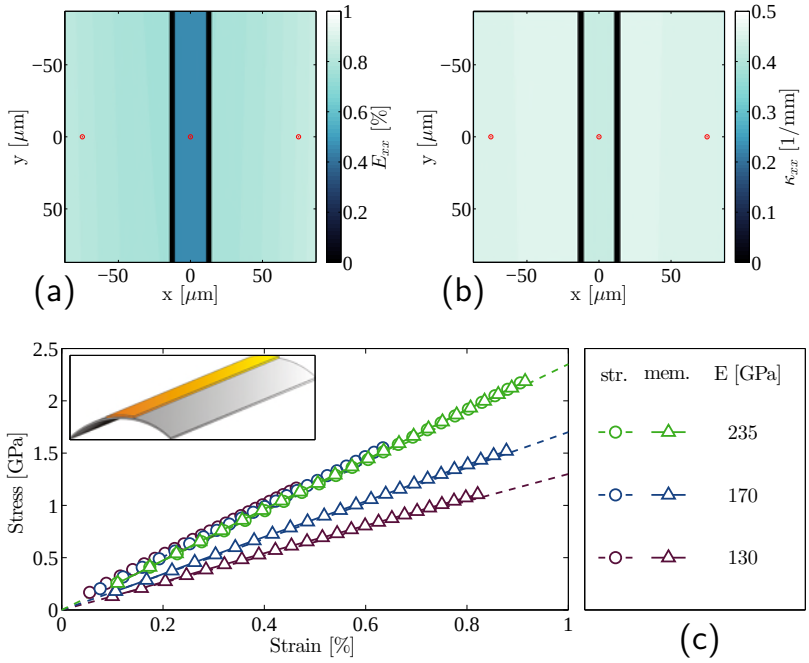

Figure 7.10: GDIC applied to three heterogeneous membranes, where only the Young's modulus of the membrane material is varied, and the center strip of material has a constant modulus of 235 GPa. Note that the method can capture full-field strain (a) and curvature (b) fields. The red dots in (a,b) show the location where the stress-strain depicted in (c) is taken.

7.5 Discussion and conclusions

The global DIC method has been extended to images containing height profiles, relaxing the brightness conservation principle and enabling for quantitative measurement of

in-plane and out-of-plane displacements. This extension is useful for any topographic measurement, in particular optical confocal profilometry, but also e.g. Scanning Probe Microscopes like Atomic Force Microscopy. Furthermore, the out-of-plane quantity is not limited to topography, it can be any measured field, e.g., temperature [89].

In the proposed GDIC method the image pattern and the quantified out-of-plane displacement field are both taken from the same topographical data. In order to avoid interference between them, a separation in length scales is required between the length scale of the out-of-plane displacement fluctuations and the pattern length scale. For the presented case of bulged membranes this separation of length scales is achieved by applying low order polynomial basis functions with support over the entire region of interest and by controlling the surface marking with a deposition of small clusters of nanoparticles. Considering that the membrane mechanics are the goal of the analysis, it is important that the added pattern does not mechanically influence the membrane. For the discussed cases it was shown that the pattern did not significantly influence the mechanics.

The introduced polynomial basis is particularly suited for the bulging of membranes, and not limited to square or rectangular membranes. The polynomial basis functions have a wide support and capture the membrane kinematics with only a few degrees of freedom. This makes the method highly robust with respect to noise, but also with respect to the initial guess. Moreover, the measured displacement fields are C^∞ continuous, making them ideal for the calculation of curvature fields.

Through the use of virtual experiments, where the input (FE) displacement field is known, the reference solution can be compared with the measured (via GDIC) displacement fields, through which the accuracy of the method was analyzed. The accuracy depends on the level of the acquisition noise and the richness of the kinematics that is controlled through the number of basis functions. Too restricted kinematics will give inaccurate results because the kinematics of the experiment is not adequately captured; too rich kinematics will make the solution sensitive to noise also leading to inaccurate results.

In a real experiment no reference displacement field exists to asses if an optimal basis is applied. To identify this optimum, it is suggested to perform DIC calculations for increasing number of degrees of freedom until the residual field stabilizes. The residual field should always decrease for increasing number of degrees of freedom, but when the residual decrease becomes small, it suggests that modes that cannot be measured are progressively included thereby inducing a degradation of the conditioning of the tangent GDIC problem, and hence an increased noise sensitivity.

The proposed method recovers the displacement fields, from which strain fields are trivially computed, regardless of the shape or thickness of the membrane. Moreover, the proposed method recovers curvature fields, and it is shown that for particular cases (i.e. plane-strain, biaxial, or axisymmetric strain-states) the stress fields can be recovered. Consequently, the bulge membrane shape can be any shape, and as long as the interrogated area fulfills one of these particular strain-states, then it is possible to obtain the stress in that respective area. For cases with more complex kinematics, a coupling with numerical method is to be made in order to obtain the stress.

As a proof-of-principle, bulge test experiments are performed for 100 nm thick Silicon Nitride films. Both the GDIC method and the plane-strain bulge equations are applied to the data, and give comparable results. This shows that the GDIC method at least matches the accuracy of the bulge equations for this particular case. However, the applicability regime of the GDIC method is much less restrictive.

The method applies the same assumption (negligible flexural moments) as the plane-strain bulge equations to obtain stresses. However, by considering only a small portion of the membrane, the assumption is less restrictive. Therefore, application of the method to inhomogeneous membranes with less restrictions on the membrane thickness has shown to accurately recover the stress-strain response of the various materials in the field of view. Consequently, the proposed method is less restricted in terms of membrane thickness, membrane homogeneity and membrane shapes, thereby, alleviating these shortcomings of the original bulge test.

Chapter 8
A time-resolved integrated digital image correlation identification method

Reproduced from; J. Neggers, J.P.M. Hoefnagels, M.G.D. Geers, F. Hild and S.G. Roux, *A time-resolved integrated digital image correlation identification method*, *submitted*

Abstract

This paper discusses a method which provides the direct identification of constitutive model parameters by intimately integrating a Finite Element Method (FEM) with Digital Image Correlation (DIC), connecting the experimentally obtained images for all time increments directly to the unknown material parameters. The problem is formulated as a single minimization problem which incorporates all the experimental data. It allows for precise specification of the unknowns, which can be, but is not limited to, the unknown material properties. The tight integration between FEM and DIC creates enables direct identification of the unknown parameters while providing necessary regularization of the DIC problem, making the method robust and noise insensitive. Through this approach, the versatility of the FEM method is translated to the experimental realm, enhancing the analyses of existing experiments and creating new experimental possibilities.

8.1 Introduction

Accurate prediction of complex mechanical phenomena, such as viscoplasticity, interface delamination, or material failure, enables the design of advanced materials, systems, and devices with novel mechanical functionality or improved material properties, processed through intelligent (thermo-)mechanical manufacturing routes. Predictive simulations of complex mechanical behavior require accurate constitutive models with often many material parameters that need to be determined experimentally. For instance, it is not uncommon that non-linear material models include more than ten parameters [13, 16, 91]. To correctly identify these parameters, traditionally, a plethora of individual mechanical experiments would have to be performed, each of which sensitive to certain parameters. However, with the advance of real-time *in-situ* full-field acquisition techniques (e.g. optical photography, electron microscopy, x-ray tomography, etc. [4]), it is now increasingly realistic to identify all model parameters from a single mechanical test in which the evolv-

ing deformation field is captured in a sequence of images. Nevertheless, such a full-field inverse parameter identification strategy remains challenging, because the influence of a parameter on the deformation field is often on the order of the image acquisition noise. Therefore, the algorithm to extract the underlying deformation field from the noisy image sequence should employ as few degrees of freedom (*dof*) as possible to enhance accuracy and robustness. Ideally, by intelligently incorporating constraints on the mechanical behavior in the identification algorithm, it becomes possible to reduce the number of *dof* to the number of material parameters in the constitutive model. Such an optimal one-step parameter identification routine is now feasible, by correlating the image patterns using only those kinematically-admissible 'deformation modes' that correspond to the change of a single model parameter.

In the literature, a multitude of full-field identification strategies have been proposed, see e.g. the review by Avril et al. [4]. However, the vast majority of proposed methodologies follow an indirect two-step approach, i.e. (*i*) the experimental deformation field is first determined from the full-field measurement data, and (*ii*) an inverse procedure is adopted to determine the model parameters by minimizing the difference between the simulated deformation field and its experimental counterpart. With respect to step (*i*), Digital Image Correlation (DIC) is usually applied to obtain the deformation field. However, DIC methods are inherently *ill-posed* because they aim to obtain a vectorial field (i.e. the displacement field) from a scalar field (i.e. the change in image pattern). Additionally, the presence of image acquisition noise adds to the ill-posedness. The solution for this problem is to reduce the number of unknowns that describe the displacement field. This can be done by regularizing the displacement field with a set of interpolation functions, which are either chosen to span local zones of interest (or subsets) [24, 112] or span the global region of interest [14, 51]. Typically, a wider support of the interpolation functions increases the noise robustness at the price of reducing the displacement resolution. Alternative approaches have been proposed, such as the equilibrium gap method which decouples the regularization from the applied DIC discretization [29, 127]. Note that, all these techniques to determine the displacement field typically do not exploit prior knowledge of the problem's kinematics and, therefore, a relatively large number of interpolation functions (i.e. *dof*) is still needed to describe the displacement field, especially for cases where non-linear material properties are investigated. Regarding step (*ii*), the most straight-forward and well-known inverse parameter identification approach is probably the Finite Element Method Updating (FEMU) method, where the difference between a FEM generated displacement field and the measured displacement field is minimized by iteratively optimizing the unknown material parameters. Many alternative and often elegant approaches have been proposed to minimize the noise sensitivity [4, 65, 91] for instance by weighting with the estimated DIC uncertainty [75] or with virtual fields [43]. However, all these approaches use the extracted deformation field (or a derivative), and not the actually measured images, as a starting point, i.e. there is no direct transfer of information from images to properties and the identification process works unidirectionally only.

Ideally, step (*i*) and (*ii*) should be combined in a single inverse parameter identification procedure that enables a bidirectional information transfer and fully exploits the problem's kinematics. The constitutive model contains the mechanically-admissible kine-

matic fields. As done in the equilibrium gap method, such kinematics can be successfully applied to regularize the DIC problem. However, the conventional two-step approach separates the constitutive model from the DIC problem. Recently, methods appeared which directly connect the constitutive model with the experimentally obtained images, so-called Integrated DIC (IDIC) algorithms [75, 105]. For instance, Réthoré [103] proposed an IDIC method to optimize for the unknown constitutive parameters in an elegant formulation that connects the mechanics to the images by connecting the FE mesh to an equivalent mesh used in the DIC problem. Alternative IDIC algorithms formulate the DIC interpolation functions through closed-form solutions of the displacement field as a function of the unknown parameters [105, 106]. For instance, Mathieu et al. [88], solve for the displacement field surrounding a crack tip, by using the elastic Williams crack tip solution as the displacement interpolation functions. In these IDIC methods, the degrees of freedom are the unknown constitutive parameters, which are directly identified from the experimental data. This alleviates the need to determine the intermediate displacement field, which typically requires an excessive number of degrees of freedom. However, the closed-form solutions make these IDIC methods highly specific and closed-form solutions are not available for all experiments. Therefore, the current chapter introduces a generic one-step Integrated-DIC inverse parameter identification approach that makes full use of the problem's mechanics, while employing bidirectional information transfer for maximum noise reduction. FEM simulations are used to generate a minimum number of kinematically-admissible 'deformation modes' (each belonging to the perturbation of a single parameter in the FEM constitutive model) with which the image patterns are correlated to identify the associated *dof*, i.e. the material parameters.

The chapter is structured as follows. Section 8.2 treats the mathematical framework of the one-step Integrated-DIC approach, including the extensions of the framework to incorporate time integration and virtual boundaries. The potential of the approach is demonstrated in sections 8.3 and 8.4, by two challenging examples, i.e. identification of the history- and rate-dependent constitutive behavior of a glassy polymer, and the parameter identification for two joined materials in a structured sample loaded by a bulge test setup. Finally, a discussion of the strengths and weaknesses of the methodology is given in section 8.5.

8.2 Methods

8.2.1 Integrated DIC

As with any DIC algorithm, this method starts with assuming that the captured images contain a pattern which moves affinely with the material below the pattern. Therefore, the brightness of one material point is constant in all images, which is known as the brightness conservation [50],

$$f(\vec{x}) = g(\phi(\vec{x})) + \eta(\vec{x}), \qquad \phi(\vec{x}) = \vec{x} + \vec{u}(\vec{x}), \tag{8.1}$$

where f is the reference image and g the deformed image, $\vec{x}$ a position vector, which is mapped to the deformed state by the mapping function ϕ. The displacement field

is the unknown and quantity to be identified. Both images contain image noise, which is described with the additional unknown field $\eta(\vec{x})$. The two scalar fields (images) are not rich enough to permit direct identification of the unknown fields, making the DIC problem naturally *ill-posed*. To remedy this the displacement field is parameterized with a limited number of unknowns [51],

$$\vec{u}^*(\vec{x}, \underline{\lambda}) \approx \vec{u}(\vec{x}), \tag{8.2}$$

where $\vec{u}^*$ is the approximated displacement field, and $\underline{\lambda}$ is a vector with n degrees of freedom,

$$\underline{\lambda} = [\lambda_1, \lambda_2, \lambda_i, \ldots, \lambda_n]. \tag{8.3}$$

From this point onward, the superscript asterisk is omitted since the dependence of a field on $\underline{\lambda}$ indicates that it is an approximated quantity.

The residual image is then defined as the difference between the gray values in the reference image and the gray values in the deformed image taken at the deformed coordinates,

$$r_1(\vec{x}, \underline{\lambda}) = f(\vec{x}) - g(\phi(\vec{x}, \underline{\lambda})), \qquad \phi(\vec{x}, \underline{\lambda}) = \vec{x} + \vec{u}(\vec{x}, \underline{\lambda}), \tag{8.4}$$

where the deformation mapping is now a function of the degrees of freedom. The gray values at the deformed coordinates are typically not at integer pixel locations, and thus require pixel interpolation, which is here performed using a standard cubic b-spline interpolation method [111].

Finding the optimum values for the degrees of freedom requires minimization of the difference between the two images, reducing the residual field to the acquisition noise and an additional error caused by the approximated displacement field. In DIC algorithms, a least squares potential Φ_1 is typically formulated,

$$\underset{\underline{\lambda}}{\mathrm{Argmin}}\big(\Phi_1(\underline{\lambda})\big) = \int_\Omega \Big[r_1(\vec{x}, \underline{\lambda})\Big]^2 \,\mathrm{d}A \qquad \mathrm{d}A = \,\mathrm{d}x\,\mathrm{d}y, \tag{8.5}$$

where Ω is the region of interest (ROI) over which the residual field is minimized, which can also be a 3D volume if Digital Volume Correlation is considered [76]. The solution for the optimal degrees of freedom is a non-linear problem, which is linearized and solved for iteratively, for instance, with a Newton-Raphson scheme [24]. The linearized system of equations is usually written in matrix form as,

$$\underline{\underline{M}}\delta\underline{\lambda} = \underline{b}, \tag{8.6}$$

with $\delta\underline{\lambda}$ is the iterative update of the degrees of freedom,

$$\underline{\lambda}^{k+1} = \underline{\lambda}^k + \delta\underline{\lambda}, \tag{8.7}$$

where $\underline{\lambda}^k$ is initialized with an initial guess $\underline{\lambda}_0$. The components of the Correlation matrix $\underline{\underline{M}}$ and the right hand member $\underline{b}$ are,

$$\underline{\underline{M}}_{ij} = \int_\Omega \Big[\vec{\nabla} f \cdot \vec{\varphi}_i \vec{\nabla} f \cdot \vec{\varphi}_j\Big] \,\mathrm{d}A, \tag{8.8}$$

$$\underline{b}_j = \int_\Omega \Big[\vec{\nabla} f \cdot \vec{\varphi}_j \; r_1\Big] \,\mathrm{d}A, \tag{8.9}$$

where, $\vec{\nabla} f$ is the applied image gradient (assuming small deformations, see chapter 6), and $\vec{\varphi}_i$ are the basis functions. In the DIC literature these functions are generally introduced as a choice with respect to which the approximated displacement field is expressed. Mathematically they originate from the linearization scheme (see chapter 6), and are defined as,

$$\vec{\varphi}_i(\vec{x}, \underline{\lambda}) = \frac{\partial u(\vec{x}, \underline{\lambda})}{\partial \lambda_i}. \tag{8.10}$$

If the displacement field is parameterized with linearly independent basis functions, then $\vec{\varphi}_i$ are indeed the chosen basis functions corresponding to the degrees of freedom. However, in this article, the degrees of freedom are the unknown material parameters, therefore, it is unlikely that these form a linearly independent basis, which is also not required.

The derivative of the displacement field with respect to a degree of freedom also represents the sensitivity map of that degree of freedom. For some particular cases, it is possible to formulate closed-form relations between the unknown material parameters and the displacement field [88]. For cases where this is not feasible, it is almost always possible to approximate these sensitivity maps by numerical differentiation of the simulated displacement fields. To this end, the reference displacement field, obtained with the current degrees of freedom $\underline{\lambda}^k$ (from a FEM simulation), is perturbed n times, each time perturbing only one degree of freedom with a small perturbation factor ϵ,

$$\vec{\varphi}_i(\vec{x}, \underline{\lambda}^k) \approx \frac{\vec{u}^k(\vec{x}, (1+\epsilon)\lambda_i^k) - \vec{u}^k(\vec{x}, \underline{\lambda}^k)}{\epsilon \lambda_i^k}. \tag{8.11}$$

The sensitivity maps are computed on the pixel coordinates (i.e. $\vec{x}$), which are not equal to the nodal coordinates. This introduces an interpolation step, for which the same cubic b-spline interpolation method is applied as used to compute the residual field (equation 8.4). To compute the residual for the current iteration, the same reference displacement field is used:

$$r_1^k(\vec{x}, \underline{\lambda}^k) = f(\vec{x}) - g(\phi(\vec{x}, \underline{\lambda}^k)), \qquad \phi(\vec{x}, \underline{\lambda}^k) = \vec{x} + \vec{u}^k(\vec{x}, \underline{\lambda}^k) \tag{8.12}$$

All ingredients required to solve for the update of the degrees of freedom are in place. The resulting iterative procedure is solved until convergence is met. In this chapter, the convergence criterion is based on the 2-norm of the right hand member,

$$\|\underline{b}\| < 10^{-5}, \tag{8.13}$$

Evidently, it is also possible to define a convergence criterion in terms of the length of the iterative update $\|\delta\underline{\lambda}\|$ [103].

Using the sensitivity maps as the basis functions of the DIC algorithm is an important characteristic of the proposed method. It provides a direct connection between the measured images and the unknown material parameters, which creates a bidirectional information transfer between images and mechanical properties, allowing direct material parameter identification while providing strong regularization of the DIC algorithm, assuring optimal accuracy and noise robustness. Using FEM simulations makes

the method easily applicable and versatile. Moreover, the constitutive model is generally implemented in a FEM framework. Therefore, no additional implementation effort is required. The resulting FEM model with identified parameters can be used directly for research or design purposes.

The FEM simulation does not need to be limited to the imaged surface. Areas which are outside of the imaged field of view, can be included in the simulation. This allows for the identification of parameters which influence the imaged surface but are defined from outside the field of view, or from deeper in the material (3D), similarly as discussed by [103]. For instance, for events occurring below the imaged surface, if they sufficiently influence (i.e. deform) the observed surface, then the corresponding constitutive parameters can be identified.

A point of attention of the proposed method is that the user has to choose a constitutive model before analyzing the experimental results. Attempting to identify a constitutive model which does not (or poorly) apply to the materials at hand will produce erroneous results. It is important to realize, however, that such problems can be identified by studying the residual image r_1, which will show structured patterns on top of the random acquisition noise where the identification process fell short.

A second point of caution is the computational cost of the method. Each IDIC iteration requires $n+1$ simulations, to compute the reference displacement field and the perturbed displacement fields. The cost of these simulations will generally outweigh all the other computational steps in the DIC algorithm, such as computing the image gradients, or interpolating the back-deformed image. It should be noted that, since the simulations are independent of each other, they can be performed in parallel, which considerably speeds up the algorithm.

8.2.2 Time integration

The above discussed method deals with the comparison of two images only. However, nowadays large series of images are easily captured during an experiment (e.g. > 100 frames). During the experiment the same material is imaged, ergo, the corresponding constitutive model should apply to all captured frames. Therefore, a method is required which includes all measurement frames into a single minimization problem, following the same reasoning as proposed by Besnard et al. [11], applied to the Integrated DIC method discussed in this paper.

Material parameters governing history independent behavior (e.g. elastic properties), can be identified for each combination of image frames and then averaged. However, identifying the unknown material parameters at once for all frames increases the identification robustness by directly attenuating the acquisition noise. Moreover, history-dependence related parameters, e.g. as used to describe plasticity or rate-dependency, are impossible to capture from a single combination of two images.

To define a single minimization problem, the residual is reformulated by realizing that the deformed images are actually the field f captured at a different time t. The residual

as a function of time then reads

$$r_1(\vec{x}, t, \underline{\lambda}) = f(\vec{x}, t_0) - f(\phi(\vec{x}, t, \underline{\lambda})), \qquad \phi(\vec{x}, t, \underline{\lambda}) = \vec{x} + \vec{u}(\vec{x}, t, \underline{\lambda}). \tag{8.14}$$

The above equation is the equivalent of stacking all images together into one large (3D) matrix. The residual is formed by deforming each image frame back to the initial configuration (i.e. at $t = t_0$) by applying the mapping function for the corresponding time and comparing it to the initial frame (figure 8.1).

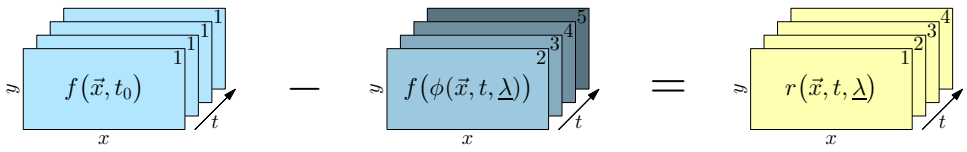

Figure 8.1: Schematic representation of the time-resolved brightness conservation, as written in equation 8.14.

Note that, it is also possible to formulate the residual in an updated Lagrangian framework, where, instead of comparing each frame to the initial frame, each frame is compared to the previous frame. The mapping function ϕ then defines the mapping of material points between consecutive frames. This updated version requires the computation of the differential displacement fields from the FEM displacement fields, with the benefit that the method becomes less sensitive to changes in the pattern. For instance a loss of a patch of paint will only effect one residual frame, while in the original method it will effect all frames after that event. The remaining implementation is the same for the updated or total Lagrange formulations. Therefore, only the total Lagrange method is further discussed.

Analogous to the previous section, the degrees of freedom $\underline{\lambda}$ are the unknown material parameters. The minimization of the residual with respect to the degrees of freedom is performed ass before, using an iterative Newton-Raphson method. Consequently equation (8.6) remains valid, and only the definition of the components of $\underline{\underline{M}}$ and $\underline{b}$ need to be updated,

$$\underline{\underline{M}}_{ij} = \int_\tau \int_\Omega \left[\vec{\nabla} f \cdot \vec{\varphi}_i \vec{\nabla} f \cdot \vec{\varphi}_j \right] \mathrm{d}A \, \mathrm{d}t, \tag{8.15}$$

$$\underline{b}_j = \int_\tau \int_\Omega \left[\vec{\nabla} f \cdot \vec{\varphi}_j \; r_1 \right] \mathrm{d}A \, \mathrm{d}t. \tag{8.16}$$

The only difference with equations (8.8) and (8.9) is the time integration, with τ being the time equivalent of a ROI. It should be realized that in practice the discussed fields are all discrete in space (pixels), and discrete in time (image frames). As a result, the integrals in the above equations are easiest implemented as discrete summations, however, for ease of discussion they are written here in continuum form. All fields within the integrals above are time dependent, i.e. stacked fields with one frame for each considered moment in time. The image gradient is the spatial gradient for each time frame. For the total

Lagrange method only the gradient of the reference frame is required, which is applied to each subsequent time frame.

The sensitivity maps are again obtained from FEM simulations. Non-linear FEM simulations generally require the boundary conditions to be applied incrementally. Consequently, the simulated displacement fields are known at each increment. The time incrementation in the simulation should preferentially contain (as a subset) all time increments at which the experimental images were taken. Alternatively, the incremental displacement fields can be interpolated at the experimental time increments.

The sensitivity maps again result from a numerical differentiation as in equation (8.11). The difference is that the fields are now the displacement fields interpolated at the pixel coordinates stacked for each time frame,

$$\vec{\varphi}_i(\vec{x}, t, \underline{\lambda}^k) \approx \frac{\vec{u}^k(\vec{x}, t, (1+\epsilon)\lambda_i^k) - \vec{u}^k(\vec{x}, t, \underline{\lambda}^k)}{\epsilon \lambda_i^k}. \tag{8.17}$$

Note that the time-dependent sensitivity maps, which are akin to DIC basis functions, are naturally obtained from the FEM simulations only. For non-linear FEM simulations these increments are always required, hence causing no additional computation cost. The final ingredient to the time integrated version of the IDIC method is the computation of the residual, for which the gray values of all frames $f(\vec{x}, t)$ are interpolated at the current estimate of the deformed coordinates $\phi(\vec{x}, t, \underline{\lambda}^k)$.

8.2.3 Additional experimental data

In a typical experiment, additional data is measured, for instance the displacement or the force measured at the clamps of the tensile stage or images recorded by a second camera. To clarify the incorporation of supplementary experimental data in the proposed IDIC framework, the measured force is next used as an example.

For some cases, it is possible to include the measured force by load-controlled FEM simulations with the recorded force history (e.g. section 8.4). However, this is not feasible for structurally softening samples, which require displacement control because of the snap-through response (e.g. section 8.3). To include the experimentally measured force in the minimization procedure, a second residual is defined,

$$r_2(t, \underline{\lambda}) = F_{\mathsf{exp}}(t) - F_{\mathsf{sim}}(t, \underline{\lambda}), \tag{8.18}$$

where F_{exp} is the experimentally measured force as a function of time, and F_{sim} is the corresponding simulated reaction force, which depends on the degrees of freedom. The residual is again formulated in a least squares sense,

$$\Phi_2(\underline{\lambda}) = \int_\tau \Big[r_2(t, \underline{\lambda}) \Big]^2 \, \mathrm{d}t. \tag{8.19}$$

The minimum of Φ_2 will most likely not coincide with the minimum of the image residual

Φ_1. Therefore, a combined potential is defined as

$$\Phi(\underline{\lambda}) = (1-\alpha)\frac{1}{\beta_1}\Phi_1(\underline{\lambda}) + \alpha\frac{1}{\beta_2}\Phi_2(\underline{\lambda}), \tag{8.20}$$

where Φ_1 is the optical residual as defined in equation (8.5) but now with the time integration,

$$\Phi_1(\underline{\lambda}) = \int_\tau \int_\Omega \Big[r_1(\vec{x}, t, \underline{\lambda})\Big]^2 \,\mathrm{d}A\,\mathrm{d}t, \tag{8.21}$$

and r_1 is the residual image as defined in equation (8.14). The parameters β_1 and β_2 are normalization constants, and $\alpha \in [0,1]$ is the corresponding weight for each potential. Typically, more weight is put on the optical potential, i.e. $\alpha \ll 1$ [103], but the influence of α is not investigated further.

The two potentials are independent of each other, and therefore can be linearized independently, resulting in the following linear system of equations, which is applied iteratively,

$$\underline{\underline{M}}\,\delta\underline{\lambda} = \underline{b} \tag{8.22}$$

$$\Big((1-\alpha)\frac{1}{\beta_1}\underline{\underline{M}}_1 + \alpha\frac{1}{\beta_2}\underline{\underline{M}}_2\Big)\delta\underline{\lambda} = \Big((1-\alpha)\frac{1}{\beta_1}\underline{b}_1 + \alpha\frac{1}{\beta_2}\underline{b}_2\Big), \tag{8.23}$$

The optical part of this linearized system, $\underline{\underline{M}}_1$ and $\underline{b}_1$, is as above defined (equations (8.15) and (8.16)). The force part of the system results from the Newton-Raphson scheme, giving,

$$\underline{\underline{M}}_{2(ij)} = \int_\tau \Big[\rho_i \rho_j\Big]\,\mathrm{d}t, \tag{8.24}$$

$$\underline{b}_{2(j)} = \int_\tau \Big[\rho_j r_2\Big]\,\mathrm{d}t, \tag{8.25}$$

where $\underline{\rho}(t, \underline{\lambda})$ are force sensitivity maps complementary to the displacement sensitivity maps $\underline{\vec{\varphi}}(\vec{x}, t, \underline{\lambda})$. These maps are obtained through numerical differentiation of the FEM simulations,

$$\rho_i(t, \underline{\lambda}) \approx \frac{F^k(t, (1+\epsilon)\lambda_i^k) - F^k(t, \underline{\lambda}^k)}{\epsilon\lambda_i^k}. \tag{8.26}$$

Any additional experimental data can be added to the minimization problem in this manner, as long as it has a numerical counterpart. For instance, measured temperature fields can be compared to thermo-mechanical FEM results.

This completes the proposed FEM-based Integrated DIC method. The flow of information in the proposed method is summarized as a block diagram in figure 8.2. The implementation does not differ substantially from a typical global DIC implementation. The major difference is that the basis functions are not chosen in advance, since they are the sensitivity maps obtained by numerical differentiation of the FEM simulations. In addition, since it is almost trivial to compute time-resolved sensitivity maps from

the FEM data it is natural to formulate a time-resolved residual image, which allows for robust identification of history-dependent parameters. Additionally, the experimental force, needs to be included in the method in order to obtain absolute values for the stiffness, otherwise only stiffness ratios can be determined.

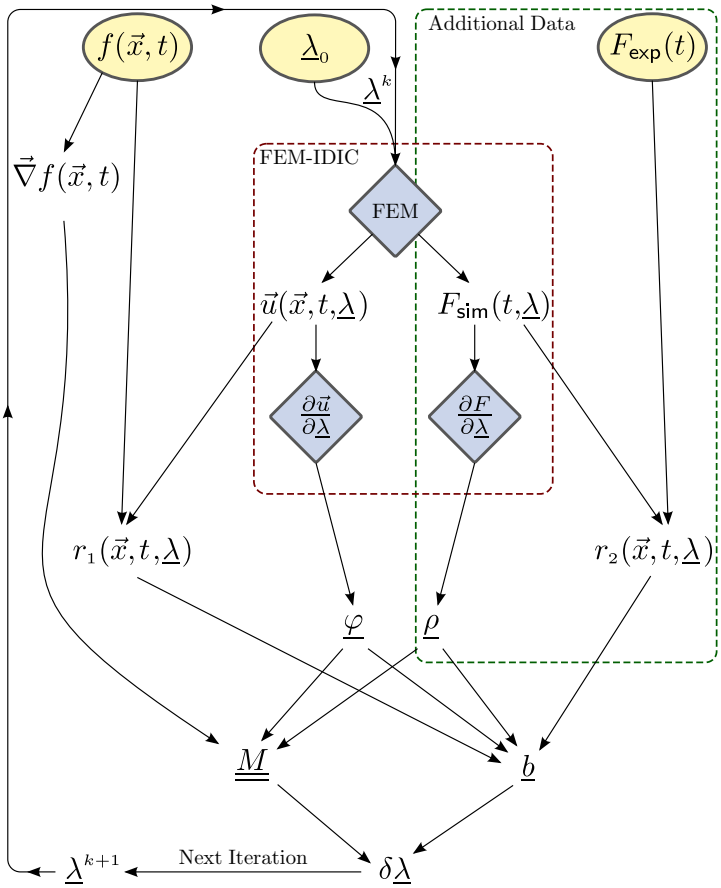

Figure 8.2: Block diagram of the proposed IDIC framework.

8.2.4 Additional degrees of freedom

Up to this point, the discussed degrees of freedom were the unknown material parameters. However, the proposed method is not limited to identifying material parameters. Any defined parameter, which has an influence on the minimization problem can be identified. A typical case of interest for these additional degrees of freedom are characteristics of the experiment which are suspected to be inaccurate. For instance, the rotational alignment of a specimen in the experimental setup is often inaccurate. If the FEM boundary conditions are defined as a function of a rotation angle parameter, then simply adding the

rotation parameter to the list of degrees of freedom $\underline{\lambda}$ automatically creates an additional sensitivity map (basis function) through the numerical differentiation (equation 8.17).

In this manner, an arbitrary set of degrees of freedom can be added to the system, although not without consequences. Any additional degree of freedom increases the solution space for the minimization problem, and therefore reduces its regularization properties. Consequently, the sensitivity to acquisition noise increases, decreasing the accuracy of the identification. Moreover, an extra FEM simulation has to be performed for each additional degree of freedom, adding to the computational cost. Moreover, additional degrees of freedom may degrade the conditioning or even cause non-uniqueness of the solution. A simple example for this is when, in a purely uniaxial elastic problem, both the external force and the stiffness are unknowns. Increasing the force and increasing the stiffness correspondingly would result in exactly the same deformed geometry, and thus would not change the residual. Such extreme cases are uncommon, but the foresign of ill-posedness is poor conditioning of $\underline{\underline{M}}$ (i.e. this matrix will have near-parallel eigenvectors or a determinant which is close to zero).

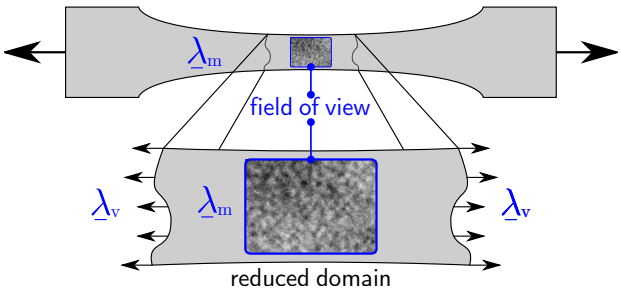

Figure 8.3: Additional degrees of freedom $\underline{\lambda}_v$ (complementary to the material degrees of freedom $\underline{\lambda}_m$) applied to create a virtual boundary, effectively reducing the FEM domain.

A most versatile use of additional degrees of freedom is to provide virtual boundaries. Typically, the captured field of view does not contain the entire sample. However, to apply the correct boundary conditions, the entire sample is modeled in the FEM simulation. By applying a parameterized boundary located intermediately between the real sample boundary and the field of view, and adding these parameters to the degrees of freedom, the simulated domain can be greatly reduced, which reduces the computational cost per simulation (figure 8.3).

8.3 Polycarbonate characterization

As a first proof-of-principle example the constitutive properties of PolyCarbonate (PC) are identified. PC is a glassy polymer which is rate dependent (visco-elastic) and history dependent. The polymer chains tend to diffuse to a low energy state which compacts the material, thereby increasing the yield stress. Material flow induces rejuvenation which has a reverse effect on the yield stress, causing flow-induced softening [90, 124]. It is this

softening behavior combined with the stress- and temperature-dependent viscosity which makes this material a challenging test case for the proposed IDIC method.

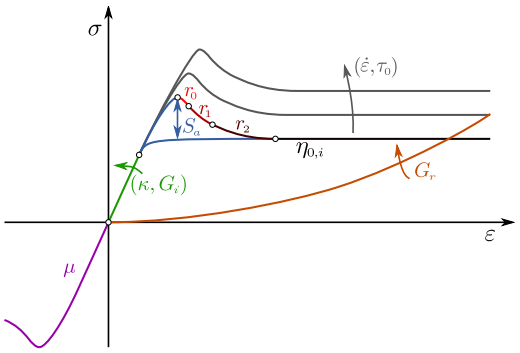

(a)

λ_1	G_r	26	[MPa]
λ_2	S_a	27	[-]
λ_3	r_0	0.965	[-]
λ_4	r_1	-3	[-]
λ_5	r_2	50	[-]
λ_6	τ_0	0.7	[MPa]
λ_7	μ	0.08	[-]
λ_8	κ	3.75	[GPa]
λ_9	G_1	634	[MPa]
λ_{10}	$\eta_{0,1}$	$1.47 \cdot 10^{11}$	[MPa · s]

(b)

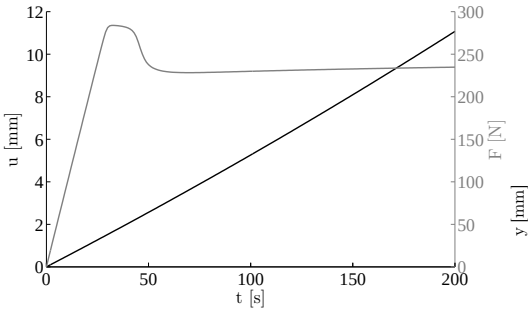

(c)

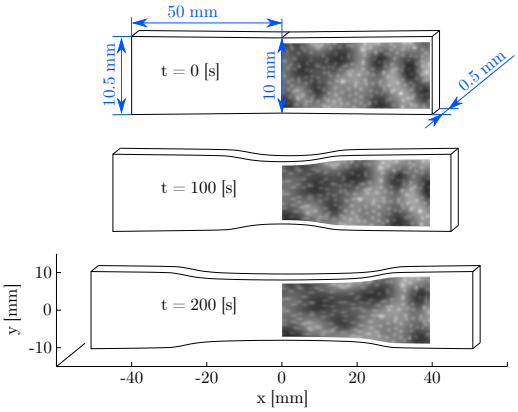

(d)

Figure 8.4: (a) A sketch of the influence of the various EGP parameters on the stress-strain response. (b) The reference single mode EGP parameters for the polycarbonate sample [21]. (c) The applied displacement boundary condition, and the measured force response. (d) The contour of the mesh at the undeformed, intermediate, and deformed state. The adopted DIC pattern is depicted in the mesh.

8.3.1 Glassy polymer model

A particular constitutive model which is well suited for modeling PC is the Eindhoven Glassy Polymer (EGP) model, which is actively being developed by van Breemen et al. [19, 20]. For details about the model the reader is referred to [73]. To introduce the material parameters the constitutive model is briefly discussed in appendix C.

The influence of the EGP constitutive parameters on the stress-strain response is illustrated in figure 8.4a. The two contributions to the stress tensor $\boldsymbol{\sigma}_s$ and $\boldsymbol{\sigma}_r$ are shown separately, whereby the network contribution $\boldsymbol{\sigma}_r$ (shown in orange) is controlled by the neo-Hookean modulus G_r. The driving stress $\boldsymbol{\sigma}_s$, is controlled by the other 9 parameters. Five of which are typical non-Newtonian parameters, with κ the bulk modulus, G_i the

inter-molecular contribution to the shear modulus, $\eta_{0,i}$ the corresponding zero-viscosity and τ_0 the characteristic stress. The remaining four parameters control the aging and rejuvenation, where S_a is the aging state parameter which depends on the history of the material, and r_0, r_1 and r_2 are fitting parameters which describe the softening response. The state S_a is particularly important since it is used to predict the product lifetime [35, 134].

8.3.2 Virtual experiment

In order to accurately identify all EGP parameters it is important that they are solicited during the experiment and influence the observed pattern. Because PC exhibits flow induced softening and strain hardening, a simple tensile experiment will form a neck which subsequently grows in a stable fashion. It is known that the necking geometry is sensitive to the aging and rejuvenation kinetics [90]. Moreover, the moving neck creates an area with a gradient in strain and strain rate. It is therefore assumed that a simple tensile experiment on a strip of PC contains sufficient information (including time history) to identify all 10 EGP parameters.

To test the performance of the identification process it is important that the targeted parameters are known exactly on beforehand, such that they can be compared to the obtained parameters. To this end, a virtual experiment is performed, where the images normally obtained by a camera are artificially generated by deforming a reference pattern with the deformation field obtained from a reference FEM simulation. The virtual experiment enables a controlled addition of artificial measurement uncertainties such as acquisition noise, to evaluate noise robustness.

The applied tested sample is a PC strip ($10.5 \times 100 \times 0.5$ mm^3) which tapers slightly towards the center to enforce that necking starts in the center. The applied EGP parameters are listed in table 8.4b, and are typical for Polycarbonate [21]. The sample is loaded in tension with a constant global strain rate of $\dot{\varepsilon} = 0.001$ [s^{-1}] for 200 seconds, see figure 8.4c.

Because of the large strains occurring in the experiment, a relatively sparse pattern is applied, as shown in figure 8.4d. The sample shape and pattern are shown in figure 8.4d for the initial, intermediate and final deformation states, clearly showing the necking phenomenon.

8.3.3 Parameter sensitivity

Figure 8.5 shows the evolution of the x- and y-component of the displacement for three time increments (i.e. at 60, 120, and 200 s). Next to the three time-slices a y-slice is presented which shows the respective component of the displacement vector for all time steps at a single y-location, i.e. $y = 8$ mm. This x-t representation is useful since the variations along the y-direction are typically obvious. Note, how the onset of necking and stable neck propagation is visible as a line feature at an angle in the x-t plane starting at approximately 50 s.

The basis functions applied in the proposed IDIC method are the sensitivity maps (equation 8.17) of the displacement field with respect to the unknowns, which for this example are the 10 EGP parameters (table 8.4b). The sensitivity maps can be computed before the experiment is performed and are at that state already a useful tool to diagnose the sensitivity of the parameters for the planned experiment. Each computed sensitivity map $\vec{\varphi}_i$ is a 3D volume of 2D vectors as for the above discussed displacement maps. Additionally, there is a force sensitivity map ρ_i, which is a 1D scalar field. Both vector components of $\vec{\varphi}_i$ and the force sensitivity ρ_i are connected to a single degree of freedom. The reverse reasoning is also true; the effect of changing one degree of freedom is expressed by the combination of all three fields, ergo, together they form the sensitivity of the method to a single degree of freedom.

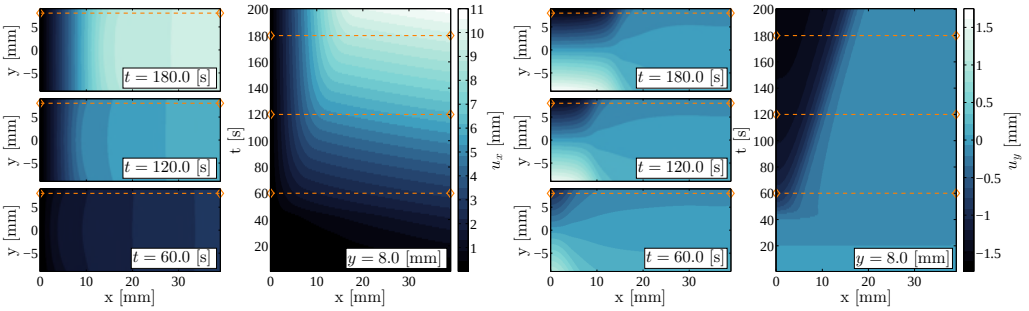

(a) u_x (b) u_y

Figure 8.5: The x-component (a) and the y-component (b) of the displacement field for three time increments and for a single y-plane, for all time increments.

For the ease of plotting, all sensitivity maps are scaled with their respective (absolute) maximum value of the $x-$component of the map, (i.e. $\hat{\lambda}_i$). Figure 8.6 shows a single x-t-plane (at $y = 8$ mm) for all 10 scaled sensitivity maps. Degrees of freedom which have limited impact on the force or displacement field will have low values in the sensitivity map, which is most visible in the value of the respective $\hat{\lambda}_i$, shown at the top of each sensitivity map. In this case r_1, has the lowest displacement sensitivity, followed by μ and $\eta_{0,1}$. The reduced sensitivity for these degrees of freedom is expected. The r_1 parameter only influences a limited regime in the stress-strain curve, see figure 8.4a. Consequently, only a small volume of material is affected by r_1 at each time increment. The μ parameter controls the pressure dependence, and for this particular experiment it is indeed unlikely that large differences in pressure occur. Sensitivity for the zero-viscosity $\eta_{0,1}$ requires large differences in strain rate. The area in the neck is straining at a different rate as the area in front of the neck, however, the expected strain rate differences are small compared to what is typically applied to quantify the zero-viscosity. As a consequence to the small variations in strain rate, also a low sensitivity is expected in the characteristic stress τ_0. However, this parameter also controls the onset of flow, to which this experiment is sensitive.

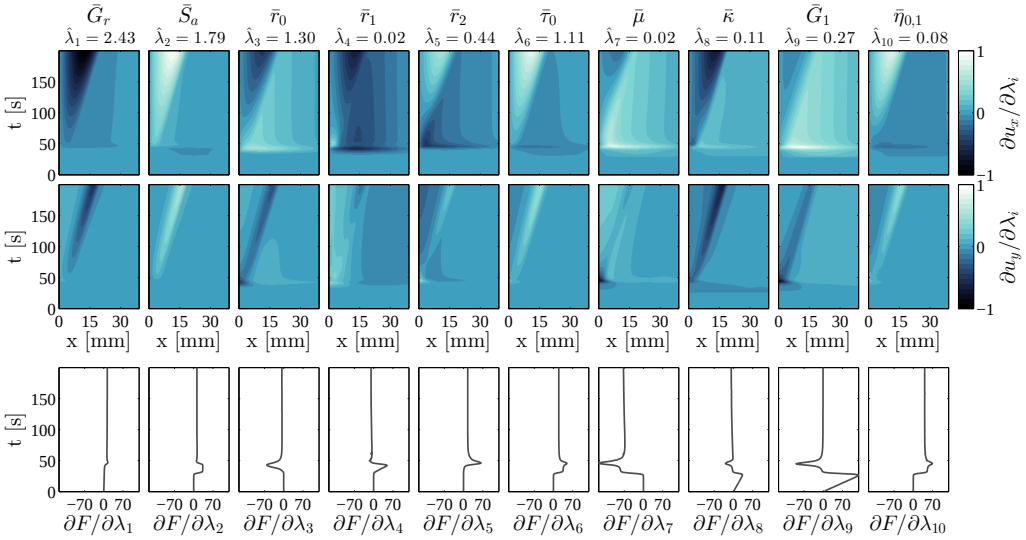

Figure 8.6: The scaled sensitivity maps (or basis functions) for all 10 unknown material parameters, for a single y-plane. The three figures in one *dof* column combine to one sensitivity map. The values of the scaling parameters $\hat{\lambda}_i$ are shown on top of the respective sensitivity maps.

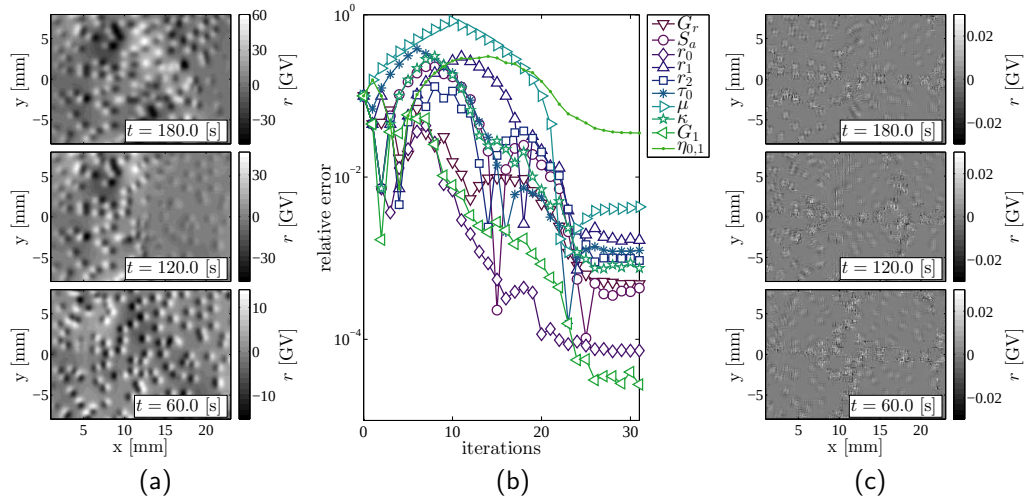

Figure 8.7: (a) Three residual images taken at the start (i.e. based on the initial guess of 110% relative to the reference). (b) The convergence behavior of the IDIC routine, identifying all 10 EGP material parameters. (c) Three final residual images (i.e. from the final iteration). Note the difference in scale bar values between the initial and the final residual.

As a proof-of-principle experiment the identification procedure was initiated with an initial guess for each parameter equal to 110% of their reference value. After 30 iterations

convergence is reached, and values for all 10 EGP parameters have been identified. To evaluate the quality of the identification, first the residual field (stack) is analyzed. Figure 8.7 shows the residual from before (i.e. using the initial guess) and after the IDIC procedure. Since this (virtual) procedure contained no measurement noise, the residual field is reduced to almost zero, the only visible features are due to the sub-pixel interpolations.

The analysis of the residual is important and always possible. However, since a virtual experiment method is applied here, the reference displacement field is known as well. The difference between the obtained displacement field and the reference displacement field is analyzed next, which is defined as,

$$\mathcal{E}_{u_x} = [u_x]_{\text{ref}} - [u_x]_{\text{idic}}, \tag{8.27}$$

$$\mathcal{E}_{u_y} = [u_y]_{\text{ref}} - [u_y]_{\text{idic}}. \tag{8.28}$$

Both error fields are shown in figure 8.8. The largest displacement error is in the x-displacement, occurring at the onset of necking and equals 0.3 µm, which is 0.3% of the pixel size (i.e. 93 µm.). This is well below the typical 1% sub-pixel accuracy typically obtained in regular DIC algorithms [51]. This good accuracy in the displacement field translates to the obtained parameters as shown in table 8.1. All obtained parameters are within 1% of the expected values, except for the zero-viscosity $\eta_{0,1}$ which stagnates at 3.5% accuracy. The accuracy in the material parameters highlights the stringent demands on the displacement accuracy.

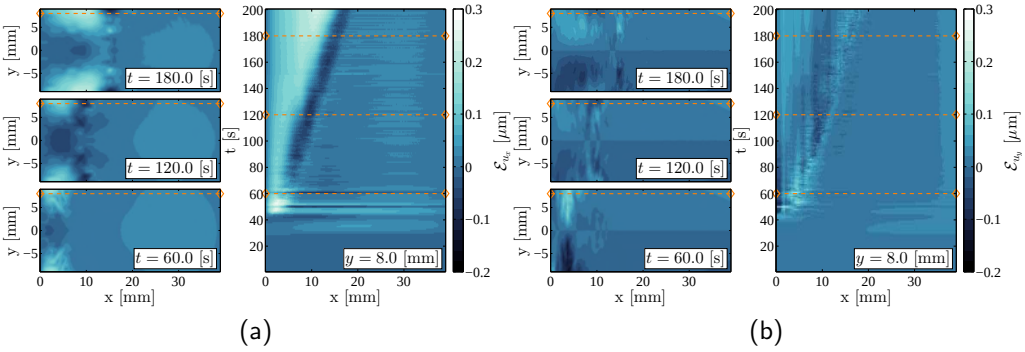

Figure 8.8: The x-component (a) and the y-component (b) of the displacement error field for three time increments, for a single y-plane, for all time increments.

λ_1	λ_2	λ_3	λ_4	λ_5	λ_6	λ_7	λ_8	λ_9	λ_{10}
G_r	S_a	r_0	r_1	r_2	τ_0	μ	κ	G_1	$\eta_{0,1}$
[MPa]	[-]	[-]	[-]	[-]	[MPa]	[-]	[GPa]	[MPa]	[MPa · s]
26.01	26.99	0.965	4.99	-2.99	0.70	0.080	3.753	6.34	$1.42 \cdot 10^{11}$
0.05%	-0.04%	0.01%	-0.17%	-0.09%	0.12%	0.44%	0.07%	-0.003%	-3.48%

Table 8.1: The obtained EGP parameters (the initial guess for each degree of freedom was 10% off the expected value.)

As predicted by the analyses of the sensitivity maps, the three degrees of freedom with the least sensitivity are also the three where the identification is the least accurate. This sensitivity analysis is only based on the numerical results and does not include the image gradient. The combined effect of the sensitivity maps and the pattern gradient is best evaluated by analyzing the correlation matrix M, as discussed by Hild and Roux [51]. The correlation matrix is presented graphically in figure 8.9a, where high values of M indicate a high sensitivity. From figure 8.9a it is immediately clear that the rows and columns belonging to $\underline{\lambda}_4$ and $\underline{\lambda}_7$ are the least sensitive. To show this more clearly, a spectral decomposition of M is applied,

$$M = QDQ^{-1} \tag{8.29}$$

where D is a diagonal matrix with the eigenvalues γ_i of M on the diagonal, shown in figure 8.9b. Q is the associated eigenvector matrix where each column represents an eigenvector corresponding to the respective eigenvalue, shown in figure 8.9c. Consider the three eigenvalues with the lowest values, corresponding to the three left most columns in figure 8.9c. Since these three eigenvalues have relatively low values, their corresponding eigenvectors represent combinations of degrees of freedom (directions in the solution space) to which the method is particularly insensitive. These three vectors are mostly dominant in $\lambda_7 = \mu$, $\lambda_{10} = \eta_{0,1}$ and $\lambda_4 = r_1$. Additionally, the remaining eigenvectors show inferior dependence of those three degrees of freedom. This leads to the conclusion that not only $\underline{\lambda}_4$ and $\underline{\lambda}_7$ are suspected to be insensitive, as visible from M, but also $\underline{\lambda}_{10}$, which is consistent with the obtained accuracy as shown in table 8.1. This shows that, a for this case, the contrast in accuracy could have been assessed on beforehand.

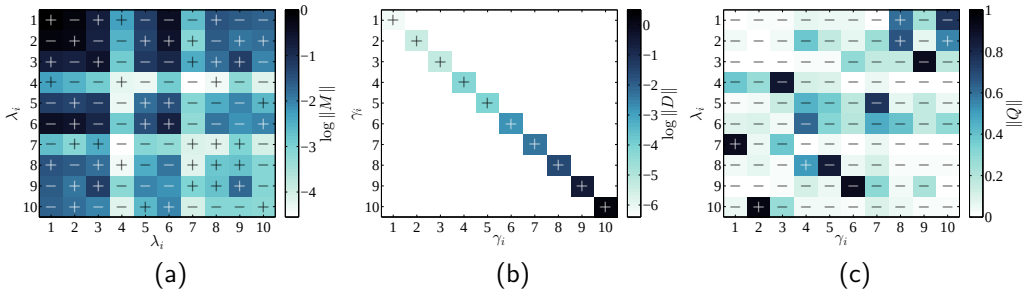

Figure 8.9: Graphical representation of the correlation matrix M and the eigenvalue matrix D and the eigenvector matrix Q. The sign of the the matrix values is displayed by the symbol in the center of each matrix component.

8.3.4 Robustness with respect to the initial guess

Inverse methods are often compromised by non-uniqueness or non-convexity problems [2, 92]. The applied Newton-Raphson minimization scheme is known for its excellent convergence properties when close to the solution. However, it may to converge to a local minimum, or not converge at all, when initiated too far from the solution.

The test the robustness against poor initial guesses, the discussed example case was re-initiated at various distances from the reference solution. The 'distance' is specified as a relative error for each degree of freedom compared to the reference value. Figure 8.7b showed the convergence behavior for all 10 degrees of freedom when initiated at 10% of the reference. The figure reveals that, during the first iterations where some degrees of freedom tend to undergo large changes, the iterative procedure is dampened by restraining the update $\delta\underline{\lambda}$ to a maximum of 5% of the current value of the respective degree of freedom. After approximately 25 iterations the procedure is converged, resulting in the previously discussed accuracy. Figure 8.10a shows the final result for IDIC procedures initiated at various distances from the reference solution. As expected, the final result does not depend on the initial guess for initial guesses close to the solution, however at an initial guess of $\geq$20% error the procedure fails to converge.

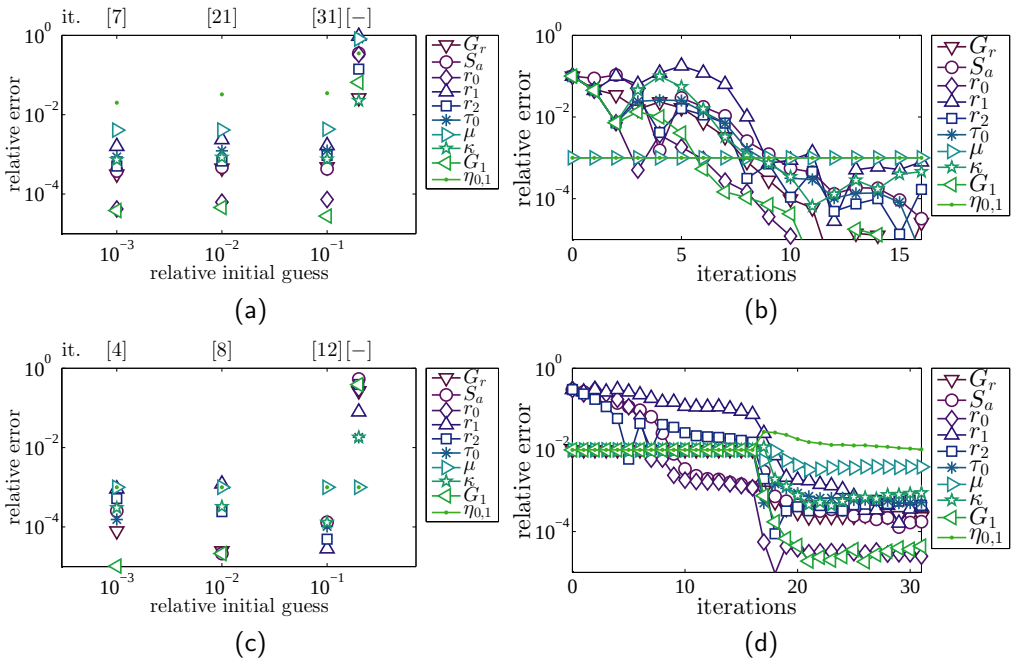

Figure 8.10: (a) The converged relative error for the identified parameters as a function of the relative initial guess, identifying all 10 EGP material parameters. (b) The convergence behavior of the IDIC routine, starting from an initial guess where each DOF is initiated at 10% of the real value, identifying 8 EGP parameters, assuming μ and $\eta_{0,1}$ are known. (c) The converged relative error as a function of the relative initial guess, identifying 8 EGP material parameters. (d) The convergence behavior of the IDIC routine, starting from an initial guess where each DOF is initiated at 30% of the real value, identifying only the 4 rejuvenation EGP parameters, i.e. S_a, r_0, r_1 and r_2. After iteration 16, the 6 locked EGP parameters are released improving the identification of all parameters except $\eta_{0,1}$. The number of the particular iteration is depicted above the respective relative error values of subfigures (a) and (c), not converged procedures are indicated with [−].

From the analyses of the sensitivity maps and the correlation matrix, it was concluded that of the 10 EGP parameters, three parameters have reduced conditioning, namely r_1, μ and $\eta_{0,1}$. The proposed IDIC method does not require that all constitutive parameters are included as degrees of freedom. If the pressure dependence parameter and the zero-viscosity are accurately known from other experiments, then these parameters can be locked at known values. Figure 8.10b shows the convergence history of the IDIC procedure initiated at 10% of the reference solution, identifying the remaining 8 EGP parameters. By excluding the compromised 2 degrees of freedom, the convergence rate is noticeably improved. Additionally, the accuracy of the remaining 8 parameters is improved, as shown in figure 8.10c. However, the convergence radius did not increase. Again, initial guesses of $\geq$20% distance to the solution fail to converge.

Reducing the parameter space further, only the four aging/rejuvenation parameters can be chosen as the identification targets. A similar analysis is performed where the other six parameters are locked at 101% of their respective reference value (i.e. all including a small error). Now with only four degrees of freedom the initial guess robustness improves significantly. Figure 8.10d shows the convergence history where these four parameters are initiated at a distance of 30% from the reference, while the remaining 6 parameters are frozen. In this state, with four degrees of freedom, the procedure required 15 iterations to converge, after which the remaining 6 parameters are released continuing the procedure with 10 degrees of freedom. Using such a two step iterative scheme allowed the IDIC procedure to converge from an imperfect initial guess and achieve an accuracy of within 1% of their expected value for most parameters.

8.3.5 Noise sensitivity

To investigate the accuracy of the method as a function of the acquisition noise, artificial white noise is added to all applied images (i.e. the entire stack of images). For this particular test case 8-bit images are used, providing 256 integer gray values (GV). The applied noise levels are given in terms of the standard deviation of the applied Gaussian noise field multiplied with the Root Mean Square (RMS) of the pattern (i.e. RMS = 122 [GV], see figure 8.11a). Only 8 degrees of freedom will be identified, assuming that μ and $\eta_{0,1}$ are known and set close to the reference value. Figure 8.11b shows the converged relative error for each parameter for various levels of image noise. For noise levels below 1% the solution is largely unaffected. The method remained robust up to a standard noise level of 10% even though the accuracy is affected.

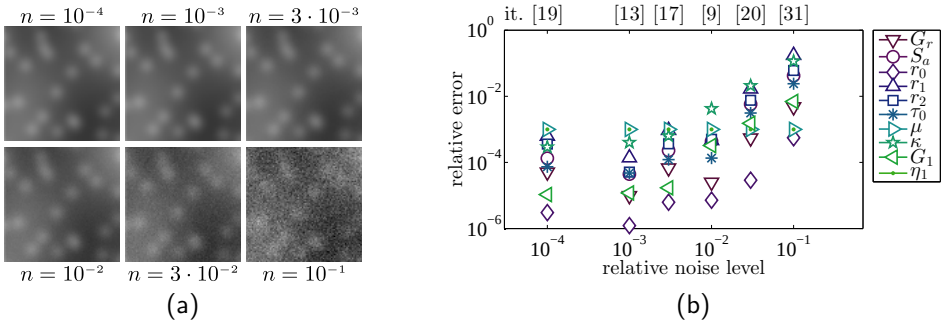

Figure 8.11: (a) small sections of the pattern with various noise levels. (b) The sensitivity of the identification procedure as a function of the noise level (relative to the RMS of the pattern).

8.3.6 IDIC for EGP discussion

A typical identification procedure for the EGP model requires a plethora of experiments, each using separate samples to identify each parameter individually [19]. This is not only cumbersome, but identifying the history dependent aging parameter is troublesome since it tends to vary from sample to sample, or even within one sample. The proposed IDIC method showed the ability to identify all 10 EGP parameters under the condition that a reasonable initial guess is provided. The convergence radius can be improved by differentiating between parameters with high sensitivity and other which have less sensitivity. Accordingly, accuracy improves when the pressure dependent parameter μ and the zero-viscosity $\eta_{0,1}$ are known, likewise the initial guess robustness improves when only the four aging/rejuvenation parameters are targeted.

The applied experiment in this example was not optimized for EGP model parameter identification, and from the *a priori* analyses of the sensitivity maps it was already diagnosed that the experiment would be less sensitive to a few parameters. Designing experiments (DOE) where these parameters are activated more strongly may lead to improved robustness and accuracy. For instance, loading the sample first in compression and then in tensile will improve the sensitivity to μ and applying greater variations in the applied strain rate will improve the sensitivity for $\eta_{0,1}$.

A point of caution regarding this example is the use of a single Maxwell mode for the EGP model. van Breemen et al. [21] have showed that to accurately describe polycarbonate in complex loading situations up to 17 Maxwell modes are required with 2 parameters per mode. Identifying an EGP model with 42 degrees of freedom will definitely require optimization of the experiment for which the IDIC method is to be used.

8.4 Bulge tests of metal-elastomer membranes

Instead of identifying multiple constitutive parameters of a single material, it is also possible to identify the constitutive parameters of heterogeneous samples. For instance the material response of micro-scale specimens where the geometrical length scale interacts with the intrinsic microstructural length scales, tends to deviate from the bulk material response [95, 133] and is influenced by neighboring materials or phases [3, 46]. For those cases, it is interesting to identify the materials closely to the situation where they are applied in the eventual device. Examples of this are the structured metal interconnects adhered to elastomer substrates as encountered in stretchable electronic applications [83, 107, 130].

8.4.1 Virtual bulge test experiment

The presented test case in this example consists of a 2 µm thick elastomer membrane (1×6 mm^2) with a line of high purity aluminum (Al) deposited on top of the elastomer membrane. The Al film has a thickness of 200 nm, and is 100 µm wide covering the full 6 mm length of the sample. The sample is loaded in a bulge test setup (as discussed in chapter 7), where a pressure difference is applied causing the membrane to bulge outwards (see figure 8.12a). The bulge profile (including the surface roughness) is measured using optical confocal microscopy.

Again a virtual experiment is used to perform an accurate assessment of the accuracy of the method, while excluding unknown experimental influences. Due to the slender aspect ratio of the membrane ($b \gg a$), it is assumed that the strain in the y-direction (see figure 8.12a) is negligible. Therefore, the virtual experiment is modeled with 2D plane strain, quadrilateral elements. For the elastomer substrate, thermoplastic urethane (TPU) is chosen, which is commonly found in stretchable electronic applications [83]. For the adopted bulge test, the strains in the substrate will remain below 10%, therefore, the TPU is modeled with a neo-Hookean model with a single parameter, the modulus $C_{10} = 3.3$ MPa, see figure 8.12b. Typically the metal interconnects in these electronic devices are produced using printed circuit board or lithographic techniques, often yielding high purity materials. Therefore, for this test case high purity aluminum, as discussed by Janssen et al [62], is used described by an elasto-plastic model with isotropic hardening, figure 8.12c.

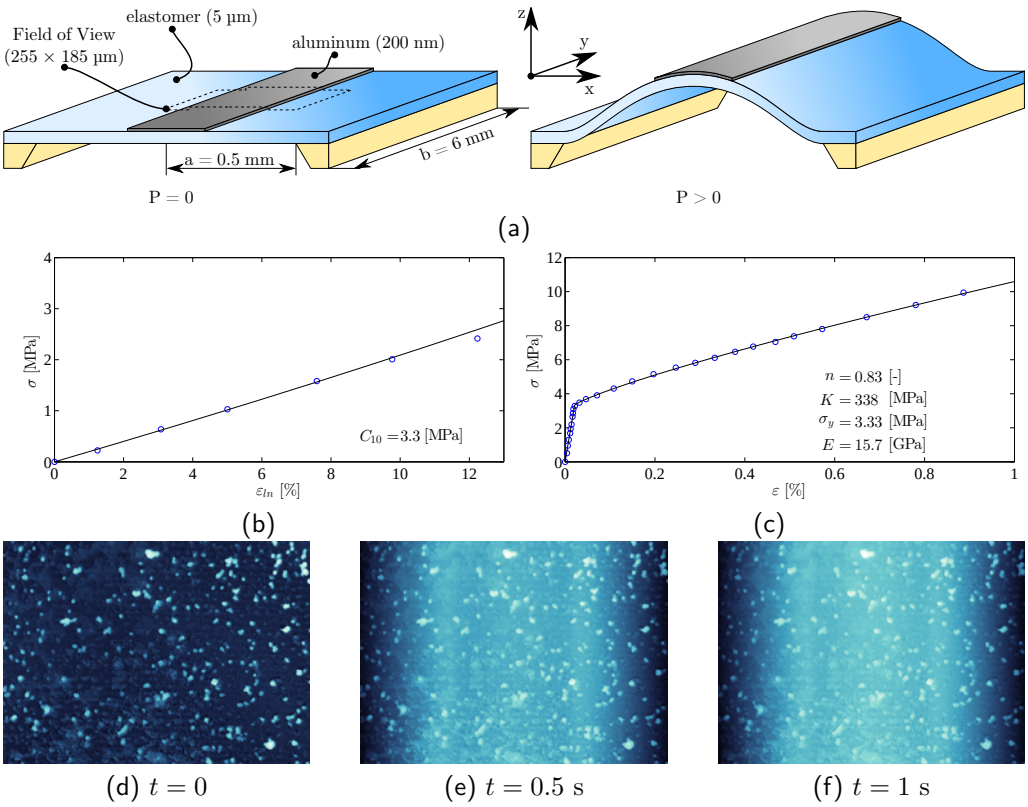

Figure 8.12: (a) The elastomer membrane sample dimensions with aluminum structure on top, deformed to a bulged shape by a pressure difference. (b) The experimental reference material response and the fitted models which will be used as a reference material in the virtual experiment for the TPU elastomer substrate, fitted with a neo-Hookean model, and (c) the high purity aluminum fitted with an elasto-plastic model with isotropic hardening. (d,e,f) Three image increments as applied in this example, where the time is a pseudo time.

The applied pattern is an actual pattern of a bulge test measured with an optical confocal profilometer, as discussed in chapter 7. In this virtual experiment, the pattern and the out-of-plane displacement are measured by the profilometer, in the same way as in chapter 7. Consequently, the quasi-3D or topography correlation principle is applied in this example, i.e. f now represents the height instead of the brightness. In this method the brightness/height conservation relation is relaxed by adding an additional field, which in this case is the out-of-plane displacement,

$$f(\vec{x}, t_0) = f(\phi(\vec{x}, t, \underline{\lambda}), t) + u_z(\vec{x}, t, \underline{\lambda}) + \eta(\vec{x}, t, \underline{\lambda}) \tag{8.30}$$

where $u_z(\vec{x}, t, \underline{\lambda})$ is the out-of-plane displacement field. Following the same procedure as in chapter 7, an extra set of basis functions is required, which within the proposed IDIC procedure translates to an additional component in the sensitivity maps. Note that the displacement field, and thus also each sensitivity map is a 3D vector field as a function of

a 2D position vector, $\vec{x}$ and time, t. For instance, the displacement field can be written as:

$$\vec{u}(\vec{x},t,\underline{\lambda}) = u_x(\vec{x},t,\underline{\lambda})\vec{e}_x + u_z(\vec{x},t,\underline{\lambda})\vec{e}_y + u_z(\vec{x},t,\underline{\lambda})\vec{e}_z, \qquad \vec{x} = x\vec{e}_x + y\vec{e}_y. \tag{8.31}$$

This additional field is naturally obtained by computing the derivative of the z-component of the displacement towards the degrees of freedom, using exactly the same formulation as expressed in equation 8.17.

The data obtained from a confocal profilometer can be seen as a digital image, where the gray values have the physical meaning of height. Additionally, the gray value discretization is not simply binned in 8-bit (or similar). The height values are obtained through the interpretation of many confocal images, discretized as 32-bit floating point numbers. For this particular profilometer (Sensofar plμ 2300) with a 20× objective applied in confocal mode, the images contain 557×768 px^2 with a field of view of 255×185 µm^2 (see figure 8.12def).

8.4.2 Parameter sensitivity

Due to the plane strain nature of this experiment, there are no variations in the sensitivity fields along the y-direction, since $u_y(\vec{x},t,\underline{\lambda}) = 0$. Consequently, the data is presented in a 2D x-t-figure, taken at a single y-plane. For instance the x- and z-components of the displacement are shown in figure 8.13ab.

For this example case, the experimental force is the pressure driving the bulge test. This pressure is included in the FEM simulations as a load controlled boundary condition. Therefore, it is not required to add the force to the minimization procedure in the form of an extra potential (such as discussed in section 8.2.3). As a result, the sensitivity maps only have displacement components in x and z (plane strain).

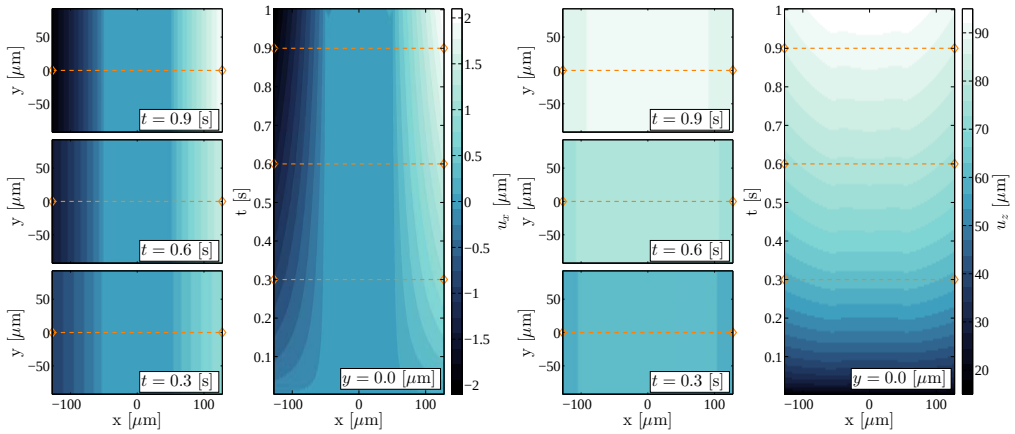

Figure 8.13: The x-component (a) and the z-component (b) of the displacement field for three time increments and for a single y-plane, for all time increments.

Figure 8.14 shows the scaled sensitivity maps applied in the IDIC procedure. Both the x- and z-component of one sensitivity map are scaled with the same scaling constant (i.e. $\hat{\lambda}_i$), shown above the respective map. Similarly as before, the sensitivity maps can be used to diagnose potential identification problems. The difference in sensitivity is best expressed in the scaling constants $\hat{\lambda}_i$. The first observation is the contrast in sensitivity between the first degree of freedom C_{10} and the other parameters. The observed contrast in sensitivity was expected since the elastomer substrate, which is much larger than the field of view, has a large impact on the displacement field. Moreover, the location of the aluminum strip, as well as the onset of plasticity can be recognized in the profile of the sensitivity maps. These maps reveal adequate sensitivity for all parameters, even though, the identification will be less sensitive to the Young's modulus E and the Hardening modulus K, with the lowest values $\hat{\lambda}_2 = 0.34$ and $\hat{\lambda}_4 = 0.80$. A spectral analysis similar to the one discussed in the previous example (section 8.3.3) can also be performed. However, for this case the sensitivity maps already reflect the correct sensitivity balance between the five degrees of freedom.

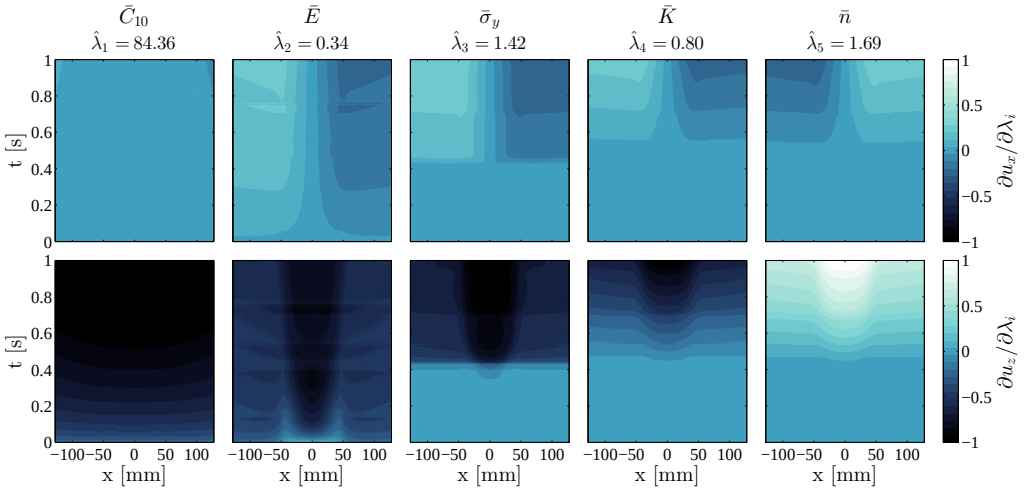

Figure 8.14: The scaled sensitivity maps (or basis functions) for all five unknown material parameters, for a single y-plane. Both figures in one *dof* column combine to one sensitivity map. The values of the scaling parameters $\hat{\lambda}_i$ are shown on top of the respective sensitivity maps.

As a first proof-of-principle for this example, the proposed IDIC method is applied to identify the five constitutive parameters, where the initial guess is taken equal to 130% of to the reference values for the material parameters (listed in figures 8.12bc). Similarly, as with the previous (EGP) example, the residual field (stack) is analyzed for present patterns in the residue. Figure 8.15 shows the initial residual and the final residual. The residual almost vanishes completely, which is expected since no additional acquisition noise was added. The only remaining visible features in the residual are the scars left behind by the sub-pixel interpolation.

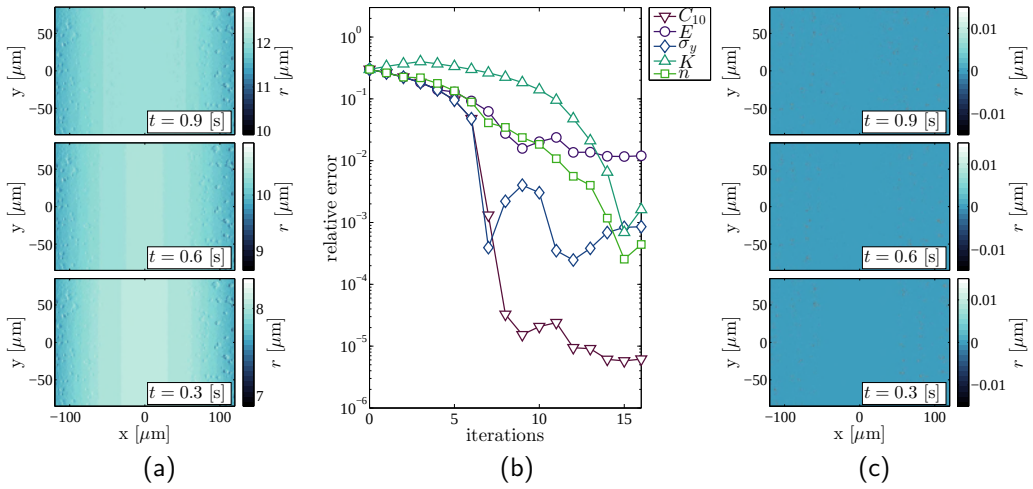

Figure 8.15: (a) Three initial residual images (i.e. based on the initial guess of 130% relative to the reference). (b) Convergence of the IDIC method in terms of relative error for this bulge test example. (c) Three corresponding final residual images. Note the difference in scale bar values between the initial and final residual.

For this virtual experiment, the reference displacement field is again known, enabling a direct comparison between the obtained and reference displacement field. Figure 8.16 reveals that the largest error in the displacement field is found in the aluminum strip in the elastic part of the experiment ($\mathcal{E}_{u_z} = -0.4$ nm), which compared to the pixel size (332 nm) translates to approximately 0.1% sub-pixel accuracy. Compared to conventional DIC algorithms, where typically a displacement error of 1% is considered as good [51], the achieved adequate accuracy of the proposed method is noteworthy.

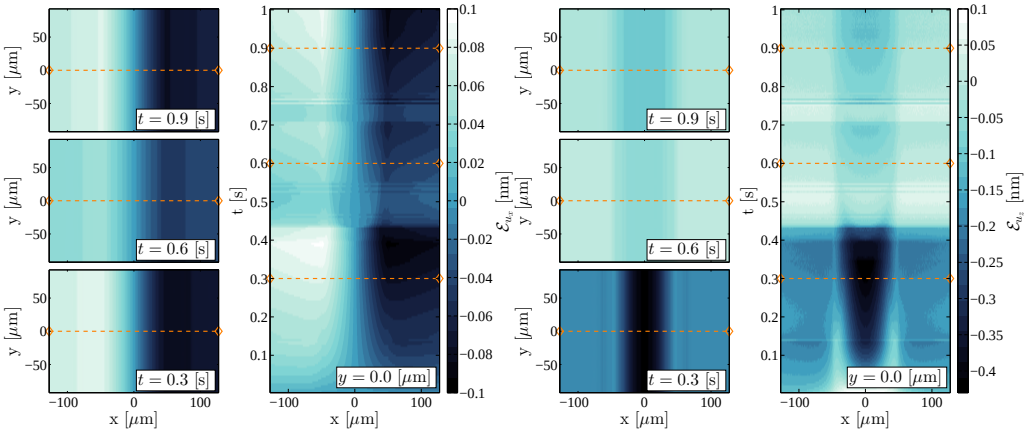

(a) $\mathcal{E}_{u_x}$ (b) $\mathcal{E}_{u_z}$

Figure 8.16: The x-component (a) and the y-component (b) of the displacement error field for three time increments, for a single y-plane and for all time increments (in nm).

Figure 8.15b shows the evolution of the relative error between the identified and the reference constitutive parameters. The procedure converges in 16 iterations, where the elastomer modulus and the yield stress (C_{10} and σ_y) converge first, followed by the other three parameters. This behavior is consistent with the analyses of the sensitivity maps. Additionally, the sensitivity maps forecast that the Young's modulus and the hardening Modulus (E and K) are less sensitive, resulting a reduced, yet still adequate accuracy (compared to the high displacement accuracy), reflected by the relative error in the converged state. Akin to the EGP example, the achieved accuracy in the material parameters emphasizes the high requirements on the displacement field accuracy in order to obtain sufficiently accurate constitutive parameters.

8.4.3 Robustness with respect to the initial guess

The initial guess robustness is next analyzed for this bulge test example. A number of IDIC identification routines are performed at various distances to the reference values for the constitutive parameters. Figure 8.17 shows the relative error for all degrees of freedom in the converged state. As expected, the obtained values do not depend on the initial guess for small to moderate distances to the solution. The results show that this example case is more robust than the EGP case (i.e. a larger convergence radius), and converged for all tested initial guess distances, with the largest tested radius at 170%. An improved robustness was expected, since this example has less degrees of freedom which are stronger expressed in the sensitivity maps.

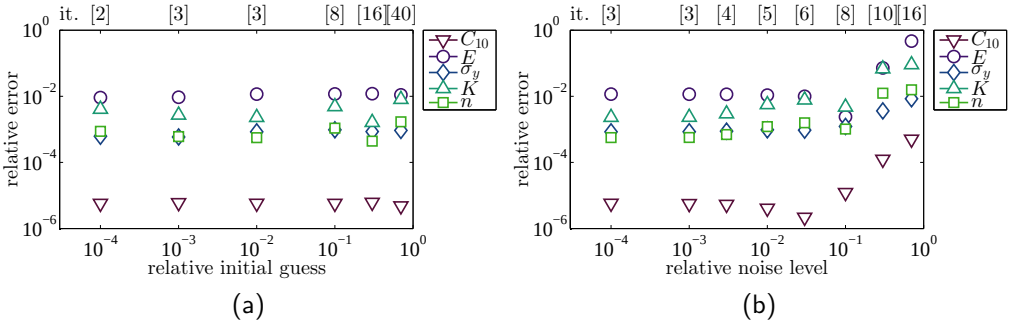

Figure 8.17: (a) The converged relative error of the IDIC method applied to the bulge test example case for various initial guesses. The relative initial guess is defined as the relative distance of all degrees of freedom to the reference value. (b) The converged relative error for different levels of acquisition noise. The relative noise level is defined as standard deviation of the white noise scaled with the RMS of the DIC pattern. The number of iterations is shown above the respective relative error values.

8.4.4 Noise sensitivity

The higher robustness of this example (relative to the EGP example) is also reflected in the noise sensitivity. Figure 8.17 shows the relative error for all degrees of freedom in the converged state, where additional noise is added to all images (i.e. in the entire stack). Different-noise levels are added, again defined as the standard deviation of the white noise multiplied with the RMS value of the pattern (1.5 µm) in the reference image. The accuracy of the identified parameters remains preserved for noise levels up to 3%, subsequently an increase in error is observed for increasing noise levels. Unexpectedly, at a noise level of 10% the best accuracy is observed. At that noise level, the interpolation artifacts are overshadowed by the white noise, which may explain the improved accuracy because the random noise is more strongly attenuated then the non-random interpolation artifacts. Overall, the noise sensitivity for the example is low. This is due to the quasi-3D nature of the bulge test method and the use of profilometric data. The out-of-plane displacement, due to the bulging of the membrane, enters the IDIC procedure through a cylindrical shape in the roughness pattern, see figure 8.12ef. This cylinder is more pronounced than the sample roughness pattern, thereby stabilizing the iterative procedure. Close to the solution, the surface roughness pattern is required to provide sensitivity to the smaller in-plane displacements.

8.4.5 Bulge test discussion

The bulge test example was chosen to prove that the proposed IDIC method can be applied to identify the constitutive parameters of multiple materials in one sub-structured monolithic sample. This is important, especially for micro-electronics applications, where different materials shaped in thin and small structures deviate in properties from their

bulk counterparts. The identification of these parameters is a challenge at that scale. The presented example shows that the adopted identification procedure is robust (i.e. relatively insensitive to the initial guess and acquisition noise). Additionally, this example showed the relative ease with which the proposed IDIC method was extended to incorporate quasi-3D topographical profilometer data. The additional components required in the sensitivity maps, naturally follow from the differentiation of the FEM displacement fields with respect to the degrees of freedom.

8.5 From images to properties: Conclusions

An Integrated Digital Image Correlation (IDIC) method has been proposed, which relies on a bi-directional information transfer from images to the identification of the constitutive parameters, and reversely from the mechanics to the images by regularizing the DIC problem with "mechanically" admissible fields (implying kinematic and static admissibility as well as the obedience to a given constitutive law). These fields, sometimes called basis functions or shape functions, are not chosen manually, but obtained by computing the sensitivity of the displacement with respect to each degree of freedom. The proposed way to compute these sensitivity maps, is by numerical differentiation of the displacement fields obtained from Finite Element Method (FEM) simulations. This requires $n + 1$ simulations, one for the current guess of the degrees of freedom and one perturbed simulation for each degree of freedom.

This unique way of applying FEM-computed sensitivity maps as the DIC basis functions maximizes the regularization of the (*ill-posed*) DIC problem, by limiting the solution to the 'deformation modes' defined by the unknown material parameters. Moreover, the construction of the sensitivity maps is only limited by the types of problems that can be simulated in a FEM setting. Especially the second example (section 8.4) showed that, extension from 2D to quasi-3D (digital height topography) or to 3D is a small step, and merely requires a FEM simulation to be performed with adequate dimensions. Moreover, the tight integration with FEM has the additional benefit that the identified constitutive model is directly available for further application, for which the constitutive model was originally developed, e.g. materials research, design optimization, etc.

The accuracy of the method was discussed for two examples. The first example demonstrated that it is possible to identify a complex 10 parameter history- and rate-dependent glassy polymer model by only analyzing the captured images of a single, simple tensile experiment. The second example demonstrated the possibility to identify two materials in a monolithic sample tested in a (bulge) experiment. This is particularly useful for small scale testing where it is difficult to separate the individual materials, and where the material properties often depend strongly on the manufacturing process and structural dimensions. Nevertheless, these examples do not yet disclose the full potential or application regime of the presented method. The generality of the method spans a wider range of cases. Any experiment, with any acquisition method, with full freedom of choice for the unknown parameters is at reach.

The inclusion of the data of all time increments into a single identification problem

(from image to property) is shown to be a powerful property of the proposed method. It allows the robust identification of history- or rate-dependent properties, and substantially enhances noise robustness. However, the data footprint increases exponentially, putting a high requirement on the available physical memory in the used computer system. Moreover, to create the sensitivity maps, one simulation has to be performed for each degree of freedom for each DIC iteration, which is computationally costly, yet easy to parallelize.

The finally obtained system is non-linear, and possibly non-convex. For the minimization a Newton-Raphson algorithm is applied, which is known to converge rapidly when close to the solution, but easily captures a local (rather than a global) minimum. Therefore, the accuracy and efficiency of the method depend on the quality of the initial guess. This non-uniqueness problem was explored for the two example cases. Distances of 10% from the reference material parameters showed effortless convergence, while distances of 70% or more from the reference solution were still feasible. Other minimization techniques, such as the Levenberg-Marquardt method to name one, were not explored and may provide further improvements in terms of noise robustness.

It was demonstrated that, by analyzing the sensitivity maps, one can diagnose sensitivity problems before an experiment is performed. Similar to e.g. FEMU, VFM, and other full-field methods, the experiment no longer needs to trigger homogeneous deformation or stress fields, it is possible to optimize the envisioned experiment by modeling the experiment in FEM and analyzing the effect of certain design choices in the experiment on the sensitivity maps. The sensitivity maps do not yield insight on the influence of the pattern, therefore, to diagnose possible sensitivity problems in relation to limitations of the DIC pattern, the correlation matrix can be analyzed, which is constructed from the sensitivity maps and the gradient of the pattern. A traditional eigenvalue and eigenvector decomposition of the correlation matrix aptly identifies which degrees of freedom will be less sensitive. Finally, after convergence is reached, the residual fields have to be analyzed. If the proposed constitutive model does not fit the tested material (i.e. there is a significant model error), the dissident kinematics will limit the minimization of the residual field, which will leave systematic patterns behind in the residual field.

To conclude, the proposed method can be applied to a wide range of experiments, where many of the choices made in defining the experiment will impact the accuracy of the method. The proposed method gives an abundance of freedom, which is favorable for the applicability of the method, but which also puts a great deal of responsibility in the hands of the user. The sensitivity maps, correlation matrix and residual field enable a reasonable interpretation of the quality of the identification method for the particular case at hand, however they do not guarantee unconditional success. Therefore, a note of caution is given using a phrase from the computer science field: “garbage in, garbage out”.

Acknowledgment

L.C.A. van Breemen is gratefully acknowledged for his support and input in this research, especially regarding the implementation and discussions considering the EGP model.

Chapter 9
General conclusions and recommendations

9.1 Conclusions

Exceptionally high interface fracture toughness values have been measured for the metal-elastomer interfaces typically found in stretchable electronic devices. The large difference in elastic mismatch, combined with high macroscopic interface toughness, causes the soft material near the interface to deform notably during delamination. The goal of this thesis was set to unravel the micromechanics responsible for the large macroscopically observed interface toughness, and develop methods to identify the constitutive properties of structured interfaces, as found in stretchable electronics applications.

A number of analysis techniques were applied to investigate the interface delamination of peel test experiments. The soft elastomer exhibited large deformations in the vicinity of the peel front, which were captured by optical microscopy. Besides the measured peel force, these "lift-off" geometries were successfully applied to characterize the traction-separation law (TSL) constitutive parameters required to adequately describe the experiment with a Finite Element Method (FEM) simulation with interface elements. Analyses of the FEM results revealed that, the macroscopically applied crack opening angle is not directly transferred to the fracture process zone. For cases which are macroscopically close to mode-II (i.e. shear loading) the fracture process zone remains loaded in mode-II, however, for a macroscopic mode-I experiment (i.e. normal loading) it was observed that the interface opening angle rotates towards mode-II in front of the crack tip, effectively causing the fracture process zone to be loaded at roughly 45°.

To expose the delamination micromechanics, the progressing peel front was imaged *in-situ* in an Environmental Scanning Electron Microscope (ESEM). The high magnification ESEM visualization revealed that, at the peel front a fibrillation process occurs. Depending on the interface roughness, approximately 30 µm fibrils are formed from the elastomer material, which either rupture or debond from the metal surface. Imaging these fibrils in-situ was imperative for quantitative analyses of their geometry due to the tendency of the fracture process to continue after the experiment is stopped. A delicate balance between the debonding and rupturing of the stretched fibrils was demonstrated by analyzing the two new surfaces. Occasionally, the fibril attachment was strong enough to force the crack through the metal (i.e. copper) causing measurable amounts (up to 1%) of the elastomer surface to be covered with copper residue. Likewise, analyzing the cop-

per surface after delamination revealed significant amounts of elastomer residue (up to 50% coverage). This showed that for a large portion of the fracture process the crack front progressed through the though elastomer material instead of progressing along the interface. A specialized Digital Image Correlation (DIC) algorithm was employed, inspired by the methods developed in part B, to find the location of one fracture surface with respect to the other fracture surface. This method performed surface topology correlation (i.e. quasi 3D), on two dissimilar surfaces with enhanced robustness, required to converge successfully. Performing the correlation allowed for a quantitative comparison of the mismatch between the surfaces after delamination. The method was applied to the PDMS-copper interface, where was concluded that the amount of measured mismatch would account for 1 µm of irreversible crack opening or less, from which was concluded that irreversible deformation during delamination is not significantly contributing to the macroscopically observed fracture toughness.

Clearly, the experimental investigation revealed that the delamination mechanics is a multi-scale problem and deserves attention at all length scales. Experimenting at the microscale presents challenges, partly related to sample creation and sample handling, partly related to the difficulties of observing and measuring at the small scale. Both challenges have been successfully solved by combining a bulge test setup with an optical confocal profilometer. The full-field topography type data of the profilometer required an extension of the Global DIC (GDIC) method, which was successfully implemented and explored to expand the applicability regime of the existing bulge test method. Not only removing the limitations of the initial shape of the bulge window, but simultaneously simplifying the experiment. The proposed GDIC-bulge method directly measures the stress and strain in non-structured pressure deflected membranes without resorting to a-priori known formulations such as bulge equations. To successfully analyze the performance of structured membranes, as found in stretchable electronics applications, an Integrated-DIC (IDIC) method was developed which intimately combines FEM with DIC. In this method the regularization effort is expanded beyond smart choices for the DIC basis functions, maximizing the accuracy and noise robustness by minimizing the number of degrees of freedom to the unknown parameters in an experiment. It is advised to choose the unknown constitutive parameters as degrees of freedom, but the method is not limited to those, and additional unknown aspects, such as boundary conditions, can be included in the set of degrees of freedom. The IDIC method is applied to two test cases showing that it is possible to robustly obtain; all 10 parameters of the Eindhoven Glassy Polymer model, from a single tensile experiment, and that it is possible to identify both the metal and the elastomer material properties from a single bulge test of a structured stretchable electronic like sample. Besides obtaining the full-field stress and strain everywhere in the sample (even outside the field of view), the obtained constitutive parameters can directly be applied in other FEM models, for instance for optimizing the device designs.

The multi-scale experimental investigation of delaminating interfaces has unraveled the mechanics occurring at the microscale cascading through the length scales causing the macroscopically high fracture toughness observed for these high elastic mismatch interfaces. Three length scales are defined, where the largest is the macroscale, defined by the sample or device length scales. One scale smaller is the mesoscale, best defined by

the length of the fracture process zone (or cohesive zone). Due to the large elastic mismatch, large deformations occur in the large fracture process zone, storing large amounts of strain energy. At the microscale a complex mechanism is revealed where up to 30 µm long fibrils are formed from the elastomer material, which ultimately rupture or debond from the copper surface. The fibrillation process is initiated by the copper surface roughness, where mechanical interlocking led to strong attachment points. Subsequently, areas of large negative hydrostatic stress cause cavitation at the roughness peaks, initiating the fibrils. Interestingly, the results suggest that the macroscopically observed large fracture toughness does not need to originate from irreversible deformation during the formation and elongation of the fibrils, since no evidence of significant permanent deformation is found. It is hypothesized that the stored strain energy which is released at fibril failure, is partly lost due to dynamic dissipation. Additionally, it was found that at these high roughness, ductile interfaces are insensitive to the macroscopic crack opening angle. Arguably, the low bending stiffness of the fibrils and the microscale geometric complexity cause that the macroscale load angle is not transferred to the microscale.

9.2 Recommendations

Commonly, delamination experiments are merely analyzed from a macroscopic point of view, which is in contrast with the multi-scale behavior discussed in this thesis. Therefore, it proposed to apply the experimental techniques displayed in this thesis on similar investigations targeted to understand interface integrity. The in-situ aspect was proven to be essential to observe the fracture process zone and the delamination micromechanics. Stopping the motion of the clamps does not immediately stop the peel-front from progressing. Consequently, intermittent stopping to allow for easier imaging, with improved quality, will yield anomalous results. Besides the in-situ methods, a number of post delamination techniques are displayed; measuring the area fraction of residue on each new surface, and applying DIC to accurately find the location of one fracture surface with respect to the other, to digitally compare the mismatch between the two surfaces after delamination.

The topic of mechanical interlocking has attained a fair share of attention, notably in the work of Packham [97, 98] but also for instance in Shen et al. [115] and van der Sluis et al. [118]. However, the most important hypothesis of part A is the mechanical interlocking of the elastomer, which initiates the fibrillation mechanism and ultimately leads to the impressive fracture toughness observed at the macro-scale. Therefore, it is proposed to pursue this topic more, and in more detail. The peel test experiment is an easy to perform experiment, however, the forest of fibrils which occurs at the peel front, each at a different levels of stretch, causes challenges in the evaluation of the evolution of the fibril traction up to fibril failure. Moreover, the natural and thus chaotic roughness pattern which was found in the interfaces in part A, is adding to the complexity of the analysis. To make the next step in understanding and identifying the various dissipative mechanisms in these large elastic mismatch interfaces, it is recommended to move to better controlled, geometrically simpler experiments, preferentially with only a single fibril, or a single roughness valley.

From the numerical perspective, the presented work clearly showed that interface delamination mechanics is a multi-scale problem, which is naturally modeled with a multi-scale constitutive description. As was already recognized in the PhD project of B.G. Vossen, see for instance [136]. Vossen et al. [136] apply an interface element at the large scale, similar to typical cohesive zone element implementations. Except that, the constitutive behavior is not a predefined traction-separation law, but is transferred from the response of a model of the microscale. Since the microscale model will describe a certain volume of material, it would be logical to have finite thickness interface elements at the meso-scale. Micro-mechanical features, such is fibrillation, or surface roughness can then be added to the micro-model, which will govern the traction opening response of the meso-scale cohesive zone elements.

The full-field global DIC enhanced bulge test method is ready to be used and is not limited to stretchable electronics, or interface problems. The full-field extension where GDIC is applied to optical profilometer measurements did not only improve the applicability regime, but additionally removed a number of possible experimental complications, simplifying the experimental procedure. Through the DIC method the strain and stress are measured directly from local data, measured at the material points. Consequently, any drift or motion of the setup will not enter the results. Therefore, it is recommended to utilize the enhanced stability to investigate the long term behavior of materials such as creep and relaxation.

The main message of chapter 6 was to always follow a linearization/minimization routine as consistently as possible since that will give more insight in the problem at hand. In this case, this led to the remarkably simple formulation of the basis functions in chapter 8. However, Chapter 6 discusses various image gradients, and some authors have even applied mixed gradients (e.g. [10]), adding to the number of possible DIC image gradients. It is recommended to evaluate the performance of the various image gradients, in terms of initial guess robustness, and in terms of displacement accuracy, especially for cases with large gradients in the displacement field.

The proposed IDIC method (chapter 8) not only enables the use of non-standard non-homogeneous experiments, but these are actually encouraged. The more complex the deformation (and deformation history) to more likely that all properties of a material are triggered. It is recommended to explore various non-standard experimental methods, and evaluate their identification performance, similar to the work of Rossi et al. [108]. The ultimate goal would be to formulate a new standard in experimental testing and parameter identification based on a single experiment which allows identification of all materials.

Finally, the proposed multi-scale experiments can be combined in the IDIC framework to investigate and improve the interface integrity in stretchable electronic applications. The IDIC framework allows the incorporation of data from various sources and various length scales and connect them to a single multi-scale simulation. It is recommended to apply the proposed method to the various complex and challenging interfaces, for instance those found in stretchable electronic applications, and analyze the influence of the various microstructures and micromechanics on the fracture toughness.

References

[1] Abanto-Bueno, J., Lambros, J., 2005. Experimental determination of cohesive failure properties of a photodegradable copolymer. Experimental Mechanics 45, 144–152.

[2] Ahmadian, H., Mottershead, J.E., Friswell, M.I., 1998. Regularisation methods for finite element model updating. Mechanical Systems and Signal Processing 12, 47–64.

[3] Arzt, E., 1998. Size effects in materials due to microstructural and dimensional constraints: a comparative review. Acta Materialia 46, 5611–5626.

[4] Avril, S., Bonnet, M., Bretelle, A.S., Grédiac, M., Hild, F., Ienny, P., Latourte, F., Lemosse, D., Pagano, S., Pagnacco, E., Pierron, F., 2008. Overview of Identification Methods of Mechanical Parameters Based on Full-field Measurements. Experimental Mechanics 48, 381–402.

[5] Axisa, F., Brosteaux, D., De Leersnyder, E., Bossuyt, F., Gonzalez, M., Vanden Bulckel, M., Vanfleteren, J., 2007. Elastic and conformable electronic circuits and assemblies using MID in polymer. IEEE Polytronic 2007 Conference .

[6] Beams, J.W., 1959. Mechanical properties of thin films of gold and silver. John Wiley and Sons, New York, NY.

[7] van Beeck, J., Neggers, J., Schreurs, P.J.G., Hoefnagels, J.P.M., Geers, M.G.D., 2014. Quantification of three-dimensional surface deformation using Global Digital Image Correlation. Experimental Mechanics (accepted).

[8] Bergers, L.I.J.C., Hoefnagels, J.P.M., Delhey, N.K.R., Geers, M.G.D., 2011. Measuring time-dependent deformations in metallic MEMS. Microelectronics Reliability 51, 1054–1059.

[9] Bergers, L.I.J.C., Neggers, J., Geers, M.G.D., Hoefnagels, J.P.M., 2013. Enhanced Global Digital Image Correlation for Accurate Measurement of Microbeam Bending, in: Altenbach, H., Kruch, S. (Eds.), Advanced Materials Modelling for Structures. Springer, Berlin, Heidelberg. volume 19 of *Advanced Structured Materials*, pp. 43–51.

[10] Besnard, G., Hild, F., Roux, S., 2006. Finite-Element Displacement Fields Analysis from Digital Images: Application to Portevin-Le Châtelier Bands. Experimental Mechanics 46, 789–803.

[11] Besnard, G., Leclerc, H., Hild, F., Roux, S., Swiergiel, N., 2012. Analysis of image series through global digital image correlation. The Journal of Strain Analysis for Engineering Design 47, 214–228.

[12] Boelen, B., den Hartog, H., van der Weijde, H., 2004. Product performance of polymer coated packaging steel, study of the mechanism of defect growth in cans. Progress in Organic Coatings 50, 40–46.

[13] Bonnet, M., Constantinescu, A., 2005. Inverse problems in elasticity. Inverse Problems 21, R1–R50.

[14] Bornert, M., Brémand, F., Doumalin, P., Dupré, J.C., Fazzini, M., Grédiac, M., Hild, F., Mistou, S., Molimard, J., Orteu, J.J., Robert, L., Surrel, Y., Vacher, P., Wattrisse, B., 2008. Assessment of Digital Image Correlation Measurement Errors: Methodology and Results. Experimental Mechanics 49, 353–370.

[15] van den Bosch, M.J., Schreurs, P.J.G., Geers, M.G.D., 2006. An improved description of the exponential Xu and Needleman cohesive zone law for mixed-mode decohesion. Engineering Fracture Mechanics 73, 1220–1234.

[16] van den Bosch, M.J., Schreurs, P.J.G., Geers, M.G.D., 2008a. Identification and characterization of delamination in polymer coated metal sheet. Journal of the Mechanics and Physics of Solids 56, 3259–3276.

[17] van den Bosch, M.J., Schreurs, P.J.G., Geers, M.G.D., van Maris, M.P.F.H.L., 2008b. Interfacial characterization of pre-strained polymer coated steel by a numerical-experimental approach. Mechanics of Materials 40, 302–317.

[18] Bossuyt, F., Guenther, J., Löher, T., Seckel, M., Sterken, T., de Vries, J., 2011. Cyclic endurance reliability of stretchable electronic substrates. Microelectronics Reliability 51, 628–635.

[19] van Breemen, L.C.A., Engels, T.A.P., Klompen, E.T.J., Senden, D.J.A., Govaert, L.E., 2012a. Rate- and temperature-dependent strain softening in solid polymers. Journal of Polymer Science Part B: Polymer Physics 50, 1757–1771.

[20] van Breemen, L.C.A., Govaert, L.E., Meijer, H.E.H., 2012b. Scratching polycarbonate: A quantitative model. Wear 274-275, 238–247.

[21] van Breemen, L.C.A., Klompen, E.T.J., Govaert, L.E., Meijer, H.E.H., 2011. Extending the EGP constitutive model for polymer glasses to multiple relaxation times. Journal of the Mechanics and Physics of Solids 59, 2191–2207.

[22] Brosteaux, D., Gonzalez, M., Vanfleteren, J., 2007. Design and Fabrication of Elastic Interconnections for Stretchable Electronic Circuits. IEEE Electron Device Letters 28, 552–554.

[23] Brown, K., Hooker, J.C., Creton, C., 2002. Micromechanisms of Tack of Soft Adhesives Based on Styrenic Block Copolymers. Macromolecular Materials and Engineering 287, 163.

[24] Bruck, H.A., McNeill, S.R., Sutton, M.A., Peters III, W.H., 1989. Digital image correlation using Newton-Raphson method of partial differential correction. Experimental Mechanics , 261–267.

[25] Burn, D., 1961. The Economic History Of Steelmaking 1867-1939. Cambridge University Press, Cambridge.

[26] Cahn, R.W., Haris, B., 1969. Newer Forms of Carbon and their Uses. Nature 221, 132–141.

[27] Cheng, P., Sutton, M.A., Schreier, H.W., McNeill, S.R., 2002. Full-field speckle pattern image correlation with B-spline deformation function. Experimental Mechanics 42.

[28] Chu, T.C., Ranson, W.F., Sutton, M.A., 1985. Applications of digital-image-correlation techniques to experimental mechanics. Experimental mechanics , 232–244.

[29] Claire, D., Hild, F., Roux, S., 2004. A finite element formulation to identify damage fields: the equilibrium gap method. International Journal for Numerical Methods in Engineering 61, 189–208.

[30] Cranford, S.W., Tarakanova, A., Pugno, N.M., Buehler, M.J., 2012. Nonlinear material behaviour of spider silk yields robust webs. Nature 482, 72–76.

[31] Creton, C., Hooker, J.C., Shull, K.R., 2001. Bulk and interfacial contributions to the debonding mechanisms of soft adhesives: Extension to large strains. Langmuir 17, 4948–4954.

[32] Creton, C., Kramer, E.J., Hui, C.Y., Brown, H.R., 1992. Failure mechanisms of polymer interfaces reinforced with block copolymers. Macromolecules , 3075–3088.

[33] Crosby, A.J., Shull, K.R., Lakrout, H., Creton, C., 2000. Deformation and failure modes of adhesively bonded elastic layers. Journal of Applied Physics 88, 2956–2966.

[34] Cyganowski, A., Minev, I.R., Vachicouras, N., Musick, K., Lacour, S.P., 2012. Stretchable Electrodes for Neuroprosthetic Interfaces.

[35] Engels, T.A.P., van Breemen, L.C.A., Govaert, L.E., Meijer, H.E.H., 2011. Criteria to predict the embrittlement of polycarbonate. Polymer 52, 1811–1819.

[36] Eyring, H., 1936. Viscosity, Plasticity, and Diffusion as Examples of Absolute Reaction Rates. The Journal of Chemical Physics 4, 283.

[37] Fedele, R., Raka, B., Hild, F., Roux, S., 2009. Identification of adhesive properties in GLARE assemblies using digital image correlation. Journal of the Mechanics and Physics of Solids 57, 1003–1016.

[38] Freund, L.B., Suresh, S., 2003. Thin film materials: stress, defect formation, and surface evolution. Cambridge University Press, New York, NY.

[39] Geiß ler, G., Kaliske, M., 2010. Time-dependent cohesive zone modelling for discrete fracture simulation. Engineering Fracture Mechanics 77, 153–169.

[40] Georgiou, I., Hadavinia, H., Ivankovic, A., Kinloch, a.J., Tropsa, V., Williams, J.G., 2003. Cohesive zone models and the plastically deforming peel test. The Journal of Adhesion 79, 239–265.

[41] Gibson, R.F., 2010. A review of recent research on mechanics of multifunctional composite materials and structures. Composite Structures 92, 2793–2810.

[42] Gonzalez, M., Axisa, F., Vanden Bulcke, M., Brosteaux, D., Vandevelde, B., Vanfleteren, J., 2007. Design of metal interconnects for stretchable electronic circuits using finite element analysis. EuroSimE , 110–115.

[43] Grédiac, M., Pierron, F., Surrel, Y., 1999. Novel Procedure for Complete In-plane Composite Characterization Using a Single T-shaped Specimen. Experimental Mechanics , 142–149.

[44] Greer, J.R., Oliver, W.C., Nix, W.D., 2005. Size dependence of mechanical properties of gold at the micron scale in the absence of strain gradients. Acta Materialia 53, 1821–1830.

[45] Gross, D., Seelig, T., 2011. Fracture Mechanics - with an introduction to micromechanics. Second ed., Springer, New York, NY.

[46] Gruber, P.A., Böhm, J., Onuseit, F., Wanner, A., Spolenak, R., Arzt, E., 2008. Size effects on yield strength and strain hardening for ultra-thin Cu films with and without passivation: A study by synchrotron and bulge test techniques. Acta Materialia 56, 2318–2335.

[47] van Hal, B.A.E., Peerlings, R.H.J., Geers, M.G.D., van der Sluis, O., 2007. Cohesive zone modeling for structural integrity analysis of IC interconnects. Microelectronics Reliability 47, 1251–1261.

[48] Han, K., Ciccotti, M., Roux, S., 2010. Measuring nanoscale stress intensity factors with an atomic force microscope. Europhysics Letters 89, 66003.

[49] Hetényi, M., 1952. Application of Maclaurin series to the analysis of beams in bending. Journal of the Franklin Institute .

[50] Hild, F., Roux, S., 2006. Digital Image Correlation: from Displacement Measurement to Identification of Elastic Properties - a Review. Strain 42, 69–80.

[51] Hild, F., Roux, S., 2012. Comparison of Local and Global Approaches to Digital Image Correlation. Experimental Mechanics 52, 1503–1519.

[52] Hild, F., Roux, S., Gras, R., Guerrero, N., Marante, M.E., Flórez-López, J., 2009. Displacement measurement technique for beam kinematics. Optics and Lasers in Engineering 47, 495–503.

[53] Hill, R., 1950. A theory of the plastic bulging of a metal diaphragm by lateral pressure. Philosophical Magazine 4, 1133–1142.

[54] Hoefnagels, J.P.M., Neggers, J., Timmermans, P.H.M., van der Sluis, O., Geers, M.G.D., 2010. Copper-rubber interface delamination in stretchable electronics. Scripta Materialia 63, 875–878.

[55] Hsu, F.P.K., Liu, A.M.C., Downs, J., Rigamonti, D., Humphrey, J.D., 1995. A triplane video-based experimental system for studying axisymmetrically inflated biomembranes. Biomedical engineering 42, 442–450.

[56] Hsu, F.P.K., Schwab, C., Rigamonti, D., Humphrey, J.D., 1994. Identification of response functions from axisymmetric membrane inflation tests: implications for biomechanics. International Journal of Solids and Structures 31, 3375–3386.

[57] Hsu, Y.Y., Gonzalez, M., Bossuyt, F., Axisa, F., Vanfleteren, J., Vandevelde, B., de Wolf, I., 2010a. Design and analysis of a novel fine pitch and highly stretchable interconnect. Microelectronics International 27, 33–38.

[58] Hsu, Y.Y., Gonzalez, M., Bossuyt, F., Axisa, F., Vanfleteren, J., de Wolf, I., 2009. In situ observations on deformation behavior and stretching-induced failure of fine pitch stretchable interconnect. Journal of Materials research , 3573–3582.

[59] Hsu, Y.Y., Gonzalez, M., Bossuyt, F., Axisa, F., Vanfleteren, J., de Wolf, I., 2010b. The effect of pitch on deformation behavior and the stretching-induced failure of a polymer-encapsulated stretchable circuit. Journal of Micromechanics and Microengineering 20, 1–11.

[60] Hsu, Y.Y., Gonzalez, M., Bossuyt, F., Vanfleteren, J., de Wolf, I., 2011. Polyimide-enhanced stretchable interconnects: design, fabrication, and characterization. IEEE Transactions on Electron Devices 58, 2680–2688.

[61] Hutchinson, J.W., Suo, Z., 1992. Mixed mode cracking in layered materials. Advances in applied mechanics 29, 63–191.

[62] Janssen, P.J.M., Hoefnagels, J.P.M., de Keijser, T.H., Geers, M.G.D., 2008. Processing induced size effects in plastic yielding upon miniaturisation. Journal of the Mechanics and Physics of Solids 56, 2687–2706.

[63] Kalkman, A.J., Verbruggen, A.H., Janssen, G.C.A.M., Radelaar, S., 2002a. Transient creep in free-standing thin polycrystalline aluminum films. Journal of Applied Physics 92, 4968–4975.

[64] Kalkman, A.J., Verbruggen, A.H., Radelaar, S., 2002b. High-temperature tensile tests and activation volume measurement of free-standing submicron Al films. Journal of Applied Physics 92, 6612–6615.

[65] Kavanagh, K.T., Clough, R.W., 1971. Finite element applications in the characterization of elastic solids. International Journal of Solids and Structures 7, 11–23.

[66] Kendall, K., 1975. Thin-film peeling-the elastic term. Journal of Physics D: Applied Physics 8, 1449–1452.

[67] Keplinger, C., Sun, J.Y., Foo, C.C., Rothemund, P., Whitesides, G.M., Suo, Z., 2013. Stretchable, transparent, ionic conductors. Science (New York, N.Y.) 341, 984–7.

[68] Khang, D.Y., Jiang, H., Huang, Y.Y., Rogers, J.A., 2006. A stretchable form of single-crystal silicon for high-performance electronics on rubber substrates. Science 311, 208–212.

[69] Kim, D.H., Ahn, J.H., Choi, W.M., Kim, H.S., Kim, T.H., Song, J., Huang, Y.Y., Liu, Z., Lu, C., Rogers, J.A., 2008. Stretchable and foldable silicon integrated circuits. Science 320, 507–11.

[70] Kim, D.H., Rogers, J.A., 2008. Stretchable Electronics: Materials Strategies and Devices. Advanced Materials 20, 4887–4892.

[71] Kim, J.K., Sham, M.L., 2000. Impact and delamination failure of woven-fabric composites. Composites Science and Technology 60, 745–761.

[72] Kim, K.S., Aravas, N., 1988. Elastoplastic analysis of the peel test. International Journal of Solids and Structures 24, 417–435.

[73] Klompen, E.T.J., Govaert, L.E., 1999. Nonlinear viscoelastic behaviour of thermorheologically complex materials. Mechanics of Time-Dependent Materials 3, 49–69.

[74] Lacour, S.P., Wagner, S., Huang, Z., Suo, Z., 2003. Stretchable gold conductors on elastomeric substrates. Applied Physics Letters 82, 2404.

[75] Leclerc, H., Périé, J.N., Roux, S., Hild, F., 2009. Integrated digital image correlation for the identification of mechanical properties, in: Computer Vision/Computer Graphics CollaborationTechniques. Springer, Berlin Heidelberg, pp. 161–171.

[76] Leclerc, H., Périé, J.N., Roux, S., Hild, F., 2010. Voxel-Scale Digital Volume Correlation. Experimental Mechanics 51, 479–490.

[77] Leplay, P., Réthoré, J., Meille, S., Baietto, M.C., 2010. Damage law identification of a quasi brittle ceramic from a bending test using Digital Image Correlation. Journal of the European Ceramic Society 30, 2715–2725.

[78] Li, T., Huang, Z., Suo, Z., Lacour, S.P., Wagner, S., 2004. Stretchability of thin metal films on elastomer substrates. Applied Physics Letters 85, 3435–3437.

[79] Li, T., Huang, Z.Y., Xi, Z.C., Lacour, S.P., Wagner, S., Suo, Z., 2005a. Delocalizing strain in a thin metal film on a polymer substrate. Mechanics of Materials 37, 261–273.

[80] Li, T., Suo, Z., Lacour, S.P., Wagner, S., 2005b. Compliant thin film patterns of stiff materials as platforms for stretchable electronics. Journal of Materials research 20, 3274–3277.

[81] Liechti, K.M., Wu, J.D., 2001. Mixed-mode, time-dependent rubber/metal debonding. Journal of the Mechanics and Physics of Solids 49, 1039–1072.

[82] Litteken, C.S., Dauskardt, R.H., 2003. Adhesion of polymer thin-films and patterned lines. International Journal of Fracture 119/120, 475–485.

[83] Loeher, T., Manessis, D., Heinrich, R., Vanfleteren, J., DeBaets, J., Ostmann, A., Reichl, H., 2006. Stretchable electronic systems. Electronics Packaging Technology Conference , 271–276.

[84] Loeher, T., Manessis, D., Ostmann, A., 2007. Stretchable electronic systems. Onboard Technology FebruaryOnboard Technology February 1, 18–19.

[85] Lumelsky, V., Shur, M., Wagner, S., 2001. Sensitive skin. IEEE Sensors Journal 1, 41–51.

[86] Madou, M.J., 2002. Fundamentals of Microfabrication. 2nd ed., CRC Press LLC, Boca Raton.

[87] Martins, P., Delobelle, P., Malheire, C., Brida, S., Barbier, D., 2009. Bulge test and AFM point deflection method, two technics for the mechanical characterisation of very low stiffness freestanding films. European physical journal of applied physics 10501.

[88] Mathieu, F., Hild, F., Roux, S., 2013. Image-based identification procedure of a crack propagation law. Engineering Fracture Mechanics 103, 48–59.

[89] Maynadier, A., Poncelet, M., Lavernhe-Taillard, K., Roux, S., 2011. One-shot Measurement of Thermal and Kinematic Fields: InfraRed Image Correlation (IRIC). Experimental Mechanics 52, 241–255.

[90] Meijer, H.E.H., Govaert, L.E., 2003. Multi-Scale Analysis of Mechanical Properties of Amorphous Polymer Systems. Macromolecular Chemistry and Physics 204, 274–288.

[91] Meuwissen, M.H.H., Oomens, C.W.J., Baaijens, F.P.T., Petterson, R., Janssen, J.D., 1998. Determination of the elasto-plastic properties of aluminium using a mixed numericalexperimental method. Journal of Materials Processing Technology 75, 204–211.

[92] Mottershead, J.E., Friswell, M.I., 1993. Model updating in structural dynamics: a survey. Journal of sound and vibration .

[93] Munch, E., Launey, M.E., Alsem, D.H., Saiz, E., 2008. Tough, bio-inspired hybrid materials. Science , 1516–1520.

[94] Neggers, J., Hoefnagels, J.P.M., Hild, F., Roux, S., Geers, M.G.D., 2012. A Global Digital Image Correlation Enhanced Full-Field Bulge Test. Procedia IUTAM 4, 73–81.

[95] Nix, W.D., 1989. Mechanical properties of thin films. Metallurgical transactions A 20A, 2217–2245.

[96] Ostmann, A., Loeher, T., Seckel, M., Boettcher, L., Reichl, H., 2008. Manufacturing concepts for stretchable electronic systems, in: 3rd International Microsystems, Packaging, Assembly and Circuits Technology Conference, IMPACT 2008, pp. 25–28.

[97] Packham, D.E., 2003. Surface energy, surface topography and adhesion. International Journal of Adhesion and Adhesives 23, 437–448.

[98] Packham, D.E., 2010. Discontinuities at the Interface and Adhesion. The Journal of Adhesion 86, 1231–1243.

[99] Pei, Y.T., Galvan, D., de Hosson, J.T.M., Cavaleiro, A., 2005. Nanostructured TiC/a-C coatings for low friction and wear resistant applications. Surface and Coatings Technology 198, 44–50.

[100] Pei, Y.T., Galvan, D., de Hosson, J.T.M., Strondl, C., 2006. Advanced TiC/a-C:H nanocomposite coatings deposited by magnetron sputtering. Journal of the European Ceramic Society 26, 565–570.

[101] Ramesh, R., Spaldin, N.A., 2007. Multiferroics: progress and prospects in thin films. Nature materials 6, 21–29.

[102] Reibold, M., Paufler, P., Levin, A.A., Kochmann, W., Pätzke, N., Meyer, D.C., 2006. Carbon nanotubes in an ancient Damascus sabre. Nature 444, 286.

[103] Réthoré, J., 2010. A fully integrated noise robust strategy for the identification of constitutive laws from digital images. International Journal for Numerical Methods in Engineering 84, 631–660.

[104] Réthoré, J., Hild, F., Roux, S., 2008. Extended digital image correlation with crack shape optimization. International Journal for Numerical Methods in Engineering 73, 248–272.

[105] Réthoré, J., Roux, S., Hild, F., 2009. An extended and integrated digital image correlation technique applied to the analysis of fractured samples. European Journal Computational Mechanics 18, 285–306.

[106] Réthoré, J., Roux, S., Hild, F., 2011. Optimal and noise-robust extraction of Fracture Mechanics parameters from kinematic measurements. Engineering Fracture Mechanics 78, 1827–1845.

[107] Rogers, J.A., Someya, T., Huang, Y.Y., 2010. Materials and mechanics for stretchable electronics. Science (New York, N.Y.) 327, 1603–1607.

[108] Rossi, M., Pierron, F., Pascal, L., Dimitri, D., 2013. Development of a Test Simulator to Perform Optimized Experiment Design, in: Ventura, C.E., Crone, W.C., Furlong, C. (Eds.), Experimental and Applied Mechanics, Volume 4. Springer, New York, NY. volume 4 of *Conference Proceedings of the Society for Experimental Mechanics Series*. chapter 40, pp. 345–347.

[109] Savitzky, A., Golay, M.J.E., 1964. Smoothing and differentiation of data by simplified least squares procedures. Analytical chemistry 36, 1627–1639.

[110] Schreier, H., Orteu, J.J., Sutton, M.A., 2009. Image Correlation for Shape, Motion and Deformation Measurements. Springer US, Boston, MA.

[111] Schreier, H.W., Braasch, J.R., Sutton, M.A., 2000. Systematic errors in digital image correlation caused by intensity interpolation. Optical Engineering 39, 2915–2921.

[112] Schreier, H.W., Sutton, M.A., 2002. Systematic Errors in Digital Image Correlation Due to Undermatched Subset Shape Functions. Experimental Mechanics 42, 303–310.

[113] Sekitani, T., Noguchi, Y., Hata, K., Fukushima, T., Aida, T., Someya, T., 2008. A rubberlike stretchable active matrix using elastic conductors. Science (New York, N.Y.) 321, 1468–1472.

[114] Shen, B., Paulino, G.H., 2010. Direct Extraction of Cohesive Fracture Properties from Digital Image Correlation: A Hybrid Inverse Technique. Experimental Mechanics 51, 143–163.

[115] Shen, Z., Zhao, Z., Peng, H., Nygren, M., 2002. Formation of tough interlocking microstructures in silicon nitride ceramics by dynamic ripening. Nature 417, 266–269.

[116] van der Sluis, O., Hsu, Y.Y., Timmermans, P.H.M., Gonzalez, M., Hoefnagels, J.P.M., 2011a. Stretching-induced interconnect delamination in stretchable electronic circuits. Journal of Physics D: Applied Physics 44, 034008.

[117] van der Sluis, O., Noijen, S.P.M., Bouquet, J.B., Timmermans, P.H.M., 2011b. Analysis of Combined Adhesive and Cohesive Cracking at Roughened Surfaces. Key Engineering Materials 488-489, 117–121.

[118] van der Sluis, O., Remmers, J.J.C., Thurlings, M.A.C., Welling, B.J., Noijen, S.P.M., 2014. The competition between adhesive and cohesive fracture at a micropatterned polymer-metal interface. Key Engineering Materials 577-578, 225–228.

[119] van der Sluis, O., Timmermans, P.H.M., van der Zanden, E.J.L., Hoefnagels, J.P.M., 2009. Analysis of the three-dimensional delamination behavior of stretchable electronics applications. Key Engineering Materials 418, 9–12.

[120] van der Sluis, O., Yuan, C.A., van Driel, W.D., Zhang, G.Q., 2008. Advances in Delamination Modeling, in: Nanopackaging. chapter 4, pp. 61–91.

[121] Small, M.K., Nix, W.D., 1992. Analysis of the accuracy of the bulge test in determining the mechanical properties of thin films. Journal of materials research 94305, 1553–1563.

[122] Sutton, M.A., Mingqi, C., Peters III, W.H., Chao, Y.J., McNeill, S.R., 1986. Application of an optimized digital correlation method to planar deformation analysis. Image and Vision Computing 4, 143–150.

[123] Tabata, O., Kawahata, K., Sugiyama, S., Igarashi, I., 1989. Mechanical property measurements of thin films using load-deflection of composite rectangular membranes. Sensors and Actuators 20, 135–141.

[124] Tervoort, T.A., Klompen, E.T.J., Govaert, L.E., 1996. A multi-mode approach to finite, three-dimensional, nonlinear viscoelastic behavior of polymer glasses. Journal of Rheology 40, 779–797.

[125] Thompson, C.V., 1993. The yield stress of polycrystalline thin films. Journal of Materials Research 8, 1992–1993.

[126] Timoshenko, S., 1987. Theory of Plates and Shells. McGraw-Hill, New York, NY.

[127] Tomičević, Z., Hild, F., Roux, S., 2013. Mechanics-aided digital image correlation. The Journal of Strain Analysis for Engineering Design 0, 1–14.

[128] Tsakalakos, T., 1981. The bulge test: A comparison of the theory and experiment for isotropic and anisotropic films. Thin Solid Films 75, 293–305.

[129] Tvergaard, V., Hutchinson, J.W., 1993. The influence of plasticity on mixed mode interface toughness. Journal of the Mechanics and Physics of Solids 41, 1119–1135.

[130] Vanfleteren, J., Loeher, T., Gonzalez, M., Bossuyt, F., Vervust, T., de Wolf, I., Jablonski, M., 2012. SCB and SMI : two stretchable circuit technologies, based on standard printed circuit board processes. Circuit World 38, 232–242.

[131] Vella, D., Bico, J., Boudaoud, A., Roman, B., Reis, P.M., 2009. The macroscopic delamination of thin films from elastic substrates. Proceedings of the National Academy of Sciences of the United States of America 106, 10901–10906.

[132] Vervust, T., Buyle, G., Bossuyt, F., Vanfleteren, J., 2012. Integration of stretchable and washable electronic modules for smart textile applications. The Journal of The Textile Institute 103, 1127–1138.

[133] Vinci, R.P., Vlassak, J.J., 1996. Mechanical behavior of thin films. Annual Review of Materials Science 26, 431–462.

[134] Visser, H.A., Bor, T.C., Wolters, M., Warnet, L.L., Govaert, L.E., 2011. Influence of physical aging on impact embrittlement of uPVC pipes. Plastics, Rubber and Composites 40, 201–212.

[135] Vlassak, J.J., Nix, W.D., 1992. A new bulge test technique for the determination of Young's modulus and Poisson's ratio of thin films. Journal of Materials Research 7, 3242–3249.

[136] Vossen, B.G., Schreurs, P.J.G., van der Sluis, O., Geers, M.G.D., 2014. Multiscale modelling of delamination through fibrillation. Journal of the Mechanics and Physics of Solids submitted.

[137] Wagner, S., Lacour, S.P., Jones, J., Hsu, P.h.I., Sturm, J.C., Li, T., Suo, Z., 2004. Electronic skin: architecture and components. Physica E: Low-dimensional Systems and Nanostructures 25, 326–334.

[138] Wang, Y., Lava, P., Coppieters, S., Houtte, P.V., Debruyne, D., 2013. Application of a Multi-Camera Stereo DIC Set-up to Assess Strain Fields in an Erichsen Test: Methodology and Validation. Strain 49, 190–198.

[139] Wattrisse, B., Chrysochoos, A., 2001. Analysis of strain localization during tensile tests by digital image correlation. Experimental Mechanics 41, 29–39.

[140] Wei, Y., Hutchinson, J.W., 2007. Peel Test and Interfacial Toughness, in: Comprehensive Structural Integrity. Elsevier, Oxford. chapter 8.05, pp. 18–217.

[141] Xiang, Y., Chen, X., Vlassak, J.J., 2005a. Plane-strain bulge test for thin films. Journal of materials research 20, 2360–2370.

[142] Xiang, Y., Li, T., Suo, Z., Vlassak, J.J., 2005b. High ductility of a metal film adherent on a polymer substrate. Applied Physics Letters 87, 1–3.

[143] Xiang, Y., Vlassak, J., 2006. Bauschinger and size effects in thin-film plasticity. Acta Materialia 54, 5449–5460.

[144] Xu, W., Yang, J.S., Lu, T.J., 2011. Ductility of thin copper films on rough polymer substrates. Materials & Design 32, 154–161.

[145] Yao, Q., Qu, J., 2002. Interfacial Versus Cohesive Failure on Polymer-Metal Interfaces in Electronic PackagingEffects of Interface Roughness. Journal of Electronic Packaging 124, 127–134.

[146] Zhang, G.Q., van Driel, W.D., Fan, X.J., 2006. Mechanics of Microelectronics. Springer, Berlin, Heidelberg.

Appendix A
A fracture surface matching method

In chapter 4, the two sides of the fractured interface are digitally repositioned on top of each other to compare both fracture surfaces locally. To this end, Digital Image Correlation (DIC) is applied to find the displacement field required to deform one image such that it resembles the other. Usually, DIC deals with one reference gray scale image of a patterned sample $f(\vec{x})$, and a second image of the same sample, yet in a deformed state $g(\vec{x})$, where $\vec{x}$ is the camera coordinate system, for details see [14]. DIC starts from the concept of brightness conservation, where the gray values of one material point must be the same in the image f and the image g. A residual image is formed by comparing the gray values at the reference coordinates in f and the deformed coordinates in g,

$$r(\vec{x}) = f(\vec{x}) - g(\vec{x} + \vec{u}(\vec{x})), \tag{A.1}$$

This residual image is minimal when the correct displacement field is applied. In DIC, the displacement field is typically parameterized with a limited set of degrees of freedom,

$$\vec{u}(\vec{x}, \underline{\lambda})) = \sum_{i=1}^{n} \lambda_i \varphi_i(\vec{x}), \tag{A.2}$$

where n is the number of unknowns and φ are a set of chosen basis functions corresponding to the degrees of freedom λ. The basis functions can be any type of interpolation functions, e.g. FEM shape-functions. For the present case polynomials with a full support over the entire region of interest will be applied, similarly to chapter 7. At this point the residual is minimized iteratively, thereby optimizing the degrees of freedom.

For chapter 4, the images are surface topographies measured by optical confocal microscopy (figure 4.17). Consequently, the brightness conservation is relaxed to allow out of plane displacements,

$$r(\vec{x}) = f(\vec{x}) - g(\vec{x} + \vec{u}(\vec{x}, \underline{\lambda})) - w(\vec{x}, \underline{\lambda}), \tag{A.3}$$

where $w(\vec{x})$ is a field describing the out-of-plane displacement, see also Neggers et al. [94], Bergers et al. [9] and van Beeck et al. [7].

It is not possible to apply a pattern to the fracture surfaces since this obscures the fracture topology. The consequence is that the natural texture on the surface is used as a pattern, thereby limiting the performance of the DIC algorithm. Additionally, the two images (or topologies) at hand are not two images of the same surface of a sample, but are two images of separated surfaces. This compromises the brightness conservation, putting a heavy requirement on the robustness of the method. Therefore, a minimal set of degrees

of freedom is applied to maximize the robustness of the method. In particular, only zero order and first order polynomial basis functions are applied which have support over the entire region of interest. A few large features in the pattern are used as to set an initial guess in the DIC algorithm, which due to the minimal freedom, robustly converges to obtain the displacement field. With this displacement field, the PDMS surface is deformed such that corresponding features are shown in the same location in the field of view as in the copper surface topology.

Note that the topographical images, which have a physical meaning connected to the gray values, combined with the 3D topology DIC method are ideally equipped to analyze such dissimilar surfaces. The reason is that DIC methods are derived from brightness conservation. If the two surfaces would have been imaged with optical (or electron) methods, then it is unlikely that the gray-values of one surface correlate with the gray-values of the other surface. The topographical measurement creates an equal basis for the meaning of the gray-values (i.e. height). Therefore, it is natural to compare the two topographies in terms of gray level conservation, i.e. height conservation.

Appendix B
A detailed introduction to global digital image correlation

Co-authored by; J. Neggers, B. Blaysat, J. van Beeck, J.P.M. Hoefnagels and M.G.D. Geers

Introduction to DIC

DIC deals with finding the displacement field $\vec{u}(\vec{x}_0)$ from two images, where one is (usually) the reference image $f(\vec{x}_0)$ and the other a deformed image $g(\vec{x})$, see figure B.1. The brightness of material point P in both figures must be equal thus we can write

$$f(\vec{x}_0) = g(\vec{x}), \tag{B.1}$$

which is the so-called brightness conservation relation.

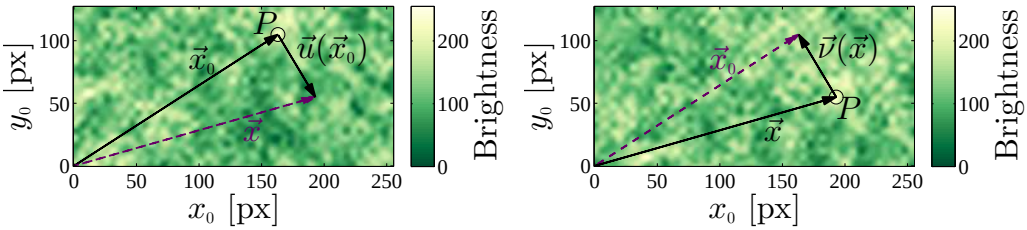

reference image $f(\vec{x}_0)$ deformed image $g(\vec{x}_0)$

Figure B.1: An example reference and deformed image, with the vectors $\vec{x}_0$, $\vec{x}$, $\vec{u}(\vec{x}_0)$ and $\vec{\nu}(\vec{x})$ illustrated.

In other words the vector $\vec{x}_0$ points to P in image f and the vector $\vec{x}$ points to P in image g. The relation between the two vectors is the displacement which is,

$$\vec{u}(\vec{x}_0) = \vec{x}(\vec{x}_0) - \vec{x}_0, \tag{B.2}$$

$$\vec{\nu}(\vec{x}) = \vec{x}_0(\vec{x}) - \vec{x}. \tag{B.3}$$

Note that, the vector $\vec{u}$ is defined with its origin in the frame of $\vec{x}_0$ pointing towards $\vec{x}$. The reverse displacement can also be defined $\vec{\nu}(\vec{x})$ which is the same as switching the reference and the deformed image, and is therefore not discussed further.

Local versus Global DIC

Digital Image Correlation development started from already existing Particle Image Velocimetry (PIV) techniques, and back then many of the advancement in the technology are attributed to the work of M.A. Sutton and his colleagues [110]. The DIC algorithms originating from that work are today referred to as "local DIC", and are still used today. Almost all commercial codes are based on the "local DIC" method [14]. In local DIC the image is divided in separate parts, sometimes called facets or subsets, which are individually correlated, and have thus no influence on each other. In other words the DIC problem is solved locally.

In the early 2000's a new way of solving the problem was introduced. These methods are usually referred to as "Global DIC", and are used in academic problems [10, 50]. In "Global DIC" the DIC problem is solved for the entire region of interest, hence "global". The global displacement field can take on complex shapes which in Global DIC are approximated with a limited set of degrees of freedom. An example of such an approximation is for instance the FEM mesh, with its nodes as degrees of freedom, and the element interpolation functions as basis functions. The reason why Global DIC is preferred in academic problems is that it can outperform Local DIC if the correct displacement discretization is chosen [51]. Actually, it is possible to choose the displacement discretization in such a way that the method is equivalent to the Local DIC method. It can thus be said that Global DIC is a more general formulation.

This appendix is written with Global DIC in mind. Nevertheless, since Local DIC also fits inside the Global DIC framework most of the derivations and corresponding conclusions are also valid for Local DIC.

Derivation of a 1D solvable system

Obtaining the system of equations for DIC is easiest explained in one dimension (1D). Thus, we consider 1D images f and g, shown in figure B.2. Note that, for now f and g are assumed to be continuous functions. However, the figure already hints at the discrete (pixel) character of images.

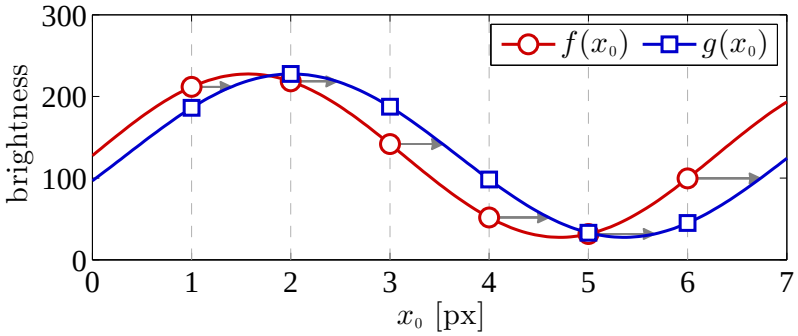

Figure B.2: Very simple 1D reference and deformed image.

Rearranging (B.1) to define a residual,

$$f(x_0) - g\big(x_0 + u(x_0)\big) = \Psi(x_0) \approx 0, \tag{B.4}$$

where $\Psi(x_0)$ is the residual image, which will be zero everywhere, assuming $u(x_0)$ is perfect and in absence of acquisition noise.

Minimization potential

In order to find the optimal displacement field, let us use a least squares approach on the field residual,

$$u(x_0) = \underset{u(x_0)}{\text{Argmin}}(\Phi) = \underset{u(x_0)}{\text{Argmin}} \int_{\Omega_0} \Big[f(x_0) - g\big(x_0 + u(x_0)\big)\Big]^2 \,\mathrm{d}x_0, \tag{B.5}$$

where Ω_0 denotes the Region Of Interest (ROI) defined in the reference frame x_0. The ROI is essential in DIC because the conservation of brightness can only be observed for material points which are visible in both images. In most experiments, a part of image f moves out of frame in image g.

Reducing the solution space

Minimizing this potential towards the continuous field $u(x_0)$ yields an infinite solution space. To reduce the solution space, which also reduces noise sensitivity, the displacement field is parameterized using a chosen set basis functions $\varphi_j(x_0)$ and corresponding degrees of freedom λ_j,

$$u(x_0) \approx u^*(x_0, \underline{\lambda}) = \sum_{j=1}^{m} \lambda_j \varphi_j(x_0), \tag{B.6}$$

$$\underline{\lambda} = \lambda_1, \ldots, \lambda_m, \tag{B.7}$$

where $u^*(x_0, \underline{\lambda})$ is the approximated version of $u(x_0)$. This way of formulating a set of linearly independent basis functions is desirable, but is not strictly required. The non-linear form is not further discussed. The result of (B.6) is substituted in (B.5) to obtain,

$$\underset{\underline{\lambda}}{\text{Argmin}}(\Phi) = \underset{\underline{\lambda}}{\text{Argmin}} \int_{\Omega_0} \Psi^2 \, \mathrm{d}x_0, \tag{B.8}$$

$$\Psi = f(x_0) - g\big(x_0 + u^*(x_0, \underline{\lambda})\big), \tag{B.9}$$

From a minimization problem to a root finding problem

Minimizing the above is the same as finding the root of the derivative of the potential towards the pivots which are in this case the degrees of freedom.

$$\forall_j \quad \Gamma_j = \frac{\partial \Phi}{\partial \lambda_j} = 0, \tag{B.10}$$

which gives m equations which equal zero.

Linearizing and iterative solving

Solving (B.10) is a non-linear problem, therefore, an iterative (Newton-Raphson) scheme is used where the degrees of freedom are split in an initial guess part λ_i and a to be solved update $\delta\lambda_i$,

$$\lambda_i^{\mathsf{it}+1} = \lambda_i^{\mathsf{it}} + \delta\lambda_i. \tag{B.11}$$

Linearizing (B.10),

$$\forall_j \quad \Gamma_j^{\mathsf{it}+1} \approx \Gamma_j^{\mathsf{it}} + \sum_{i=1}^{m} \frac{\partial \Gamma_j^{\mathsf{it}}}{\partial \lambda_i^{\mathsf{it}}} \, \delta\lambda_i = 0, \qquad \Gamma_j^{\mathsf{it}} = \Gamma_j(\underline{\lambda}^{\mathsf{it}}), \tag{B.12}$$

which is rewritten in the common form,

$$\forall_j \quad \sum_{i=1}^{m} \frac{\partial \Gamma_j^{\mathsf{it}}}{\partial \lambda_i^{\mathsf{it}}} \, \delta\lambda_i = -\Gamma_j^{\mathsf{it}}, \tag{B.13}$$

which is usually written in a matrix form as,

$$\underline{\underline{M}} \underline{\delta\lambda} = \underline{b}, \qquad \text{where} \quad M_{ij} = \frac{\partial \Gamma_j^{\mathsf{it}}}{\partial \lambda_i^{\mathsf{it}}} \tag{B.14}$$

The right hand member

The iterative solution for the system of equations is defined in (B.13), with two parts which still need to be detailed. Starting with Γ_j^{it},

$$\Gamma_j^{\mathsf{it}} = \frac{\partial \Phi}{\partial \lambda_j^{\mathsf{it}}} = \int_{\Omega_0} 2\Psi \frac{\partial \Psi}{\partial \lambda_j^{\mathsf{it}}} \, \mathrm{d}x_0 = 0, \tag{B.15}$$

$$\frac{\partial \Psi}{\partial \lambda_j^{\mathsf{it}}} = -\frac{\partial}{\partial \lambda_j^{\mathsf{it}}} \Big[g\big(x(x_0, \underline{\lambda}^{\mathsf{it}})\big) \Big] = -\frac{\partial}{\partial x} \Big[g\big(x(x_0, \underline{\lambda}^{\mathsf{it}})\big) \Big] \frac{\partial}{\partial \lambda_j^{\mathsf{it}}} \Big[x(x_0, \underline{\lambda}^{\mathsf{it}}) \Big], \tag{B.16}$$

where $[\,]$ should be interpreted as the derivative applied to whatever is inside the brackets. Starting with the rightmost part of the above equation, remembering that the deformed coordinate is a function of the reference coordinate,

$$x(x_0, \underline{\lambda}^{\mathsf{it}}) = x_0 + u(x_0, \underline{\lambda}^{\mathsf{it}}), \tag{B.17}$$

then its derivative towards the degrees of freedom is,

$$\frac{\partial}{\partial \lambda_j^{\mathsf{it}}} \Big[x(x_0, \underline{\lambda}^{\mathsf{it}}) \Big] = \frac{\partial}{\partial \lambda_j^{\mathsf{it}}} \Big[u(x_0, \underline{\lambda}^{\mathsf{it}}) \Big] = \varphi_j(x_0). \tag{B.18}$$

Interestingly, the basis functions are independent of the iterative values of the degrees of freedom, as a result they can be reused for all iterations.

The image gradient is slightly more complicated, because it is the gradient towards the deformed coordinate. Let us first consider this function g, which is a function of x, which is in turn a function of x_0,

$$\frac{\partial}{\partial x_0} \Big[g\big(x(x_0, \underline{\lambda}^{\mathsf{it}})\big) \Big] = \frac{\partial}{\partial x} \Big[g\big(x(x_0, \underline{\lambda}^{\mathsf{it}})\big) \Big] \frac{\partial}{\partial x_0} \Big[x(x_0, \underline{\lambda}^{\mathsf{it}}) \Big], \tag{B.19}$$

Through the chain rule, two components are found on the right hand side, one of which is the one we are looking for,

$$\frac{\partial}{\partial x} \Big[g\big(x(x_0, \underline{\lambda}^{\mathsf{it}})\big) \Big] = \frac{\partial}{\partial x_0} \Big[g\big(x(x_0, \underline{\lambda}^{\mathsf{it}})\big) \Big] \left(\frac{\partial}{\partial x_0} \Big[x(x_0, \underline{\lambda}^{\mathsf{it}}) \Big] \right)^{-1} \tag{B.20}$$

$$= \frac{\partial}{\partial x_0} \Big[\tilde{g}(x_0) \Big] \left(\frac{\partial}{\partial x_0} \Big[x(x_0, \underline{\lambda}^{\mathsf{it}}) \Big] \right)^{-1}, \tag{B.21}$$

where $\tilde{g}(x_0)$ is the back deformed image of $g(x)$, i.e. the gray values of g from the locations of x applied to the locations x_0. This intermediate image $\tilde{g}$ naturally approaches f when converged, therefore, assuming a certain closeness to the solution, the following can be written,

$$\frac{\partial}{\partial x} \Big[g\big(x(x_0, \underline{\lambda}^{\mathsf{it}})\big) \Big] \approx \frac{\partial}{\partial x_0} \Big[f(x_0) \Big] \left(\frac{\partial}{\partial x_0} \Big[x(x_0, \underline{\lambda}^{\mathsf{it}}) \Big] \right)^{-1} = \frac{\partial}{\partial x_0} \Big[f(x_0) \Big] \mathbf{F}^{-T}, \tag{B.22}$$

where $\mathbf{F}$ is the deformation gradient tensor, which for this 1D case is a scalar. Additionally, if the large deformations component is neglected we arrive at,

$$\frac{\partial}{\partial x}\Big[g\big(x(x_0,\underline{\lambda}^{\mathsf{it}})\big)\Big] \approx \frac{\partial}{\partial x_0}\Big[f(x_0)\Big] \equiv \nabla_0 f. \tag{B.23}$$

Combining the results into (B.15) gives the familiar form,

$$\Gamma_j^{\mathsf{it}} = -2\int_{\Omega_0}\Big[\nabla_0 f\,\varphi_j\,\Psi\Big]\,\mathrm{d}x_0 = -b_j. \tag{B.24}$$

The correlation matrix

To find the tangent matrix, (B.24) needs to be derived once more towards the degrees of freedom,

$$\frac{\partial \Gamma_j^{\mathsf{it}}}{\partial \lambda_i^{\mathsf{it}}} = -2\int_{\Omega_0}\frac{\partial \Psi}{\partial \lambda_i^{\mathsf{it}}}\nabla_0 f\,\varphi_j\,\mathrm{d}x_0. \tag{B.25}$$

The solution for $\partial\Psi/\partial\lambda_j^{\mathsf{it}}$ is already discussed in the previous section, arriving at the following form for the tangent matrix,

$$\frac{\partial \Gamma_j^{\mathsf{it}}}{\partial \lambda_i^{\mathsf{it}}} = 2\int_{\Omega_0}\Big[\nabla_0 f\varphi_i\nabla_0 f\varphi_j\Big]\,\mathrm{d}x_0 = M_{ij}. \tag{B.26}$$

Actually, an extra term appears when using an image gradient which depends on λ, e.g. $\nabla_0\tilde{g}$. Moreover, yet another term appears when the basis functions are not linearly independent [24, 27]. Usually these extra terms can be neglected, even in these cases, because they will not influence the result, only the convergence rate, for more details, see chapter 6.

Final form

Finally, substituting (B.24) and (B.26) in (B.13), results in the linearized iterative solution scheme

$$\forall_j \quad \sum_{i=1}^{m} M_{ij} \quad \delta\lambda_i = \quad b_j \tag{B.27}$$

$$\forall_j \quad \sum_{i=1}^{m}\int_{\Omega_0}\Big[\nabla_0 f\,\varphi_i\,\nabla_0 f\,\varphi_j\Big]\,\mathrm{d}x_0\,\delta\lambda_i = \int_{\Omega_0}\Big[\nabla_0 f\,\varphi_j\,\big(f-\tilde{g}\big)\Big]\,\mathrm{d}x_0, \tag{B.28}$$

where,

$$\tilde{g} = g\big(x_0 + u^*(x_0,\underline{\lambda}^{\mathsf{it}})\big), \tag{B.29}$$

which represents the gray values of the $\mathrm{it}^{\mathrm{th}}$ approximation at the locations $x(x_0, \underline{\lambda}^{\mathrm{it}})$ in image g, which if converged are equal to the gray values at $f(x_0)$.

From (B.28) it becomes obvious that there are only three important quantities in DIC, the residual $f-\tilde{g}$, the basis functions φ_j and the image gradient. In other words, because $\underline{b}$ is minimized, the projection of the residual against the product of the basis functions and the image gradient is minimized. This means that anywhere where either the basis functions or the image gradient is zero, there no driving force on the degrees of freedom. Simpler put, only displacements can be found where there is an image gradient. For example, the y displacement in a barcode type pattern is impossible to detect.

The used image gradient in (B.28) is no longer the one which naturally follows from the linearization process, but it can be considered to be close to the "correct" image gradient, for most typical DIC cases. Not using the "correct" image gradient results in a tangent operator which is no longer the Newton-Raphson tangent, and will not have the quadratic convergence behavior. It should be noted that using the "correct" image gradient is possible, and the additional cost per iteration may easily return itself by the faster convergence rate. The "correct" (large deformation) form of the linearized iterative solution is (more on this in chapter 6),

$$\forall_j \quad \sum_{i=1}^{m} \int_{\Omega_0} \left[\mathbf{F}^{-T} \nabla_0 \tilde{g}\, \varphi_i\, \mathbf{F}^{-T} \nabla_0 \tilde{g}\, \varphi_j \right] \mathrm{d}x_0\, \delta\lambda_i = \int_{\Omega_0} \left[\mathbf{F}^{-T} \nabla_0 \tilde{g}\, \varphi_j \left(f - \tilde{g} \right) \right] \mathrm{d}x_0. \tag{B.30}$$

1D Discrete DIC

The above section deals with formulating a system of equations, nevertheless, at this point it is still not straightforward to implement this. Most of the implementation difficulties arise from the discrete nature of digital images, i.e. the pixels. The concept of brightness conservation considers the brightness (i.e. gray value) of material points, where in image f the vector $\vec{x}_0$ points to the same material point as the vector $\vec{x}$ does in image g. However, the image g is imaged with the same camera, which typically is stationary. In other words the pixels in image g capture the same spatial location as in f. Consequently, the respective material points of $f(x_0)$ are represented at different pixels in $g(x_0)$, more precisely, at non-integer pixel locations.

In the current section, the images will be treated as $(n \times 1)$ matrices containing the brightness values of the pixels. Instead of writing the matrix, a subscript p is added to indicate that the operation should be repeated for all pixels. Again only considering the 1D case,

$$f(x_0) = f_p, \qquad p = 1..n \tag{B.31}$$

$$g(x_0) = g_p, \tag{B.32}$$

The displacements of each pixel can also be written in matrix form,

$$u(x_0) = u_p. \tag{B.33}$$

Again the displacement field is approximated with degrees of freedom like in (B.6),

$$u_p \approx u_p^* = \sum_{i=1}^{m} \varphi_{pi} \lambda_i^{\mathsf{it}}, \tag{B.34}$$

where φ is a $(n \times m)$ matrix with one column per basis function and one row per pixel. Notice that calculating u_p^* is just the matrix φ right-multiplied with the column λ.

Introducing a matrix L of the same size as φ,

$$L_{pi} = [\nabla_0 f]_p \, \varphi_{pi}, \tag{B.35}$$

allows for compact writing of the pixel version of (B.28), using a numerical integration scheme that is simply the summation over all pixels,

$$M_{ij} = \sum_{p=1}^{n} \Big[L_{ip} L_{pj} \, \Delta_x \Big], \tag{B.36}$$

$$b_j = \sum_{p=1}^{n} \Big[L_{jp} \, \Delta_x \Big] \big(f_p - \tilde{g}_p \big), \tag{B.37}$$

$$\forall_j \quad \sum_{i=1}^{m} M_{ij} \delta\lambda_i = b_j, \tag{B.38}$$

where the contribution of Δ_x (the pixel size) is equal on each side of the equation and can be canceled. The correlation matrix and right hand member can be easily computed using the matrix multiplications, $M = L^T L$ and $b = L^T (f - \tilde{g})$, respectively. With an adequate pattern for the chosen basis functions, M is a non-singular symmetric matrix of size $(m \times m)$ and is easily inverted to find the update in the degrees of freedom $\delta\lambda_i$. In Matlab, the backslash operator is typically applied to solve for the degrees of freedom, e.g:

```
dlambda = M\b;
```

At this point $\tilde{g}$ is not very well explained. It is obvious that in order to compare the gray values of f and $\tilde{g}$ it is required that they are compared in the same locations. Since,

$$\tilde{g}_p = g\big(x_0 + u^*(x_0, \lambda^{\mathsf{it}})\big), \tag{B.39}$$

is formed by the gray values at non-integer pixel locations $x_0 + u^*$, see Fig. B.1, the image g is interpolated on the pixel locations x using a non-linear sub-pixel interpolation scheme to obtain the intermediate image $\tilde{g}$. The interpolation introduces some error, which is one of the sources causing the residual field not to go to zero. However, the interpolation also gives the DIC method sub-pixel displacement accuracy.

Typically, an interpolation scheme consists of fitting the discrete data points with some general function (typically cubic splines), which then can be evaluated at the desired locations.

For example, when using Matlab, for the 1D case, this would be,

```
gt = interp1(x0,g,x0+u,'spline');
```

or in 2D,

```
gt = interp2(x0,y0,g,x0+u,y0+v,'spline');
```

Choice of Image Gradients

In most DIC algorithms the image gradient $\nabla_0 f$ appears in the final form of the iterative solution scheme. While using this gradient leads to the computationally cheapest iteration, it generally uses the most iterations to find the solution. More importantly, this solution relies the most on a certain closeness to the solution, i.e. it has the least initial guess robustness.

The reason why this method gives the cheapest iteration is because the correlation matrix M is constant for all iterations, and only needs to be computed once. Actually, the L matrix (B.35) is constant, and therefore M is also constant. All other discussed options do not have this advantage, and therefore, have higher cost per iteration.

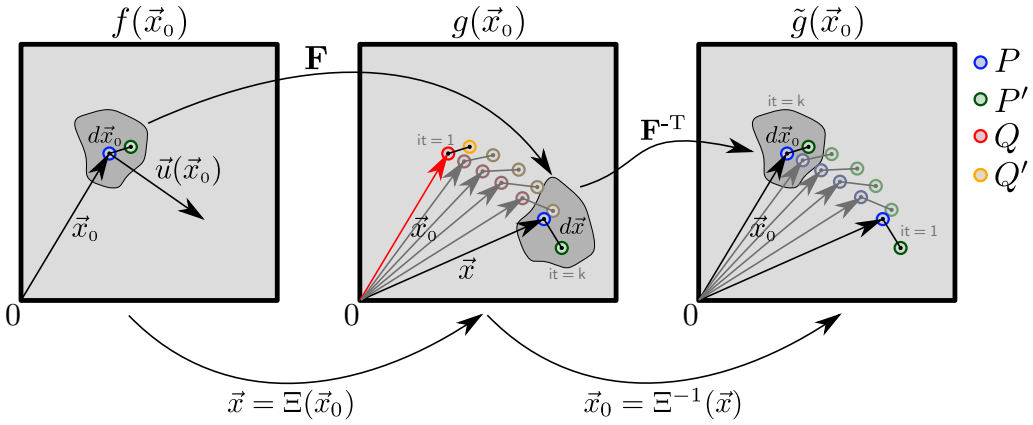

Figure B.3: The three "images" explained for four material points P, P', Q and Q'. Where $f(\vec{x}_0)$ is the reference image, $g(\vec{x}_0)$ the deformed image, and $\tilde{g}(\vec{x}_0)$ the intermediate image. $\partial g/\partial x$ is the consistent gradient (Eq. B.20) which is equal to $\mathbf{F}^{-T}\partial\tilde{g}/\partial x_0$ (Eq. B.21) and is approximated by $\partial f/\partial x_0$ (Eq. B.23). Note that, all images are defined in the pixel coordinates, i.e. $\vec{x}_0$, which form an "Eulerian" grid. The gray values in the deformed coordinates $\vec{x}$ need to be interpolated.

Figure B.3 shows the three images available in the DIC algorithm. Instead of taking the gradient of f, taking the gradient of $\tilde{g}$ will give (slightly) better convergence properties in the initial iterations, until at some point f and $\tilde{g}$ are so alike that there is no difference. Because $\tilde{g}$ changes at each iteration (since $u^*(\underline{\lambda}^{\text{it}}, x_0)$ changes), the matrices L and M need to be updated at each iteration.

The initial guess robustness can be seen as the quality of a certain gradient to point

in the correct direction, even when far from the solution. Patterns tend to be highly non-linear, and therefore, the solution space in which the gradient points to the correct direction is typically small. For that reason, the mean of both image gradients is often used, i.e. $(\nabla_0 f + \nabla_0 \tilde{g})/2$. Intuitively, $\nabla_0 f$ can be interpreted as the image gradient in the solution, which is very stable (constant), but often unrelated to the current solution, and $\nabla_0 \tilde{g}$ is the gradient in the current solution pointing to the nearest minimum. Using this mean image gradient can have a large impact on the initial guess robustness, but, close to the solution $\tilde{g}$ approximates f resulting in the same convergence rate as using only one of the two.

Moreover, all above image gradients assume small deformations, i.e. $\partial x_0/\partial x = 1$. Calculating this term is possible using the current displacement field,

$$\left(\frac{\partial}{\partial x_0}\Big[x(x_0)\Big]\right)^{-1} = \left(\frac{\partial}{\partial x_0}\Big[x_0 + u^*(x_0, \underline{\lambda})\Big]\right)^{-1} = \left(1 + \sum_{i=1}^{m} \lambda_i \frac{\partial \varphi_i}{\partial x_0}\right)^{-1}, \tag{B.40}$$

which involves only the gradient of the displacement field (or basis functions), inverting this for 1D is relatively cheap. For 2D (or 3D) this would be

$$\Big(\vec{\nabla}_0\big[\vec{x}(\vec{x}_0)\big]\Big)^{-1} = \Big(\mathbf{F}^T(\vec{x}_0)\Big)^{-1} = \mathbf{F}^{-T}(\vec{x}_0), \tag{B.41}$$

which would mean that the deformation gradient tensor $\mathbf{F}$ needs to be inverted at each pixel location (for each iteration) which can be costly. Nevertheless, using the large deformation formulation can significantly improve the convergence rate, especially when close to the solution (Fig. B.4).

Instead of using the gradients of f or $\tilde{g}$ and applying the deformation gradient tensor to get the correct large displacement image gradient, there is another possibility. The correct image gradient which follows from the Newton-Raphson procedure is $\partial g/\partial x$, see Eq. B.20, evaluated at each location x. However, the coordinate frame where the image gradient is calculated is irrelevant, only the evaluation location matters,

$$\frac{\partial}{\partial x}\Big[g\big(x\big)\Big]\bigg|_x = \frac{\partial}{\partial x_0}\Big[g\big(x_0\big)\Big]\bigg|_x \tag{B.42}$$

where, the $|_x$ indicates where the functions should be evaluated. From an implementation point of view, this would mean calculating the image gradient of g (not $\tilde{g}$), which again is constant for all iterations, and evaluating (interpolating) this field at the locations x which change during the iterative procedure. This interpolation step is numerically equivalent to the interpolation of `gt` as shown in section B, for example when using Matlab,

```
imgrad = interp1(x0,gradg,x0+u,'spline');
```

or in 2D,

```
imgrad = interp2(x0,y0,gradg,x0+u,y0+v,'spline');
```

This is theoretically equivalent to the large deformation formulation above, and yields the correct quadratic convergence behavior close to the solution. However, it does not

require a pixel-wise inversion of the deformation gradient tensor, and is therefore cheaper. Typical cases where the large deformation formulation will excel are cases where the basis functions change for each iteration (e.g. Integrated DIC). For those cases an iteration is already expensive, and the added cost of computing the consistent image gradient is probably insignificant, while reducing the number of iterations is beneficial.

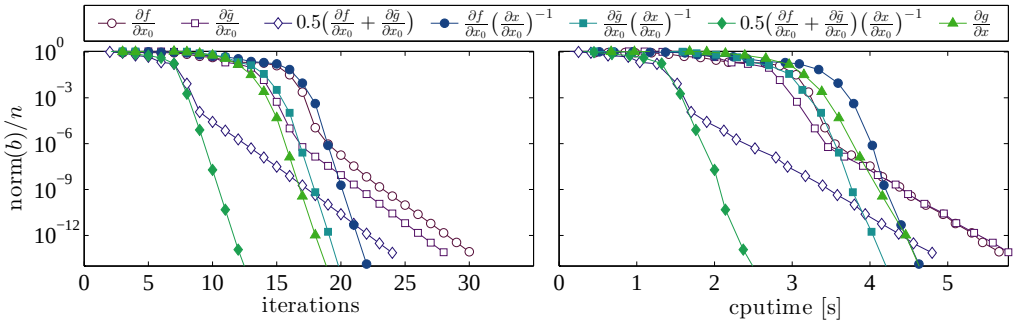

Figure B.4: The convergence rate for seven different image gradients, obtained from a 1D DIC virtual experiment with a non-linear displacement field using polynomial basis functions. All curves show two regimes, (*i*) a slow converging regime far from the solution where the combined gradients (diamond markers) perform the best, and (*ii*) a fast converging regime close to the solution where all large deformation implementations (closed markers) perform the best. These results are typical but not general, because the critical iteration to go from one regime to the next and the computational cost, depend on the pattern, the basis functions and the initial guess.

Virtual or Synthetic images

New DIC methods need to be tested to prove their working principle and bench-marked to find their accuracy. Using simulated data for this is an obvious choice. Not only is the *input* displacement field exactly known, but this method also allows for injecting measurement noise in a controlled fashion. Nevertheless, if the virtual experiment is flawed, it is impossible to analyze the accuracy of the DIC method.

The question is how to create the synthetic image $g(x_0)$ from an image $f(x_0)$ and a known *input* displacement field $u(x_0)$. Consider again the brightness conservation,

$$f(x_0) = g(x) = g\big(x_0 + u(x_0)\big), \tag{B.43}$$

realizing that x is just a function of x_0, we can write,

$$f(x_0) = g\big(x(x_0)\big), \tag{B.44}$$

applying the inverse function x^{-1} on both sides,

$$f\big(x^{-1}(x_0)\big) = g(x_0). \tag{B.45}$$

To find the solution for $x^{-1}(x_0)$ lets assume

$$x^{-1}(x_0) = \gamma \tag{B.46}$$

where γ is an unknown position. Again applying the inverse function on both sides gives,

$$x_0 = x(\gamma) = \gamma + u(\gamma) \tag{B.47}$$

the solution is then to find γ such that

$$\gamma \in \mathbb{R} \mid x_0 - \big(\gamma + u(\gamma)\big) = 0 \tag{B.48}$$

this is a root finding problem which can be solved in the same way as already discussed, using (B.12-B.13). The problem is that this requires a Newton-Raphson procedure for each location γ, which is computationally inefficient. Moreover, the Newton-Raphson procedure is far more accurate than the error that will subsequently be introduced by the necessary interpolation step to obtain $\tilde{g}$.

For example, when using Matlab, γ can be applied by interpolating f on the locations of γ,

```
g = interp1(x0,f,gamma,'spline');
```

There is an equivalent way of doing the above (calculating and applying γ), which is more efficient. In the case of a continuous pattern, the two methods are equivalent, but for discrete images, there is an insignificant accuracy difference. It is best explained considering a real experiment, where an image is taken at the reference state $f(x_0)$, then the deformation is applied, i.e. the material points are moved, after which the second image is taken $g(x_0)$. The procedure can be replicated in the virtual world by moving the gray values of f from the old locations x_0 to the new locations $x = x_0 + u(x_0)$. The newly obtained field with gray values is not regular (i.e. the pixels are not neatly in a grid) therefore the field needs to be interpolated on the original coordinates (and field of view).

For example, when using Matlab, for the 1D case,

```
g = interp1(x0+u,f,x0,'spline');
```

or in 2D,

```
g = griddata(x0+u,y0+v,f,x0,y0,'cubic');
```

notice that for the 2D case, not the `interp2` function is used, because it cannot deal with non-regular fields. Since Matlab 2010a, besides `griddata`, also `TriScatteredInterp` can be used, which should be faster, however, the `griddata` function tends to yield more accurate results.

Height Correlation

In the previous cases, the pixel intensities of the image had no extra physical meaning besides a material marker to allow for correlation through brightness conservation. However, sometimes the measured quantity captured by the full-field imaging technique has

a physical quantity attached, for instance, temperature, height topography, etc. [48, 94]. This measurement quantity is usually subject to change which compromises the principle of brightness (or better, intensity) conservation. Moreover, the intent is not only to correlate regardless of a loss of intensity conservation, but also to measure/register the change of "intensity" which can be height, temperature, etc. Throughout the next section only height topography is discussed, however, the methodology is the same for other measured quantities.

1D Height Correlation

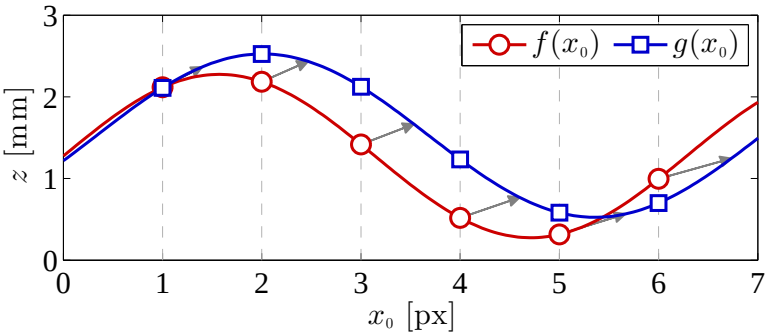

Figure B.5: Very simple 1D reference and deformed height topography.

Again the method is best explained in 1D, consider figure B.5 as an example. However, the term 1D does not exactly apply since two components of displacement field are measured in this technique. Because the images are still only 1D, the method is also not fully 2D, for that reason, the term "quasi 2D" is sometimes used.

Dealing with the *out-of-plane* displacement involves relaxing the brightness conservation as,

$$f(x_0) + w(x_0) - g\big(x_0 + u(x_0)\big) = \Psi(x_0) \approx 0, \tag{B.49}$$

where $w(x_0)$ is the out-of-plane component of the displacement. The displacement field now is a vector field,

$$\vec{u}(x_0) = u(x_0)\vec{e}_x + w(x_0)\vec{e}_z. \tag{B.50}$$

Similar as in (B.5) a least squares approach on the residual is formulated,

$$\vec{u}(x_0) = \underset{\vec{u}(x_0)}{\text{Argmin}}(\Phi) = \underset{\vec{u}(x_0)}{\text{Argmin}} \int_{\Omega_0} \Big[f(x_0) - g\big(x_0 + u(x_0)\big) + w(x_0)\Big]^2 \, \mathrm{d}x_0. \tag{B.51}$$

Analogous to (B.6) the displacement field is approximated with a finite set of degrees of freedom λ_i, however, this time the displacement field is a vector field,

$$\vec{u}(x_0) \approx \vec{u}^*(x_0, \underline{\lambda}) = \sum_{\alpha=1}^{2} \sum_{i=1}^{m} \lambda_i^\alpha \varphi_i^\alpha(x_0) \vec{e}_\alpha, \tag{B.52}$$

$$= \sum_{i=1}^{m} \sum_{\alpha=1}^{2} \lambda_i^\alpha \varphi_i^\alpha(x_0) \vec{e}_\alpha, \tag{B.53}$$

where the dimensional index α is deliberately written as a superscript, to separate it from the "degree of freedom" index. Each basis function can be applied to each vector component, which results in an additional summation over α. Mathematically, the order of the summation is irrelevant, it only influences the order in which the basis functions (and degrees of freedom) appear in the corresponding matrices. Consequently, a new index q is defined which loops over all basis functions, internally accounting for each direction,

$$\vec{u}(x_0) \approx \vec{u}^*(x_0, \underline{\lambda}) = \sum_{q=1}^{2m} \lambda_q \vec{\varphi}_q(x_0), \tag{B.54}$$

where the directional component $\vec{e}_\alpha$ is combined in the basis function, causing it to become a vector field. This last step is only a convention. Applying the result to (B.51) results in the following,

$$\underset{\lambda_q}{\operatorname{Argmin}}(\Phi) = \underset{\underline{\lambda}}{\operatorname{Argmin}} \int_{\Omega_0} \Psi^2 \, \mathrm{d}x_0, \tag{B.55}$$

$$\Psi = f(x_0) - g\big(x_0 + \vec{u}^*(x_0, \underline{\lambda}) \cdot \vec{e}_x\big) + \vec{u}^*(x_0, \underline{\lambda}) \cdot \vec{e}_z, \tag{B.56}$$

such that, $u(x_0)$ and $w(x_0)$ are substituted with the part of $\vec{u}^*(x_0, \underline{\lambda})$ working in the corresponding directions $\vec{e}_x$ and $\vec{e}_z$.

Again, in the same way as (B.10), finding the minimum of Φ with respect to the degrees of freedom, is the same is finding the root of its derivative towards these degrees of freedom,

$$\forall_k \quad \Gamma_k = \frac{\partial \Phi}{\partial \lambda_k} = 0 \tag{B.57}$$

This is a non-linear problem, solved with a Newton-Raphson iterative procedure,

$$\lambda_q^{\mathsf{it}+1} = \lambda_q^{\mathsf{it}} + \delta\lambda_q. \tag{B.58}$$

Which allows for the linearization of (B.57),

$$\forall_k \quad \sum_{q=1}^{2m} \frac{\partial \Gamma_k^{\mathsf{it}}}{\partial \lambda_q^{\mathsf{it}}} \delta\lambda_q = -\Gamma_k^{\mathsf{it}}, \tag{B.59}$$

in exactly the same way as in (B.13).

The interesting part of this digital height correlation is how this all works out when filling in the specifics. Starting with the right hand side of (B.59),

$$\Gamma_k^{\mathsf{it}} = \frac{\partial \Phi}{\partial \lambda_k^{\mathsf{it}}} = \int_{\Omega_0} 2\Psi \frac{\partial \Psi}{\partial \lambda_k^{\mathsf{it}}} \, \mathrm{d}x_0 = 0, \tag{B.60}$$

$$\frac{\partial \Psi}{\partial \lambda_k^{\mathsf{it}}} = -\frac{\partial}{\partial \lambda_k^{\mathsf{it}}} \Big[g\big(x(x_0, \underline{\lambda}^{\mathsf{it}})\big) \Big] + \frac{\partial}{\partial \lambda_k^{\mathsf{it}}} \Big[\vec{u}^*(x_0, \underline{\lambda}^{\mathsf{it}}) \cdot \vec{e}_z \Big] \tag{B.61}$$

each term is elaborated further, in the same way as in section B.

$$\frac{\partial}{\partial \lambda_k^{\mathsf{it}}} \Big[g\big(x(x_0, \underline{\lambda}^{\mathsf{it}})\big) \Big] = \frac{\partial}{\partial x} \Big[g\big(x(x_0, \underline{\lambda}^{\mathsf{it}})\big) \Big] \frac{\partial}{\partial \lambda_k^{\mathsf{it}}} \Big[x(x_0, \underline{\lambda}^{\mathsf{it}}) \Big], \tag{B.62}$$

$$= \frac{\partial}{\partial x} \Big[g\big(x(x_0, \underline{\lambda}^{\mathsf{it}})\big) \Big] \vec{\varphi}_k \cdot \vec{e}_x \tag{B.63}$$

$$\approx \frac{\partial f}{\partial x_0} \, \vec{\varphi}_k \cdot \vec{e}_x, \tag{B.64}$$

$$\frac{\partial}{\partial \lambda_k^{\mathsf{it}}} \Big[\vec{u}^*(x_0, \underline{\lambda}^{\mathsf{it}}) \cdot \vec{e}_z \Big] = \vec{\varphi}_k \cdot \vec{e}_z, \tag{B.65}$$

where again both the small deformations and the closeness of solution assumptions are used to write (B.64), see section B and B for more details. At this point a vector $\vec{G}$ is introduced for more compact writing,

$$\vec{G} = \frac{\partial f}{\partial x_0} \vec{e}_x - \vec{e}_z, \tag{B.66}$$

which results in the final form of the right hand member,

$$\Gamma_k^{\mathsf{it}} = -2 \int_{\Omega_0} \Big[\vec{G} \cdot \vec{\varphi}_k \, \Psi \Big] \, \mathrm{d}x_0 = -b_k. \tag{B.67}$$

The correlation matrix found on the left hand side of (B.59) is trivially obtained by reusing the above steps to derive (B.67) once more towards λ,

$$\frac{\partial \Gamma_k^{\mathsf{it}}}{\partial \lambda_q^{\mathsf{it}}} = 2 \int_{\Omega_0} \Big[\vec{G} \cdot \vec{\varphi}_k \, \vec{G} \cdot \vec{\varphi}_q \Big] \, \mathrm{d}x_0 = M_{qk}. \tag{B.68}$$

Finally, substituting (B.67) and (B.68) in (B.59), results in the linearized iterative solution scheme

$$\forall_k \quad \sum_{q=1}^{2m} \int_{\Omega_0} \Big[\vec{G} \cdot \vec{\varphi}_k \, \vec{G} \cdot \vec{\varphi}_q \Big] \, \mathrm{d}x_0 \, \delta\lambda_k = \int_{\Omega_0} \Big[\vec{G} \cdot \vec{\varphi}_k \, \big(f - \tilde{g} \big) \Big] \, \mathrm{d}x_0, \tag{B.69}$$

where,

$$\tilde{g} = g\big(x_0 + u^*(x_0, \underline{\lambda}^{\mathsf{it}}) \cdot \vec{e}_x\big) - \vec{u}^*(x_0, \underline{\lambda}^{\mathsf{it}}) \cdot \vec{e}_z, \tag{B.70}$$

which represents the gray values of the $\mathsf{it}^{\mathrm{th}}$ approximation at the locations $x(x_0, \underline{\lambda}^{\mathsf{it}})$ in image g, corrected with the *out-of-plane* displacements.

2D Height Correlation

At this point all the ingredients are there to formulate the solution to the 2D DHC problem (also known as Quasi-3D DIC). Solving the 2D global DIC problem is similar but easier, and is therefore not discussed. Again starting from the relaxed version of topography conservation,

$$f(\vec{x}_0) - g\big(\vec{x}_0 + u(\vec{x}_0)\vec{e}_x + v(\vec{x}_0)\vec{e}_y\big) + w(\vec{x}_0) = \Psi(\vec{x}_0) \approx 0, \tag{B.71}$$

where,

$$\vec{x}_0 = x_0\vec{e}_x + y_0\vec{e}_y, \tag{B.72}$$

is a 2D vector field and,

$$\vec{u}(\vec{x_0}) = u(\vec{x}_0)\vec{e}_x + v(\vec{x}_0)\vec{e}_y + w(\vec{x}_0)\vec{e}_z, \tag{B.73}$$

a 3D displacement vector field.

Similarly as before, the displacement field is approximated with a finite set of degrees of freedom λ_i,

$$\vec{u}(\vec{x}_0) \approx \vec{u}^*(\vec{x}_0, \underline{\lambda}) = \sum_{\alpha=1}^{3}\sum_{i=1}^{m} \lambda_i^\alpha \varphi_i^\alpha(\vec{x}_0)\vec{e}_\alpha, \tag{B.74}$$

$$\vec{u}^*(\vec{x}_0, \underline{\lambda}) = \sum_{q=1}^{3m} \lambda_q \vec{\varphi}_q(\vec{x}_0), \tag{B.75}$$

where the order in which each basis function is sorted regarding the vector components is free to choose. More precisely, not every basis functions is required in all directions, or basis functions can be formulated in more directions while having only a single (coupled) degree of freedom (e.g. to describe rotation). However, this is outside of the scope of this report. For now, all basis functions are assumed to exist exactly once for each dimension.

Formulating the least squares minimization potential on the residual field gives,

$$\underset{\lambda_q}{\text{Argmin}}(\Phi) = \underset{\lambda_q}{\text{Argmin}} \int_{\Omega_0} \Psi^2 \,\mathrm{d}A_0 \qquad\qquad \mathrm{d}A_0 = \,\mathrm{d}x_0\,\mathrm{d}y_0 \tag{B.76}$$

with,

$$\Psi = f(\vec{x}_0) - g\big(\vec{x}_0 + u^*(\vec{x}_0, \underline{\lambda})\vec{e}_x + v^*(\vec{x}_0, \underline{\lambda})\vec{e}_y\big) + w^*(\vec{x}_0, \underline{\lambda}), \tag{B.77}$$

with,

$$u^*(\vec{x}_0, \underline{\lambda}) = \vec{u}^*(\vec{x}_0, \underline{\lambda}) \cdot \vec{e}_x, \tag{B.78}$$

$$v^*(\vec{x}_0, \underline{\lambda}) = \vec{u}^*(\vec{x}_0, \underline{\lambda}) \cdot \vec{e}_y, \tag{B.79}$$

$$w^*(\vec{x}_0, \underline{\lambda}) = \vec{u}^*(\vec{x}_0, \underline{\lambda}) \cdot \vec{e}_z. \tag{B.80}$$

Minimizing (B.76) is done by finding the root of the derivative towards the degrees of freedom,

$$\forall_k \quad \Gamma_k = \frac{\partial \Phi}{\partial \lambda_k} = 0. \tag{B.81}$$

To solve this non-linear problem, again the iterative Newton-Raphson procedure is applied,

$$\forall_k \quad \sum_{q=1}^{3m} \frac{\partial \Gamma_k^{\mathsf{it}}}{\partial \lambda_q^{\mathsf{it}}} \delta\lambda_q = -\Gamma_k^{\mathsf{it}}, \qquad\qquad \lambda_q^{\mathsf{it}+1} = \lambda_q^{\mathsf{it}} + \delta\lambda_q. \tag{B.82}$$

In the same way as done for the 1D DHC case, vector $\vec{G}$ is defined,

$$\vec{G} = \frac{\partial f}{\partial x_0}\vec{e}_x + \frac{\partial f}{\partial y_0}\vec{e}_y - \vec{e}_z, \tag{B.83}$$

similar to the simlpe 1D DIC case (B.13) and to 1D DHC case in (B.60-B.67) the 2D DHC right hand member is obtained,

$$\Gamma_k^{\mathsf{it}} = -2 \int_{\Omega_0} \left[\vec{G} \cdot \vec{\varphi}_k \, \Psi \right] \mathrm{d}A_0 = -b_k, \tag{B.84}$$

which is not so much different than the one found in (B.67). Following this train of thought, the correlation matrix is easily obtained,

$$\frac{\partial \Gamma_k^{\mathsf{it}}}{\partial \lambda_q^{\mathsf{it}}} = 2 \int_{\Omega_0} \left[\vec{G} \cdot \vec{\varphi}_k \, \vec{G} \cdot \vec{\varphi}_q \right] \mathrm{d}A_0 = M_{qk}, \tag{B.85}$$

which is also very similar to (B.68). Finally, substituting (B.84) and (B.85) in (B.82), results in the 2D DHC linearized iterative solution scheme,

$$\forall_k \quad \sum_{q=1}^{3m} \int_{\Omega_0} \left[\vec{G} \cdot \vec{\varphi}_k \, \vec{G} \cdot \vec{\varphi}_q \right] \mathrm{d}A_0 \, \delta\lambda_q = \int_{\Omega_0} \left[\vec{G} \cdot \vec{\varphi}_k \left(f - \tilde{g} \right) \right] \mathrm{d}A_0, \tag{B.86}$$

where,

$$\tilde{g} = g\big(\vec{x}_0 + u^*(\vec{x}_0, \underline{\lambda})\vec{e}_x + v^*(\vec{x}_0, \underline{\lambda})\vec{e}_y\big) - w^*(\vec{x}_0, \underline{\lambda}), \tag{B.87}$$

which represents the gray values of the $\mathsf{it}^{\mathrm{th}}$ approximation at the locations $\vec{x}(\vec{x}_0, \underline{\lambda}^{\mathsf{it}})$ in image g, corrected with the *out-of-plane* displacements $w^*(\vec{x}_0, \underline{\lambda})$.

Interestingly, the field $w^*(\vec{x}_0, \underline{\lambda})$, is not connected with the image gradient, and is therefore independent of the choice of image gradient (discussed in section B). As a result, it also does not require interpolation, which makes this field more accurate and more robust, with respect to the in-plane fields.

2D Discrete DHC

The implementation of the previous section, considering the discrete nature of the images is actually straightforward and very akin the previously discussed 1D discrete section. Identical to that section, the images are stored in matrices. However, perhaps not in the most trivial sense. The images are stored as $(n \times 1)$ matrices containing the height values of the pixels, where n represents the total number of pixels (i.e. the number of pixel rows times the number of pixel columns).

$$f(\vec{x}_0) = f_p, \qquad p = 1..n \tag{B.88}$$

$$g(\vec{x}_0) = g_p. \tag{B.89}$$

The displacements of each pixel can also be written in matrix form,

$$u(\vec{x}_0) = u_p, \quad v(\vec{x}_0) = v_p, \quad w(\vec{x}_0) = w_p, \tag{B.90}$$

split into separate $(n \times 1)$ matrices per component.

Again the displacement field is approximated with degrees of freedom,

$$u_p \approx u_p^* = \sum_{q=1}^{3m} \vec{\varphi}_{pq} \cdot \vec{e}_x \lambda_q^{\mathsf{it}}, \tag{B.91}$$

$$v_p \approx v_p^* = \sum_{q=1}^{3m} \vec{\varphi}_{pq} \cdot \vec{e}_y \lambda_q^{\mathsf{it}}, \tag{B.92}$$

$$w_p \approx w_p^* = \sum_{q=1}^{3m} \vec{\varphi}_{pq} \cdot \vec{e}_z \lambda_q^{\mathsf{it}}, \tag{B.93}$$

where φ is a $(n \times 3m)$ matrix with one column per basis function and one row per pixel. Notice how only the shape functions related to a certain component of the displacement are selected with the inner product. This is only a writing style, as in a numerical implementation calculating one component of the displacement field (e.g. u_p) would involve selecting the correct columns of the φ matrix, and (right) multiplying this reduced matrix with a corresponding reduced version of the column $\delta\underline{\lambda}$. It is possible to write φ as a three dimensional matrix, and do a direct multiplication, however this is a matter of taste.

Introducing a matrix L of the same size as φ,

$$L_{pq} = \vec{G}_p \cdot \vec{\varphi}_{pq}, \tag{B.94}$$

allows for compact writing of the pixel version of (B.86), using a simple summation over the pixels as a numerical integration scheme,

$$M_{kq} = \sum_{p=1}^{n} \Big[L_{qp} L_{pk} \Delta_x \Delta_y \Big] \tag{B.95}$$

$$b_k = \sum_{p=1}^{n} \Big[L_{kp} \Delta_x \Delta_y \Big] \big(f_p - \tilde{g}_p \big), \tag{B.96}$$

where the pixel sizes Δ_x and Δ_y can be canceled. The calculation of the correlation matrix and the right hand member can be implemented as the matrix multiplications, $M = L^t L$, and $b = L^t(f - \tilde{g})$, respectively. The way $\tilde{g}$ is calculated is explained in detail in section B. However, for the DHC case, the *out-of-plane* displacement also needs to be applied to $\tilde{g}$.

For example, when using Matlab, this would be,

```
gt = interp2(x0,y0,g,x0+u,y0+v,'spline') - w;
```

The φ and L matrices, having the size of $(n \times 3m)$, have the potential to cause memory problems. If using double precision floating point numbers (64 bit), and a 1 Megapixel image, then L requires 8 Megabyte continuous memory space, per degree of freedom. It is easy to see that, for large images and many degrees of freedom, this can become a problem. The solution is to assemble b and M part by part, which is the obvious choice when using a FEM type discretization of the displacement field (since M and L will be sparse), but is also possible for other basis function families.

Height Correlation Considerations

The relaxation of the brightness conservation introduces a concern. The residual field, based on the pattern, is now reduced with the *out-of-plane* field, e.g. $w(\vec{x}_0)$. The pattern is used for the in-plane displacement registration, and if the out-of-plane displacement compromises the pattern, the registration is also compromised. In extreme cases, the additional freedom will even introduce a singularity in the solution, by completely "removing" the residual (for a given basis function). In order to prevent this, a separation in length scales is required between the length over which the pattern changes and the length over which the displacement fields can change,

$$L_w \gg L_{\mathsf{pat}}. \tag{B.97}$$

This way, there will always remain some pattern to drive the solution in the *in-plane* directions.

The accuracy of the *out-of-plane* field will most likely be different from the *in-plane* accuracy. The reasons for this are,

1. The signal to noise ratio is different between the *out-of-plane* field and the *in-plane* field. For example, unsigned 8-bit integers for the *out-of-plane* quantities and pixels *in-plane*. Not to speak of the different physics underlying the way these quantities are captured in the sensor.
2. The data interpolation is different, e.g. the *out-of-plane* quantities are typically just converted to floating point numbers, while the pixels are interpolated using cubic splines.
3. Looking at how $\vec{G}(x_0)$ appears in the correlation matrix, it is clear that the *in-plane* degrees of freedom require the image gradient, while the *out-of-plane* degrees of freedom do not. Actually, the *out-of-plane* degrees of freedom do not require linearization, and can typically be directly solved. Additionally, images tend to have noise, which does not behave well when attempting to calculate gradients.

Correlation Length and Image Coarsening

The solution schemes of the previous sections involve an iterative Newton-Raphson (NR) procedure, which successively linearizes the problem to find a solution. It is known that NR procedures converge well when they are close to the solution. However, such procedures can also converge to a local minimum. In a NR procedure, the update, or next guess, is determined using the image gradient (and the basis functions). Since the image is discrete, a numerical forward-backward (FB) scheme is typically deployed to find the image gradient. Such a FB scheme obtains its information from a width of three pixels, resulting in an image gradient which is very sensitive to short range changes. The result is a sensitive DIC algorithm, also for local minima, which puts a high requirement on the initial guess. Instead of the normal FB scheme, also a wider, smoothing differentiator can be used [109], or equivalently the image can be smoothed, for instance with a Gaussian blur filter, before calculating the gradient.

Instead of smoothing/blurring, typically in DIC implementations a method is used, which not only removes the short length scale information but also reduces the image size, thereby making it more efficient, which is sometimes called *coarse graining*. In this method images are created by averaging a groups of, 2×2 pixels into super-pixels. The operation is repeated on the super-pixeled images to create even coarser images, and-so-forth, see figure B.6.

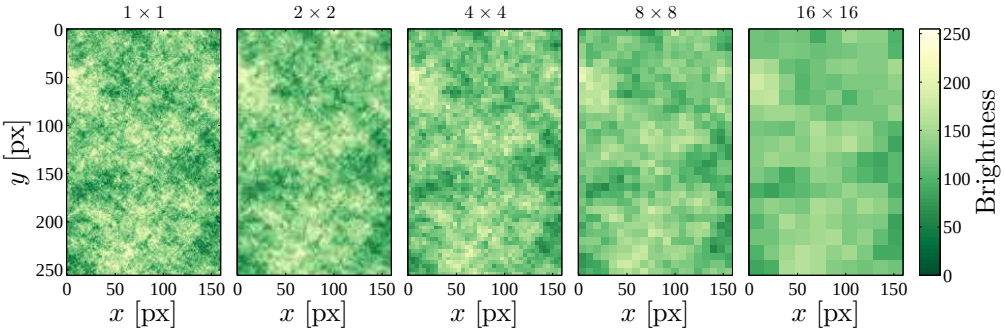

Figure B.6: An example pattern (left), which is coarse grained 4 times. The axes represent the original number of pixels, obviously, the coarse grained images have less pixels.

The correlation procedure is then first applied to the coarsest image. The obtained values for the degrees of freedom are then supplied as an initial guess to the next correlation step on a less coarse image, until finally arriving at the original image. Obviously, the coarse graining procedure exponentially reduces the number of pixels. As a result, the ratio of degrees of freedom versus pixels may become poor, resulting in a poorly conditioned correlation matrix. The solution is to reduce the number of degrees of freedom together with the number of pixels. This is possible because we are just looking for an adequate initial guess for the next coarse grain step.

The effect of coarse graining on the *initial guess robustness* can be visualized by the

auto-correlation potential,

$$A(u_x, u_y) = 1 - \frac{\mathrm{FFT}^{-1}\Big([\mathrm{FFT}(f)]^c \ \mathrm{FFT}(f)\Big)}{n\sigma^2}. \tag{B.98}$$

where FFT refers to the fast-fourier-transform function, as implemented in many programming languages, with $[\ldots]^c$ denoting the complex conjugate, n the number of pixels and σ the standard deviation of the pattern. This potential can be explained as the pattern f compared with itself at a distance u. This A is small for small distances $u \approx 0$ and increases to 1 for large u, see figure B.7. Instead of auto-correlating f with itself, f can be cross-correlated with g, which is actually the way conventional (local) DIC software packages find the displacement of one facet, hence the C in DIC.

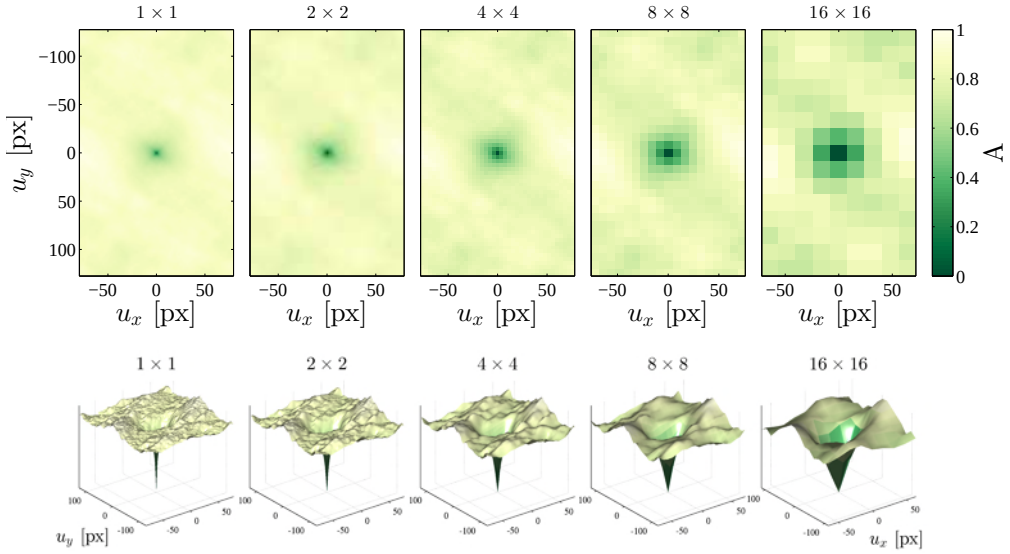

Figure B.7: The auto-correlation potentials A for the patterns shown in figure B.6, top and bottom figures are a different representation of the same data. Note that, coarse graining eliminates local minima and increases the correlation length (defined as the width of the potential at a height $A = 1 - e^{-1}$).

The shape of the potential can be interpreted as the landscape in which the NR procedure attempts to find the minimum, without taking the basis functions into account. Figure B.7 shows that coarse graining an image, smooths the short length scale features in the pattern, thereby, as desired, eliminating local minima. The figure also shows that, the shape of the potential becomes more blunt, which causes the DIC method to be less accurate (in the coarse grained image only).

Basis Functions

In the previous sections basis functions were applied, but the actual functions were is not discussed. Previously, the basis functions are introduced as a set of chosen functions φ_i with which the displacement field is approximated,

$$u(x_0) \approx u^*(x_0, \underline{\lambda}) = \sum_{i=1}^{m} \lambda_i \varphi_i(x_0), \tag{B.99}$$

where, λ_i are the corresponding degrees of freedom.

The basis functions define the solution space of the DIC problem, i.e. the kinematic restriction on the solution. In other words, if the real solution is not spanned by the basis functions, then it is never obtained. Intuitively, the richest solution space would then always give the best accuracy, which would be true if there was no acquisition noise (and no interpolation error to a lesser degree). The "smoothing" effect of using less degrees of freedom, allows for some noise averaging, which in most DIC cases is required to find any solution.

In short, *the minimal set of basis functions which span a solution space which has the real solution is the best set of basis functions.* Typically, the real solution is not known a priori, which is the reason why relatively general families of basis functions are used in DIC methods.

It is possible to categorize families of basis functions into three groups,

1. General basis functions, which are functions which have some noise smoothing but do not share any kinematic (mechanical) relation with the expected deformation field. Examples are,

Subsets/Facets, (i.e. local-DIC): these do not even enforce continuity.

Finite Elements (shape functions): these do enforce continuity. This is a useful option if the results are to be compared with a FEM simulation, especially when the same mesh is used in both worlds.

B-splines (or NURBS): these are similar to FE functions but allowing more fine grained control of the degrees of freedom.

2. Customized basis functions, which are functions which share some kinematic property with (or desirable to) the expected deformation field. Examples are,

crack/crack-tip functions, (XFEM): when studying crack growth

polynomial series, (e.g. Legendre polynomials): when the expected deformation is higher order smooth, e.g. C^2 continuity of bending problems [94]. Sometimes the material properties are linearly related to the degrees of freedom.

3. Integrated DIC basis functions, which are functions in which the degrees of freedom are precisely the parameters of a material model which is characterized on the current experiment [88]. IDIC comes in two forms,

analytic IDIC, in which the relation between u^* and its λ_i is known in closed form.

FEM-IDIC, not to be confused with the FE basis functions used above. In this form a FEM simulation is run in parallel to the DIC problem. Without going in too much detail, the unknown material parameters are used to generate basis functions with the FEM simulation (snapshots), which are then used in the DIC algorithm, this process is repeated until converged. Although generally slow, this method allows to construct a minimal kinematic basis with the ease of a FEM simulation, while having the optimum accuracy due to the limited number of degrees of freedom in DIC.

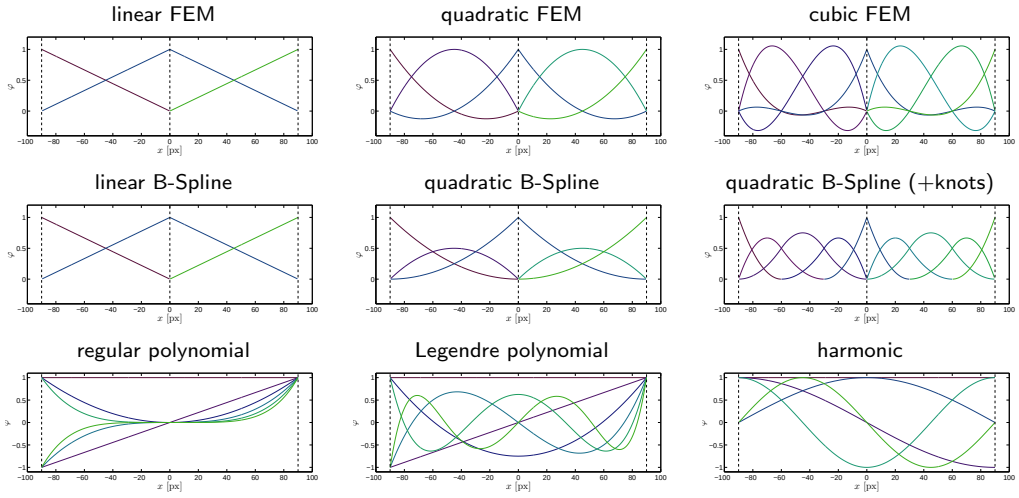

Figure B.8: Examples of 1D basis functions

Considering the third group (IDIC), a more general definition of the basis function is required,

$$u(x_0) \approx u^*(x_0, \underline{\lambda}) \tag{B.100}$$

$$\varphi_i(x_0) = \frac{\partial}{\partial \lambda_i}\Big[u^*(x_0, \underline{\lambda})\Big]. \tag{B.101}$$

For the case where the degrees of freedom in the function $u^*(x_0, \underline{\lambda})$ are only linearly dependent on each other, then (B.99) is again obtained. Although linear dependence is desirable for numerical reasons, it is not strictly required.

Finally, regarding FEM shape functions, although these seem a logical choice, they can be relatively complex to implement. The reason for this is that in DIC, the "integration points" are the pixel locations of $f(x_0)$. The locations of these points are known in the global coordinates, where in FEM the shape functions are typically defined in a coordinate

system local to the element, also known as master coordinates. For most FEM element types only the mapping from the master coordinates to the global coordinates is defined. This is no problem for most FEM uses, but for DIC the reverse mapping is required, i.e. the value of a shape function for a given pixel coordinate. The reverse mapping typically involves solving a non-linear problem which can be solved by using a (per pixel) Newton-Raphson scheme. For 1D elements, or for 2D linear triangles, the reverse mapping can be solved analytically, which makes them ideal for DIC. For non-linear elements another problem occurs, when determining to which element a pixel belongs, due to their non-straight edges.

Example 1D GDIC Matlab Code

```
% This is a minimal Global DIC Matlab code, to be used for educational
% purposes only. The code consists of four parts:
%  1) Virtual Experiment, this is where two 1D image are created virtually
%     from a specified pattern and a specified displacement field.
%  2) DIC Initialization, this is where the static components of the GDIC
%     method are calculated, e.g. the shape functions, correlation matrix,
%     etc.
%  3) Iterative solving, this is the iterative "Newton-Raphson" procedure
%     where the residual is minimized and the displacement field is found,
%     which should match with the input displacement field of part 1.
%  4) Plotting, which creates various figures detailing the results.
clear all ; close all

% options
convcrit = 1e-6;
maxiter = 20;

% create a space (field of view)
n = 300;
x = linspace(1,n,n);

% VIRTUAL EXPERIMENT
% ==========================

% create a virtual sample space (bigger than the fov)
nvir = 600;
xvir = linspace(1-0.2*n,n+0.2*n,nvir);

% generate a virtual pattern
a = [ 3  2  1  1];
b = [90 40 18  8];
c = [ 0  0  0  0];
fvir = zeros(1,nvir);
for k = 1:length(a)
   fvir = fvir + a(k)*sin(2*pi* (xvir - c(k)) ./ (b(k) ));
end

% Create a deformation field
umax = 5.5;
% this space is -1 and 1 on the left and right fov edges respectively.
uspace = (xvir-mean(x([1 end])))./(0.5*range(x));
uvir = umax*uspace.^2;
% store the deformation field on the fov space
uref = interp1(xvir,uvir,x,'spline');

% Create the reference image and deformed image (on the fov)
f = interp1(xvir,fvir,x,'spline');
g = interp1(xvir+uvir,fvir,x,'spline');
```

```
% DIC INITIALIZATION
% ==========================

% region of interest
roi(1) = 1 + 2*umax;
roi(2) = n - 2*umax;
Iroi = find(x > roi(1) & x < roi(2));
nroi = length(Iroi);
xroi = x(Iroi);
froi = f(Iroi);

% generate shape functions (linear FEM)
nphi =  8;
% node locations
nodes = linspace(roi(1),roi(2),nphi);
% initiate the basis function matrix
phi = zeros(nroi,nphi);
for k = 1:nphi
    if k == 1
        % for the left node
        I = find(xroi >= nodes(k) & xroi < nodes(k+1)) ;
        xx = xroi(I);
        w = nodes(k+1) - nodes(k);
        phi(I,k) = 1 - (xx - nodes(k))./w;
    elseif k == nphi
        % for the right node
        I = find(xroi > nodes(k-1) & xroi <= nodes(k)) ;
        xx = xroi(I);
        w = nodes(k) - nodes(k-1);
        phi(I,k) = (xx - nodes(k-1))./w;
    else
        % for the other nodes
        I = find(xroi >= nodes(k) & xroi < nodes(k+1)) ;
        xx = xroi(I);
        w = nodes(k+1) - nodes(k);
        phi(I,k) = 1 - (xx - nodes(k))./w;

        I = find(xroi > nodes(k-1) & xroi <= nodes(k)) ;
        xx = xroi(I);
        w = nodes(k) - nodes(k-1);
        phi(I,k) = (xx - nodes(k-1))./w;
    end
end

% direct fit results (for comparison only)
lambdafit = phi \ uref(Iroi)';
ufit = lambdafit' * phi';

% gradf (forward backward numerical differentiator)
dx = mean(diff(x));
gradf = gradient(froi,dx);

% least squares form of correlation matrix
L = zeros(nroi,nphi);
for k = 1:nphi
    L(:,k) = gradf(:) .* phi(:,k);
end
% the correlation matrix
M = L' * L ;

% initial guess
lambda = zeros(nphi,1);
% build initial displacement field
u = lambda' * phi';
% create the deformed version of g (gtilde)
gt = interp1(x,g,xroi+u,'cubic') ;

% ITERATIVE SOLVING
% ==========================
```

```
conv = 0;
it   = 0;
while ~conv
    it = it + 1;

    % right hand member
    b = L' * ( froi(:) - gt(:) );
    % solve for change in degrees of freedom
    dlambda = M\b;
    % update the degrees of freedom
    lambda  = lambda + dlambda;
    % create the updated displacement field
    u = lambda' * phi';
    % create g-tilde (i.e. the gray values of f, in the image g, if converged)
    gt = interp1(x,g,xroi+u,'spline') ;
    % residual
    psi = froi - gt;

    % print results to the command window
    fprintf('it:%2d, ',it);
    fprintf('norm(r):%10.3e,  ',norm(psi));
    fprintf('norm(b)/n:%9.2e,  ',norm(b)/n);
    fprintf('norm(dlambda):%9.2e\n',norm(dlambda));

    % test for convergence
    conv = (norm(b)/n) < convcrit;
    if it >= maxiter
        fprintf('!!! => Maximum iterations reached\n');
        break
    end
end

% PLOTTING
% ==========================
figure('Position',[100 50 800 1000])
ha(1) = subplot(5,1,1);
plot(x,f,'.-',x,g,'o-',xroi,gt,'*-')
ylabel('brightness');legend({'f','g','gt'},'Orientation','Horizontal')

ha(2) = subplot(5,1,2);
plot(x,uref,'.-',xroi,ufit,'o-',xroi,u,'*-')
ylabel('u [px]');legend({'uref','ufit','u'},'Orientation','Horizontal')

ha(3) = subplot(5,1,3);
h = plot(xroi,phi,'.-');
colors = mat2cell(0.8*jet(nphi),ones(1,nphi),3);
set(h,{'color'},colors)
ylabel('phi')

ha(4) = subplot(5,1,4);
plot(xroi,psi,'.-')
ylabel('psi [px]');legend({'psi'},'Orientation','Horizontal')

ha(5) = subplot(5,1,5);
plot(xroi,uref(Iroi)-u,'.-',xroi,uref(Iroi)-ufit,'o-')
ylabel('u error [px]');legend({'uref-u','uref-ufit'},'Orientation','Horizontal')

xlabel('x [px]');
set(ha,'xlim',[min(x) max(x)])
```

Appendix C
Brief description of the EGP model

In the Eindhoven Glassy Polymer (EGP) model [90], the polymer behavior is modeled by two contributions acting in parallel. The first, $\boldsymbol{\sigma}_s$, is the visco-elastic contribution related to the inter-molecular interaction which is responsible for the low-strain behavior including yield and strain softening. The second, $\boldsymbol{\sigma}_r$, is the contribution of the molecular network, responsible for strain hardening in the large-strain regime,

$$\boldsymbol{\sigma} = \boldsymbol{\sigma}_s + \boldsymbol{\sigma}_r. \tag{C.1}$$

The hardening stress $\boldsymbol{\sigma}_r$ is modeled as a neo-Hookean formulation [124],

$$\boldsymbol{\sigma}_r = G_r \tilde{\boldsymbol{B}}^d, \tag{C.2}$$

with G_r the strain hardening modulus, and $\tilde{\boldsymbol{B}}^d$ the deviatoric part of the isochoric left Cauchy-Green strain tensor. The driving stress is split in a hydrostatic and a deviatoric part, the latter is typically modeled with a combination of n parallell Maxwell elements.

$$\boldsymbol{\sigma}_s = \boldsymbol{\sigma}_s^h + \sum_{i=1}^{n} \boldsymbol{\sigma}_{s,i}^d = \kappa(J-1)\boldsymbol{I} + \sum_{i=1}^{n} G_i \tilde{\boldsymbol{B}}_{e,i}^d, \tag{C.3}$$

$$\tag{C.4}$$

where, κ is the bulk modulus, J the volume change ratio, $\boldsymbol{I}$ the unity tensor, G the shear modulus and $\tilde{\boldsymbol{B}}_e$ the elastic part of the isochoric left Cauchy-Green strain tensor. For the example discussed in section 8.3 the number of Maxwell elements equals one, making the summation redundant. The time and history dependence of the model is updated by introducing the time evolution of $\tilde{\boldsymbol{B}}_e$ and J,

$$\dot{J} = J\,\mathrm{tr}(\boldsymbol{D}), \tag{C.5}$$

$$\dot{\tilde{\boldsymbol{B}}}_{e,i} = (\tilde{\boldsymbol{L}} - \boldsymbol{D}_{p,i}) \cdot \tilde{\boldsymbol{B}}_{e,i} + \tilde{\boldsymbol{B}}_{e,i} \cdot (\tilde{\boldsymbol{L}}^c - \boldsymbol{D}_{p,i}), \tag{C.6}$$

where $\tilde{\boldsymbol{L}}$ is isochoric velocity gradient tensor and $\boldsymbol{D}_p$ the plastic deformation rate tensor. The latter is modeled with a non-Newtonian flow rule with modified Eyring viscosity η_i,

$$\boldsymbol{D}_{p,i} = \frac{\boldsymbol{\sigma}_{s,i}^d}{2\eta_i(T, \bar{\boldsymbol{\tau}}, p, S)}. \tag{C.7}$$

The modified Eyring viscosity depends on the temperature T, the equivalent stress $\bar{\boldsymbol{\tau}}$, the pressure p and the strain softening S,

$$\eta_i(T, \bar{\boldsymbol{\tau}}, p, S) = \eta_{0,i} \frac{\bar{\boldsymbol{\tau}}/\tau_0}{\sinh(\boldsymbol{\tau}/\tau_0)} \exp\left[\frac{\mu p}{\tau_0}\right] \exp\left[S(\bar{\gamma}_p)\right], \tag{C.8}$$

where the important parameters are: $\eta_{0,i}$, the zero-viscosity; τ_0, the characteristic stress; μ, the pressure dependence parameter. Finally, the model is completed through the softening function [21],

$$S(\bar{\gamma}_p) = S_a \frac{\left(1 + [r_0 \exp(\bar{\gamma}_p)]^{r_1}\right)^{(r_2-1)/r_1}}{\left(1 + r_0^{r_1}\right)^{(r_2-1)/r_1}}, \tag{C.9}$$

where S_a captures the initial thermodynamic state which increases the yield stress with respect to the rejuvenated state of the material. The parameters r_0, r_1 and r_2 are three fit parameters which control the shape of the softening response of the model as a function of the plastic strain $\bar{\gamma}_p$.

Samenvatting

Rekbare elektronica is een nieuw onderzoeksveld dat zich richt op het integreren van elektronica in en om het menselijk lichaam. Enkele voorbeelden zijn; gevoelige kunsthuid, opvouwbare beeldschermen, neuro- of retinaverbindingen en op de huid gedragen registratieapparatuur. Typische rekbare elektronica is gemaakt van elektrische componenten en bedrading in rubberen films. Deze constructie creëert een rekbaarheidsconflict tussen het uiterst rekbare rubber en de stijve componenten, vooral met de metalen bedrading. Het is bekend dat vooral de metaal-rubber grenslaag een belangrijke factor is in het faalgedrag. Een sterke grenslaag zorgt dat krachten kunnen worden doorgeleid, met als gevolg dat het loslaten van de hechting snel wordt gevolgd door het falen van het apparaat. Het begrijpen van de grenslaagmechanica is daarom essentieel in het verbeteren van rekbare elektronica. Bovendien is de karakterisering van de grenslaageigenschappen noodzakelijk voor het modelleren en voorspellen van het faalgedrag in de grenslagen.

Het eerste deel van het proefschrift bespreekt het pelgedrag van grenslagen op drie belangrijke lengteschalen, aan de hand van peltest-experimenten. Beelden bij aanzienlijke vergroting laten zien dat er 30 µm lange fibrillen ontstaan, verlengen en falen in het pelfront. Het fibrillatiemechanisme wordt geïnitieerd door de sterke ruwheid van het metaaloppervlak. Er wordt bediscussieerd dat de in de fibril opgeslagen elastische energie verloren gaat op het moment van fibrilfalen, wat leidt tot een verrassend hoge hechting. Waarschijnlijk is het mogelijk dit mechanisme te benutten door de hechting van vergelijkbare grenslagen te verbeteren.

Het tweede deel van het proefschrift beschrijft een nieuwe experimentele techniek, gericht op het testen van gestructureerde proefstukken op de microschaal. Experimenteren op de microschaal is uitdagend, vooral het verhandelen en vastklemmen van de delicate proefstukken. De besproken methode vervormt dunne membranen tot een complexe bultvorm door middel van een drukverschil. Een 3D profilometrische oppervlakmeettechniek is aangewend om de vervormingen te meten. De voorgestelde methode spiegelt het onbekende materiaalmodel direct met de gemeten oppervlakken om op die manier de onbekende materiaalparameters te vinden, met als extra gevolg robuustheid en ruisongevoeligheid. De daaruit voortvloeiende methode blijkt veelzijdig en opent experimentele deuren door experimentele complexiteit aan te moedigen en zelfs de complexiteit te benutten, zoals noodzakelijk voor de analyse van de grenslaaghechting van rekbare elektronica.

Dankwoord

Ongeveer vijf jaar geleden koos ik voor een promotieproject onder begeleiding van Johan, zonder eigenlijk te beseffen wat dat betekende. Ik was als Alice (in Wonderland), nieuwsgierig naar het einde van "the rabbit hole". Onderweg heb ik immens veel geleerd van de mensen om me heen en ik ben hen hier dankbaar voor. Met name Johan; ik wil jou bedanken voor je visie en passie, die twee essentiële ingrediënten vormden van de vele en genadeloze discussies die we gedeeld hebben, maar ook wil ik je bedanken voor de vrijheid en ruimte die je me gegeven hebt om te groeien. Marc, als promotor en begeleider wil ik je bedanken voor de rust en leiding die je me geboden hebt. De wijze waarop je respect verwerft heeft mijn bewondering gewekt en mede daardoor kijk ik met eerbied naar jou als persoon en professor. Andere Marc, bedankt voor de vele uren dat je me geholpen hebt in het lab, dat je mij de experimentele opstellingen hebt leren gebruiken, maar ook voor de begeleiding van alle studenten waar ik je mee opgezadeld heb. Alice en Leo, jullie wil ik beide bedanken voor alle zorgen tijdens de afgelopen tijd, zonder jullie was het niet mogelijk geweest. Ook alle studenten die ik heb mogen begeleiden gedurende de promotie wil ik graag bedanken; Jacqueline, Andre, Erik, Joeri, Bart, Omid, Kaipeng, Joost, Tom, Uriël, Thijs, Leo, Bram, Jeroen, Fabian, Wouter, en Don. Het was plezierig en leerzaam om bij jullie projecten betrokken te zijn. Ik wil ook graag alle M@te collega's bedanken voor de vele ongeremde discussies en leuke conferentie-uitstapjes die jullie met mij gedeeld hebben. Door de internationale mix ben ik in contact gekomen met veel culturen, en is mij nogmaals duidelijk geworden dat in alle hoeken van de wereld aardige mensen te vinden zijn. In het bijzonder wil ik graag mijn collega-kamergenoten bedanken; Paul, Tom, Bart, Danquin, Young Joon, Andre. Bedankt voor de "white board" sparring sessies waardoor ik rijkelijk gebruik heb kunnen maken van jullie kennis en vaardigheden. Uiteraard ook Lambert, met wie ik vele avonden heb zitten typen in een donker en stil W-hoog, bedankt voor je broederschap.

Uiteindelijk bedank ik mijn ouders, zus en Björn voor de steun in zowel mooie als donkere dagen. Dankzij jullie motivatie en oeverloze vertrouwen heb ik door kunnen zetten en ben ik uiteindelijk op mijn pootjes geland. Het laatste woord is natuurlijk voor de belangrijkste persoon, die het meeste heeft moeten verduren tijdens de eenzame, lange dagen van de promotie, mijn schat en liefde Denise; Ik bedank je met heel mijn hart, ik ben je voor eeuwig dankbaar.

Jan,
Oktober 2013

Curriculum vitae

Jan Neggers is born on the 3rd of February 1981 in Eindhoven, the Netherlands. After graduating secondary education and a futile period at polytechnical institutes, he enrolled in the Bachelor program of Mechanical Engineering at the Eindhoven University of Technology in 2004. Finishing the bachelor program with the project "Modeling porcine brain slices in detail", he started with the Mechanical Engineering master in the group Mechanics of Materials of prof.dr.ir. M.G.D. Geers in 2007. During the master, he performed an internship at the University of Virginia at the Center for Applied Biomechanics of prof. J.R. Crandall. The internship work lead to the publication, "Indentation Response of Human Patella with Elastic Modulus Correlation to Localized Fractal Dimension and Bone Mineral Density". Following the internship he started the master thesis within the PhD project, graduating for the master in 2009. The PhD project was titled "Novel Routes Towards Interfacial Integrity in Stretchable Electronics" at the Eindhoven University of Technology in the group of prof.dr.ir. M.G.D. Geers, under supervision of J.P.M. Hoefnagels, of which the results are presented in this dissertation. In 2011 he was awarded the best student paper award at the annual conference of the Society for Experimental Mechanics, for the work titled "Full-field Bulge Testing Using Global Digital Image Correlation".

List of publications

Publications following from dissertation chapters:

(Chap. 2) J.P.M. Hoefnagels, J. Neggers, P.H.M. Timmermans, O. van der Sluis and M.G.D. Geers, *Copper-rubber interface delamination in stretchable electronics*, Scripta Materialia, 63 (2010) 875–878

(Chap. 3) J. Neggers, J.P.M. Hoefnagels, O. van der Sluis, and M.G.D. Geers, *Multi-scale experimental analysis of metal-elastomer interface mechanics*, *submitted*

(Chap. 4) J. Neggers, J.P.M. Hoefnagels, O. van der Sluis, O. Sedaghat and M.G.D. Geers, *Characterization and analyses of metal-elastomer interface fibrillation*, *submitted*

(Chap. 5) J. Neggers, J.P.M. Hoefnagels and M.G.D. Geers, *On the Validity Regime of the Bulge Equations*, Journal of Materials Research, 27-9 (2012) 1245–1250

(Chap. 6) J. Neggers, B. Blaysat, J.P.M. Hoefnagels and M.G.D. Geers, *A consistent solution scheme for digital image correlation*, Experimental Mechanics, *review in progress*

(Chap. 7) J. Neggers, J.P.M. Hoefnagels, F. Hild, S.G. Roux and M.G.D. Geers, *Direct stress-strain measurements from bulged membranes using topography image correlation*, Experimental Mechanics, *review in progress*

(Chap. 8) J. Neggers, J.P.M. Hoefnagels, M.G.D. Geers, F. Hild, and S.G. Roux, *A time-resolved integrated digital image correlation identification method*, *submitted*

Other published work:

- J. Neggers, J.P.M. Hoefnagels, F. Hild, S.G. Roux and M.G.D. Geers, *A Global Digital Image Correlation Enhanced Full-Field Bulge Test Method*, Procedia IUTAM, 4 (2012) 73–81
- L.I.J.C. Bergers, J. Neggers, M.G.D. Geers and J.P.M. Hoefnagels, *Enhanced Global Digital Image Correlation for Accurate Measurement of Microbeam Bending*, In H. Altenbach & S. Kruch (Eds.), Advanced Materials Modelling for Structures (Vol. 19, pp. 4351). Berlin, Heidelberg: Springer
- J. van Beeck, J. Neggers, P.J.G. Schreurs, J.P.M. Hoefnagels and M.G.D Geers, *Quantification of three-dimensional surface deformation using Global Digital Image Correlation. Experimental Mechanics*, Experimental Mechanics, (2014) *accepted*
- J. R. Kerrigan, D. Sanchez-Molina, J. Neggers, C. Arregui-Dalmases, J. Velazquez-Ameijide, and J.R. Crandall, *Indentation Response of Human Patella with Elastic Modulus Correlation to Localized Fractal Dimension and Bone Mineral Density*, Journal of the mechanical behavior of biomedical materials, (2014) *accepted*.
- J. Neggers, J.P.M. Hoefnagels, O. van der Sluis O. Sedaghat, M.G.D. Geers, *Interface integrity in stretchable electronics*, Conference Proceedings of the Society for Experimental Mechanics Series 6, (2011) 577–581
- J. Neggers, J.P.M. Hoefnagels, F. Hild, S.G. Roux and M.G.D. Geers, *Full-field bulge testing using global digital image correlation*, Conference Proceedings of the Society for Experimental Mechanics Series 4, (2011) 99–103
- J. Neggers, J.P.M. Hoefnagels, F. Hild, S.G. Roux and M.G.D. Geers, *Global digital image correlation for pressure deflected membranes*, Conference Proceedings of the Society for Experimental Mechanics Series 6, (2013) 135–140